

High-Kinetic Inductance Superconducting Technology for Quantum Applications

Présentée le 20 janvier 2023

Faculté des sciences et techniques de l'ingénieur
Laboratoire d'architecture quantique
Programme doctoral en microsystèmes et microélectronique
pour l'obtention du grade de Docteur ès Sciences
par

Simone FRASCA

Acceptée sur proposition du jury

Prof. Y. Bellouard, président du jury
Prof. E. Charbon, directeur de thèse
Prof. S. Pagano, rapporteur
Prof. R. Hadfield, rapporteur
Dr G. Boero, rapporteur

ABSTRACT

Superconducting materials present unique properties, which make a potential technological platform based on superconductors extremely appealing for a wide set of applications, both classical and not. Among these classes of materials, high-kinetic inductance "dirty" superconductors, *i.e.* superconductors rich in impurities, offer an extra layer of flexibility in terms of achievable impedance and compactness, with applications in a variety of electronics devices and in particular in the field of sensing. By controlling and fine-tuning the superconducting properties of dirty superconductors, it is possible to design both materials and devices for optimal performance. In this dissertation, we present a platform based on different variants of niobium nitride, which are employed for distinct families of applications. First, we discuss various ways to deposit thin films of dirty superconductors, with respective advantages and disadvantages, and potential relevant design strategies. Then, we focus on four main fields of applications. The first application regards three-dimensional integration, with the use of superconducting through-silicon vias and its integration within the superconducting platform. The second is sensing, *i.e.* single-photon sensing and current sensing, represented respectively by superconducting nanowire single-photon detectors and nanocryotrons. Thirdly, circuits based on compact resonating structures are discussed for their applications in circuit quantum electrodynamics, first by assessing the role of kinetic inductance for internal loss and nonlinearity, and then by producing compact impedance matching structures and filters. Lastly, we present a superconducting transmon qubit based on classical superconducting materials, to be used as reference for high kinetic inductance qubits to be developed in the future.

SOMMARIO

I materiali superconduttori presentano proprietà uniche, che rendono una potenziale piattaforma tecnologica basata su superconduttori estremamente interessante per un'ampia gamma di applicazioni, sia classiche che non. Tra queste classi di materiali, i superconduttori "sporchi" ad alta induttanza cinetica, cioè superconduttori ricchi di impurità, offrono un ulteriore livello di flessibilità in termini di impedenza ottenibile e compattezza, con applicazioni in una varietà di dispositivi elettronici e in particolare nel campo dei sensori. Controllando e mettendo a punto le proprietà superconduttrive dei superconduttori sporchi, è possibile progettare materiali e dispositivi per prestazioni ottimali. In questa tesi, presentiamo una piattaforma basata su diverse varianti di nitruro di niobio, che vengono utilizzate per una svariata gamma di applicazioni. In primo luogo, discutiamo vari modi per depositare film sottili di superconduttori sporchi, con rispettivi vantaggi e svantaggi, e potenziali strategie di progettazione ottimali. Quindi, ci concentriamo su quattro principali campi di applicazione. La prima applicazione riguarda l'integrazione tridimensionale, con l'utilizzo di vie superconduttrive attraverso-silicio e la loro integrazione all'interno della piattaforma superconduttrice. La seconda riguarda la sensoristica, cioè rilevamento di singoli fotoni e rilevamento di corrente, rappresentati rispettivamente da rivelatori di singolo fotone a nanofili superconduttori e *nanocryotrons*. In terzo luogo, vengono discussi i circuiti basati su strutture risonanti compatte per le loro applicazioni nel campo dei circuiti in elettrodinamica quantistica, prima valutando il ruolo dell'induttanza cinetica per la perdita interna e la non linearità, quindi producendo dispositivi come filtri compatti e strutture per adattamento dell'impedenza. Infine, presentiamo un qubit superconduttivo, un transmone, basato su materiali superconduttori classici, da utilizzare come riferimento per qubit ad alta induttanza cinetica da sviluppare in futuro.

ACKNOWLEDGMENTS

A PhD is a journey in which you meet and work with a wide variety of people, and it gives you the chance to grow in unique ways and provides you with a skill set you can, to some extent, shape according to your own interests. Looking at it from *the other side*, I cannot recommend enough an experience like this for someone who wants to build a career not necessarily in academia, but in science in a wider sense.

My journey would have not been possible without my supervisor **Edoardo**, who gave me the opportunity to join AQUA and start the topic of superconducting technologies in his laboratory, for his guidance and for his help in the moments of need but also for the freedom to operate he always left me. Thank you for giving me the opportunity of investigate different topics during my thesis, allowing me to explore both inside and outside the box. I am also grateful to all my PhD committee, the president **Yves** and the internal and external members **Giovanni, Robert** and **Sergio**, for the great discussion during my defense. Thank you for taking the time to be there and evaluate my work.

Before proceeding with the more "detailed" acknowledgements, I'd like to give a very general big thank you to the whole EPFL. This is a great place to do science, and in particular a PhD, thanks mostly to everyone working here. I had the pleasure to interact with people from different backgrounds, fields, interests, yet still feeling part of the same community. This sense of unity is what makes EPFL unique in my eyes, and it is no doubt possible only as the result of the joint efforts of all its members.

There are countless people without whom this thesis work would have not been possible, and as hard as it could be to acknowledge all of them, I'll do my best, hoping not to leave anyone out. Thank you all for being part of this journey.

First and foremost, I want to thank **Ivo, Rebecca, Benoît, David, Grégoire, Sébastien, Louis, Kléber, Christian, Pierre, Vera, Jashandeep, Philippine, Giuliano** and **Roberto**, Master students in Microtechnology or Electrical Engineering at EPFL and future successful engineers and scientists I had the honor to supervise, for their great help throughout the years with everything was done regarding fabrication, testing, data analysis, designs, simulations... you were the fuel of the engine, I will miss you all and will be always grateful. I will very much miss our #pizzaMondays;

all of AQUA lab, in particular my friend **Jad** with whom I have been sharing the office and the several intricacies of cryogenics during these years; **Andrada, Andrei, Preethi, Bedirhan** and **Arin** for the good times spent together before I moved to Lausanne; **Claudio, Brigitte** and **Begonia** for always being available for all type of discussion and for making the lab a nice workplace;

my "other" lab's colleagues and friends, **Vincent, Fabian, Franco, Guillaume**, and more recently **Léo**, for the time inside and out of the labs, for the beers, the laughs, for sharing the pain of research and in particular, the pain of fabrication when nothing works;

my dear friends **Luchó** and **Ale** for being amazing friends inside and outside of the campus, for the *empanadas*, for the *matambre a la pizza*, for the useful discussions and for the fruitful collaborations. I'd also like to thank their supervisor **Andreas**, for being an inspiration of work integrity and for letting us explore different kind of ideas;

my EPFL community friends, **Carsten**, my reference point for anything that is cryogenics and magnetism, and for teaching me all I know about dilution systems; **Marco S** and **Fabrizio M** for all the mini-lectures, explanations, papers discussions, fabrication and problem solving times; **Enrico, Michal, Ruben, Olivier, Gözden**, for being the teaching-assistants dream team, so much laughs, so much good time, I enjoyed every single day of being TA thanks to you all; my cleanroom friends, in particular **Nino, Alessandro** and **Jean-Michel** from the cleanrooms in IPHYS, **Marica, Marco L, Alberto e Alessio M** from the CMi; my life science friends, **Alice, Bianca, Radiana, Céline** and **Katarina** for the last minute lunches with Fabio and for the good times spent together;

many EPFL faculty members: **Sandro** for the useful discussions and continuous collaborations regarding the Michelangelo process, **Fabrizio C** for the insight on electron measuring detectors and for hosting our system in his laboratory in the moment of need; **Pasquale**, for being a second supervisor not on paper but in discussions, help, contributions, collaborations: I have learnt a lot in these last two years and you opened up a new, challenging and exciting field to me and I will be always grateful;

different support staffs in EPFL: the whole CMi staff, and in particular to **Joffrey, Didier, Niccoló, Rémy, Cyrille, Giancarlo, Adrien, Blaise**, for the trainings and continuous teaching, useful discussions and guidance in developing all the processes flows from bare ideas; a special thanks goes to **Zdenek**, who has been not only the best e-beam support one could dream for, but also a friend outside of the

campus, and my personal *sensei* of photography; the IPHYS cleanroom staff, for letting me explore with fabrication recipes, being supportive even when things were not working well and being always open to ideas to make the cleanroom a better place for everyone. In particular, **Nicolas** for being an amazing cleanroom manager and a great friend, **Yoan** and **Damien** for their dedication and help; the CiMe staff, in particular **Fabienne**, **Lucie**, **Reza** and **Marco C** for the tranings in SEM, FIB and TEM and their help is in making fantastic micrographs and for the useful discussions regarding the e-SPAD experiment;

the Sinergia project members: from ETH Zürich/CERN, **Sofia** and her supervisor **Werner** for the simulations of the scintillating crystals; from EPFL PVLAB, **Janina**, **Samira** and their supervisor **Nicolas** for the collaboration on the high-aspect ratio holes fabrication; from EPFL LIB, **Michael** first and **Pol** after for their help in generating the image processing software;

the staff of the companies I have dealt with the most, in particular thanks to **Vikas** for the great discussions and the fantastic installation of the cryostat from PhotonSpot, and for his help and flexibility during the organization, to **Pietro**, for the great project that lead us to the ultrafast oscilloscope from Tektronix, and to **Jean-Luc** for the projects of the vectors analyzers from Rohde & Schwarz, it was a pleasure to work with you all;

my friends outside the workplace, because without them it would have been impossible to maintain mental stability throughout these four years, and to be completely honest with you, I have doubts we all succeeded in the mission. Thank you to **Fabio**, for being a re-found friend after such a long time, for his being the one who convinced me to move to Lausanne, for being *the Napoli supporter*, for the audio notes sent from the lab with Radio KissKiss in the background, but overall, just for being a true good friend; **Francesco R, il presidente**, also father founder of the group and unavoidable link to everyone we all may know in Lausanne; **Alessio P**, for being the nicest and most normal of us all, until we finally changed him; **Matteo**, **Andrea**, **Francesco C**, **Daniele T** and **Leonardo**, for sharing all the good memories and moments of these last years, all the Napoli games either home or at the restaurant of **Daniele M**, for being proud elements of the MUPDFQ group, for the attempted mass murder when you brought all of us on top of a crest for a "quick hike", for all the little step that we shared and that brought me here today; **Simone**, **Kazem**, **Yaquequin** and **Eduard** for being great friends for both me and Anna and for sharing great time together;

my lifelong friends, **Ciro**, **Federica**, **Francesco E** and **Francesco Q**, for always being there to support me in more ways than they can imagine, being the great friends they are; **Manuel** and **Marcello**, my brothers in arms from Pisa, for being best consultants one can have when things were not clear and I need a different point of view; **Antonio**, **Cinzia** and **Isabella**, who went from teachers to friends to family during the years, and without whom I would have never grown my passion for science and I would have not become the person I am today;

all of my french family, but in particular thanks to **Claire** and **Thierry** for being the parents in law everyone dreams of, for being present at the important steps of our lives and for making me feel accepted in their family as one of their own;

my family, as their support was crucial when the time were at their darkest. To my large, *large* family, all of you. To my **grandparents**, the three that are no longer with us and the one still ruling us all, thank you because you were and are all a true inspiration, and will always be. To **Piera**, for being the perfect second mom, for being there when I needed it, without asking anything in return, like a mom does. To my **dad**, for the great father he is and for his huge heart, for the classic phone call post-Napoli match, for the love and happiness he was able to transmit with thirty second of video call, for being the example everyone should have. To my **mom**, for the typhoon energy she is able to transmit with a smile, and for the fierceness she is ready to defend us from any pain; to my brothers, **Federico** and **Alessandro**, for being my best friends, for making all about a joke, for lifting weights when I cannot, for being so smart to make me as your older brother as proud as one can be, for pushing me to be better, to always be a worthy example to your eyes;

and finally, to my partner in life, **Anna**, which I met half way through my journey here. What to say? I don't believe words could possibly explain. If only because it lead me to you, it was all worth it.

Lausanne, December 2022

Simone Frasca

*To my brothers, for teaching me the importance
of trying to be a good example.*

CONTENTS

ABSTRACT	I
SOMMARIO	III
ACKNOWLEDGMENTS	V
CONTENTS	X
LIST OF SYMBOLS	XV
LIST OF PUBLICATIONS	XXIII
1 INTRODUCTION	1
1.1 Superconducting technology	2
1.1.1 Dirty superconductors and kinetic inductance	2
1.1.2 Josephson effect and junctions	3
1.2 Applications of superconducting technology	4
1.2.1 Single-photon detectors	5
1.2.2 Superconducting electronics	7
1.2.3 Quantum computing	8
1.3 This PhD thesis contributions	8
1.3.1 Thesis structure	9
2 HIGH KINETIC INDUCTANCE SUPERCONDUCTORS	11
2.1 Niobium-based dirty superconductors	13
2.1.1 NbN from reactive RF sputtering	13
2.1.2 NbN from atomic layer deposition	15
2.2 Titanium-based dirty superconductors	17
2.2.1 TiN from reactive RF sputtering	18
2.2.2 TiN from atomic layer deposition	18
2.3 Niobium titanium nitride	19
2.3.1 NbTiN from Nb and Ti reacting RF co-sputtering	20
2.4 High kinetic inductance from organized crystals: granular Aluminum	21
2.5 Discussion	22
3 3D INTEGRATION: THROUGH-SILICON VIAS	23
3.1 DRIE optimization	24
3.1.1 Chromium and Aluminum hard masks	26
3.1.2 Holes and trenches	28
3.2 Surface polishing: the Michelangelo step	30

3.3	Through-Silicon vias metallization	32
3.3.1	Electroplating	33
3.3.2	Metal infiltration	34
3.3.3	Superconducting TSV	36
3.4	Discussion	37
4	SUPERCONDUCTING NANOWIRE SINGLE-PHOTON DETECTORS	39
4.1	Design and fabrication	42
4.2	Characterization	45
4.2.1	Efficiency measurements	48
4.2.2	Timing jitter measurements	50
4.3	Discussion	53
5	NTRONS: THE NANOCRYOTRONS TECHNOLOGY	55
5.1	Design and fabrication	56
5.1.1	The avalanche-effect nanocryotron: the α_x Tron	57
5.2	Characterization	58
5.3	Discussion	62
6	HIGH KINETIC INDUCTANCE CIRCUITS	65
6.1	Quality factor of high- L_k resonators	66
6.1.1	Self-Kerr nonlinearity	69
6.1.2	TLS losses and aging	72
6.2	Impedance matching taper	75
6.3	Microwave filtering using periodic structures	78
6.4	Discussion	83
7	PLANAR TRANSMON QUBIT	85
7.1	Design and fabrication	86
7.2	Characterization	89
7.2.1	Relaxation time	93
7.2.2	Decoherence time	96
7.2.3	Readout fidelity measurements	96
7.3	Discussion	97
8	CONCLUSIONS AND PERSPECTIVES	99
A	FABRICATION METHODS	101
A.1	Process flows	101
A.1.1	SNSPD process flow	102
A.1.2	Superconducting circuits process flow	103
A.1.3	Through-Silicon vias process flow	104

A.1.4	Transmons process flow	105
A.2	Fabrication techniques	106
A.2.1	Thin films deposition	106
A.2.2	Patterns design and lithography	108
A.2.3	Lift-Off process	111
A.2.4	Etching process	111
A.3	Metrology techniques	114
A.3.1	Optical materials characterization	114
B	EXPERIMENTAL SETUPS	117
B.1	Cryo-optical setup	117
B.1.1	^4He sorption cryocooler	117
B.1.2	Electronics	119
B.1.3	Optics	120
B.2	Deep cryogenic temperature setup	123
B.2.1	^3He - ^4He dilution refrigerator	124
B.2.2	Electronics	125
B.3	Experiments control software	126
B.3.1	Measurement of T_C	127
C	CHIP GALLERY	129
LIST OF FIGURES		134
LIST OF TABLES		138
BIBLIOGRAPHY		140
CURRICULUM VITÆ		155

LIST OF SYMBOLS

Symbol	Meaning
$\alpha = \omega_{12} - \omega_{01}$	Anharmonicity
ADC	Analog-to-digital converter
ADRIE	Adaptive-DRIE
AFM	Atomic force microscope
ALD	Atomic layer deposition
<i>AR</i>	Aspect ratio
ARDE	Aspect ratio dependent etching
AWG	Arbitrary wave generator
$\beta = \sqrt{ZY} = \omega\sqrt{LC}$	Propagation constant
BCS theory	Bardeen, Cooper and Schrieffer theory
$\chi = \frac{g^2}{\Delta} \frac{\alpha}{\Delta+\alpha}$	Dispersive shift
CPB	Cooper pair box qubit
CPW	Coplanar waveguide
DHF	Buffured-HF
<i>C</i>	Constriction factor
CMi	Center of nano- and microtechnology
cQED	Circuit quantum electrodynamics
CMOS	Complementary metal-oxide semiconductor
Δ	Superconducting energy gap
D_B	Base dose
DBR	Distributed Bragg reflector
DCM	Diameter correction method
<i>DCR</i>	Dark count rate
<i>DDE</i>	Device detection efficiency

Symbol	Meaning
DREM	Deposit, remove, etch, multistep
DRIE	Deep reactive ion etching
$\eta_{\text{absorption}}$	Optical absorption efficiency
η_{coupling}	Optical coupling efficiency
η_{QE}	Internal quantum efficiency
η_{trigger}	Trigger efficiency
$ e\rangle$	Excited state
$E_C = \frac{e^2}{2C_q}$	Charging energy
$E_J = \frac{I_C \Phi_0}{2\pi}$	Josephson energy
$\text{erf}(x)$	Error function
$\text{erfc}(x) = 1 - \text{erf}(x)$	Complementary error function
ϕ	Superconducting phase difference
$\Phi_0 = h/2e$	Superconducting flux quantum
Φ_{ext}	External magnetic flux
ϕRM	ϕ rotation method
\mathcal{F}	Fidelity
f_{bw}	Design bandwidth frequency
$F\delta_{\text{TLS}}^0$	TLS loss rate
$FF = w/p$	Fill factor
FIB	Focused ion beam (microscope)
FWHM	Full-width at half-maximum
γ	Internal loss rate
$\gamma^{\text{Purcell}} = (\frac{g}{\Delta})^2 \kappa_r$	Purcell decay loss rate
Γ_1	Relaxation rate
Γ_2	Decoherence rate
Γ_ϕ	Pure dephasing rate
g	Coupling rate between readout resonator and qubit

Symbol	Meaning
$ g\rangle$	Ground state
G–L theory	Ginzburg and Landau theory
GUI	Graphical user interface
grAl	Granular aluminum
h	Planck's constant
$\hbar = h/2\pi$	Reduced Planck's constant
H_C	Superconducting critical magnetic field
H_{disp}	Dispersion Hamiltonian
H_{JC}	Jaynes–Cumming Hamiltonian
HEMT	High electron mobility transistor
I_{bias}	Biasing current
I_C	Superconducting critical current
I_{dep}	Superconducting critical depairing current
I_G	nTron/a _x Tron gate current
I_{hs}	Hotspot current
I_{sw}	Superconducting switching current
ICP	Inductively coupled plasma (etching)
j_{bias}	Bias current density
j_{crit}	Critical current density
j_{dep}	Depairing critical current density
$J_{\text{intrinsic}}$	Intrinsic jitter
J_{optical}	Optical jitter
$J_{\text{noise}} = 2.35 \frac{\sigma_{\text{noise}}}{S_{\text{rise}}}$	Electrical noise jitter
J_{sys}	System jitter
κ	Coupling rate
κ_r	Coupling rate between resonator and feed-line

Symbol	Meaning
K	self-Kerr nonlinearity
k_B	Boltzmann's constant
$\Lambda = (m/ne^2)$	London parameter
λ	Wavelength
$\lambda_L = \sqrt{\Lambda/\mu_0}$	London penetration depth
l_e	Electrical length
L_k	Kinetic inductance
$L_{k,o}$	Zero bias current kinetic inductance
$L_J = \frac{\hbar}{2eI_C}$	Josephson inductance
L_s	Surface inductance
LiDAR	Light detection and ranging
MEMS	Micro electro-mechanical systems
MKID	Microwave kinetic inductance detector
MIX	Microwave mixers
MMA	Methyl methacrylate
MXC	Mixing chamber
$n_{\text{crit}} = \Delta^2 / 4g^2$	Dispersion regime approximation critical photon number
n_{fr}	Fast relaxation model exponential value
$\langle n_{\text{ph}} \rangle$	Average photon number
N_{qp}	Number of quasi-particles
n_{qp}	Density of quasi-particles
$n_s(0)$	Zero energy density of states
NIR	Near infrared
NUV	Near ultraviolet
nTron	Nanocryotron
ω_d	Drive angular frequency

Symbol	Meaning
ω_0	Resonator angular frequency at zero bias
ω_r	Resonator angular frequency
ω_{ro}	Readout angular frequency
$\Psi(x) = \ln x - \frac{1}{2x}$	Digamma function
p	Pitch
P_{in}	Input power
PCB	Printed circuit board
PEALD	Plasma enhanced atomic layer deposition
PEC	Proximity effect correction
PMMA	Poly methyl methacrylate
PSF	Point spread function
PVD	Physical vapour deposition
$Q_c = \omega_r/\kappa$	Internal quality factor
$Q_i = \omega_r/\gamma$	Internal quality factor
ρ	Resistivity
ϱ	Reflection coefficient
$\varrho_0 = \frac{1}{2} \ln Z_1 Z_2$	Modified reflection coefficient from sections 1 and 2
ϱ_{max}	Design maximum reflection coefficient
R_{bias}	Biasing resistor
$R_{JJ} = \frac{\pi\Delta}{2I_C}$	Josephson junction room temperature resistance
R_{load}	Load resistance
R_n	Superconductor's normal state resistance
$R_Q = h/(2e)^2 \approx 6.45 \text{ k}\Omega$	Quantum impedance
R_s	Surface resistance
R_{\square}	Sheet resistance
RIE	Reactive ion etching

Symbol	Meaning
RO	Readout
RSFQ	Rapid single-flux quantum
$\sigma = wt$	Cross sectional area
σ_{noise}	Electrical noise standard deviation
S_{rise}	Signal's rising edge slew rate
S_{21}	Transmission scattering parameter
SDE	System detection efficiency
SEM	Scanning electron microscope
SG	Signal generator
SHG	Second harmonic generation
SMU	Source/measurement unit
SNAP	Superconducting nanowire avalanche photodetector
SNR	Signal-to-noise ratio
SNSPD	Superconducting nanowire single-photon detector
SNSPI	Superconducting nanowire single-photon imager
SPAD	Single-photon avalanche diode
SQUID	Superconducting quantum interference device
$\tau_{\text{e-ph}}$	Electron-phonon interaction time
τ_{fall}	Signal fall time
τ_{rise}	Signal rise time
$\tau_s = \hbar/k_B(T_C - T)$	Superconductors order parameters characteristic time
τ_{th}	Thermal dissipation time
t	Thickness
T_1	Relaxation time
T_1^{Purcell}	Purcell limited relaxation time
T_2	Decoherence time
T_2^*	Ramsey decoherence time

Symbol	Meaning
T_2^{echo}	Spin Echo decoherence time
T_C	Superconducting critical temperature
TBTDEN	(tert-butylimido)-tris (diethylamino)-niobium
TE	transverse electric propagation mode
TES	Transition edge sensor
THG	Third harmonic generation
TLS	Two-level system
TM	transverse magnetic propagation mode
ToF-PET	Time-of-flight positron emission tomography
TSV	Through-silicon via
$U(z)$	Step function
V_B	nTron/a _x Tron channel bias voltage
$v_{\text{ph}} = 1/\sqrt{LC}$	Phase velocity
V_{ro}	Readout voltage
VNA	Vector network analyzer
w	Width
X_π	π -pulse along the x -axis of the Bloch sphere
Z	Impedance
$Z_0 = \sqrt{Z/Y} \approx \sqrt{L/C}$	Characteristic device impedance
$Z_{\text{vac}} = \sqrt{\mu_0/\epsilon_0} \approx 377 \Omega$	Vacuum impedance
4HG	Fourth harmonic generation

LIST OF PUBLICATIONS

JOURNALS

- [J1] **S. Frasca**, I. N. Arabadzhiev, S. Y. Bros de Puechredon, J. Benserhir and E. Charbon, "*Ultrafast superconducting nanowire single-photon detector for Čerenkov radiation detection applications*", **manuscript in preparation (2023)**
- [J2] **S. Frasca**, I. N. Arabadzhiev, S. Y. Bros de Puechredon, P. Scarlino and E. Charbon "*Compact and Tunable Stepped Impedance Microwave Filters Based on NbN Technology*", **manuscript in preparation (2023)**
- [J3] L. Borasi, **S. Frasca**, E. Charbon and A. Mortensen "*The effect of size, orientation and temperature on the deformation of microcast silver crystals*", **manuscript in preparation (2023)**
- [J4] V. Jouanny, **S. Frasca**, F. Oppliger, F. De Palma, G. Beaulieu, V. J. Weibul, D. Sbroggió, E. Charbon, O. Zilberberg and P. Scarlino "*Quantum Bath Synthesizer*", **manuscript in preparation (2023)**
- [J5] **S. Frasca**, I. N. Arabadzhiev, S. Y. Bros de Puechredon, F. Oppliger, V. Jouanny, R. Musio, M. Scigliuzzo, F. Minganti, P. Scarlino and E. Charbon "*High kinetic inductance NbN films for high-quality compact superconducting resonators*", **manuscript in preparation (2023)**
- [J6] L. Borasi, **S. Frasca**, K. Nicolet-dit-Felix, E. Charbon and A. Mortensen "*Coupling silicon lithography with metal casting*", **Advanced Materials Today 29, 101647 (2022)**
- [J7] F. Gramuglia, **S. Frasca**, E. Ripiccini, E. Venialgo, V. Gate, H. Kadiri, N. Decharmes, D. Turover, E. Charbon and C. Bruschini "*Light Extraction Enhancement Techniques for Inorganic Scintillators*", **Crystals 11(4), 362 (2021)**
- [J8] M. Colangelo, A. Beyer, B. A. Korzh, J. P. Allmaras, A. Mueller, R. M. Briggs, B. Bumble, M. Runyan, M. J. Stevens, A. McCaughan, D. Zhu, S. Smith, W. Becker, L. Narv  z, J. C. Bienfang, **S. Frasca**, A. E. Velasco, E. Ramirez, A. Walter, E. Schmidt, E. E. Wollman, C. Pe  a, M. Spiropulu, R. P. Mirin,

- S. W. Nam, K. K. Berggren, and M. D. Shaw , "Impedance-matched differential superconducting nanowire detectors", *arXiv preprint, arXiv:2108.07962* (2021)
- [J9] **S. Frasca**, R. C. Leghziel, I. N. Arabadzhiev, B. Pasquier, G. F. M. Tomassi, S. Carrara and E. Charbon, "The Michelangelo step: removing scalloping and tapering effects in High Aspect Ratio Through-Silicon Via'", *Scientific Reports* **11**, 3997 (2021)
- [J10] E. E. Wollman, V. Verma, A. Walter, J. Chiles, B. A. Korzh, J. Allmaras, Y. Zhai, A. Lita, A. McCaughan, E. Schmidt, **S. Frasca**, R. Mirin, S. W. Nam, M. D. Shaw, "Recent advances in superconducting nanowire single-photon detector technology for exoplanet transit spectroscopy in the mid-infrared", *J. of Astronomical Telescopes, Instruments, and Systems*, **7(1)**, 011004 (2021)
- [J11] B. A. Korzh, Q.-Y. Zhao, J. P. Allmaras, **S. Frasca**, T. M. Autry, E. A. Bersin, A. D. Beyer, R. M. Briggs, B. Bumble, M. Colangelo, G. M. Crouch, A. E. Dane, T. Gerrits, A. E. Lita, F. Marsili, G. Moody, C. Peña, E. Ramirez, J. D. Rezac, N. Sinclair, M. J. Stevens, A. E. Velasco, V. B. Verma, E. E. Wollman, S. Xie, D. Zhu, P. D. Hale, M. Spiropulu, K. L. Silverman, R. P. Mirin, S. W. Nam, A. G. Kozorezov, M. D. Shaw and K. K. Berggren, "Demonstration of sub-3 ps temporal resolution with a superconducting nanowire single-photon detector", *Nat Photonics* **14**, 250–255 (2020)
- [J12] **S. Frasca** and E. Charbon, "Hybrid superconductor-semiconductor electronics", *Nat Electron* **2**, 433–434 (2019)
- [J13] **S. Frasca**, B. A. Korzh, M. Colangelo, D. Zhu, A. E. Lita, J. P. Allmaras, E. E. Wollman, V. B. Verma, A. E. Dane, E. Ramirez, A. D. Beyer, S. W. Nam, A. G. Kozorezov, M. D. Shaw and K. K. Berggren, "Determination of the depairing current in superconducting nanowire single-photon detectors", *Phys. Rev. B* **100**, 054520 (2019)
- [J14] D. Zhu, M. Colangelo, B. A. Korzh, Q.-Y. Zhao, **S. Frasca**, A. E. Dane, A. E. Velasco, A. D. Beyer, J. P. Allmaras, E. Ramirez, W. J. Strickland, D. F. Santavicca, M. D. Shaw, and K. K. Berggren, "Superconducting nanowire single-photon detector with integrated impedance-matching taper", *Appl. Phys. Lett.* **114**, 042601 (2019)

PATENTS

- [P1] **S. Frasca**, R. C. Leghziel, S. Carrara and E. Charbon, "System and Method for Removing Scalloping and Tapering Effects in High Aspect Ratio Through-Silicon Vias of Wafers", US Patent N. 2021351075-A1 (2021)

CONFERENCE TALKS/POSTERS

- [C1] F. Gramuglia, **S. Frasca**, E. Ripiccini, E. Venialgo, V. Gate, N. Decharmes, D. Turover, E. Charbon and C. Bruschini, "Light Extraction Enhancement Techniques for Inorganic Scintillators", in *2020 IEEE Nuclear Science Symposium and Medical Imaging Conference* (2020) pp. 1–3.
- [C2] **S. Frasca**, B. A. Korzh, M. Colangelo, D. Zhu, A. E. Lita, J. P. Allmaras, E. E. Wollman, V. B. Verma, A. E. Dane, E. Ramirez, A. D. Beyer, S. W. Nam, A. G. Kozorezov, E. Charbon, M. D. Shaw and K. K. Berggren, "Determination of depairing current of superconducting thin films by means of superconducting nanowire resonators", in *18th International Workshop on Low Temperature Detectors* (2019)
- [C3] **S. Frasca**, B. A. Korzh, M. Colangelo, D. Zhu, A. E. Lita, J. P. Allmaras, E. E. Wollman, V. B. Verma, A. E. Dane, E. Ramirez, A. D. Beyer, S. W. Nam, A. G. Kozorezov, E. Charbon, M. D. Shaw and K. K. Berggren, "Estimating the depairing current in superconducting devices", in *683.WE-Heraeus-Seminar on Physics and Applications of Superconducting Nanowire Single Photon Detectors* (2018)
- [C4] B. A. Korzh, Q.-Y. Zhao, **S. Frasca**, D. Zhu, E. Ramirez, E. Bersin, M. Colangelo, A. E. Dane, A. D. Beyer, J. Allmaras, E. E. Wollman, K. K. Berggren and M. D. Shaw, "WSi superconducting nanowire single photon detector with temporal resolution below 5 ps", in *Conference on Lasers and Electro-Optics* (2018) pp. FW3F.3.
- [C5] A. E. Velasco, D. P. Cunnane, **S. Frasca**, T. Melbourne, N. Acharya, R. Briggs, A. D. Beyer, M. D. Shaw, B. S. Karasik, M. A. Wolak, V. B. Verma, A. E. Lita, H. Shibata, M. Ohkubo, N. Zen, M. Ukibe, X. X. Xi and F. Marsili, "High-Operating-Temperature Superconducting Nanowire Single Photon Detectors based

on Magnesium Diboride", in Conference on Lasers and Electro-Optics (2017) pp. FF1E.7.

CHAPTER 1

Research is four things: brains with which to think, eyes with which to see, machines with which to measure, and fourth, money.

— Albert Szent-Gyorgyi, 1986

INTRODUCTION

Since the discovery of superconductivity in 1911 by Onnes [1], which eventually lead to the Nobel Prize in 1913, a multitude of fields of study involving superconductors have been pillars of research lead by physicists.

Superconductivity is a state of matter [2]. By cooling down a superconductor below its critical temperature, referred to as T_C , the material shows non-classical properties, such as absence of electrical resistivity and complete ejection of magnetic field lines from the superconductor, the so-called Meissner effect [3]. A first attempt to phenomenologically describe superconductivity was performed by Ginzburg and Landau in the G–L theory [4]. Shortly after, a microscopic behavior description of superconductors is explained in the BCS theory (named after Bardeen, Cooper and Schrieffer [5, 6]). BCS theory foundation relies on the opening of an energy gap Δ in the material due to condensation of Cooper pairs, pairs of bound electrons with equal and opposite momentum and spin, at very low temperatures [7].

While most common superconductors are based on metallic elements, such as Nb, Ti, Al, Ta, *etc.*, they usually present relatively low critical temperatures, in most cases below 10 K. Across one century it has been shown that compounds, being intermetallic, (*e.g.* Nb₃Sn [8]), or ceramic, (*e.g.* cuprate-based like YBCO [9]), present higher critical temperature, and only recently a superconductor based on highly-pressurized system of C–S–H operating at room temperature, with a T_C of 288 K, has been demonstrated [10].

Superconductors have been employed since their discovery in a multitude of ways due to their unique properties, such as coil material to build ultra-large magnets [11], quantum computing components [12–15], as magnetic field [16] and single-photon [17, 18] sensors, in optical communication [19, 20] and in astronomy

[J10], to cite a few. While the advantage of zero resistivity and very low losses makes the technology extremely appealing, the need for complex cryogenic operating infrastructure counterbalances it. Generally speaking, so far, superconducting technologies have succeeded where classical semiconductor technologies have proven clear limitations.

In this introductory chapter, the main discoveries and applications related to superconducting technology are presented, in particular those that will be further explained in later chapters in the Thesis.

1.1 SUPERCONDUCTING TECHNOLOGY

To some extent, we can say that superconducting devices fall generally in one of two major classes [21].

In the first class, the superconducting device is built and operated at an unstable equilibrium state. Small perturbations can cause the device to transition in and out of superconductivity. To develop devices that rely on abrupt state transitions, ultra-thin films of dirty superconductors allow optimal control of the superconducting energy gap. These films have been the building platform for optical sensors [17] and superconducting digital electronics devices [22].

In the second class, the device allows manipulation and tracking of superconducting phase between two bulk superconducting electrodes. The most common way of doing so is by means of Josephson junctions [23] and superconducting quantum interference devices, or SQUIDs. This technology is one of the building blocks for superconducting qubits.

1.1.1 DIRTY SUPERCONDUCTORS AND KINETIC INDUCTANCE

Derived from BCS theory [5, 6], the theory of dirty superconductors was first proposed in 1959 by Anderson [24] in the attempt to describe impurity rich superconducting systems. In a dirty superconductor, the elastic scattering caused by chemical or physical impurities is large compared to the superconducting energy gap Δ . Dirty superconductors have two major differences from classic superconductors: normal state resistance and kinetic inductance.

Normal state resistivity is the resistivity of the superconducting material just above its critical temperature T_C . For dirty superconductors, it can be few orders of magnitude larger than for their pure element counterpart. This effect can be used

as advantage, for instance in sensors, as a large resistance change (from zero to $k\Omega$) is easy to detect with classic electronic components.

Kinetic inductance, conventionally interpreted as the inertial mass of the current carriers in a superconductor, is a concept intrinsic to the London theory of superconductivity [25–27]. From a simple energy conservation representation, kinetic inductance can be written as $L_k = (m/ne^2)(l/\sigma)$, where $\Lambda = (m/ne^2)$ is a phenomenological parameter taking into account material contribution, and (l/σ) is the ratio of length and cross-sectional area of the superconductor, a geometric contribution.

However, while normal superconductors present quite a small contribution of L_k when compared to magnetic inductance, this is not the case for dirty superconductors. Kinetic inductance can be enhanced in two ways: by increasing (l/σ) and by increasing Λ . The first parameter is obtained by reducing the cross-sectional area of the superconductor or increasing its length, which makes the use of thin films extremely favorable to produce 2D-like narrow wires. The second, is enhanced by reducing the number density of electrons in the material. Dirty superconductors, due to their impurities rich nature, exhibit a lower contributing electron number density than normal superconductor, hence a larger Λ . It has been demonstrated [28, 29] that dirty superconducting thin films can achieve kinetic inductance several orders of magnitude larger than magnetic inductance. This effect makes high- L_k materials extremely interesting for all those applications where it is required a large and compact inductance, such as compact resonating structures and superinductors [30].

Both these effects make the dirty superconductor platforms very versatile, as we will see in the following chapters.

1.1.2 JOSEPHSON EFFECT AND JUNCTIONS

Compared to abruptly breaking the state, a milder way of interacting with superconductors is through their superconducting phase. The behavior of superconducting materials, due to the condensate of Cooper pairs, is the solution of a general, macroscopic wave function. When two superconductors are separated by a thin, non-superconducting layer, which allows Cooper pairs to tunnel, it is possible to generate a controlled phase difference at the interface. This device is known as Josephson junction and the change of its superconducting parameters is known as Josephson effect [23].

Josephson effect led to two main equations, referred to as DC and AC Josephson relations. The DC Josephson relation states that the tunneling current across the Josephson junction follows the equation $I(\phi) = I_C \sin \phi$, where $\phi = \phi_1 - \phi_2$ is the phase difference between the two superconducting electrodes and I_C is the superconducting critical current of the Junction. The AC relation instead relates the rate of change of the superconducting phase ϕ to a voltage, *i.e.*

$$\frac{\partial \phi}{\partial t} = \frac{2e}{\hbar} V. \quad (1.1)$$

Combining both these equations leads to the Josephson inductance

$$\frac{\partial I}{\partial t} = I_C \frac{\partial \phi}{\partial t} \cos \phi \quad \rightarrow \quad V = L_J \frac{\partial I}{\partial t} = \frac{\hbar}{2eI_C \cos \phi} \frac{\partial I}{\partial t} \quad (1.2)$$

and Josephson energy

$$E_J = \int VI dt = E_{J,o} (1 - \cos \phi) = \frac{I_C \Phi_o}{2\pi} (1 - \cos \phi) \quad (1.3)$$

relations, where $\Phi_o = h/2e$ is the superconducting flux quantum. It is possible, in fact, according to (1.2), correlate current flowing through the junction, current, voltage, and magnetic field. The power of the Josephson junction relies indeed here: any perturbation causing a change in superconducting phase ϕ across the Junction can be detected from a current or voltage readout.

1.2 APPLICATIONS OF SUPERCONDUCTING TECHNOLOGY

The work in this Thesis focuses on devices and applications enabled by superconductors. While the phase change detection is used in the last part of the Thesis as component of the superconducting qubit, high-kinetic inductance, dirty superconductors are the core of the work, mainly for the wide range of applications they give access to.

Hereafter the applications enabled by the high- L_k technology are briefly presented, and will be further addressed in the later chapters. The aim of next sections is to present whose advantages compared to classical approach. The devices fall in three main categories: single-photon detectors, electronics circuit components, and qubits.

1.2.1 SINGLE-PHOTON DETECTORS

The first category is sensors, in particular single-photon detectors. Superconducting devices have been first employed as single-photon detectors back in 1942 by Andrews *et al.* [31], with the first conceptualization of a transition edge sensor, or TES. TES exploit a steep temperature transition between normal and superconducting state of a thin film or wire to detect photons. TES are operated in the steep region of the transition. When energy $\hbar\omega$ is deposited in the film due to photon absorption, this causes the temperature of the film to slightly increase, but thanks to the steep transition this leads to a large variation in detector resistivity. The larger the energy of the photon, the larger the resistance variation, leading to energy resolution among other things.

While TES have multiple advantages, such as simplicity of fabrication and energy resolution, they need to be operated at well defined temperatures (at transition), and have a slow transition time as thermally dominated, which causes its timing resolution to be suboptimal. Modern superconducting detectors, such as superconducting nanowire single-photon detectors (SNSPDs [17]) and microwave kinetic inductance detectors (MKIDs [18]). MKIDs and SNSPDs exploit respectively partial or total suppression of superconductivity upon photon-absorption.

MKIDs are microwave resonating devices, generally designed as $\lambda/4$ or $\lambda/2$ resonators, hanged to a main feedline. AC impedance of superconductors can be expressed as $Z = R_s + j\omega L_s$, where R_s is the nonzero resistance of the superconductor at AC currents, due to presence of a small fraction of free electrons unpaired in Cooper pairs also defined as quasi-particles, N_{qp} , and L_s is its surface inductance, sum of kinetic and magnetic contributions. Generally, for a superconductor operating at $T \ll T_C$, $R_s \ll \omega L_s$. Upon photon absorption, the energy of the photon generates a number of quasi-particles $N_{qp} = \eta\hbar\omega/\Delta$, which contribute to a change of impedance. This, in turn, causes a frequency broadening and shift of the resonator peak because of the inductance change $\delta L_s/L_s < \delta N_{qp}/2N_{qp}\Delta$. By producing resonators with high enough quality factors, it is possible to read out the frequency shift caused by photon absorption, and estimate the energy of the absorbed photon.

SNSPDs, as will be discussed more in detail in Chapter 4, are superconducting nanowires biased with DC current just below their critical current, hence operating in a very weak equilibrium condition. Upon photon-absorption, the excess energy $\hbar\omega$ provided to the system is enough to break superconductivity. The sudden jump

Table 1.1 | Comparison of Single–Photon Detectors.

Detector Type	Operating Temp. (K)	Detection Efficiency, η	Timing Jitter, Δt (FWHM)	Dark Count Rate, DCR	Maximum Count Rate	Spectral Range	Figure of Merit, FOM
PMT (NUV-NIR)	RT	40% at 500 nm	300 ps	100 Hz	10 MHz	NUV-NIR	$4.21 \cdot 10^{10}$
PMT (IR)	200	2% at 1,550 nm	300 ps	200 kHz	10 MHz	IR	$1.05 \cdot 10^6$
MCP-PMT	RT	25% at 500 nm	55 ps	100 Hz	10 MHz	NUV-NIR	$1.44 \cdot 10^{11}$
Si SPAD (TJ)	RT	65% at 650 nm	400 ps	25 Hz	10 MHz	Visible	$2.05 \cdot 10^{11}$
Si SPAD (SJ)	RT	49% at 550 nm	35 ps	25 Hz	10 MHz	Visible	$1.77 \cdot 10^{12}$
CMOS SPAD	RT	50% at 550 nm	10 ps	1 Hz	10 MHz	Visible	$1.54 \cdot 10^{13}$
InGaAs SPAD	240	55% at 1,550 nm	55 ps	1 Hz	500 MHz	NIR	$2.24 \cdot 10^{14}$
VLPC	6	88% at 694 nm	270 ps	20 kHz	—	Visible	$2.06 \cdot 10^5$
TES	0.1	97% at 1,550 nm	100 ns	3 Hz	100 kHz	—	$1.13 \cdot 10^2$
SNSPD	1–3	98% at 1,550 nm	3 ps	10^{-5} Hz	100 MHz	X-ray – MIR	$3.63 \cdot 10^{15}$
MKID	0.1	90% at 285 nm	50 ns	1 Hz	100 kHz	—	$6.32 \cdot 10^2$

Updated version of the table presented by Hadfield [32] with a comparison of the different single–photon detector technologies and the new figure of merit values.

PMT: photomultiplier tube; MCP: multi-channel plate; SPAD: single–photon avalanche diode; VLPC: visible light photon counter; TES: transition–edge sensor; SNSPD: superconducting nanowire single–photon detector; MKID: microwave kinetic inductance detector

of impedance from zero to $k\Omega$ is detected by a readout circuit placed in parallel to the device.

Both MKIDs and SNSPDs are embedded into optical cavities [33] to enhance their optical efficiency, as will be discussed in [Section 4.1](#). The main difference between the two approaches rely on their readout: while MKIDs are easily frequency multiplexed, which gives them advantage in large scale operation of thousands of devices, SNSPDs show better timing resolution and maximum count rate, which are vital properties for specific applications.

A review of the major single–photon detector technologies is reported in [Table 1.1](#). SNSPDs, compared to other technologies, present unmatched combination of high efficiency, high timing resolution, low dark count rate, high maximum count rate, and wide spectral range. All this makes SNSPDs extremely appealing for a wide range of applications, such as quantum key distribution [20, 34], light detection and ranging (LiDAR) [35], astronomy [10], and more.

Finally, it has to be said that during these last decade, two variations of the classical architecture, based on SNSPDs, have been proposed and developed: the superconducting nanowire avalanche photodetector (SNAP [36]), where multiple nanowires are operated in cascade mode to enhance detectors SNR without losing in efficiency, and the superconducting nanowire single–photon imager, where by signal time–of–flight manipulation it was possible to spatially localize the absorption event in a large meandered structure (SNSPI [37]).

1.2.2 SUPERCONDUCTING ELECTRONICS

Superconducting electronics components are the second category of devices this Thesis focuses on. Cryogenic digital electronics and logic plays a key role in trying and succeed in large scale integration of cryogenic systems. In the past decade, cryogenic digital electronics has taken mostly one of two different, incompatible routes: rapid single-flux quantum (RSFQ) electronics [38] or cryoCMOS [39, 40].

RSFQ electronics is a superconducting electronics technology. It has the advantage of being a technology that can be easily and fully integrated into the superconducting chips, as it requires Josephson junction to process digital signals. Information is indeed stored in magnetic flux quanta and transferred via voltage pulses. While the main advantages of the technology are speed (can reach 100 GHz clock) and low-dissipation (usually in the range of 10^{-19} Joules per floating-point operation, or flop, *i.e.* the switching energy of the device [41]), the signal is extremely low-impedance, hence difficult to couple into classical CMOS-based processing devices at room temperature.

On the other hand, cryoCMOS is an extension of classical CMOS electronics, *i.e.* it is CMOS operated at cryogenic temperatures. While the technology has been developed and optimized for decades, the behavior of the devices at cryogenic temperature is not yet fully explored and still an ongoing research topic [42–44]. Modeling a part, the technology is very well known, compact, and easy to integrate, but it is still quite dissipative for modern cryogenics systems, where the thermal budget is extremely limited, even for the smallest technology nodes (usually in the range of 10^{-11} Joules per flop).

In recent years, a new superconducting device based platform has been proposed, either to be coupled to one of the two previously presented technologies [45], or to be a standalone technology [46]: the nanocryotrons, or nTrons [22]. nTrons exploit the superconducting-to-normal-state transition induced by current to generate voltage pulses, in a similar fashion to what happens in SNSPDs. While not as low-power as the RSFQ electronics (in the range of 10^{-15} Joules per flop) and not as easy to integrate as CMOS, nTrons have two main advantages on their side: ease of fabrication and impedance matching compatibility to a very wide range, which makes the technology particularly appealing [45, J12].

In parallel to digital electronics, analog superconducting components, such as microwave devices, exploit the low loss rate of superconductors to make compact and high-quality resonant structures. In particular, when working with thin films

of dirty superconductors, it is possible to scale the dimensions of such devices even further, as the inductance contribution from L_k is generally couple orders of magnitude larger than the magnetic inductance.

Recently, a multitude of superconducting devices, such as superinductors [30], impedance matching tapers [J14], microwave filters [47, 48] or directional couplers [49], have been explored. Together with the digital electronics devices, such components may potentially allow large scale integration of superconducting circuits with increasing complexity.

1.2.3 QUANTUM COMPUTING

Microwave superconducting electronics is also a fundamental part of circuit quantum electrodynamics (cQED [50]), the field of study of the interaction between a qubit and a microwave resonator. To date, superconducting transmon qubits are fabricated via Josephson junctions coupled to low loss, classic superconductors such as aluminum, niobium or more recently tantalum [51]. While there are research groups trying to implement high- L_k circuits easy to integrate with conventional qubit manufacturing [52], or even to substitute the Josephson junctions with a weak link of high- L_k material [53, 54], still little effort has been devoted to use of a high- L_k material for the main components of superconducting chips.

As convenient as it would be, a full-scale chip made of high- L_k material, such as NbN or grAl, internal quality factors, *i.e.* loss rates, of these devices still have to reach the numbers obtained by conventional superconductor technology. It is thought that in dirty superconductors, loss rate has to be larger than in pure superconductors, due to the impurities coupling and dissipating the microwave signal. Loss rate in qubits is associated to relaxation time T_1 , hence qubits made of dirty superconductor materials would exhibit low coherence times.

1.3 THIS PHD THESIS CONTRIBUTIONS

The aim of this PhD thesis is to demonstrate and provide the tools to build a working platform based on high- L_k superconducting materials for a diverse range of quantum applications. In terms of fabrication, NbN-based devices demonstrated excellent internal quality factors of 10^5 at single-photon regime while having kinetic inductance above 90 pH/ \square , high yield and a generally high constriction factors

C of 0.7 [55, J13] at base temperature. For 3D integration, both a novel polishing technique for TSV as well as new filling method are presented.

Among the superconducting devices, sub-5 ps timing resolution SNSPD in NbN, operating at a wavelength λ of 343 nm, is presented, as well as quantum efficiency saturation in the NIR range. Digital circuits components, in particular nTrons, are studied and a new design is proposed for high-sensitivity and large SNR. In the field of cQED, high- L_k resonating structures with high impedance are demonstrated to operate with large quality factors as filters and impedance matching tapers. Finally, a 100 μ s T_1 planar transmon qubit in aluminum is characterized, achieving readout fidelity of 92% for a readout time of 5 μ s.

1.3.1 THESIS STRUCTURE

This Thesis touched many different technologies, each somehow linked to high-kinetic inductance superconducting materials. As such, at the beginning of each chapter, there is a brief introduction of the technology thereby discussed followed by the results obtained and followed up by a short discussion. The manuscript has been split in the following chapters:

CHAPTER TWO: *High kinetic inductance superconductors.* In this chapter the fabrication technique of the thin films is described thoroughly, with discussions regarding the different properties, yield, and ease of fabrication.

CHAPTER THREE: *3D integration: through-silicon vias.* This chapter addresses the need and the advantage of 3D integration of superconducting chips, with a description of fabrication process and filling approaches developed, classical and not.

CHAPTER FOUR: *Superconducting nanowire single-photon detectors.* Here we present the operation mechanism of SNSPD and the results obtained by our NbN-based detectors, with a thorough description of the measurements techniques used to characterize them.

CHAPTER FIVE: *nTrons: the nanocryotrons technology.* In this chapter, the superconducting digital electronics technology of the nanocryotrons are studied as a potential CMOS–superconducting chip interface layer. DC characterization is followed by a new conceptual design aimed to increase device sensitivity, with experimental proof of the advantage on the standard approach.

CHAPTER SIX: *High kinetic inductance circuits.* Here the advantages of high-kinetic superconductors are explained for high-frequency devices, with particular attention towards resonating structures. After characterization of films quality factors and nonlinearity, we apply the technology to make impedance matching tapers and frequency tunable bandpass filters.

CHAPTER SEVEN: *Planar transmon qubit.* This chapter focuses on the fabrication and testing of a classical, non high- L_k superconducting transmon qubit, developed as reference for future integration and implementation of qubits with high- L_k components.

CHAPTER EIGHT: *Perspectives and conclusions.* Finally, this last chapter wraps up the discussion, with possible future applications for the proposed high- L_k superconducting platform.

CHAPTER 2

The experiment left no doubt that, as far as accuracy of measurement went, the resistance disappeared. At the same time, however, something unexpected occurred. The disappearance did not take place gradually but abruptly. From 1/500 the resistance at 4.2 K, it could be established that the resistance had become less than a thousand-millionth part of that at normal temperature. Thus the mercury at 4.2 K has entered a new state, which, owing to its particular electrical properties, can be called the state of superconductivity.

— Heike Kamerlingh Onnes, *Nobel Lectures in Physics, 1913*

HIGH KINETIC INDUCTANCE SUPERCONDUCTORS

Disordered superconductors, also called "dirty" superconductors, are generally type-II superconducting materials within which the impurities cause a large elastic scattering compared with the energy gap [24]. It has been demonstrated that dirty superconductors, such as but not limited to nitride-based superconductors (NbN, TiN, NbTiN, ZrN, etc.), show in certain deposition conditions, *i.e.* under a controlled material-impurities ratio, higher superconducting transition temperatures (T_C) and magnetic field resilience (H_C) than the pure superconducting element they derive from.

Disorder in superconductors, among other effects, causes an increase of resistivity of the normal state material, which, as a consequence, raises the kinetic inductance. Kinetic inductance can be interpreted as the inertia of the charge carriers, in the superconducting case the Cooper pairs, in the superconducting material. From BCS theory, we know that

$$L_k(T) = \frac{R_{\square}\hbar}{\pi\Delta} \frac{1}{\tanh \frac{\Delta}{2k_B T}}, \quad (2.1)$$

where L_k is the kinetic inductance per square of the superconducting film at temperature T , given $T < T_C$; R_{\square} is the sheet resistance, or resistance per square, of the superconductor film while non-superconducting, or in normal metal state; \hbar is the reduced Planck's constant; k_B is Boltzmann's constant; Δ is the superconducting

energy gap. This approximation works best when R_{\square} is measured close to the critical temperature: this is because superconducting alloys may have a large resistance change between room temperature condition and near the superconducting transition temperature. For the estimation of Δ , according to BCS theory, it can be approximated to $\Delta = 1.764 k_B T_C$ for $T \ll T_C$.

High-kinetic inductance thin films technology exploits this large inductivity to make compact, high-impedance devices. As R_{\square} increases with thinner films, so does the value of L_k , hence the use of thin films; one example is that of superconducting resonators. In other applications, however, the use of thin films may also have other purposes. In SNSPDs, for instance, the use of thin films has also the intent of suppressing the critical temperature, which, in turn, suppresses the superconducting energy gap Δ . Suppression of the superconducting gap is beneficial for photon detection efficiency [56]: in fact, the sensitivity of the single-photon detectors is inversely proportional to the Δ , as sensitivity is proportional to the energy required to break superconductivity itself. For this reason, a device with lower T_C is generally more sensitive to IR photons [57].

Known dirty, high- L_k superconducting materials can be classified in two major families: crystalline materials (NbN, TiN, NbTiN *etc.*) and amorphous materials (WSi, MoSi, *etc.*). While crystalline superconductors have usually higher critical temperature and better performance in terms of quality factors or sensor timing resolution, due to their shorter electron–phonon interaction time τ_{e-ph} [J11, C4], amorphous materials are generally more resistive and so inductive, and have a higher fabrication yield.

Only recently, Dane *et al.* [58] have proposed a novel fabrication technique to enhance yield of crystalline superconductors while maintaining short τ_{e-ph} by depositing films using the so-called bias–sputtering. The thin films are deposited while RF power is applied to the substrate, which causes a plasma agitation that simulates high-temperature deposition at the cost of slower deposition rate. The result is smaller crystals and enhanced homogeneity, at the expense of critical temperature.

The following chapter is organized as follows: first, the fabrication process of NbN, TiN and NbTiN materials is presented; the difference between different deposition techniques is discussed, *e.g.* reactive sputtering and atomic layer deposition, with a brief discussion on advantages and disadvantages of either process. Then, the more recent case study of granular superconductors is discussed, *i.e.* granular aluminum, with its advantages and disadvantages compared to other films.

2.1 NIOBIUM-BASED DIRTY SUPERCONDUCTORS

While one could debate if amorphous superconducting materials, such as WSi and MoSi, may be a better choice for high- L_k applications, as they are intrinsically more inductive and very easy to fabricate due to their amorphous nature, we need to consider that these are also intrinsically more lossy materials. For some applications, such as superconducting circuit components (see [Chapter 5](#)) they may prove to be the better choice, but for resonating structures and cQED devices in general, losses are detrimental.

Considering the ease of fabrication and the large compatibility with most fabrication processes, the first material developed during this work was niobium nitride. NbN is among the most commonly sputtered dirty superconductors, and thanks to the abundance of information that can be found in literature, it was a relatively easy material to work with if compared to more exotic materials.

2.1.1 NbN FROM REACTIVE RF SPUTTERING

By tuning the disorder (*i.e.* by controlling the degree of impurity) of NbN, it is possible to vary the properties of the alloy extensively. A Kenosistec RF magnetron sputtering system has been used for most of the depositions described in this chapter. Pure niobium thin films have been first sputtered to address the unwanted impurities due to the system. For ultra thin films of 15 nm thickness, the critical temperature T_C was in the order of 5 K and sheet resistivity R_{\square} of 10 Ω/\square . The T_C was measured in a PhotonSpot Cryospot4 ^4He sorption cryogenic system (see [Appendix B.1](#)), which reached a base temperature of 850 mK. For information regarding the methods of characterization of critical temperature, please refer to [Appendix B.3.1](#).

While not state-of-the-art results for ultra-thin films, the critical temperature and the roughness of the film were relatively satisfying to proceed further. Following the addition of N_2 in the deposition chamber atmosphere and the deposition of NbN films, a first optimization was made to ensure that the parameters such as deposition rate and sheet resistance were in the range suggested from literature [37], as well as yield and repeatability. In this instance, we have compared sputtered and bias-sputtered [58] ultrathin films of stoichiometric NbN. It is known that

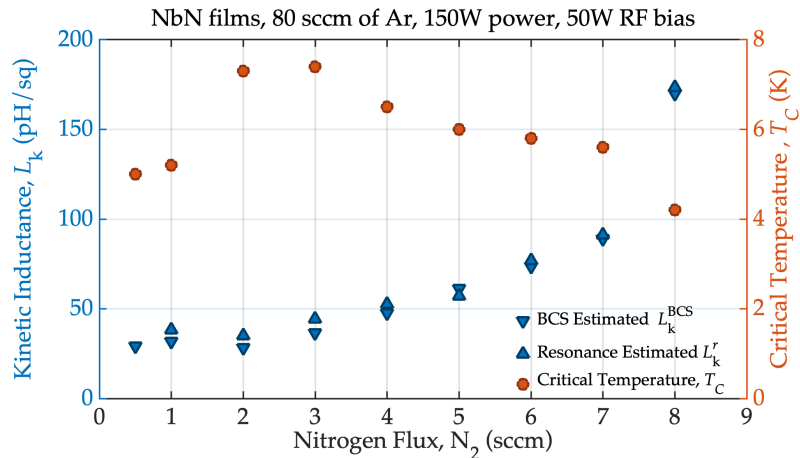


Figure 2.1 | Disorder analysis of bias-sputtered superconducting thin films in NbN. The drift of critical temperature and resistivity were measured with simple resistivity measurements performed at cryogenic temperature with the PhotonSpot system (see Appendix B.3.1). The kinetic inductance (values in blue) was both estimated by BCS theory as of in (2.1) (L_k^{BCS}) and measured by the resonant frequency of superconducting resonators (L_k^r , more in Section 6.1). The experimental values agree quite well with the predictive theory.

stoichiometric NbN deposition conditions in a reactive sputtering system occur when, at a given target power, the N₂ flux causes a kink of voltage at the target [59].

As expected, reactive sputtered thin films had faster deposition rate and critical temperature compared to the bias-sputtered ones, but the size of the crystals was so large that devices yield was far from optimal. It is worth noting that deposition temperature increase in the chamber could have improved this aspect, but the Kenosistec system did not allow for deposition above 200°C, which was not a high enough temperature to observe a relevant improvement.

For all the reasons above, the Thesis work focused the study on bias-sputtered thin films. Aside the advantage of having a high-yield, highly-reproducible fabrication process thanks to the polycrystalline nature of bias-sputtered deposited films, bias-sputtered NbN lower T_c and larger R_{\square} also enhances kinetic inductance. These are advantages from both sensor design and high-impedance circuit design perspectives.

To improve repeatability of the deposited film between sessions, the introduction of the so-called target poisoning [60–62], a pre-deposition treatment performed at very high nitrogen flow rates, allows for a more homogeneous chemical composition during the deposition and a much more robust process. In order to perform the poisoning, plasma power is set up on the target, and the voltage at different nitrogen flow conditions is monitored: the poisoning should be performed at the condition in correspondence to the knee of the voltage-flow rate function.

Table 2.1 | NbN Sputtering Deposition Parameters.

Process	RF Target Power (W)	RF Bias Power (W)	Ar/N ₂ flow rate (sccm)	Film Resistivity, ρ , ($\mu\Omega\cdot\text{cm}$)	Kinetic Inductance, $L_{k,\square}$ (pH/ \square)	Thickness nm	Critical Temperature (K)
1	150	50	80/0	48.2	10.5	14.7	5.0
2	150	50	80/0.5	186	37.1	17.5	5.1
3	150	50	80/1	193	34.9	16.1	5.2
4	150	50	80/2	204	29.1	13.6	7.3
5	150	50	80/3	264	37.4	13.5	7.4
6	150	50	80/4	292	49.8	13.0	6.5
7	150	50	80/5	339	65.0	12.7	5.9
8	150	50	80/6	387	78.7	12.5	6.0
9	150	50	80/7	441	95.9	12.2	5.7
10	150	50	80/8	474	112	12.0	5.4
11	150	50	80/10	569	201	11.1	4.1

Optimization of NbN reactive sputtering process ultra thin films on 100 nm Si₃N₄ buffer layer on Si substrate.

Once found the parameters to get the most homogeneous thin films, a parametric sweep of N₂ flow rate was performed as shown in Dane *et al.* [58] to control the impurities of the film. As expected and reported in Figure 2.1, the presence of N₂ in the film for small quantities (slightly disordered superconductor, for N₂ flow rate below 3 sccm) increases T_C and resistivity in similar amounts, causing the kinetic inductance to remain quite stable around 30 pH/ \square for 15 nm films. Further raise of N₂ in the chamber atmosphere intensifies film disorder, causing an increase of resistivity and a decrease of T_C , causing the boosting of kinetic inductance.

Stoichiometric conditions were reached at gas atmosphere made of 80 sccm of Ar and 3 sccm of N₂ flows, at room temperature and at a deposition pressure of 5 μ bar. For a 15 nanometers thick stoichiometric NbN film, the measured critical temperature was of 7.4 K, the resistivity ρ around 260 $\mu\Omega\text{cm}$ and the kinetic inductance in the range of 40 pH/ \square . In Figure 2.2 it is possible to see the cross-section transmission electron micrograph of a stoichiometric 10 nm thick film used for SNSPDs.

The internal quality factor of superconducting resonators made of NbN films deposited with this technique are presented in Section 6.1. This work eventually lead to the publication reported in [J5].

2.1.2 NbN FROM ATOMIC LAYER DEPOSITION

Atomic layer deposition (or ALD, [63]) of materials allows extreme thickness control and homogeneity thanks to its self-limiting single reaction, which gives the name to

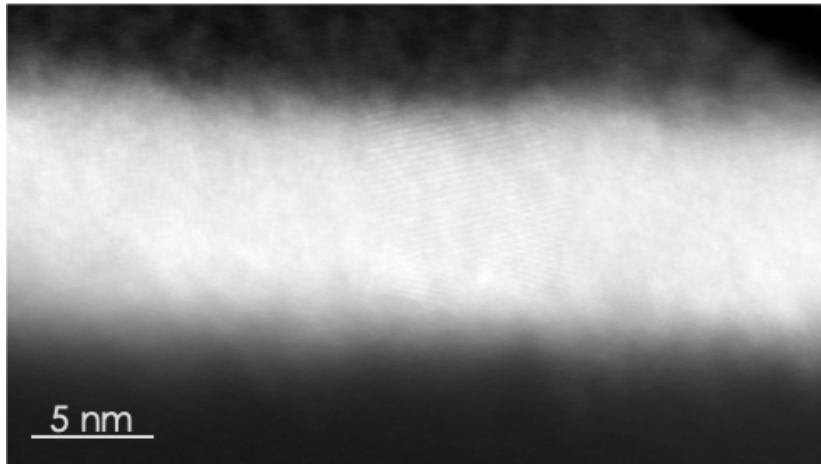


Figure 2.2 | Transmission Electron Micrographs (TEMs) of NbN. The film was deposited according to the methods described in Subsection 2.1.1. As shown from the figure, the dimension of the crystals is much smaller of the thickness of the film, hence increasing fabrication yield.

the process. The advantages of such deposition technique are equally balanced by the complexity required to develop a working recipe. It has been reported by multiple research groups that ALD processes are extremely prompt to contamination, in particular of Cl_2 and O_2 , as two of the most common precursors for different ALD processes. The interest in ALD NbN thin-films will be explained more in depth in Section 3.3. Here we will treat the fabrication challenges of developing such a process.

Thermal atomic layer deposition of NbN has been extensively studied in the '90s [64–66], but due to presence of chlorine in the precursors, *e.g.* NbCl_5 , film contamination is a non-negligible issue that affects superconducting properties. However, more recently Ziegler *et al.* [67] developed a plasma-enhanced atomic layer deposition (PEALD) process using the metal organic precursor (tert-butylimido)-tris (diethylamino)-niobium, also called for simplicity TBTDEN, and hydrogen plasma.

Since then, several groups have investigated this new fabrication process, either from superconducting materials [68–70] or from the applications, seeing it fit to develop SNSPDs [71, 72], and high-Q resonators [73] for MKIDs and quantum computing.

We used the Beneq TFS200 atomic layer deposition system in CMi. An additional turbopump was purchased and installed in the system in order to purge the system from contaminants and reach lower pressure values to control the stability of the plasma in the PEALD process. Moreover, lower base pressure during deposition implies lower contamination of the films. The first step, according to Ziegler *et al.* [74], was to set the right starting parameters for the plasma in the chamber, before fine tuning the parameters for the optimization of the process. For instance, Sowa

et al. [69] show that increased plasma power allows deposition of less resistive film, which have in turn a higher critical temperature. Ziegler *et al.* [74] instead show that minimum plasma pressure allows for better film quality: from a resistivity of 2000 $\mu\Omega\text{m}$ at a pressure of 80 mTorr down to less than 10 $\mu\Omega\text{m}$ for pressures below 8 mTorr. For what concerns the plasma time, however, an optimal condition has to be found in terms of resistivity, while for the temperature dependence, both groups [67, 69] show better film quality when deposited at higher temperature. Finally, the effects of the H₂ and N₂ flow rates in the plasma have to be taken into account. Despite Ziegler *et al.* [67] shows a deterioration of performance with increasing H₂ flow, more recently both Sowa *et al.* [69] and Ukibe and Fujii [68] have demonstrated the opposite.

After a preliminary study, taking into account the capabilities of our system, the starting deposition parameters were set to a chamber pressure of 6 mTorr, temperature of 300°C, plasma power of 300 W to be exposed for 40 s, and flow rates of H₂ and N₂ of 80 sccm and 5 sccm respectively. The preliminary process is indicated as process o. Despite several attempts, it was not possible to deposit good quality NbN. The films were extremely inhomogeneous, with macroscopic droplets deposition, probably caused by improper use of the plasma. In terms of superconductivity, the films never showed any transition to a superconducting state all the way down to 850 mK.

These data point towards a contamination problem of the chamber, given the ALD in CMi is used for a wide variety of processes, ranging from powder depositions to oxides, which are notoriously detrimental for superconducting properties.

2.2 TITANIUM-BASED DIRTY SUPERCONDUCTORS

Another major player in the crystalline superconducting thin films field is titanium nitride. While Nb as an element presents critical temperature of 9.26 K in bulk (and around 5 K in ultra thin films), Ti has a much lower transition temperature, in the range of 300 mK in bulk (hence less than that in thin films). However, when growing TiN by adding N₂ in the deposition chamber, thin films have shown critical temperatures in the range of 5 K, tunable down to 1 K by controlling the degree of disorder of the film.

Having lower critical temperature, TiN thin films have lower superconducting energy gap Δ than NbN (and NbTiN, as we will see in Section 2.3), making it a much more sensitive material to infrared radiation [35], interesting property for what

concerns for instance LIDAR applications as well as astronomy [J10]. Moreover, TiN has proven to date to be the highest internal quality factor high- L_k material for superconducting resonators, making it a strong candidate for MKIDs and quantum computing applications.

2.2.1 TiN FROM REACTIVE RF SPUTTERING

TiN presents, in general, higher kinetic inductance than NbN due to the lower T_C and generally higher sheet resistivity, and it has shown lower loss rate than any other dirty superconductor: these features are extremely attractive from the resonating structure standpoint, where large kinetic inductance allows design of much higher impedance structure, but they do not necessarily line up with SNSPDs requirements. Larger kinetic inductance usually means slower rise and fall times for a given SNSPD sensor area, which in turns represents lower timing resolution and maximum count rate, not advisable for SNSPDs.

TiN was sputtered in the Kenosistec system following the same approach described in Subsection 2.1.1. The stoichiometric condition was studied for sputtered TiN thin films, reached at gas atmosphere made of 80 sccm of Ar and 2 sccm of N₂ flows, at room temperature and at a deposition pressure of 5 μ bar. Critical temperature was measured around 2.5 K, with a resistivity ρ of around 350 $\mu\Omega\text{cm}$. From these values, kinetic inductance was estimated to be in the range of 110 pH/ \square for a 15 nm thick film.

Despite TiN being a very interesting material for specific applications, the study of TiN remained only superficial. The motivation behind the development of TiN thin films is due to its larger kinetic inductance compared to NbN, but the potential increment of L_k was deemed insufficient to motivate a full scale optimization as it was performed for NbN. Instead, time was invested in the development of another material, with yet even lower T_C but much higher kinetic inductance (see Section 2.4).

2.2.2 TiN FROM ATOMIC LAYER DEPOSITION

As ALD-deposited NbN was not a success either due to contaminations, plasma instability or else, we tried to develop the ALD process for titanium nitride. TiN had already been successfully deposited in a Beneq system, the equipment we have in CMi, elsewhere [75]. Starting from the recipe developed by Xie *et al.* [75], we tried

Table 2.2 | TiN Atomic Layer Deposition relevant recipes parameters (values for 4000 ALD cycles).

Process	Pressure (mTorr)	Chamber Temp. (°C)	N ₂ flow rate (sccm)	TiCl ₄ Time (ms)	Purging Time (ms)	NH ₃ Time (ms)	Purging Time (ms)	Thickness (nm)	Resistivity, ρ (μΩ·cm)
0	6	400	200	150	1000	100	1000	75 ± 5	4500 ± 300
1	6	425	200	150	1000	100	1000	80 ± 5	1400 ± 100
2	6	400	200	150	1000	150	1000	70 ± 5	1200 ± 50
3	6	425	200	150	4000	100	4000	75 ± 5	1000 ± 50
4	6	400	200	50	2000	200	2000	85 ± 5	950 ± 50
5	6	425	200	100	2000	200	2000	90 ± 5	850 ± 50
6	6	425	200	50	2000	250	2000	83 ± 5	800 ± 50
7	6	425	200	100	2000	300	2000	85 ± 5	1300 ± 100

Optimization of TiN atomic layer deposition process on 100 nm SiO₂ buffer layer on Si substrate.

to setup a thermal ALD process based on TiCl₂ precursor reacting with ammonia [76]. The results were far from satisfying, as the film resistivity was almost an order of magnitude larger than what reported in literature.

After months of optimization and tens of depositions, as reported in [Table 2.2](#), we were finally able to produce thin films of 40 nm with a resistivity of 800 μΩcm, which we suspected being close enough to the 455 μΩcm value described in [75] to achieve superconductivity. The films unfortunately did not show any trace of superconducting transition when cooled down at 850 mK, suggesting a potential transition temperature below 800 mK, if any.

While getting closer to a functioning recipe, due to the regular contamination of the chamber from other precursors, the process became highly unstable and between September 2021 and March 2022, we measured resistivity variation of 400% between same recipes. Due to the impossibility to have a stable process, TiN and NbN ALD processes were likewise abandoned, different approaches were followed. The effects of this changes strongly affected the timeline of some projects, as it will be explained in detail in [Chapter 7.3](#).

2.3 NIOBIUM TITANIUM NITRIDE

As TiN was supposed to replace NbN for applications where we needed larger kinetic inductance, NbTiN was chosen to be the high-temperature alternative. The goal for NbTiN was to develop devices capable of operating at liquid He temperature without major losses in terms of superconducting properties and quality factors.

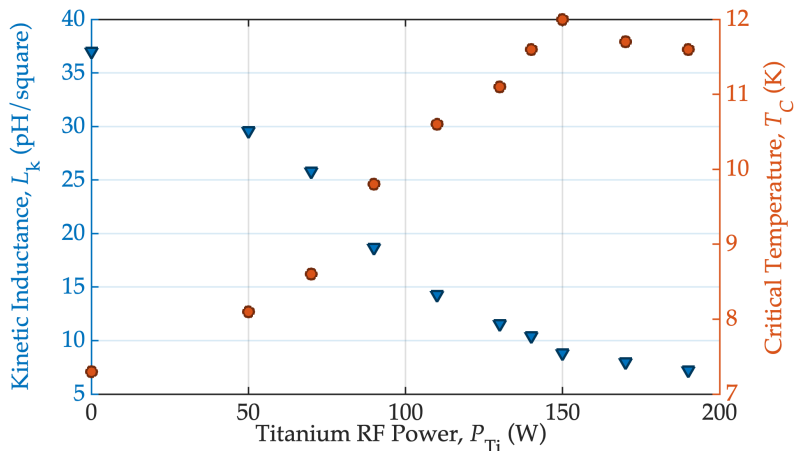


Figure 2.3 | Disorder analysis of three plasma-sputtered superconducting thin films in NbTiN. The measurement were performed according to Appendix B.3.1. The kinetic inductance (values in blue) was estimated by BCS theory as of in (2.1). The addition of Ti to NbN enhances the critical temperature from 7.4 K all the way to 12 K. As expected, the drawback is a reduction of kinetic inductance.

NbTiN was also chosen as it does not differ particularly from either NbN or TiN in terms of depositions technique, as it was also deposited in the same Kenosistec system as the other two. This allowed us to minimize potential contaminations.

2.3.1 NbTiN FROM Nb AND Ti REACTING RF CO-SPUTTERING

For the NbTiN depositions, we developed what we called a three plasmas (two targets and substrate) sputtering deposition process. The process consists of reactive co-sputtering of Nb and Ti targets, applying, on the same idea of Dane *et al.* [58], a third plasma on the substrate to get the advantages of the bias-sputtering. While bias-sputtered materials should exhibit a suppressed critical temperature, the advantage of the film yield was judged worth the extra marginal degree of critical temperature.

Differently from a simple sputtering process, co-sputtering processes have a larger number of variables to be optimized: Nb and Ti plasma powers, N₂ and Ar flow rates, substrate (anode) power and chamber pressure. However, to simplify the optimization and to ensure high T_c , we limited the number of permutations by choosing the flow rate that granted stoichiometric NbN deposition.

First degree optimization was performed by sweeping the target power (*i.e.* the deposition rate) of Ti, which is known to strongly affect the superconducting properties of the thin films [77]. After some attempts, which are shown in Figure 2.3 we obtained 15 nm thin NbTiN films with critical temperature of 12 K, sheet

Table 2.3 | NbTiN Sputtering Deposition Parameters.

Process	RF Target Powers (W)	RF Bias Power (W)	Ar/N ₂ flow rate (sccm)	Film Resistivity, ρ , ($\mu\Omega\cdot\text{cm}$)	Kinetic Inductance, $L_{k,\square}$ (pH/ \square)	Thickness nm	Critical Temperature (K)
1	150/0	50	80/3	264	37.4	13.5	7.4
2	150/50	50	80/3	234	29.6	13.6	8.1
3	150/70	50	80/3	216	25.8	13.5	8.6
4	150/90	50	80/3	179	18.7	13.9	9.8
5	150/110	50	80/3	148	14.3	14.2	10.5
6	150/130	50	80/3	125	11.5	13.8	11.1
7	150/150	50	80/3	103	8.8	13.7	12.0
8	150/170	50	80/3	91	8.0	14.1	11.7
9	150/190	50	80/3	81	7.2	14.4	11.6

Optimization of NbTiN reactive sputtering process on 100 nm Si₃N₄ buffer layer on Si substrate.

resistivity of roughly 75 Ω/\square and an estimated sheet kinetic inductance of 10 pH/ \square . The films turned out to be extremely homogeneous, reaching device yield in excess of 95% for a 7 nm thick film.

These films were later employed for superconducting digital circuits elements such as the nTrons (see [Chapter 5](#)), thanks to high critical temperature, yield and critical current density, a parameter which allows the designer to get larger signal-to-noise ratio with small footprint devices.

2.4 HIGH KINETIC INDUCTANCE FROM ORGANIZED CRYSTALS: GRANULAR ALUMINUM

Dirty superconductors are not the only way to achieve high kinetic inductance. Another way to achieve large inductance using superconductors is by fabrication of a superconducting junction (the Josephson junction) where the two electrodes are separated by an insulator thin enough to allow electrons to tunnel through it [[14](#)].

Despite Josephson junctions are usually fabricated as macroscopic features, it is possible to deposit superconducting films which exploit the Josephson inductance at a much smaller scale. These films are called granular superconductors and were discovered in the late '60s by Abeles, Cohen and Stowell [[78](#)]. In granular superconductors, the superconducting material crystal grains are "coated" by an insulating thin layer [[79](#)], so as to form sort of barriers with the nearby grains. Each grain, being so localized, shows enhanced superconducting properties, both in terms of critical temperature and magnetic field resilience.

Due to their nature, granular superconductors, and in particular granular aluminum (or grAl), have been recently revisited for their potential applications as superconducting high- L_k material, in particular from Prof. Ioan Pop's group at KIT [52, 53, 80, 81].

We sputtered grAl thin films in the Kenosistec RF sputtering system described previously in the chapter. In order to control the grain size, we installed a high-precision and low O₂ flow line in the system to ensure proper atmospheric deposition conditions. We deposited 20 nm thick grAl film with kinetic inductance in the range of a nH/ \square and critical temperature in the range of 2 K. These films have only been partially characterized at the time of the writing of this thesis, but grAl superconducting resonators show quite high internal quality factors in single photon regime, in the range of 5×10^5 , for a 500 pH/ \square thin film at a resonant frequency of 3 GHz.

2.5 DISCUSSION

The materials described and analyzed in the chapter are the building pillars of the remainder of this Thesis. From a quite versatile material such as NbN, where critical temperature can be tuned as well as its kinetic inductivity within a wide range, can be built most of the high- L_k technology described further on. However, we also reported the development of more application-specific materials, where we optimized determined parameters critical for the end purpose. NbTiN, which shows high-yield as well as critical temperature in excess of 12 K, present all the key specification needed from a superconducting electronics perspective, such as nTrons applications. On the other end, grAl, which was demonstrated kinetic inductance in excess of 500 pH/ \square for 20 nm thin films, seems to be a very promising material for high-frequency electronics applications, to make much more compact resonating structures than they would be in a lesser L_k material, and pushing further the achievable impedance.

CHAPTER 3

The only way out is through.

— Dante Alighieri

3D INTEGRATION: THROUGH-SILICON VIAS

Superconducting devices require, at times, complex readout schemes, that may cause large scale integration particularly challenging. That is indeed the case for both SNSPDs and quantum computing chips based on transmons.

Large scale integration of SNSPDs is possibly to date the highest barrier to the success of the technology. While SNSPD specifications, in particular efficiency and timing resolution, exceed both the likes of SPADs and MKIDs, readout schemes are so challenging that make it very hard to scale.

As shown by Verma *et al.* [82] first and by Allman *et al.* [83] and Wollman *et al.* [84] later, one possible solution is to read rows and columns separately, and by running the detectors in coincidence mode, it is possible to back trace which detector fired across the array. This readout scheme has however two main drawbacks: timing performance of the detectors degrade very quickly with the number of pixels, and the scaling mechanism itself is quite limited. For an $N \times N$ detectors array, this approach only reduces the number of readout lines from N^2 to $2N$, making it unusable for very large arrays.

Another path is to integrate the detector with logic electronics, *e.g.* rapid single flux quantum (RSFQ) circuitry as it was developed by Miki *et al.* [85], which being superconducting, show extremely low power consumption, and does not affect the device performance. In their work, Miki *et al.* demonstrated an 8×8 detector array without any relevant loss of performance. Wire routing, however, ended up being the limiting factor. In fact, in order to bias the inner detectors of the array, it was necessary to run superconducting biasing lines to the center pixels, and since the SNSPD fabrication process is a planar process, that resulted in loss of fill factor.

Similar problems have been shown in large scale integration of transmon-based quantum processors, where each qubit needs its readout resonator to be operated in

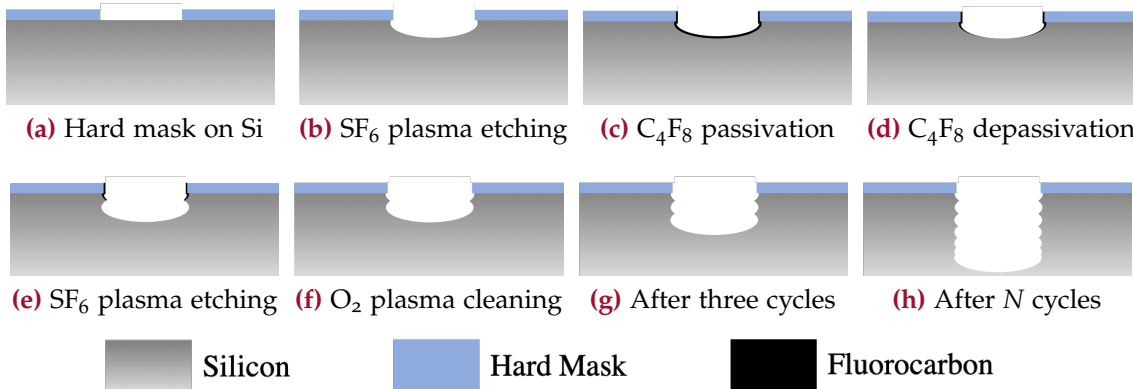


Figure 3.1 | Bosch process schematics. After patterning the features on an hard mask (a), the etching step (b) is followed by fluorocarbon passivation (c), subsequent depassivation on the bottom of the holes (d) and a new etching step (e). The extra step of O₂ plasma cleaning (f) allows to reduce the surface roughness on the walls of the holes Xu *et al.* [87].

a non-destructive way. As the number of qubits increases, the connection crowding can result into large losses and impact qubit performance [86].

In order to address these issues, we here propose as solution a 3D integration process with superconducting through-silicon vias. We developed a process flow for High Aspect Ratio Through-Silicon Vias (HAR-TSVs) [88–90] for silicon wafers. The process flow is reported in Figure A.3. While this is a pretty standard process, the novelty resides in the metallization step.

In this chapter, the fabrication optimization for the through-silicon vias is presented, as well as the Michelangelo step, a polishing step of the inner walls of the TSVs which eventually lead to [J9]. Finally, we go through the different options of metallization, and we introduce a novel filling technique for TSV [J6].

3.1 DRIE OPTIMIZATION

In order to etch the holes in the silicon substrate, we used the deep reactive ion etching process (DRIE, or more commonly Bosch process). Bosch process consists in the alternate use of passivation with fluorocarbon chemistry (C₄F₈) and plasma etch by means of fluorine chemistry (SF₆) to achieve high anisotropy. In Figure 3.2 we show one of the first through-silicon via geometries produced during this work.

Interesting effect of DRIE processes can be seen from Figure 3.2(b). The different depths shown here are related to the different apertures of the holes: the deeper

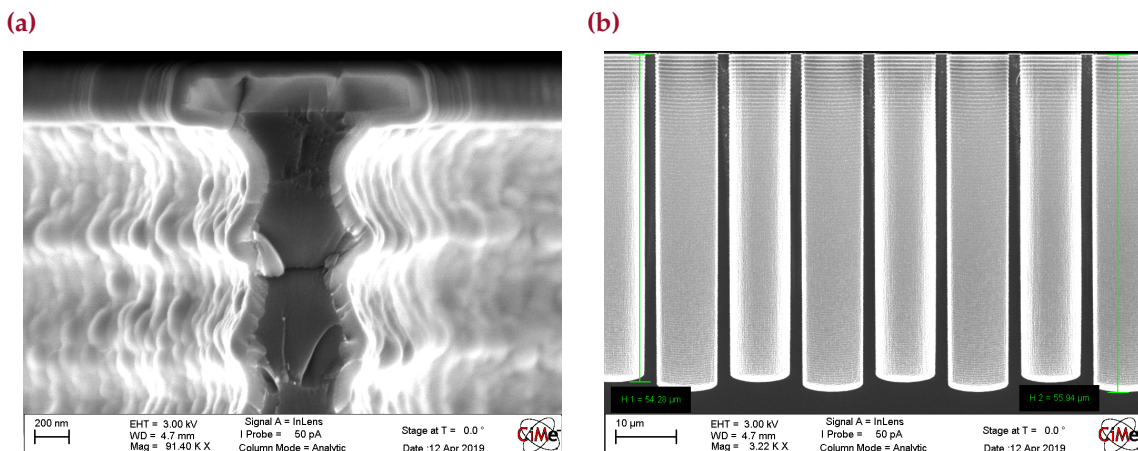


Figure 3.2 | Bosch process. Scanning Electron Micrographs (SEMs) of the through-silicon vias (TSVs) ready for the metallization step. It is possible to notice both the super-conformality of the atomically layer deposited Al_2O_3 insulation layer (a) and the different etching depth achieved from circular and rectangular holes (b) with critical dimension of $5 \mu\text{m}$.

ones have been obtained by etching $10 \times 10 \mu\text{m}^2$ squares, while the shallower had a circular shape with $10 \mu\text{m}$ diameter.

This effect is the so-called Aspect Ratio Dependent Etching (or ARDE). ARDE causes etch rate variation depending on the ratio between the gas entry surface and the etching surface. While increasing depth during DRIE, the gas entry area remains the same while the etching area increases linearly with depth. ARDE is caused by the etcher not having time to vacate the post-reaction products from the inside of the hole as fast as it did at the beginning of the process, when the aspect ratio was much smaller. This causes a reduction of etch rate which can be visibly stated also by the reduction of scalloping [91], the characteristic shape in Figure 3.2(a), with depth. Eventually, ARDE causes the saturation of the DRIE process and to a cycle etching rate of approximately zero [92].

A first optimization run based on classical Bosch process variations lead to etching holes as small as $3 \times 3 \mu\text{m}^2$ for a depth of $55 \mu\text{m}$, for an equivalent aspect ratio of 18.3:1 after full etch of the hard mask. However, the hole size at the bottom resulted to be 10–20% narrower than design, resulting in a conical shaped via with severe scalloping.

To address the concern related to the shape of the via as well as the limited aspect ratio caused by process saturation, we tried to make changes to enhance anisotropy of the process. A process consisting of three pulses of passivation (C_4F_8), depassivation (O_2) and etching (SF_6), performed at lower temperature and lower pressure, showed remarkably better results. The additional step of depassivation

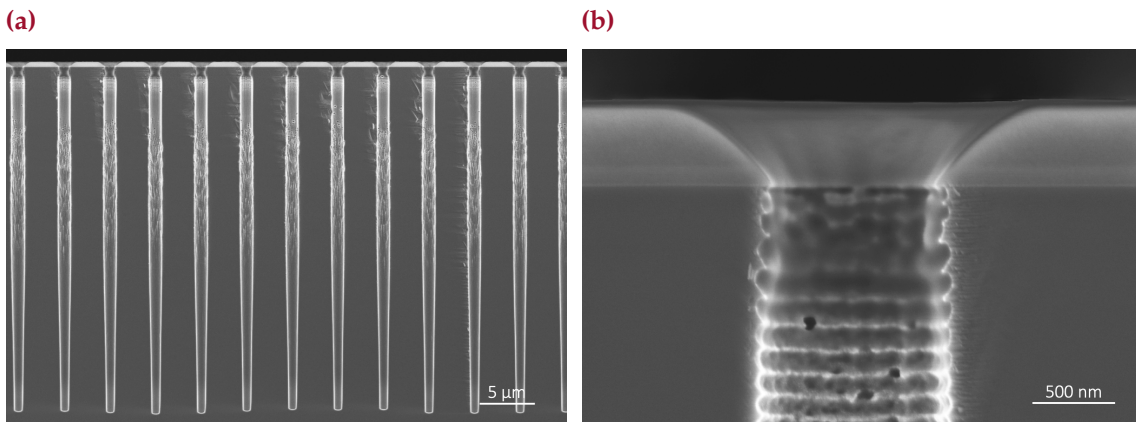


Figure 3.3 | Sharp process. Differently from the classical two-steps Bosch process, the sharp process is optimized for narrow and high-AR features. The main difference are the addition of the oxygen plasma depassivation step, lower pressure, higher bias power and lower process temperature. This allows for much larger aspect ratio for small features (a) and much more controlled scalloping (b) for holes with a critical dimension of 1 μm .

performed at large bias values would remove the C_4F_8 coating mostly at the bottom of the TSV, allowing for a more anisotropic etching of the SF_6 .

With this process we obtained holes as small as 1.3 μm diameter and 35 μm deep, for an aspect ratio of 27:1 (see Figure 3.3). Thanks to the lower temperature, the reactivity of SF_6 was reduced and the erosion rate of the mask with it. However, also in this case we incurred into process saturation, which seems inevitable reached a specific aspect ratio.

Following the idea proposed by Chang *et al.* [93] and Parasuraman *et al.* [94], we developed a process which adjusts the etching parameters throughout the process. The results reported in Figure 3.4 show a clear reduction of the tapering effect due to the avoidance of the saturation due to the process parameters. We tried to sweep either SF_6 etching pulse duration, in the so-called DREM-type processes, or the RF bias power, in the processes that we called ADRIE, or adaptive-DRIE. The several processes parameters tested are reported in Table 3.1.

3.1.1 CHROMIUM AND ALUMINUM HARD MASKS

In order to further optimize the process, we considered changing mask material. Indeed, SiO_2 is not as resilient to SF_6 etching as metals like chromium or aluminum are, which depending on the process show little to zero etch rates [95–99]. However, the fabrication process simplicity added by a simple SiO_2 oxidation to the process made it the perfect mask to start with.

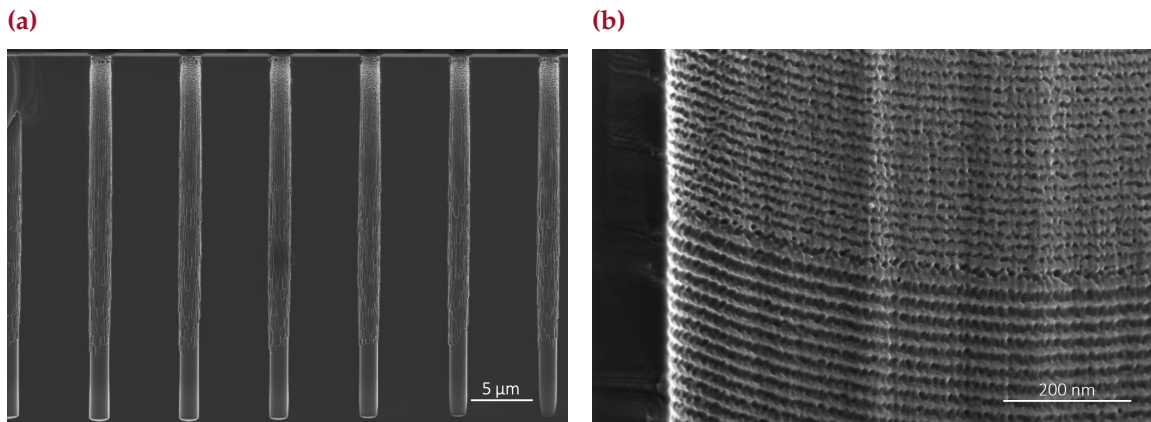


Figure 3.4 | DREM process. Surrogate of the Sharp process, the DREM process adjusts the pulse length of the SF₆ step while keeping constant both the C₄F₈ and Oxygen plasma steps. The holes appear to have less tapering (a), even if the wall roughness increases. At specific depths, when the pulse time changes, we can notice the scalloping separation between the two steps (b).

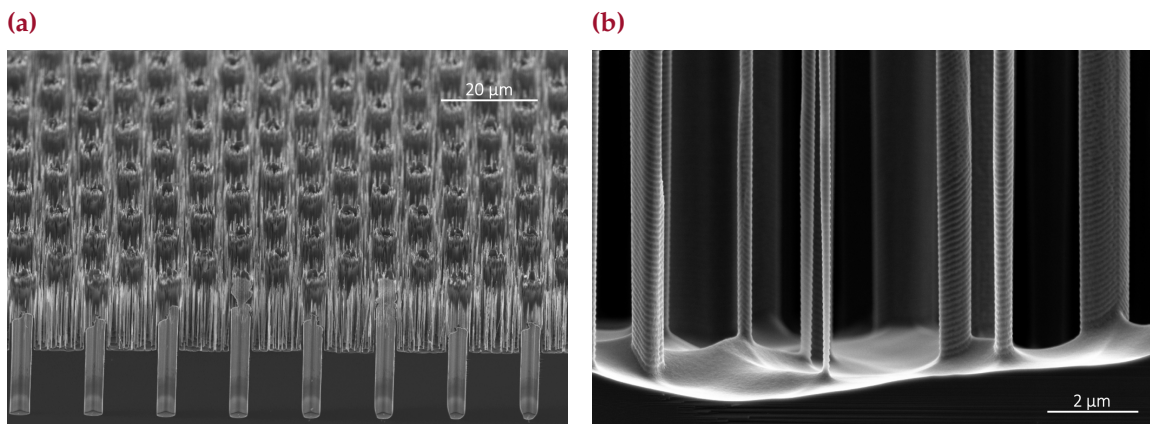


Figure 3.5 | Sputtering effect of the Cr mask. After the etching of the photoresist which lays on the hard mask, the chromium gets exposed and erodes quickly due to the sputtering effect. This erosion is non-homogeneous and ends up in vertical, ultrahigh aspect ratio, unwanted nanopillars.

We fabricated TSVs using either chromium (Cr) or aluminum (Al) masks. The masks were evaporated using a Leybold-Optics LAB600H e-beam evaporator for masks thicknesses ranging between 100 and 200 nm.

The first tests were not as expected. Using the previously optimized recipes, we noticed quick mask erosion due to the so-called sputtering effect of the mask, consequence of the too high ratio of bias power and pressure (see Figure 3.5). Reducing the bias power helped avoiding fast mask erosion, but at the same time caused a more relevant drop in etch rate, hence it could not be employed as solution.

Following more tests and analyses, we noticed that changing the frequency of the RF bias strongly affected the behavior of the metallic mask. While a low-frequency bias caused strong damage on the metallic mask, using high-frequency

Table 3.1 | DRIE Processes.

Process	Gases flux (sccm) [C ₄ F ₈ , O ₂ , SF ₆]	Pulse duration (s) [C ₄ F ₈ , O ₂ , SF ₆]	Pressure (mbar)	Source Power (kW)	RF Bias Power (W)	Temp. (°C)	Process Time (min)	Holes Aspect Ratio (AR)
Bosch Standard	[300,0,300]	[2,0,6]	4.0	1.8	45	25	40 (300 cy)	12:1
Bosch Standard	[300,0,300]	[2,0,6]	4.0	1.8	45	25	70 (525 cy)	15:1
Bosch LP	[200,0,300]	[2,0,5]	2.0	1.8	100	20	30 (257 cy)	20:1
Bosch HiPo	[250,100,300]	[2,1,4]	2.0	2.5	40	20	40 (343 cy)	XX:1
Bosch HiPo HP	[250,100,300]	[2,1,4]	1.0	2.5	40	20	40 (343 cy)	20:1
Bosch HiPo HF	[250,100,550]	[2,1,3;7]	2.0	2.5	40	20	40 (358 cy)	20:1
SOI Sharp	[300,100,300]	[2,1,3]	2.0	1.5	90	0	40 (400 cy)	22:1
SOI Sharp	[300,100,300]	[2,1,3]	2.0	1.5	90	0	70 (700 cy)	28:1
SOI Sharp LF	[300,100,100]	[2,1,6]	2.0	1.5	90	0	30 (200 cy)	15:1
SOI Sharp HFI	[300,100,450]	[2,1,2;7]	2.0	1.5	90	0	70 (737 cy)	27:1
SOI Sharp HFII	[300,100,550]	[2,1,2;5]	2.0	1.5	90	0	70 (764 cy)	28:1
SOI Sharp HP	[300,100,300]	[2,1,3]	1.0	1.5	90	0	70 (700 cy)	25:1
SOI Sharp HiPo	[300,100,300]	[2,1,3]	2.0	2.0	100	0	70 (700 cy)	25:1
DREM 325	[300,100,300]	[2,1,3;5]	2.0	1.5	90	0	60 (- cy)	22:1
DREM 3210	[300,100,300]	[2,1,3;10]	2.0	1.5	90	0	55 (- cy)	27:1
ADRIE 902100	[300,100,300]	[2,1,3]	2.0	1.5	90:100	0	69 (690 cy)	28:1
ADRIE 902120	[300,100,300]	[2,1,3;3;5]	2.0	1.5	90:120	0	90 (- cy)	26:1
ADRIE VF	[300,100,225:400]	[2,1,2;7;3]	2.0	1.5	90:100	0	70 (- cy)	27:1
ADRIE LF	[300,100,100:300]	[2,1,3;6]	2.0	1.5	90:110	0	70 (- cy)	25:1

Comparison of several deep reactive ion etching processes.

made damage way milder. While the origin of this effect is not yet fully understood, we believe it may be related to some capacitive coupling between the mask and the substrate holder. The results are presented in [Figure 3.6](#). The etching of the chromium mask was, for the high-frequency RF bias process, negligible: 15 nm of chromium was etched after over 40 minutes of process, which lead to a maximum etch depth of 70 μm for 20 μm trenches, leading to a selectivity higher than 4500.

3.1.2 HOLES AND TRENCHES

In order to compare the obtained results with literature, we designed a mask with holes and trenches, which are the most common features used for calibration of DRIE. Before proceeding with the comparison, we need to bear in mind that our process was optimized for holes etching, and trenches optimization may have different parameters thanks to the larger etchant entry area. In fact, Parasuraman *et al.* [94], have shown deep silicon trenches with an aspect ratio of 160:1 by extreme process optimization and 250 nm trench size, while Owen *et al.* [100] achieved an AR of 97:1 with trenches as large as 3 μm. The following comparison was done to

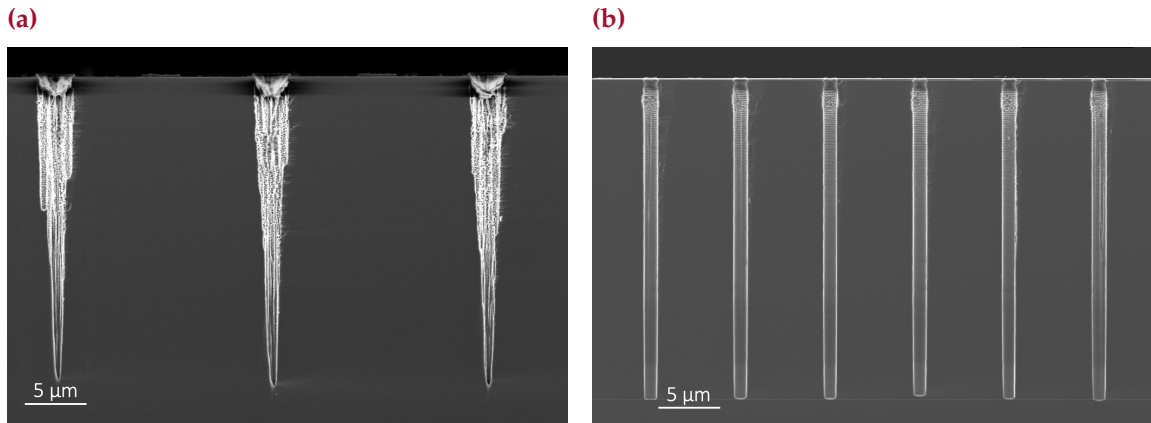


Figure 3.6 | Bias Frequency effect on Cr mask. Low frequency biasing conditions (hundreds of kHz) cause the metallic mask to charge and with a bias power of 90 W that would mean strong interaction between the electric field of the capacitor-like mask and the plasma (a), which ends up in strong damage of the trenches. Reducing the bias power (b) allows for a weaker capacitive coupling, which leads to negligible overall effect on the holes etching.

estimate a relationship between holes and trenches AR and to establish the status of our optimization.

The new mask consisted of deep holes, deep loops (which are rectangular shape closed loops made by trenches) and deep trenches (which are very long etched lines), so to compare our results with what has been demonstrated in the literature [87, 94]. The holes, loops and trenches were patterned with different critical dimensions to compare AR .

As expected, we see a very different etch rate in holes, loops and trenches. Some of the results are presented in Figure 3.7. With the same process and 1 μm critical dimensions features we obtained an AR of the order of 30 for deep holes Figure 3.7(a) and an AR of 75 for the same feature size deep trenches Figure 3.7(b). We can also notice that there is a non-negligible difference between trenches and loops. Deep loops have a lower gas entry area with respect to the trenches, which turns out to be relevant even for quite large loops geometries. For instance in Figure 3.7(b) we compare the depth of a $20 \times 20 \mu\text{m}^2$ loop (AR of 67) of 1 μm width and deep trenches also of 1 μm width (AR of 75).

After collecting all the data from different etching recipes, the data were analyzed following the approach described in Parasuraman *et al.* [94], *i.e.*

$$AR = \frac{a \log(1 + bw)}{w}, \quad AR_{\max} = \lim_{w \rightarrow 0} \frac{a \log(1 + bw)}{w} = ab \quad (3.1)$$

where w is the critical dimension of the features, and a and b are fitting constants dependent on the process parameters. In Figure 3.8 it is possible to see the trend of

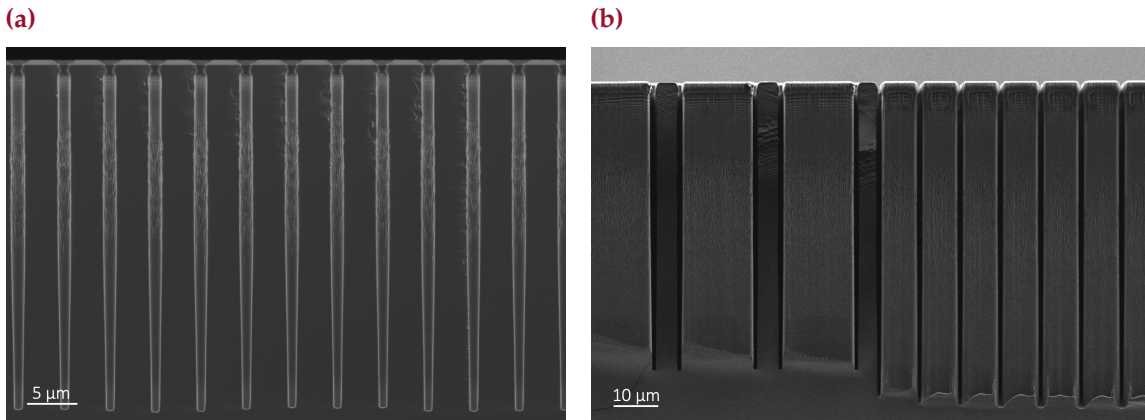


Figure 3.7 | Holes depth vs trench depth. Comparison of the depth of 1 μm wide loops, trenches and holes. While the holes only go as deep as 32 μm (a), for an overall aspect ratio of roughly 30, the loop and the trenches achieve similar maximum aspect ratios of 67 and 75 respectively (b) due to their large collaborative cross-sectional areas.

etched depth and aspect ratio with respect to the feature size. We fitted these values to obtain a and b values from (3.1) for each process and for each geometry. The R^2 value for each of this fitting was higher than 0.98. It appears that the parameter a is dependent on the process parameters but is quite insensitive of the etched geometry, while b seems much more sensible to geometry variations.

3.2 SURFACE POLISHING: THE MICHELANGELO STEP

According to the literature [89, 101, 102] one of the main problems with the standard through-silicon vias fabrication is related to the scalloping effect. Its presence may affect the quality of the seed layer, and in turn, of the electroplating. Non-homogeneous insulator or seed layer deposition due to scalloping can strongly affect the quality of electroplating. Even if atomic layer deposition was used for the insulation and seed layers to ensure homogeneity, scalloping may still cause concentration of stress and electric field in the insulator and the barrier layer of the TSV [103], leading to dielectric breakdown and Cu diffusion during the electroplating step [104].

In order to avoid the scalloping, a novel fabrication process has been developed: we call it the Michelangelo process [J9]. This new process exploits the anisotropic etching properties of potassium hydroxide (KOH) of silicon in order to completely remove the scalloping after the Bosch process has been performed. As shown in Figure 3.9(b), the KOH etching rate differs 1-to-3 orders of magnitude between the majority of crystalline orientations of silicon and the $\langle 111 \rangle$ orientation depending

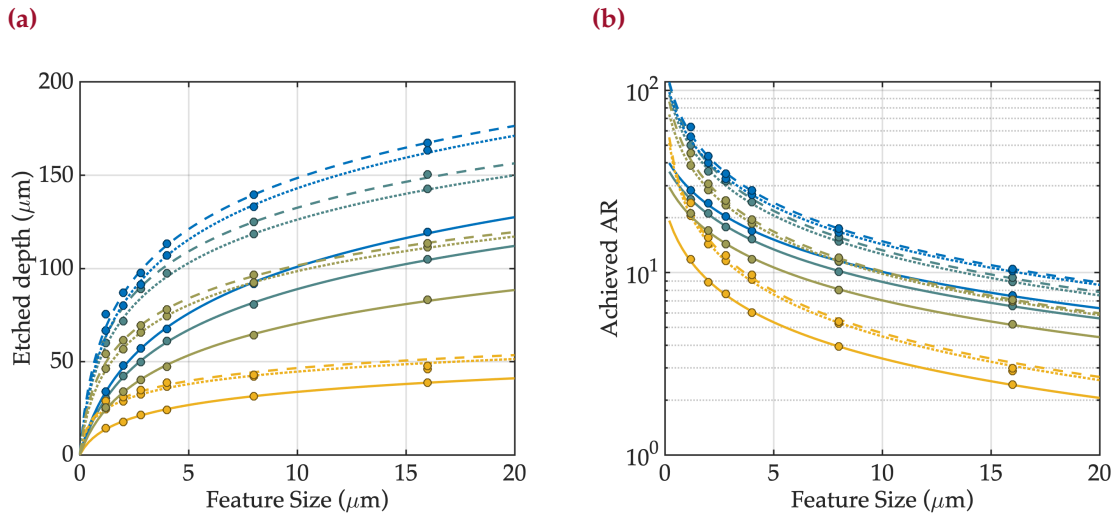


Figure 3.8 | Analysis of the deep reactive ion etching processes. We compare etched depth (a) and achieved aspect ratio (b) of four different processes for holes (solid line), loops (point line) and trenches (dashed line). Different processes have different line color.

on the KOH concentration. It has been shown [105, 106] that this effect, when well engineered and combined with the deep reactive ion etching, can help fabricate smooth and well controlled nanostructures.

We processed Si $\langle 110 \rangle$, 100 mm wafers. These wafers crystalline orientation is such that one of the $\langle 111 \rangle$ plane is perpendicular to the surface, tilted by 35.26° with respect to the main flat. We designed a new mask which instead of having circles and/or squares shaped openings, had rhomboidal structures whose edges were lining up with the $\langle 111 \rangle$ plane underneath them (see Figure 3.9(a)). After the deep reactive ion etching, the wafers were immersed in a 40% KOH solution, which shows an acceptable selectivity between Si $\langle 111 \rangle$ and the other crystalline orientations of at least 80, in order to etch all that was coming from the scalloping effect and leave the vertical faces without any surface roughness. After cleaning hole by the "excess" silicon, the wafer was put into a HCl bath for potassium particles removal. Follows an O₂ plasma descum and then a buffered hydrofluoric acid (BHF, NH₃F (40%):HF (50%) 7:1) bath at room temperature for the removal of the excess SiO₂ hard mask. The results showing TSVs fabricated without and with Michelangelo step are reported in Figure 3.9(c)–(d).

The reason why we called it Michelangelo process is related to the famous quote by Michelangelo Buonarroti:

The sculpture is already complete within the marble block, before I start my work. It is already there, I just have to chisel away the superfluous material.

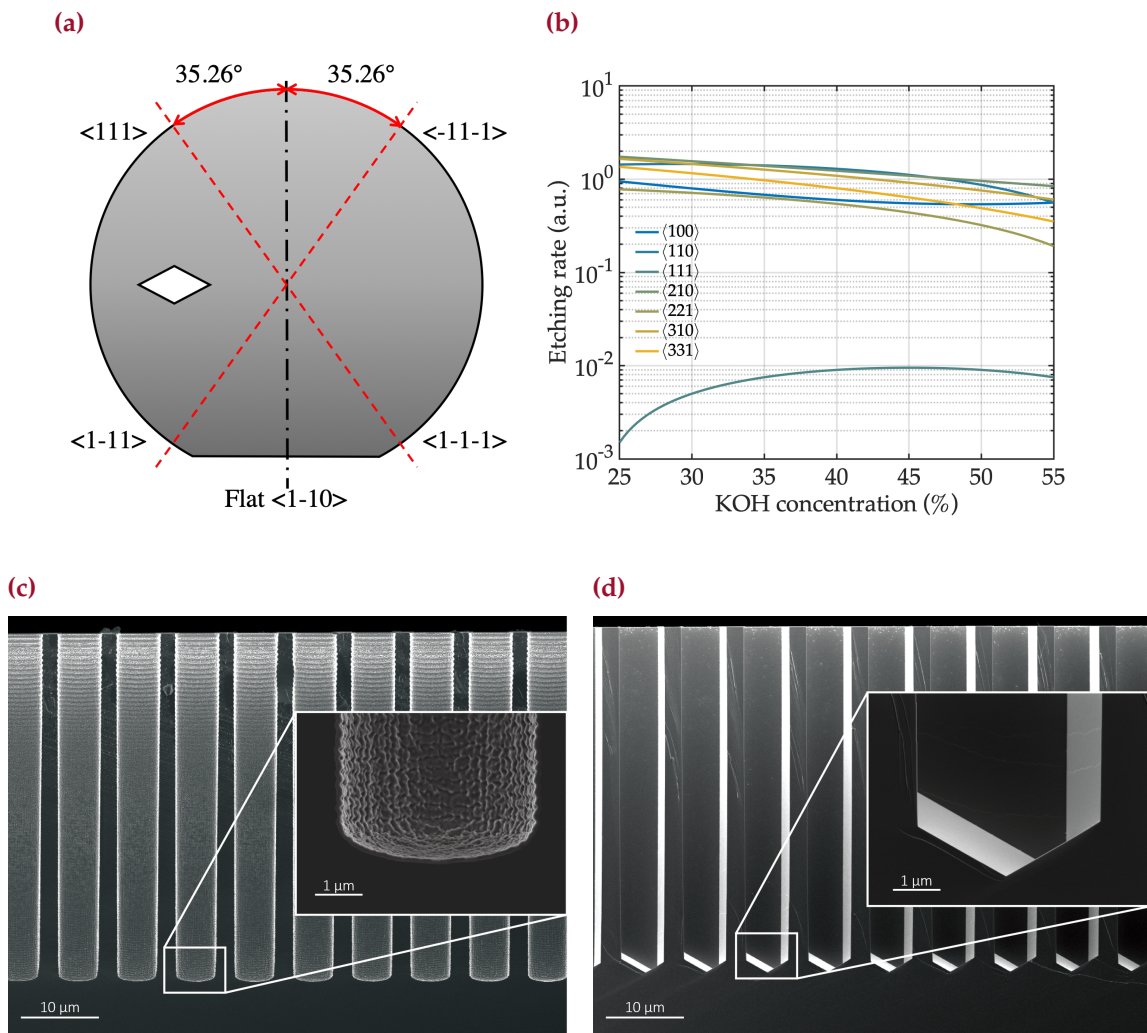


Figure 3.9 | Michelangelo process. The process exploits the verticality of crystalline of the $\langle 111 \rangle$ planes in Silicon in $\langle 110 \rangle$ wafers (a) and the anisotropicity of KOH etch rate for the different silicon crystal orientations (b). Data from Silex, Inc. Scanning Electron Micrographs (SEMs) of through-silicon vias (TSVs) etched without (c) and with (d) the Michelangelo process.

Indeed, with the final KOH etching step, we just selectively remove all that is superfluous, *i.e.* the scalloping. The Michelangelo process has been patented [P1] in 2020.

3.3 THROUGH-SILICON VIAS METALLIZATION

Final step of the TSV fabrication is the metallization step. Before proceeding with the filling, to ensure proper insulation and to avoid metal diffusion in the silicon substrate, a dielectric "barrier" layer is grown, either via thermal oxidation of the silicon into 200 nm of SiO_2 , or via ALD deposition of 100 nm of Al_2O_3 .

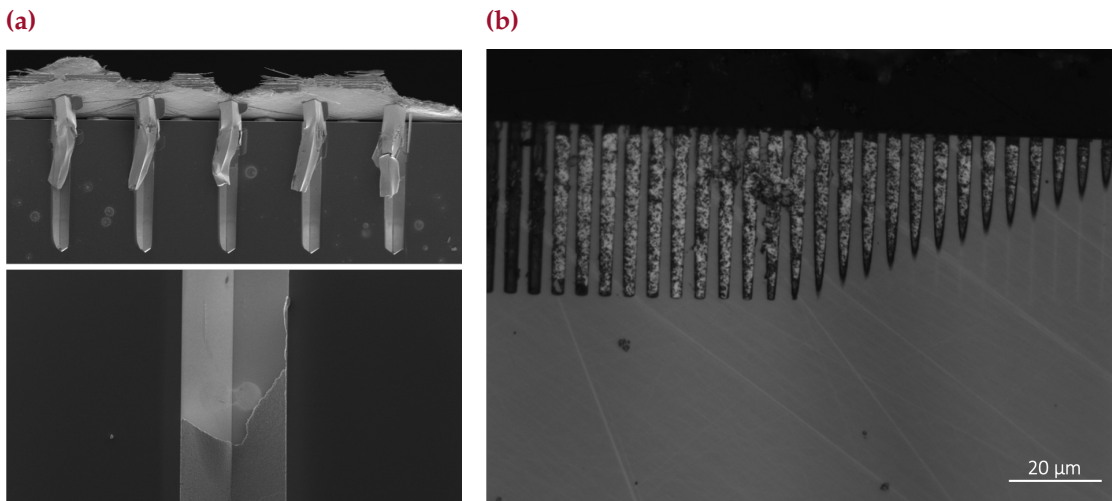


Figure 3.10 | metallization of the through-silicon vias. Scanning Electron Micrographs (SEMs) of through-silicon vias after the electroplating (a) and optical microscope micrographs of the metal injection technique (b).

We processed three different metallization steps: the most conventional Cu electroplating, the novel metal infiltration technique, and the cryogenics-only superconducting TSV, which is nothing else but an ALD coating of the inner walls of the TSV with superconducting material (NbN or TiN).

3.3.1 ELECTROPLATING

The electroplating step was performed as comparison to the other processes since it is known as the "standard" TSV filling process. In electroplating, a copper bar (source) and the target wafer, which has been coated with a conducting layer, are immersed into an electrolyte bath. The composition of the bath is a mixture of copper sulfate (CuSO_4), methanesulfonic acid (MSA, $\text{CH}_3\text{O}_3\text{S}$), chloride ion (Cl^-), a so-called suppressor and an accelerator. Note that, in order to deposit the copper on the wafer, it first needs to be coated with a seed layer deposition on top of the insulation layer. For this process, we performed a deposition of 30 nm of Pt via ALD to ensure maximum homogeneity of the seed layer.

As described and analyzed recently by Wang *et al.* [107], there are three different regimes in electroplating: sub-conformal, conformal and super-conformal plating (see Figure 3.11). Given a copper bath, current density is the main control parameter to define the quality of the electroplating: at the lowest current density values, the plating generally shows only seam defects (conformal plating) which are negligible in terms of practical use of the TSV. Increasing the current density, the dimension

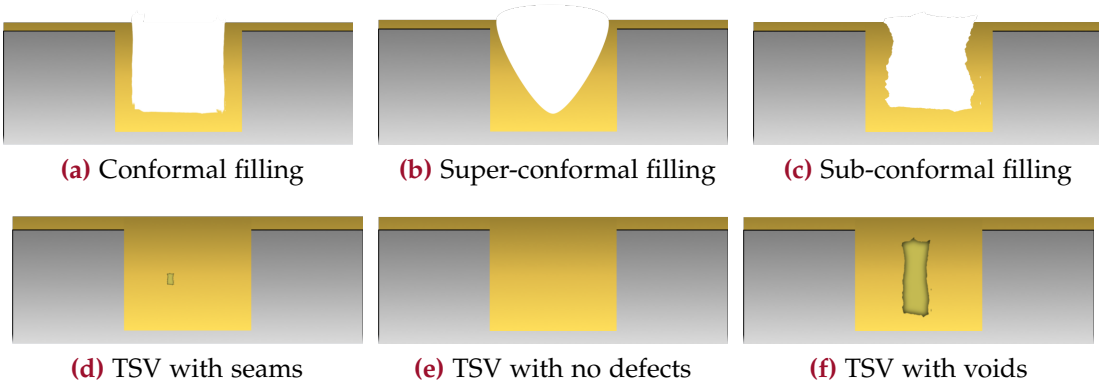


Figure 3.11 | Cu electroplating process. Increasing the current density the filling process is identified as conformal (a), super-conformal (b) and finally sub-conformal (c). The deposition rate increases with current density. However, conformal plating leads to seams defects (d) and sub-conformal to voids (f). The only defect-free process is the super-conformal (e), as it fills the via in a "bottom-up" morphology.

of the seeds is reduced until eventually the process is defects-free, *i.e.* the super-conformal. However, when too high current density is provided during deposition, the coating gets rougher and void defects start appearing, which are associated with the sub-conformal regime.

Before the plating is performed, it is necessary to preprocess the wafer in order to exclude air in the via and to wet the seed layer. The wafer is put into a vacuum bottle with deionized water and intermittent ultrasonic vibration is applied to remove the surface bubbles until no more bubbles appear. Then, the TSV chip is rapidly moved to the plating bath and kept stationary for a sufficient time to ensure adequate diffusion of the plating solution within the via.

The electroplating was performed at 5 mA/cm^2 , which for our bath composition was found to be the current density *sweetspot* for super-conformal filling. The result is shown in Figure 3.10(a).

3.3.2 METAL INFILTRATION

The second approach explored for through-silicon vias filling is metal infiltration, also called metal casting. The process is conceptually much simpler than the electro-chemical deposition, but with the drawback of no thickness control on the filling. This work was performed in collaboration with Prof. Andreas Mortensen and Luciano Borasi of the LMM lab at EPFL, and lead to the publication [J6].

The process is reported in Figure 3.12. The sample is placed into a graphite crucible in a pressure controlled furnace. On top of the open TSV surface is placed a

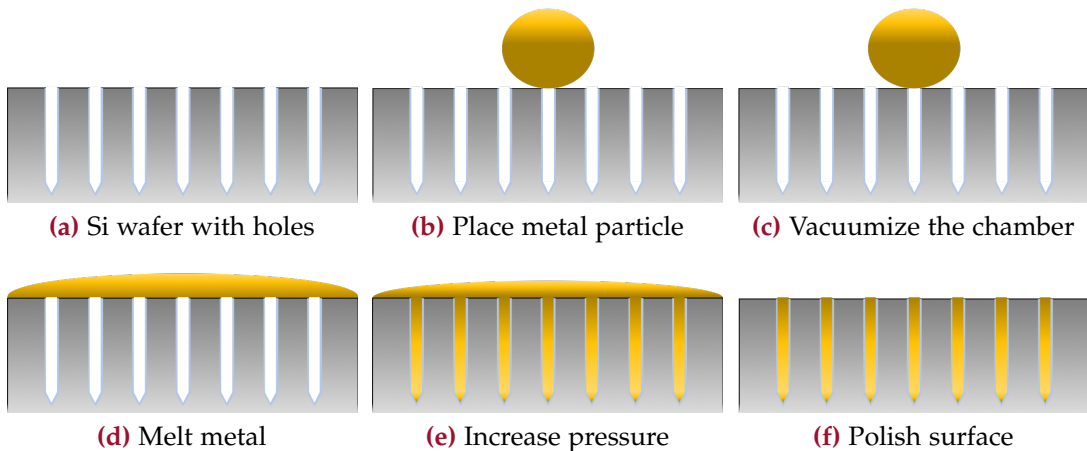


Figure 3.12 | Metal infiltration process. The already partially processed wafer (a) is put in a furnace with a infiltrant metal grain on it (b). The chamber is first vacuumized to extract air from the deep holes (c), and then warmed up until the temperature in the chamber is increased to several hundreds of °C to melt the metal (d) which will cover the holes due to capillarity effects. Pressure in the chamber is increased (e) to push the melted metal in the holes, and slowly the temperature is reduced while the pressure is maintained. Finally the wafer is polished (f).

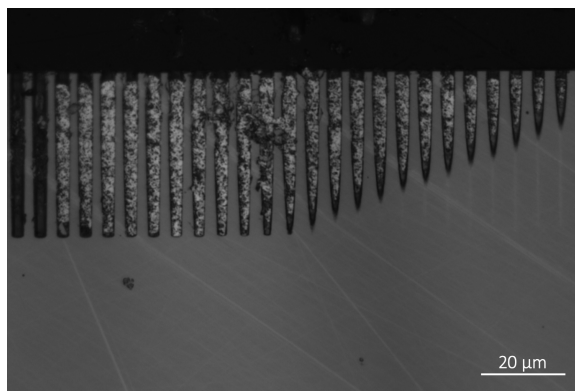
piece of the infiltrant metal. After vacuuming the chamber, the temperature is risen above the melting point of the metal, which by capillarity effect melts and covers the whole chip (Figure 3.12(d)). Then, by increasing the pressure in the furnace while keeping the temperature constant, the metal is injected into the vias, filling them, partially or entirely, depending on the applied pressure. Finally, the sample is cooled down while maintaining the chamber pressure constant. The excess metal is then removed and polished from the top surface. Among the advantages of this technique, which allows for a simple and fast filling of TSVs, are the low amount of defects as well as super-conformal capabilities of the filling technique in spite of aspect ratio considerations, which is not true for electroplating. The produced TSVs are reported in Figure 3.13.

Potentially interesting metals for this process are collected in Table 3.2. The metal should have low resistivity ρ as well as a low enough melting temperature T_f to allow CMOS compatible processing temperatures. Among the candidates, tin, indium and some of the many tin-based alloys are preferred options as they present good thermal and mechanical properties. Moreover, some of the metals in Table 3.2 show superconducting behavior, as indicated from the column of T_C where critical temperatures are also reported. Superconducting filled vias fabricated this way would ensure not only a lossless electrical connection, but would also (to some extent) suppress phononic transmission of heat coming from the warmer control chip, ensuring better thermal insulation than a normal metal.

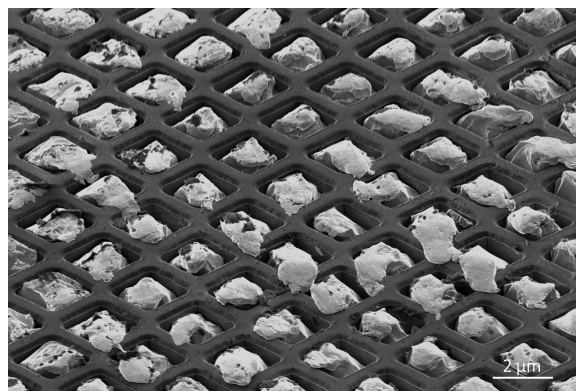
Table 3.2 | Metals considered for the infiltration process.

Name	Type	Formula	Resistivity, ρ ($\mu\Omega\cdot\text{cm}$)	Melting Temperature, T_f ($^{\circ}\text{C}$)	Critical Temperature, T_c (K)
Aluminum	Pure metal	Al	2.65	660	1.20
Zinc	Pure metal	Zn	5.90	419.5	0.855
Indium	Pure metal	In	8.37	157	3.4
Tin	Pure metal	Sn	10.9	232	3.72
Gallium	Pure metal	Ga	14.0	29.7	1.09
In52	Alloy	In ₅₂ Sn ₄₈	15.0	118	?
Bi58	Alloy	Bi ₅₈ Sn ₄₂	34.0	138	?
Sn ₉₀ Au ₁₀	Alloy	Sn ₉₀ Au ₁₀	15.2	217	?
Niobium-Tin	Alloy	Nb ₃ Sn	90.0	Diff. of Sn?	18.3

(a)



(b)

**Figure 3.13** | Metal infiltration TSVs. Scanning electron micrographs of the resulting chips after metal infiltration of Ag in 2 μm holes.

3.3.3 SUPERCONDUCTING TSV

The third and last approach explored for through-silicon vias filling is the fabrication of superconducting through-silicon vias. As we have seen in [Section 3.2](#), using the Michelangelo step we can produce scalloping-free TSVs. Because of that, when using superconductors, filling the whole TSV is no more a requirement, as thin film coating of the TSV could operate just as well in terms of electrical properties: the absence of scalloping will ensure the deposition of the thin film to be conformal enough to show no suppression of superconducting properties. This is the main reason behind the development of the atomic layer deposition processes of niobium nitride ([Subsection 2.1.2](#)) and titanium nitride ([Subsection 2.2.2](#)) described in the previous chapter.

For an SNSPDs array, for instance, succeeding with this process would allow the fabrication of a 3D stacked large array of single-photon detectors, which could be then coupled to either an interposer or a control chip via indium microbump

chip-to-chip bonding. Superconducting materials present not only zero electrical resistance, but also a very low thermal conductivity as long as the superconducting state is preserved. Having just a thin layer of material transferring the heat to the detectors could work also as an high-impedance thermal layer and could ensure sub- T_C operation of the sensor array.

3.4 DISCUSSION

Despite not intrinsically innovative in the approach of the fabrication of through-silicon vias, the results presented in the chapter represent few novelties in the process of TSVs. The addition of the Michelangelo polishing step, for applications where $\langle 110 \rangle$ -oriented silicon wafers are an option (MEMS, custom sensors, *etc.*), allows for a more robust and repeatable filling process, as the elimination of scalloping leads to less potential TSV failure, either due to cracks in the insulation layer or to electrical breakdown of the dielectric.

Regarding the metallization methods, we have introduced a new filling technique based on metal casting. Among the advantages of this approach, the most interesting probably resides in the choice of metals to infiltrate. While electroplating or chemical depositions limit in the number of metals that can be used as fillers, our process allows infiltration of any metal (in particular if done in a "via-first" way) as long as its melting temperature is below the melting temperature of silicon or its barrier layer (usually SiO_2 or Al_2O_3 , hence not limiting).

Finally, given the absence of scalloping thanks to the Michelangelo step, it is possible to develop process where the metallization is performed by just superconducting thin-films. The apart from the advantage related to the simplicity of the step compared to electroplating or infiltration, for good quality superconductors this film could also represent the main film of the chip, reducing the number of steps required for the full integration dramatically.

CHAPTER 4

*Astonishing how great the precautions that are needed in these delicate experiments.
Patience. Patience.*

— Michael Faraday, 1847

SUPERCONDUCTING NANOWIRE SINGLE-PHOTON DETECTORS

Superconducting nanowire single-photon detectors [17] are single-photon detectors based on ultra-thin, dirty superconducting films. The devices exploit their superconducting–normal state transition upon photon absorption as detection mechanism. Classical readout scheme for SNSPDs is to be placed in parallel to a readout circuit with impedance R_{load} , and to read them out as a voltage divider. Hence, to ensure a strong signal, they have been fabricated from dirty superconductors due to their large value of normal state resistance R_n .

SNSPDs have shown quasi-unity detection efficiency [108, 109], extremely wide spectral range from x-ray [110] to mid-infrared [111], very low dark count rate [112] and ultra-high temporal resolution [J11, C4]. In the last decade, widespread effort by the SNSPD community has improved the theoretical understanding of the detection mechanism in SNSPDs, guided by both the experimental [55, 113–119, J13] and the theoretical groups [56, 120–127].

A simplification of the detection mechanism of SNSPDs is shown in Figure 4.1. At the beginning the detector is at rest, biased at a value I_{bias} lower than the switching current I_{sw} , which is the experimental current bias condition at which the superconductivity is broken in the detector. As explained by Kerman *et al.* [55], this switching value is always smaller than the superconducting critical depairing current I_{dep} because of imperfection (constrictions) during the device fabrication process.

Upon photon absorption, as the energy deposited $\hbar\omega \gg \Delta$, being Δ the superconducting gap, the superconductivity is locally broken and Cooper pairs split into

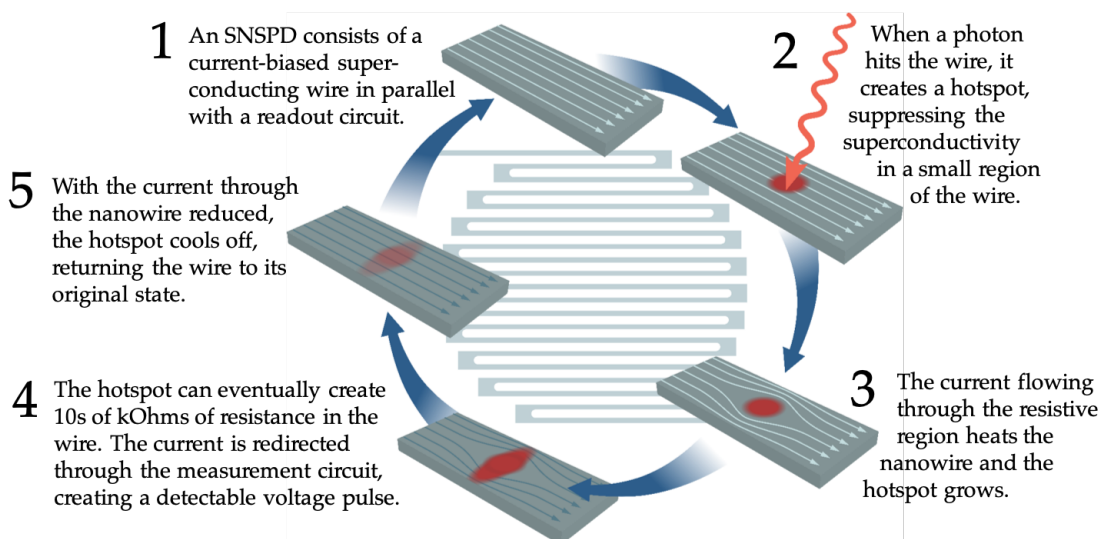


Figure 4.1 | Working principle of superconducting nanowire single-photon detectors. SNSPDs are current biased with dc supercurrent close to their critical current (1); upon photon absorption (2) superconductivity is broken in the so-called *hotspot* region, and starts heating up due to Joule dissipation (3). Due to heat diffusion, the hotspot grows until eventually the current density in the remaining superconducting cross-sectional area reaches the critical depairing current density, causing a full transition of the area in normal state (4). At this point, currents are redirected towards the readout circuit from the large impedance of the SNSPD, causing no current to flow in the device. Finally, the heat is dissipated in the substrate (5), the superconductivity is restored and the superconducting current is allowed in (1) ready for next photon absorption event (image credits to E. E. Wollman, after Gol'tsman *et al.* [17]).

hot electrons. This "hot" area is called *hotspot*. As these hot electrons thermally diffuse in the nanowire, the energy is distributed to more Cooper pairs, that break into more hot electrons (or dissipated in the substrate [126]), resulting in *hotspot* growth and superconductivity suppression in a larger region. If the number of hot electrons, or quasi-particles, is such to suppress superconductivity in a large enough portion of the nanowire cross-section, the supercurrent, still running through the nanowires in the superconducting region, reaches critical density j_{crit} , causing abrupt loss of superconductivity across the whole cross-section of the nanowire.

Due to Joule heating, the normal region expands until the resistance of the nanowire becomes much larger than the readout load impedance R_{load} , and the current is re-directed to the readout circuit. Once the current is expelled from the nanowire to be detected from the readout circuit, the heat generated can diffuse to the substrate and the superconductivity can be restored. The current can then go back to the nanowire and the device is ready for a new detection.

As reported by Korzh *et al.* [J11], there is a clear link between the latency of the detection mechanism (*i.e.* the time between absorption of the photon and time at which the nanowire superconductivity is broken) and the energy of the absorbed

photon $\hbar\omega$. It was in fact observed that higher energy photons would make the detector click faster. This effect, as subsequently explained by Allmaras *et al.* [56], is related to the fluctuations (called Fano fluctuations, [126]) in the energy distribution between electron and phonon systems in the superconducting film: when more energy is deposited, the electron system achieves the threshold energy, *i.e.* the number of hot electrons required to fully break superconductivity, faster, hence the superconductivity is more promptly lost.

Throughout the years, different materials have been proposed as SNSPD platform: at the beginning, Gol'tsman *et al.* [17] demonstrated the technology in NbN, which is a crystalline and polycrystalline material. However, shortly after, new materials have made their appearance in the technology, mainly NbTiN and TiN as other crystalline materials, and WSi and MoSi as amorphous superconductors. Our goal was to fabricate devices with timing resolution in the order of few picoseconds, as reported in [J11, C4], for potential ToF-PET applications. For this purpose, the requirements are mostly on timing resolution and sensor efficiency in the NUV.

Due to their shorter electron–phonon interaction time τ_{e-ph} , crystalline and polycrystalline materials show much better timing performance with respect to the amorphous counterpart, which are, in turn, easier to fabricate and show notoriously an higher fabrication yield. Another reason, as explained in Chapter 2, the sensitivity of SNSPD to longer wavelengths drops with superconducting energy gap Δ , which is proportional to critical temperature. Generally, as amorphous thin films have a lower T_C , they show higher sensitivity to NIR/MIR photons [57, 108].

In this chapter we report the results obtained from the fabrication of SNSPDs in NbN material system. The choice of NbN is explained by the fact that we are interested in good timing resolution and high efficiency in the NUV range, giving us no reason to move towards amorphous materials. To enhance the SNSPD yield, the films were bias sputtered [58] according to Section 2.1. The drawbacks of such a choice are related to loss of critical temperature, but at the same time also means better sensitivity in the NIR. The results reported herein are part of the work included in [J1].

SNSPDs characterization was carried out in the PhotonSpot cryogenic system, due to the capability of optically probe the detectors. The devices were wirebonded to a PCB and connected through SMA semi-rigid cables running in the cryostat all the way to the room temperature stage. At every stage, the SMA line was interrupted with a thermalization interface made of glass beads SMA-to-SMA connectors. Outside the cryostat, the devices were biased and read-out by means of precision coaxial cables (DC-18 GHz SMA cables, Crystek) connected to high-

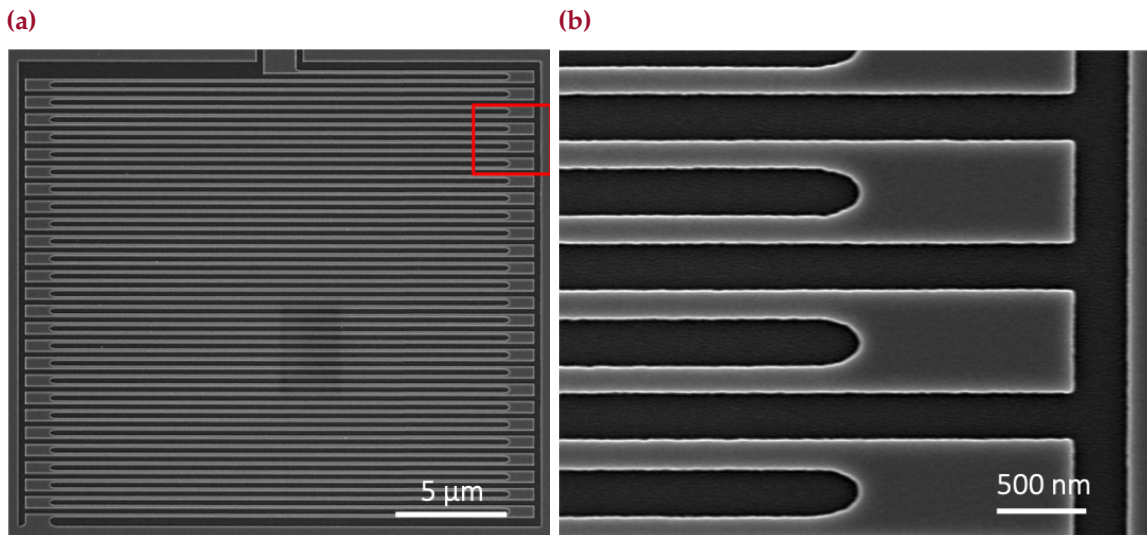


Figure 4.2 | Fabrication of a meandered pixel SNSPD. Scanning electron micrographs (SEM) of a $20 \times 20 \text{ } \mu\text{m}^2$, single pixel meandered SNSPD with nanowire width of 140 nm. The SNSPD was fabricated on Si substrate with an insulating layer of 100 nm of thermally grown oxide. The NbN was deposited by reactive RF sputtering and etched by reactive ion etching using CF_4 chemistry.

quality sources (SMU, Keysight). The laser used to excite the detectors is either the NKT Origami 10-100, as described in [Appendix B.1.3](#). For more setup information, refer to [Appendix B.1](#).

In order to ensure repeatable and energy efficient experiments, every piece of hardware was connected and controlled via either GPIB or LAN connection by an experiment computer. The experiment routines were written in python using the pyvisa package, to ensure high reliability and throughput [Appendix B.3](#).

4.1 DESIGN AND FABRICATION

The devices were designed by means of a custom code based on the python library gdsCAD. To compare the fabrication yield of classical meandered-shaped SNSPDs, multiple devices with different pixel size were designed to investigate the constriction factor dependence on pixel's active area.

SNSPDs are relatively easy to design from the lithographic perspective, as they are meander-like nanowires connected to a 50Ω impedance line, the so-called launcher PAD. Main design parameters when designing SNSPDs are the width w of the nanowire, usually in the range of 100 nm; the pitch p between the meandered lines, or alternatively the fill factor $FF = w/p$; and the pixel dimensions, usually in

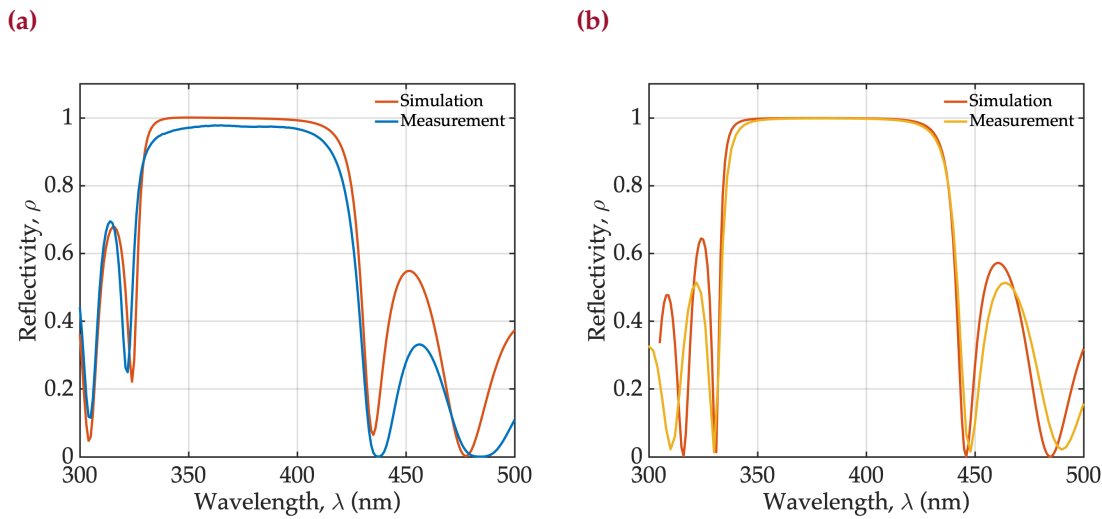


Figure 4.3 | Fabrication and optimization of the Bragg reflector. In red, the simulations of the DBR mirror reflectivity spectrum, considering the (n, k) values estimated for SiO_2 and Ta_2O_5 using ellipsometry (see Appendix A.3.1). In blue (a), measured spectrum of reflectivity of the deposited DBR, measured using a Varian Cary 500 high performance UV-Vis-NIR spectrophotometer, before roughness optimization. In yellow (b), measured spectrum of reflectivity after roughness optimization.

the range of 10 μm by 10 μm . Same applies for SNAPs [36], as their main design parameters do not change particularly more than that.

However, optical design of the SNSPDs is not as trivial. To enhance the efficiency of the detectors, we fabricated them embedded in a vertical optical stack [33, 108]. In the stack, the patterned thin film of superconductor is encapsulated either in the middle of a $\lambda/2$ cavity or on top of a $\lambda/4$ cavity, to intensify the electric field in correspondence to the superconducting film to enhance its absorption efficiency. The process flow developed for SNSPDs is reported in Appendix A.1.1. To define the optical cavity, both metallic and dielectric mirrors have been used in the literature, however the latter showed better performance as they can achieve larger reflectivity at the designed wavelengths and do not present any plasmonic modes losses.

Following the fabrication optimization reported in Appendix A.2.1, we were able to develop deposition methods for both SiO_2 and Ta_2O_5 with minimal residual roughness. The improvement of the roughness gave us an improved reflectivity (see Figure 4.3), as the peak reflectivity increased from 0.96(2) to 0.99(8) at the design wavelength of 380 nm. Despite the deposited Ta_2O_5 showed relatively low absorptivity in the NUV range (200–300 nm wavelengths) it was very hard to properly estimate the (n, k) values reliably, which explains why in Figure 4.3 the simulations agree with the measurement better in the longer wavelengths.

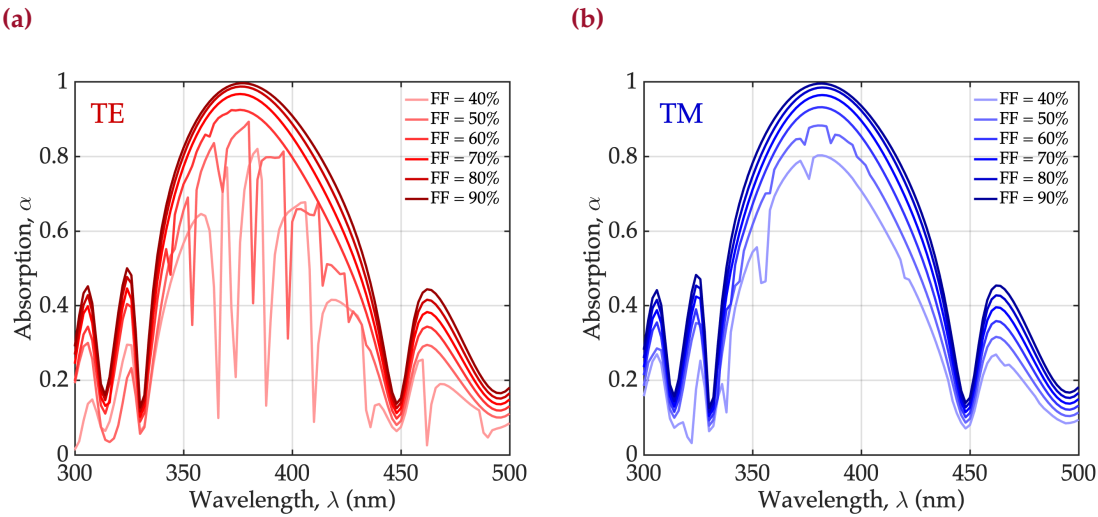


Figure 4.4 | SNSPDs Optical stack simulations. Results of the simulations performed with COMSOL Multiphysics for the optical stack. The NbN thin film was 7 nm thick, split in 5 repetitions of 120 nm widths and varying pitch depending on the fill factor FF . Both TE (a) and TM (b) polarizations are analyzed to take into account for any polarization-sensitivity of the designs. From the results, it seems that TE polarization resdshifts the peak of absorbance, while TM polarization blueshifts.

After simulation and fabrication of the DBR, it is necessary to analyze the behavior of the optical stack as a whole. The following simulations were performed using the 2D Wave Optics module of COMSOL Multiphysics. COMSOL is a finite-elements method solver, and the Wave Optics module is fully based on the numerical solution of Maxwell equations. In the 2D simulation, we analyzed the whole optical stack (Si substrate, DBR, $\lambda/4$ cavity and NbN thin film) and extracted the absorption factor α . The superconducting device was at first considered as a planar thin film to simplify the case study. After validation of the simplified COMSOL model by means of alternative methods such as rigorous coupled-waves analysis (RCWA) or classical optical transfer-matrix method, the thin film was segmented in few isolated thin structures of width w of 120 nm and varying fill factor FF .

The results of the simulations for different values of FF are reported in Figure 4.4. As the nanowires in the simulation are modeled as infinitely long stripes, it is important to check the effect of polarization of light to address any design polarization sensitivity, hence the study of both TE and TM polarized light. For TE polarization and low FFs , the devices present unstable absorptive behavior, mostly due to higher modes and standing waves within the cavity.

4.2 CHARACTERIZATION

Before characterizing the devices themselves, it was important to get an estimate of the critical depairing current associated to the films, so to be able to estimate properly the constriction factor [55] of SNSPDs. The critical depairing current I_{dep} was estimated using the method described in [J13]. Coplanar waveguide resonators with width in the same range of the SNSPDs where fabricated out of the same film of the detectors. Using the setup reported in Figure B.4, the resonators spectrum was recorded at different DC biasing conditions. When driven by DC current I_{bias} , high- L_k superconductors experience an increase of kinetic inductance. This increase is described by Clem and Kogan [120] and depends on the ratio $j_{\text{bias}}/j_{\text{dep}}$, where j_{dep} is the depairing current density of the superconducting film. Considering that for a coplanar waveguide the resonant frequency $\omega_r = 1/\sqrt{L_r C_r}$, with $L_r \approx L_k$ and C_r constant are inductance and capacitance of said resonator, it is possible to associate the kinetic inductance change $L_k(I_{\text{bias}})/L_{k,0}$ to the frequency change $\omega_0/\omega(I_{\text{bias}})$, where the subscript "0" stands for zero biasing current conditions. This $L_k(I_{\text{bias}})/L_{k,0} - I_{\text{bias}}$ relation leads to the estimate of I_{dep} following one of two models as described in [120], depending on resonator frequency. In the fast relaxation model approximation, the resonator oscillation time τ_{osc} is much larger than the relaxation time of the order parameters in the G-L description, *i.e.* $\tau_s = \hbar/k_B(T_C - T)$, which for NbN is estimated to be 1 ps; in the slow relaxation model, $\tau_{\text{osc}} \ll \tau_s$. As the resonator is operating in the GHz range, the fast relaxation model is more accurate and provides better estimate of depairing current.

The estimated depairing current for the films used to develop SNSPDs is $I_{\text{dep}} = 40.7 \mu\text{A}$ for a nanowire 120 nm wide and 7 nm thick.

The first screening test after a new fabrication run was a current–voltage characteristics of a few devices at base temperature (I–V curve). I–V curves are of critical importance for SNSPDs, as many parameters can be extracted from them. An SNSPD I–V curve is shown in Figure 4.6(a).

The readout scheme to collect an I–V curve of an SNSPD is relatively simple. The device is voltage biased through a room temperature resistor R_{bias} , which usually has a resistivity in the range of 25 kΩ. A high-impedance voltmeter is connected to the bias line after the resistor, to measure the voltage drop across the device.

At the beginning of the curve, the device is superconducting, hence supercurrent flows through it and directly to ground with no voltage drop. Once the bias current I_{bias} reaches the switching current value I_{sw} , the superconductivity is broken and the

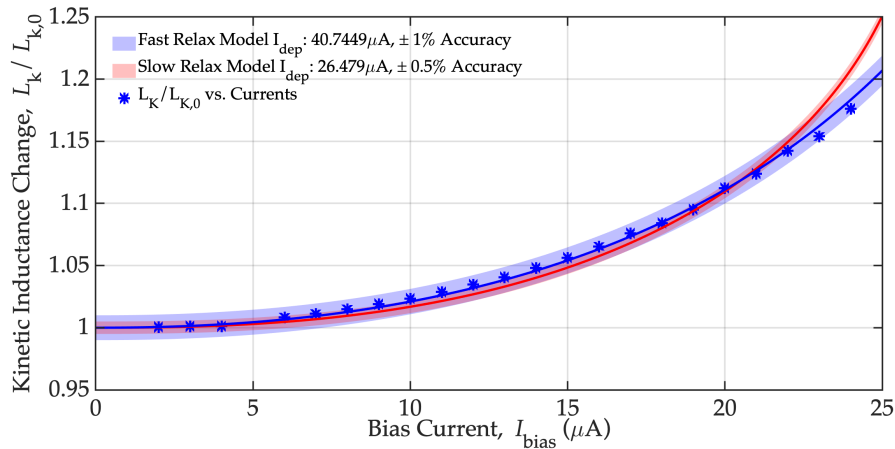


Figure 4.5 | Thin films estimation of depairing current. Kinetic inductance change with DC biasing current is reported in figure for a long resonator with width w of 120 nm, thickness t of 7 nm and resonant frequency of 4 GHz. The value of L_k changes up to an increase of 20% compared to the zero bias condition right before the switching current of the resonator, at I_{sw} of 24 μ A. This suggests a constriction factor $C = I_{sw}/I_{dep}$ of roughly 59% for the long resonator, *i.e.* leading to I_{dep} of 40.7 μ A and a depairing current density of the film j_{dep} of roughly $4.85 \cdot 10^4 \mu\text{A } \mu\text{m}^{-2}$.

device becomes suddenly resistive, causing an abrupt increase of readout voltage and a drop of biasing current. The value I_{sw} does not have to be confused with the critical depairing current I_{dep} , which is the maximum physical current that can be driven within the superconductor while keeping it in the superconducting state. As SNSPDs are based of extremely thin films and narrow widths, the concept of constriction factor $C < 1$ [55] has to be taken into account as a fabrication imperfection factor. At the same time, the biasing current can also be limited by *latching* effect [128], suppressing the potential achievable current even further. In general, we can say that $I_{sw} \leq CI_{dep}$. As shown in Figure 4.6(a), the 120 nm wide nanowire achieved a switching current of 29 μ A, *i.e.* a constriction factor C of 0.72 [J13]. As the I–V characteristics continues after the switching current, the normal resistive behavior shows linear trend (blue curve).

SNSPD I–V characteristics generally exhibit an hysteretic behavior, *i.e.* if the voltage is reduced back to zero from the resistive state, the curve will not reach I_{sw} again (red curve). In fact, while reducing the voltage, the I–V characteristics shows a knee followed by a current plateau. The value of this plateau is referred to as "hotspot" current, or I_{hs} . This current is defined as the self-sustaining current required for the hotspot to remain in the normal domain due to Joule heating. While the voltage is reduced, the size of the hotspot (hence the normal state resistivity R_n) is reduced, until eventually the superconductivity is restored and the voltage drop across the device goes back to zero.

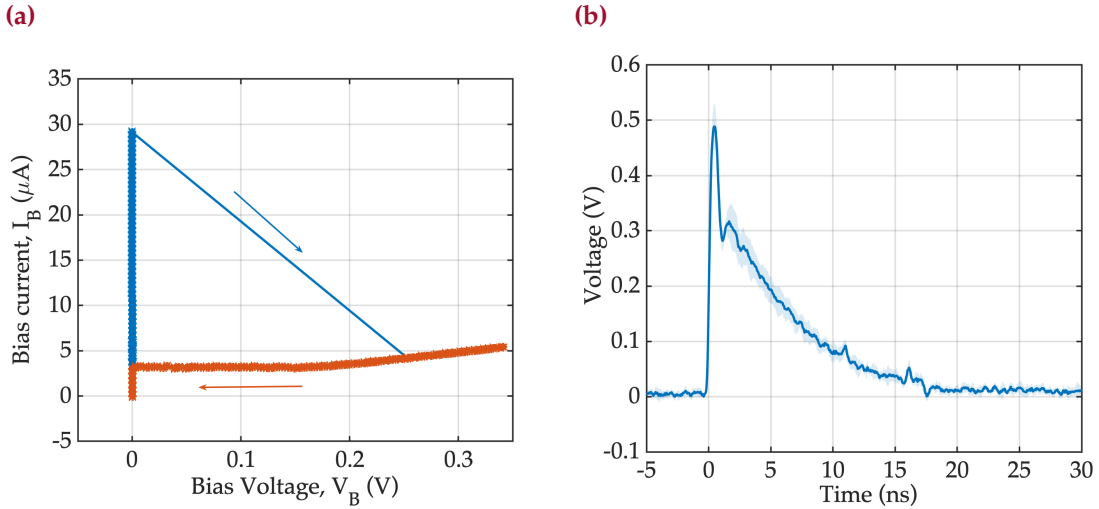


Figure 4.6 | SNSPDs preliminary measurements. The first measurement performed with SNSPDs is DC current–voltage characteristics (I–V curve, (a)). In superconducting state the current flows with no voltage drop; once reached I_{sw} and beyond that, the device transition into normal state and behaves resistively. Hysteresis points out another important parameter, the hotspot current I_{hs} which is the current required to sustain the normal state all the way until superconductivity recovery. I_{sw} and I_{hs} fix the maximum signal we can get from the SNSPD. After the I–V curve, we measure the pulses of the device at the oscilloscope (b). From the pulse rise and fall times, we can obtain a rough estimate of maximum count rate and timing jitter of the device.

I_{sw} , R_n and I_{hs} are three parameters of an SNSPD of most importance, as they can provide information regarding the constriction factor C (thanks to I_{sw}), the voltage pulse generated by the SNSPDs in case of photon absorption event (proportional to $I_{\text{sw}} - I_{\text{hs}}$), and even information regarding the upper limit of the timing capability of the devices (as R_n is inversely proportional to the rise time of the pulse generated by the SNSPD, as we will see later).

Together with the I–V curve, another preliminary test that can be done is the electrical pulse analysis. Once the device is cold, it is possible to check photon responsivity of the device by shining light in the cryostat (even by turning on the light in the room) and monitoring on an oscilloscope the RF-end of a the bias tee connected to the device (hence the readout line). If enough current is flown through the device, either photon sensitivity or dark count rate will cause the device to send voltage pulses. The pulses contain, just as much as the I–V curves, useful information for the subsequent characterization of the device, which can be used to perform an initial screening of the good devices, as rise and fall times are both proportional to the kinetic inductance of the device:

$$\tau_{\text{rise}} = \frac{L_k}{R_n + R_{\text{load}}}, \quad \tau_{\text{fall}} = \frac{L_k}{R_{\text{load}}}. \quad (4.1)$$

As shown from the rise time formulation, the kinetic inductance plays a key role in the timing response of the detector: the lower the kinetic inductance, the faster the rise time, the steeper the voltage pulse and the lower the noise contribution into the final jitter of the detector. However, kinetic inductance cannot be chosen as small as possible without drawbacks. Depending on the amount of time the detector requires to dissipate the heat after an absorption event, that we will call "thermal time" τ_{th} , a too small kinetic inductance would lead to a $\tau_{\text{fall}} \leq \tau_{\text{th}}$. If that is the case, after readout, the current may be pushed back in the detector while it is still warmer than the bath temperature. This would lead to the device clicking again, reaching the so-called latching state [128].

In order to address the other properties of the devices, such as efficiency or timing resolution, a pulsed laser source was required. Starting from a femtosecond laser at 1030 nm wavelength, with second and third harmonics generation we covered three wavelengths to characterize the devices in NIR, visible and NUV ranges. The details of the optical setup are thoroughly presented in [Appendix B.1.3](#).

4.2.1 EFFICIENCY MEASUREMENTS

Efficiency measurements are extremely complex measurements to perform. When trying to estimate efficiency via measurements, we compare the number of photon events detected by our system and we compare them to the number of photons we expect to have sent to the device. When doing so, the measured quantity is what we define as system detection efficiency (*SDE*), which is the total efficiency of the experiment. *SDE* is a product of various contributions of efficiencies, and the device detection efficiency (*DDE*) is just one of them. In the SNSPDs case, the *SDE* can be defined as:

$$\begin{aligned} SDE &= \eta_{\text{coupling}} \times \eta_{\text{trigger}} \times DDE \\ &= \eta_{\text{coupling}} \times \eta_{\text{trigger}} \times \eta_{\text{absorption}} \times \eta_{\text{QE}} \end{aligned} \tag{4.2}$$

where η_{coupling} is the optical coupling efficiency representing the fraction of light that reaches the devices from the experimental setup; η_{trigger} is the trigger efficiency, *i.e.* the electronics efficiency representing how many electrical pulses reach the amplification stage and how many cause a counter click; $\eta_{\text{absorption}}$ is the optical efficiency, *i.e.* the probability that a photon reaching the devices is actually absorbed in the superconducting thin film; and finally η_{QE} is the quantum efficiency of the

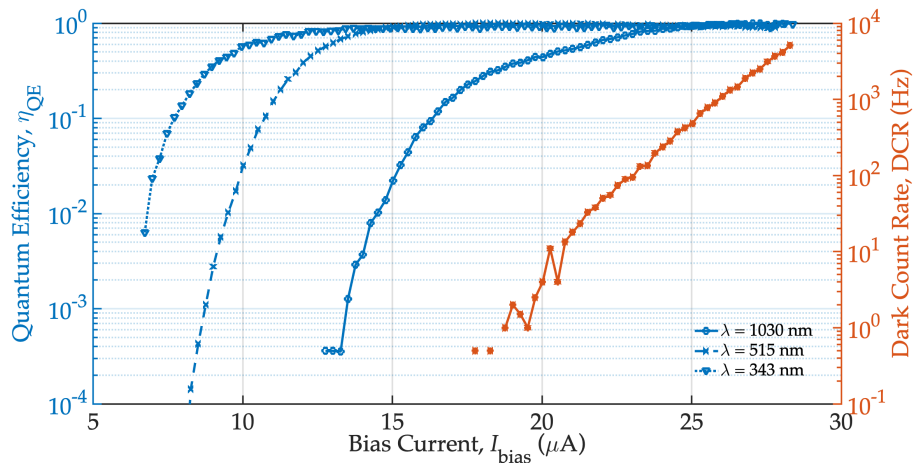


Figure 4.7 | SNSPDs quantum efficiency measurements. Differently from absorption or coupling efficiencies, quantum efficiency η_{QE} is strongly dependent on biasing conditions of the SNSPD. Increasing bias current in the device leads to larger quantum efficiency, until the device reaches the so-called *plateau*, at which unitary quantum efficiency is achieved. However, increasing biasing current also increases the noise detection floor in an exponential way.

devices, *i.e.* the probability to get a voltage pulse every time a photon is absorbed in the superconducting thin film.

As a proper *SDE* estimation when using pulsed lasers requires extremely complex calibration routines [129], which are beyond the scope of this work, we did not measure the global system efficiency. SNSPDs quantum efficiency is relatively easy to estimate, and under the assumption that the absorption efficiency does not vary dramatically at low temperature, *e.g.* due to variations in the refractive index values of the components of the optical stack, we can roughly estimate the $DDE = \eta_{\text{absorption}} \times \eta_{QE}$ as the product of these two contributions.

Classical example of quantum efficiency curves in SNSPDs are reported in Figure 4.7. The quantum efficiency dependence on biasing current can be interpreted as follows: when a photon with energy $\hbar\omega \gg \Delta$ is absorbed in a superconducting nanowire, it creates a high-energy electron-hole pair. The electron-hole pair interact with the phononic and electronic system, and by energy downconversion generates quasi-particles, *i.e.* hot electrons, in the Cooper pairs bath. If the photon had sufficient energy, the superconductivity is suppressed. Despite the actual mechanism is still under debate, the current understanding [125] is that this process depends on reduced bias current in the nanowire $I_{\text{bias}}/I_{\text{sw}}$ and critical temperature.

As expected, the larger the photon energy, the smaller the bias current I_{bias} required to reach the quantum efficiency plateau. In the same conditions and setup, it is possible to estimate the count noise of our detector, also called dark count rate (*DCR*). Dark count rate, in the same fashion of the efficiency, is a sum of

different sources. Environmental noise (DCR_{env}), *i.e.* noise coming from unwanted light sources, is probably the major contributor: as SNSPDs have usually very small superconducting energy gap when compared to visible and NIR light (NbN film with T_C of 7 K has a energy gap $\Delta = 1.764 k_B T_C$ of 1 meV, while a green photon has an energy $\hbar\omega$ of approximately 2.5 eV), any stray light particle absorbed in the film has a nonzero probability of being detected, contributing to noise. Electrical noise (DCR_{readout}) also plays a big role, in particular when operating very close to the switching current I_{sw} : any potential high-frequency fluctuation of the biasing current can cause the device to transition state. Intrinsic noise (DCR_{int}) has been experimentally and theoretically studied in recent years, leading to a much more comprehensive understanding. From recent work, for instance, it has been experimentally demonstrated that large contribution to the intrinsic noise comes from the turns of the meanders [130].

For all the reasons above, when measuring DCR it is absolutely crucial to make sure that the system is not exposed to stay light and that it is biased with a low-noise source. In order to do so, the measurements were performed substituting the optical window of the cryostat with metallic blanks and the optical fibers closed and covered at the higher stages of the cryostat, to ensure no stray light hit the devices coming from them. From the electrical point of view, using low-pass filters on the biasing current line and on the power supplies reduced further the DCR of the detectors.

4.2.2 TIMING JITTER MEASUREMENTS

Timing jitter characterization was performed on the devices with the setup reported in [Appendix B.1.3](#). System jitter is mostly given by the sum of three different contributions:

$$J_{\text{sys}} = \sqrt{J_{\text{optical}}^2 + J_{\text{intrinsic}}^2 + J_{\text{noise}}^2}. \quad (4.3)$$

In order to properly estimate the jitter of a detector, it is imperative to measure and characterize the setup used for the measurements first. In order to do so, we first estimated the optical contribution J_{optical} : the signal coming from the fast photodiode (rise time of 20 ps) was split in two with an high-frequency splitter and connected at the two ports of the fast oscilloscope, which has a bandwidth of 50 GHz. The oscilloscope was set to measure the time difference between the two pulses when reaching a defined voltage threshold. In order to measure the optical jitter, applying a time skew on one of the two channels of the oscilloscope of

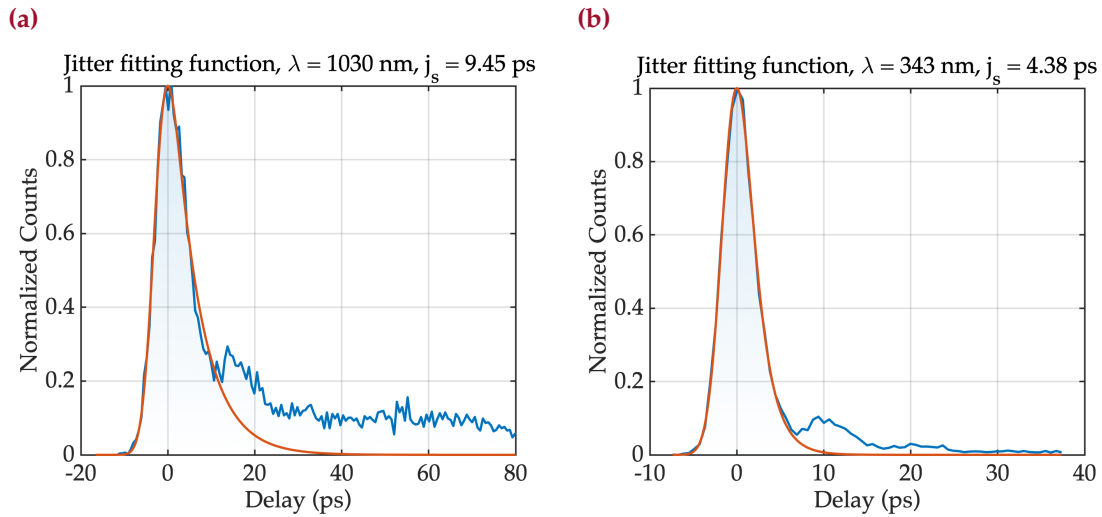


Figure 4.8 | SNSPDs jitter fitting routine. Due to its delay-related nature and to its relation to the energy distribution fluctuations in the electron and phonon baths [126], timing jitter of ultra-fast SNSPDs is not a symmetric Gaussian distribution but an exponentially decaying one. To properly fit the timing characteristic of SNSPD we used (4.5), as done in previous work [J11]. Here we have the comparison of jitter measured at different wavelengths but in the same biasing conditions, to show the clear energy dependence of device timing performance, hinting to mostly intrinsic contributions. The best achieved jitter was 9.45 ps full-width at half-maximum (FWHM) when excited with 1030 nm wavelength light (a), *i.e.* in the NIR range, and 4.38 ps with 343 nm wavelength (b), *i.e.* in the NUV.

a multiple of the laser pulse repetition rate, ensures the jitter is indeed estimated between consecutive pulses. If this is not the case, the measurement would show the timing jitter between a photodiode pulse and itself, which would lead to measuring the jitter of the oscilloscope alone, and consequent underestimation of the noise.

The result of the measurement is generally a time-domain Gaussian distribution, and J_{meas} is the full width at half maximum of the distribution. From it we can extract $J_{\text{optical}} = J_{\text{meas}} / \sqrt{2}$, as the measured jitter contains twice the variance of the single pulse-to-pulse jitter. This measurement includes jitter contributions of both the oscilloscope and the optical source. In our setup, J_{optical} was estimated to be roughly 150 fs. In this estimation, we are neglecting potential time broadening of the optical pulse, for instance when passing through the nonlinear crystals, the lenses, and the windows, which have been estimated to contribute less than 100 fs in the most pessimistic case (see Appendix B.1.3).

The electrical noise contribution J_{noise} was estimated by an analysis of the pulse shape and the noise of the electrical signals. From the pulse rise time and the voltage magnitude of the signal, we can estimate the slew rate, defined as $S_{\text{rise}} = V_{\text{pulse}} / \tau_{\text{rise}}$. For the electrical noise of the system, we measured the noise of the device when no bias current is applied in the same measurement conditions, and from the distribution of the noise values we estimated the standard deviation

σ_{noise} of the noise distribution (which is assumed to be a Gaussian). The noise jitter was estimated as

$$J_{\text{noise}} = \frac{2.35 \sigma_{\text{noise}}}{S_{\text{rise}}} \quad (4.4)$$

to be for most of the high-speed detectors in the order of a few picoseconds in FWHM.

After estimating the jitter contribution from the setup, the timing jitter measurement of the device was performed. The oscilloscope trigger was set on the readout pulse coming from the detectors, and the oscilloscope was to measure and send to the measurement computer the timestamps between the SNSPD pulse trigger and the reference pulse. The "sweetspots" for the triggers were found to be at 35% for the SNSPD pulse and at 50% for the fast photodiode reference pulse. These are the points that minimized overall jitter, and are usually in correspondence to the steepest part of the electric pulse. In order to avoid pulse height fluctuations due to the limited sampling points, the oscilloscope traces were interpolated with a $\sin x/x$ method internally to the scope. Despite the oscilloscope was running at 100 GS/s mode, equivalent to a measured point every 10 ps, being the fast photodiode pulse only 50 ps caused some height fluctuations on the reference pulse depending on which points were sampled. To improve even further, we found out that setting the trigger to a constant voltage threshold made this fluctuation effect less relevant.

The delay distribution between the SNSPD and the reference were fitted, according to [J11] to an exponentially-decaying Gaussian distribution $f(x; \mu, \sigma, \lambda)$:

$$f(x; \mu, \sigma, \lambda) = \frac{\lambda}{2} e^{\frac{\lambda}{2}(2\mu + \lambda\sigma^2 - 2x)} \text{erfc}\left(\frac{\mu + \lambda\sigma^2 - x}{\sqrt{2}\sigma}\right), \quad (4.5)$$

where $\text{erfc}(x)$ is the complementary error function defined as

$$\text{erfc}(x) = 1 - \text{erf}(x) = \frac{2}{\sqrt{\pi}} \int_x^\infty e^{-t^2} dt, \quad (4.6)$$

where λ represents the exponential contribution, and σ the Gaussian contribution. The reason for the asymmetry of the jitter distribution has been explained in [56] and it only appears when the measurement is not dominated by a large contribution of J_{noise} , which is purely Gaussian.

Measurements of the jitter distribution are reported in Figure 4.8 for both 1030 nm and 343 nm wavelengths. As expected and explained by Allmaras *et al.* [56], the higher the photon energy, the faster and less jittery is the superconductivity disruption, which causes less intrinsic contribution.

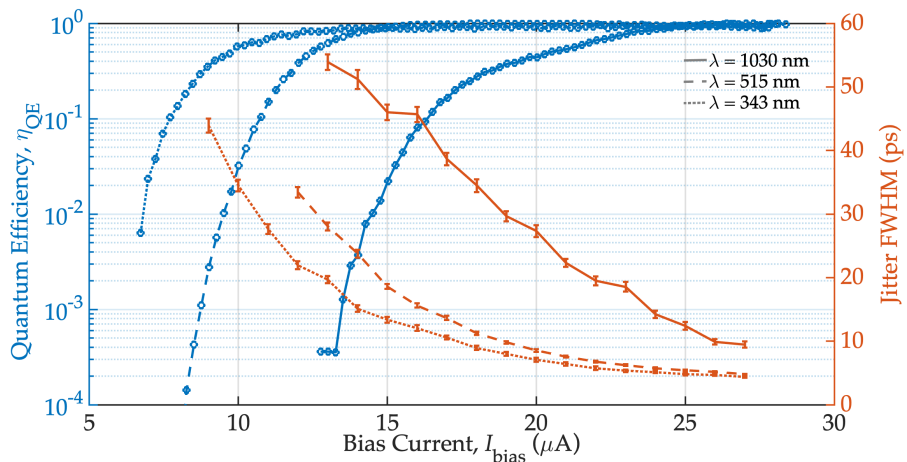


Figure 4.9 | SNSPDs jitter–efficiency correlation. As both detection quantum efficiency and timing jitter are supposedly ruled by the same phenomenon called Fano fluctuations [126], if taken correctly, intrinsic jitter and efficiency should show a similar bias current relationship, as shown in figure. Increasing the biasing current, in fact, suppresses the energy gap of the superconductor, causing lower energy photons absorbed in the nanowire to cause a generation of a large enough number of quasi-particles capable of suppressing superconductivity. In the same way, suppressing the superconducting gap makes also the achievement of hot electrons critical mass faster, causing snappier devices with lower timing uncertainty, hence better jitter. Here we can see how both jitter and efficiency improve with current until they both reach a plateau. The higher the photon energy, the lower the current required to reach the plateau.

In Figure 4.9 the trend of internal quantum efficiency and timing resolution are shown as function of biasing current I_{bias} . As done in previous work [J11], this results shows that the intrinsic timing resolution of SNSPDs is driven by the same physical phenomena behind the quantum efficiency, the aforementioned Fano fluctuations [126], energy fluctuation in the energy distribution coming from the quasi-particles in the phononic and electronic baths.

4.3 DISCUSSION

The reported SNSPDs made in NbN show single-photon detection internal quantum efficiency saturation at 1030 nm wavelength, good signal-to-noise ratio, and very fast timing resolution, at best below the 5 ps threshold for the highest photon energy of 343 nm. This proves good quality of the fabrication process and good characterization capabilities.

Despite the interest in the technology, mainly due to their high–efficiency in the NIR and excellent timing resolution, it seems challenging to develop systems based on SNSPDs for everyday applications, as the cryogenic requirements are still a big limiting factor. Potential applications in the medical imaging may be viable

as the temperature requirements for the system differ slightly from the commonly used system, which are already cooled by liquid nitrogen. However, in order to become competitive with silicon-based technologies, large scale integration must be addressed. In the next chapters of this Thesis, we will try to address these problems and present few potential solutions.

CHAPTER 5

Frankly, I didn't expect to be so precise.

— Gordon Moore, 2015

nTRONS: THE NANOCRYOTRONS TECHNOLOGY

Nanocryotrons, or nTrons, are three-terminal devices generally made of dirty superconductors. A schematics of the device taken from the original paper from McCaughan and Berggren [22] is reported in Figure 5.1. The device is fabricated on a thin film of NbN of thickness t and it is composed of a main channel, having narrowest width w_{ch} and critical current $I_{sw}^{ch} = j_{crit} t w_{ch}$, several times wider than the gate, which has choke width $w_{gt} \approx w_{ch}/10$ and critical current $I_{sw}^{gt} = j_{crit} t w_{gt}$, where j_{crit} is the critical current density of the superconducting film. By suppressing the critical current on the gate, a resistive *hotspot* area is formed which expands within the channel: for large enough biasing condition of the channel, *i.e.* for $I_B \rightarrow I_{sw}^{ch}$, it is possible to control the superconducting state of a wide superconductor line by just driving a very small current in the much narrower gate. This effect was first exploited by the collaborating groups of the University of Salerno and the CNR of Pozzuoli, Italy [131, 132], and then reformulated and rebranded by MIT.

While the intrinsic high-kinetic inductance of dirty superconductors only partially plays a role in nTrons, which are commonly operated in *latching* mode, the reason for wanting dirty superconductors is mostly due to the large resistance achievable when the device transition in normal state. The voltage signal of an nTron is indeed proportional to its normal state resistance and to the biasing current.

In recent years, the group of Prof. Karl Berggren at MIT and his collaborators Dr. McCaughan and Dr. Zhao have carried out most of the experiments to develop nTrons-based electronic circuits, with applications ranging from simple characterization of device [133], new approaches to break the superconductivity, *e.g.* exploiting geometrically-induced current crowding [134] or localized heat [45], and more sophisticated readout schemes for either SNSPDs or SQUIDs [135, 136].

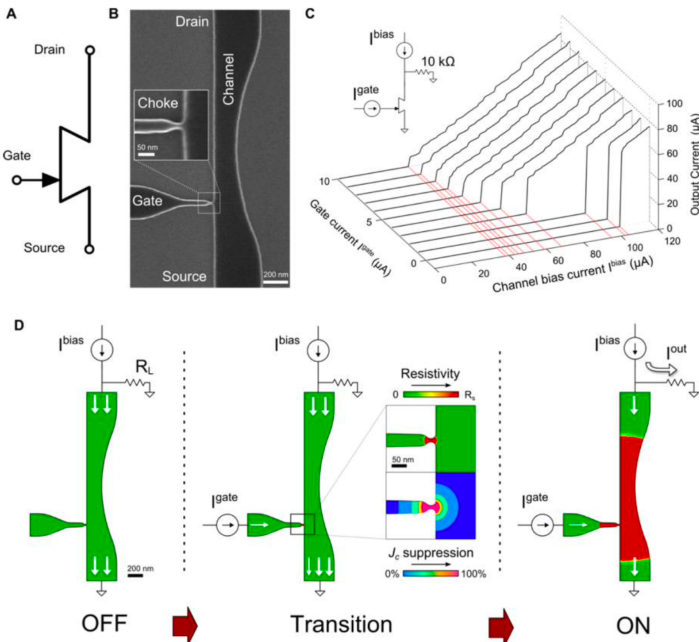


Figure 5.1 | nTron operations. Scanning electron micrograph, characteristic curves and operation schematics of the original nTrons work from 2014 (from McCaughan and Berggren [22]).

In this chapter we present the development of the technology achieved so far, starting from the simple devices, and ending up to a new concept developed to increase device sensitivity and SNR.

5.1 DESIGN AND FABRICATION

Fabrication of nTrons is quite similar to the process for SNSPDs, but with one major simplification: no optical cavity is required. Details of the fabrication process of nTrons are reported in [Appendix A.1.2](#).

While for SNSPDs we are interested in keeping the critical temperature T_C under control to enhance photon-sensitivity, for nTrons development the main objective is to achieve high yield and largest critical temperature. Because of that, the perfect material for nTrons is NbTiN (see more in [Section 2.3](#)).

nTrons are current sensitive devices, however they can be operated in either a current or a voltage readout mode. In what we define current mode, the current flowing through the device is fixed and controlled externally, having the device biased through a very high-impedance circuit. In voltage mode, the current flowing through the channel is set by a bias resistor with resistivity R_{bias} , generally in the range of the normal state resistance of the nTron R_n . The main difference among the two modes consists that controlling the voltage, currents can self-adjust in voltage

bias mode, reducing dissipation. This effect allows for faster recovery times as it generally generates less heat to dissipate in the substrate. In the following Sections, we will describe behavior obtained by voltage operating the devices. When referring to biasing currents, it will be estimates of currents set by controlling the voltage and assuming the state of the device to be superconducting, *i.e.* $I_B = V_B / R_{\text{bias}}$.

Main design parameters of nTrons are, as we said, the values of the channel and gate widths w_{ch} and w_{gt} . By playing with these two parameters, it is possible to tune the response of the nTrons. As it can be shown, increasing w_{ch} would lead to a better SNR, as the overall readout current would be larger, but would also make the devices bulkier, slower in high-frequency response, and more dissipating when in normal state. On the other hand, larger w_{gt} would lead to a device which requires larger gate signal to trigger but would also be less sensitive to gate noise. Overall, a large $w_{\text{ch}}/w_{\text{gt}}$ ratio would lead to a higher device gain, but lower sensitivity, as a smaller *hotspot*, associated to a smaller w_{gt} , may not be sufficient to cause the state transition of the nTron channel.

In order to characterize and quantify the yield and the sensitivity of different configurations, we fabricated devices in a variety of channel and gate widths, using an approach similar to one of a transistors farm.

5.1.1 THE AVALANCHE-EFFECT NANOCRYOTRON: THE a_x TRON

While trying to find a way to optimize sensitivity and SNR together, we designed (inspired from [36]) a device exploiting cascade effect: we called this device the avalanche-nTron, or a_x Tron. Differently from standard nTrons, the channel is split in x smaller channels of widths $w_x = w_{\text{ch}}/x$. An a_2 Tron has its channel split in two branches, an a_3 Tron in three, and so on. By doing so, the overall channel critical current $I_{\text{sw}}^{\text{ch}}$ (which limits the SNR) is maintained, but both sensitivity and speed should improve. The operation principle is very simple: as long as an a_x Tron channel with x subsections is biased at a biasing current $I_B > I_{\text{sw}}^{\text{ch}}(x-1)/x$, then as soon as gate current is large enough to suppress superconductivity in the much narrower subsection, the device will fully transition to the normal state. Indeed, following an avalanche-like effect on the other subsections, the excess biasing current is redirected among the other sections and will exceed their critical currents, causing the avalanche.

Let us consider Figure 5.2, where a phenomenological schematics is presented to show the main difference for the a_x Tron compared to a classical nTron. For low

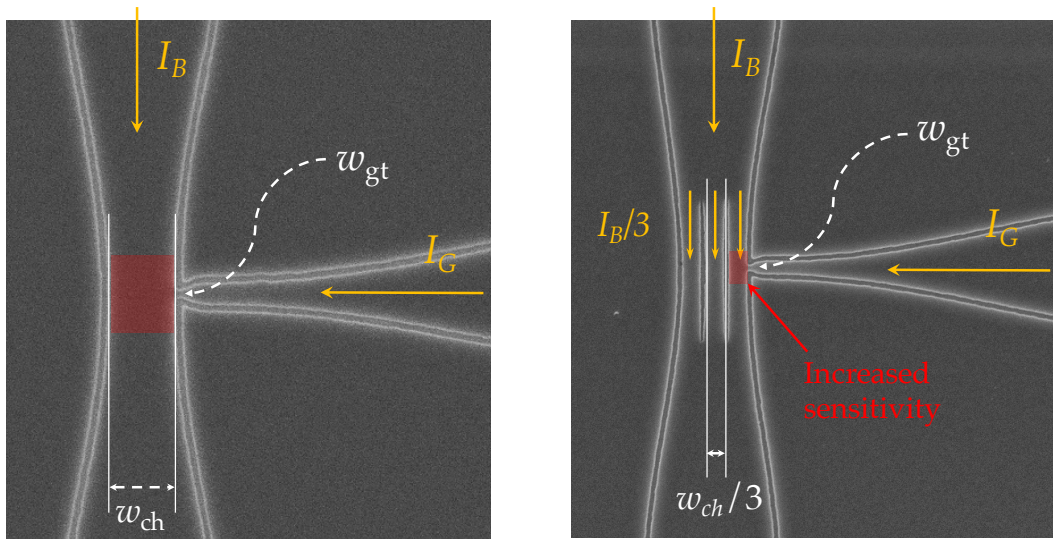


Figure 5.2 | nTron and a_x Tron schematics. Schematic depicting the main difference between an nTron and an a_x Tron, in particular an a_3 Tron. As the channel is split in 3 subsections, as long as the channel current satisfies the relation $I_B > I_{sw}^{ch}$ ($2/3$), making one subsections switch leads to an avalanche effect that suppresses superconductivity of the whole device, leading to a device trigger. However, given the smaller ratio between the subsection $w_{ch}/3$ and gate w_{gt} compared to the standard nTron design, the device should show better sensitivity and timing performance than a normal nTron.

gate current, the hotspot generated by the a_x Tron is large enough to suppress the superconductivity in the section of the channel, which cascades and makes the whole device switch; however, in the single channel nTron, the hotspot generated by the gate does not suppress the main channel, hence the gate current is not large enough to cause any readout voltage.

In terms of speed, there is also an advantage. Given a current pulse injected at the gate large enough to make both devices switch in latching conditions, an avalanche propagation should be faster than a thermal diffusion propagation, as the physical timescales are very different. Lesser current requirements and higher speed give the a_x Trons an edge over the nTrons, in particular as no deviations from the fabrication are required.

5.2 CHARACTERIZATION

The fabricated nTrons and a_x Trons were characterized at low-frequency conditions. Despite one of the claims of a_x Trons is that these devices are faster than conventional nTrons, due to lack of equipment and time it was not possible to characterize the

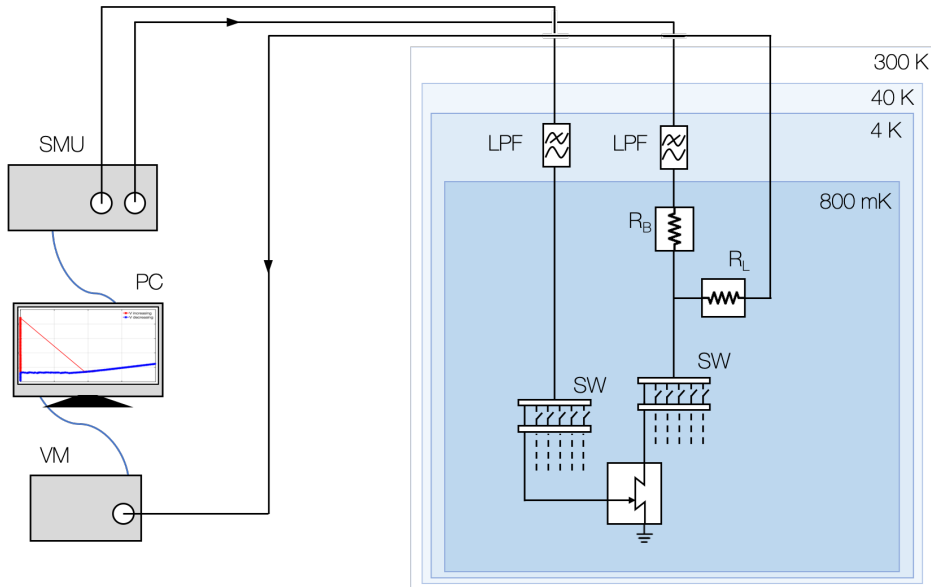


Figure 5.3 | nTrons characterization setup. Gates and channels of the devices under test are connected to cryogenic switches (R573 series, Radiall Inc.) and then to SMA cables. The channel line is then split into the readout and bias lines: the readout line has a $R_L = 50 \Omega$ resistor to avoid current leaking in the readout during biasing conditions, while the bias line has a R_{bias} resistor in the order of $10 \text{ k}\Omega$ to convert voltage into current. Both bias and gate lines are filtered at 4 K with a low-pass filter (SLP 1.9+ series, Mini Circuits Inc.) and connected to an SMU. The readout line is directly connected to a voltmeter VM (HMC8012 series, Rohde & Schwarz).

devices at high-frequency. However, from the low-frequency characterization, the results confirmed the improved sensitivity.

The devices were characterized in PhotonSpot cryogenic system (see [Appendix B.1](#)) which could be operated either at the base temperature of 880 mK and at 3.1 K. The readout schematics are reported in [Figure 5.3](#).

The channel voltage and gate current biases are swept with an SMU, and the resistance of the devices is then estimated from the readout voltage V_{ro} measured with a voltmeter. When the channel bias is low, so that the currents flowing through the nTrons channel is well below the critical, the device behaves as a short to ground, and readout voltage is zero. When the gate bias reaches the current required to break superconductivity in the channel, the nTron abruptly becomes a normal metal with a large characteristic resistance (in the order of $10 \text{ k}\Omega$), causing a large voltage swing at readout.

In [Figure 5.4](#) two nTrons in NbN and NbTiN are shown at operating temperatures of 880 mK and 3.1 K. As expected, the gate current and bias voltage ranges are much larger for the NbTiN device, while the resistivity is larger for the NbN. When characterized at higher temperatures, NbTiN biasing point deviation from base temperature is quite marginal, while it is much more evident in the NbN devices.

This is related to the suppression of critical current due to temperature, which is inversely proportional to the critical temperature T_C . Here, the NbTiN has a critical temperature of 12 K, while the NbN only 7 K. Operating at 25% or at 50% of T_C causes a much smaller suppression of superconductivity, making the NbTiN more suitable for potential application electronics at 3 K stage or when coupled to more heat dissipating CMOS chips.

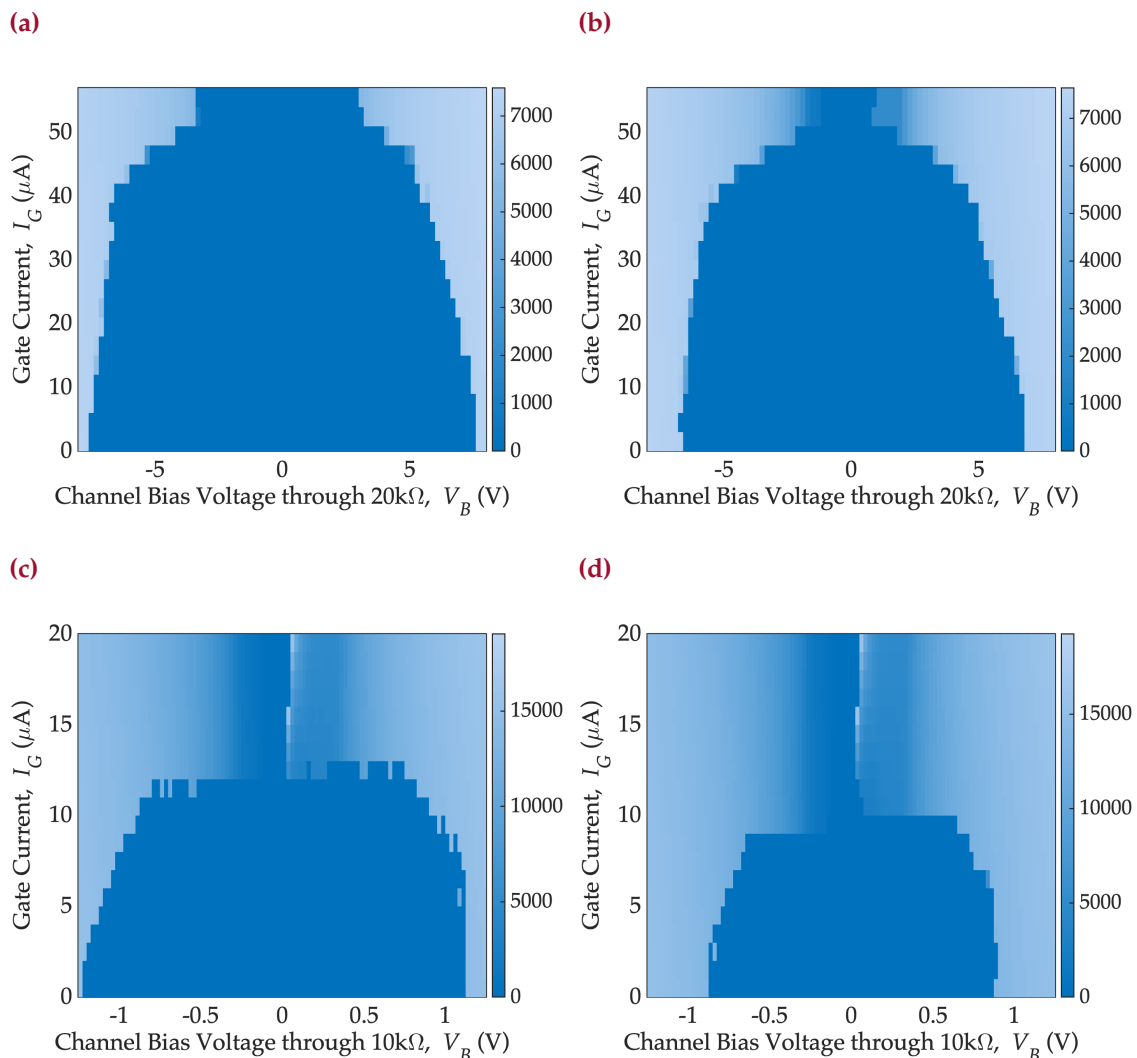


Figure 5.4 | nTrons temperature dependence. nTrons characteristic curves show the resistance of the device at different biasing conditions of gate and channel. nTrons are fabricated in NbTiN (a)–(b) and in NbN (c)–(d) operated at base and 3 K temperatures. While the NbTiN device is very robust with respect to temperature changes (b) thanks to its very high T_C of 12 K, the NbN device shows a much larger suppression of the superconducting condition when brought at 3 K (d).

The asymmetry between the positive and negative bias conditions can be interpreted as follows: while driving a positive V_B and a positive I_G causes currents to sum up towards the ground, increasing the overall current density in the shunted

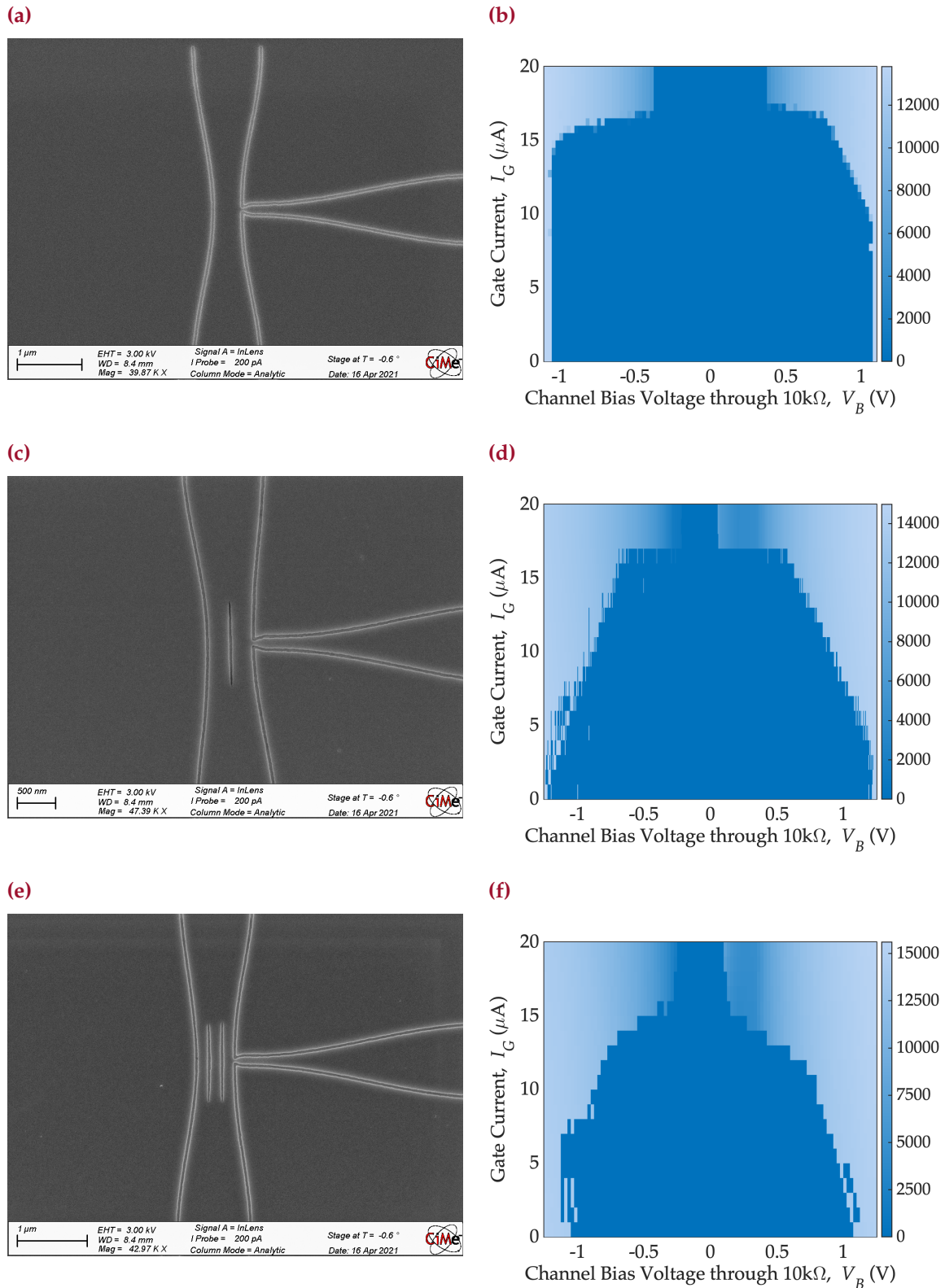


Figure 5.5 | Comparison between nTrons and a_x Trons. Scanning Electron Micrographs (SEMs) of the nTron (a), a_2 Tron (c) and a_3 Tron (e) with their respective characterization plots (b)–(d)–(f). As the number of sections within the channel increases, the required gate current to switch to normal state is reduced, making the device more sensitive.

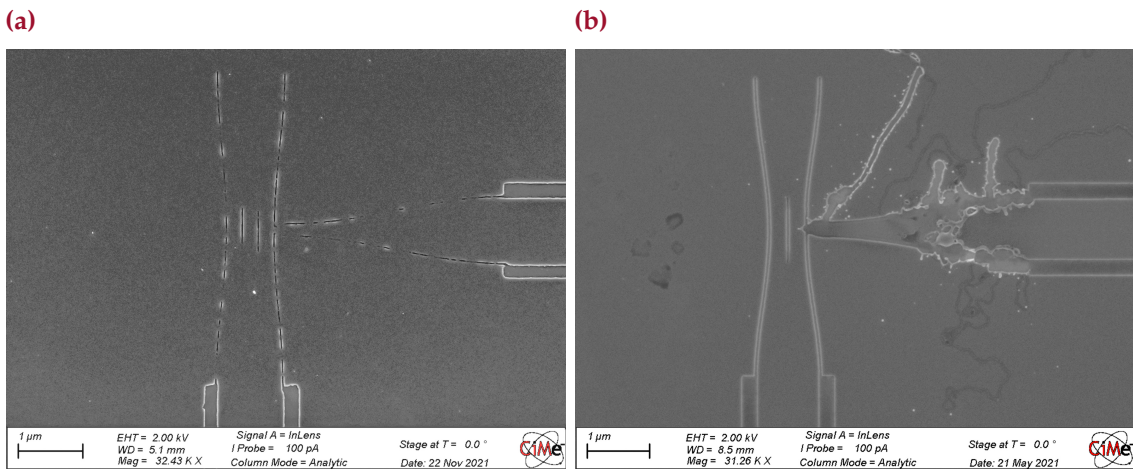


Figure 5.6 | nTrons failure causes. Scanning Electron Micrographs (SEMs) of two main examples of nTrons failures during the duration of the project. For roughly 5 months the electron-beam lithography resulted in sub-optimal patterning at very high-resolution due to beam calibration issues (a). Electrostatic discharge damage of an a_2 Tron during wirebonding.

part of the channel, applying opposite biases causes the currents to subtract, hence reducing the overall current density in the channel. Indeed, for large, inverse channel bias voltages, the positive side transition shows a less steep slope, hinting a better sensitivity when compared to the negative side.

Less trivial to interpret, however, is the characterization of the a_x Trons. In Figure 5.5 we report SEMs of the fabricated devices and their respective characteristic curves. All the devices tested were designed with same channel and gate widths, hence the critical conditions should be met at the same biasing conditions, which is confirmed by the graphs: zero gate bias, channel switching currents I_{sw}^{ch} are reached at V_B of roughly 1 V (corresponding to a biasing current of 100 μ A) for all the three devices reported. The characteristic curves seem to suggest an overall trend of increased sensitivity, as the gate current required for a channel to switch is less and less the more the channel is split in multiple sections.

5.3 DISCUSSION

While the fabrication, design, characterization and data interpretation of the nTrons required good amount of effort, this was just enough to obtain operating devices characterized at low-frequency. Indeed, the technology proved non-trivial to fabricate and to characterize. During the project timeline, we encountered more than a setback.

After a first promising run, a critical issue with the electron-beam lithography system caused most of the devices lithographic step to fail, as the beam was regularly defocused after calibration, affecting both gates resolution and e-beam dose (see [Figure 5.6\(a\)](#)). This error persisted for several months and, as it only affected lithographic steps which required a resolution of 5–10 nm, it went on undetected for a months before identified and fixed. Moreover, issues related to electrostatic discharge during wirebonding, transport and installation of the sample caused the gates of the devices to blow-off, making them unusable for the characterizations (see [Figure 5.6\(b\)](#)).

While the results above show operating devices with good yield and reproducible critical characteristics, much work is required to develop electronics based on these devices. However, the first steps were made in the right direction and reliable devices were fabricated and tested, showing also an improvement of sensitivity for the new design.

6

CHAPTER

Quality is not act. It is a habit.

— Aristotle

HIGH KINETIC INDUCTANCE CIRCUITS

High-kinetic inductance superconducting materials present multiple advantages compared to standard superconducting circuits, in particular in terms of cQED components compactness and achievable impedance. Due to their large inductance, generally couple orders of magnitude larger than the geometric inductance, it is possible to engineer transmission lines having phase velocity $v_{\text{ph}} = 1/\sqrt{L_0 C_0}$ just a small fraction than standard superconductors [37], reducing dramatically lengths of coplanar waveguides-like resonating structures.

At the same time, high- L_k materials allow for simple fabrication of superinductors [137], *i.e.* inductors with characteristic impedance $Z_0 = \sqrt{L_0/C_0}$ higher than the quantum impedance $R_Q = h/(2e)^2 \approx 6.45 \text{ k}\Omega$ [52]. In normal inductors, quantum fluctuations of charge $\delta q = \delta Q/(2e)$ are at least an order of magnitude larger than flux fluctuations $\delta\phi = \delta\Phi/\Phi_0$. As the maximum impedance achievable by geometric inductance is $Z_{\text{vac}} = \sqrt{\mu_0/\epsilon_0} \approx 377\Omega$, the ratio $\delta q/\delta\phi = R_Q/Z_0$ cannot be lower than $R_Q/Z_{\text{vac}} = 16.97$ [138]. In other words, this means that small fluctuations of flux lead to large fluctuations in charge. However, for high- L_k materials, it is possible to exceed such limiting factors and produce nanowire waveguides with impedances in excess of $10 \text{ k}\Omega$, reducing the asymmetry between flux and charge fluctuations.

On the other hand, as we will see later in Chapter 7, the coupling between harmonic systems is given by (7.6), and it is proportional to the averaged impedance $\sqrt{Z_1 Z_2}$ of the two harmonic systems. Developing resonators with large impedance and high quality factor may allow experimental study of quantum systems in the little explored ultra-strong and deep ultra-strong coupling regimes.

In this chapter we report few applications of microwave devices based on high kinetic inductance thin films, mostly for cQED applications. In Section 6.1, we

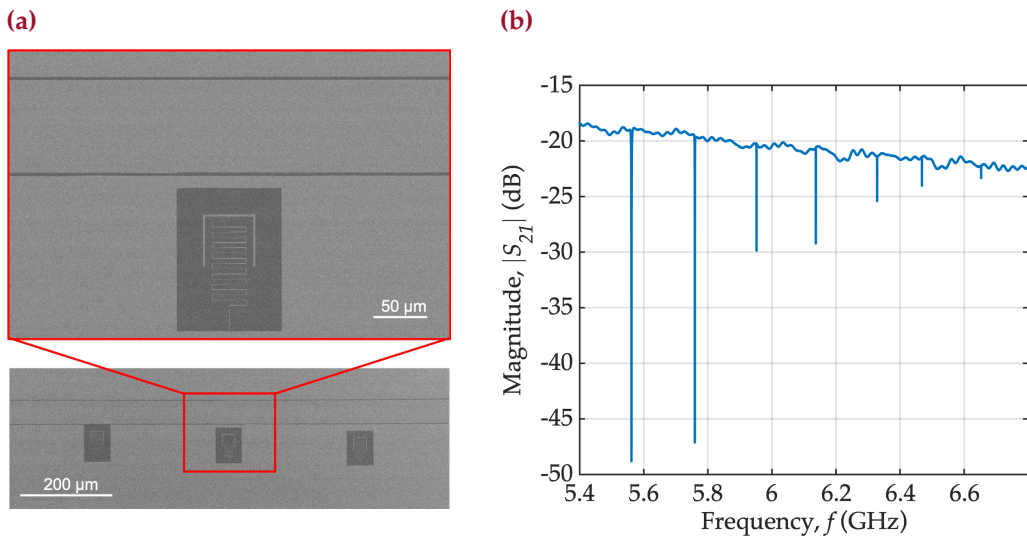


Figure 6.1 | Resonators micrograph and spectrum. Scanning electron micrograph (SEM) of a hanged LC resonator (a) and transmission spectrum of a sample device consisting of seven notch filter resonators (b). The resonators have larger coupling κ at lower frequencies.

will present the approach used to characterize the superconducting resonators, to estimate internal quality factors, self-Kerr nonlinearity and aging of the devices. Then, we will focus on two devices based on high- L_k materials which can be used to either match to high-impedance structures through a microwave transformer (Section 6.2) or to filter unwanted microwave signals (Section 6.3).

6.1 QUALITY FACTOR OF HIGH- L_k RESONATORS

Superconducting resonators, whether they are designed as distributed or lumped elements, have very high internal quality factors due to their dissipationless nature. High-kinetic inductance superconductors, in particular NbN, have proven to reach just a fraction of the quality factor achievable from other "pure" superconductors such as aluminum or tantalum. An accredited theory is that the higher the kinetic inductance, the higher the film coupling strength to two-level systems fluctuators intrinsic to the superconducting thin film (TLS, [139, 140]). In the following section, we present a full-scale analysis of superconducting film-based resonators and their quality factors. The results herein have been reported also in [J5].

To characterize superconducting films quality factor, hanged resonators were made out of different NbN films. To reduce TLS contributions, the films were deposited on high-resistive Si wafers ($\rho \geq 10 \text{ k}\Omega\text{cm}$). Before deposition, both a Piraña bath and an HF bath were performed to clean the silicon surface and remove

any organic and oxide traces. The films were then bias-sputtered [58] according to [Section 2.1](#) and patterned by means of electron-beam lithography and reactive ion etching (more information in [Appendix A.1](#)).

There are different advantages in using hanged resonators design, instead of reflection or transmission configurations. First, in hanged configuration, multiple resonators can be "hanged" to the same coupling feedline: this allows us to have the freedom to design resonators with a variety of coupling strengths. The coupling between an harmonic system and a waveguide, usually denominated as κ , is defined as

$$\kappa = \omega_r \frac{Z_0}{Z_r} \left(\frac{C_c}{C_r + C_c} \right)^2, \quad (6.1)$$

where ω_r is the resonant angular frequency of the harmonic resonator, Z_0 is the impedance of the waveguide, Z_r the impedance of the resonator, C_c is the coupling capacitance between the waveguide and harmonic systems, and $C_c + C_r$ the total capacitance of the resonator. According to [140], to get a precise estimation of the internal quality factor $Q_i = \omega_r / \gamma$, with ω_r the resonant frequency of the resonator and γ the loss rate, κ has to be the same order of magnitude of γ , *i.e.* the resonator should be critically coupled.

When considering coupling rate and loss rate in resonators, three different regimes are possible: overcoupled regime ($\kappa \gg \gamma$), undercoupled regime ($\kappa \ll \gamma$) and critically coupled regime ($\kappa \approx \gamma$). To minimize fitting errors, one should aim to the latter regime. However, as internal quality factor depends on multiple contributions that are hard to estimate *a priori*, design of critically coupled resonators can be a challenge. To better estimate the internal quality factors, we fabricated seven hanged resonators with different κ 's that span around an educated-guessed value, so to produce at least one resonator operating at critically coupling conditions. Another advantage of the hanged configuration lies in the self-calibration. As the resonator is basically a notch filter, the baseline does not require calibration as it is the coupling feedline transmission itself.

For the linear hanged resonator, the transmission scattering parameter S_{21} is given by:

$$S_{21} = 1 - \frac{\kappa}{\kappa + \gamma} \frac{e^{i\phi}}{\cos \phi} \frac{1}{1 + 2i\delta}, \quad \text{with } \delta \equiv \frac{\omega_d - \omega_r}{\kappa + \gamma}, \quad (6.2)$$

where $e^{i\phi}$ is a contribution referred to as ϕ rotation method (ϕ RM, [141]) that takes into account impedance mismatch in the circuit, and $\cos \phi$ is a improvement factor of the ϕ RM, called diameter correction method, or DCM [142, 143], applied to avoid

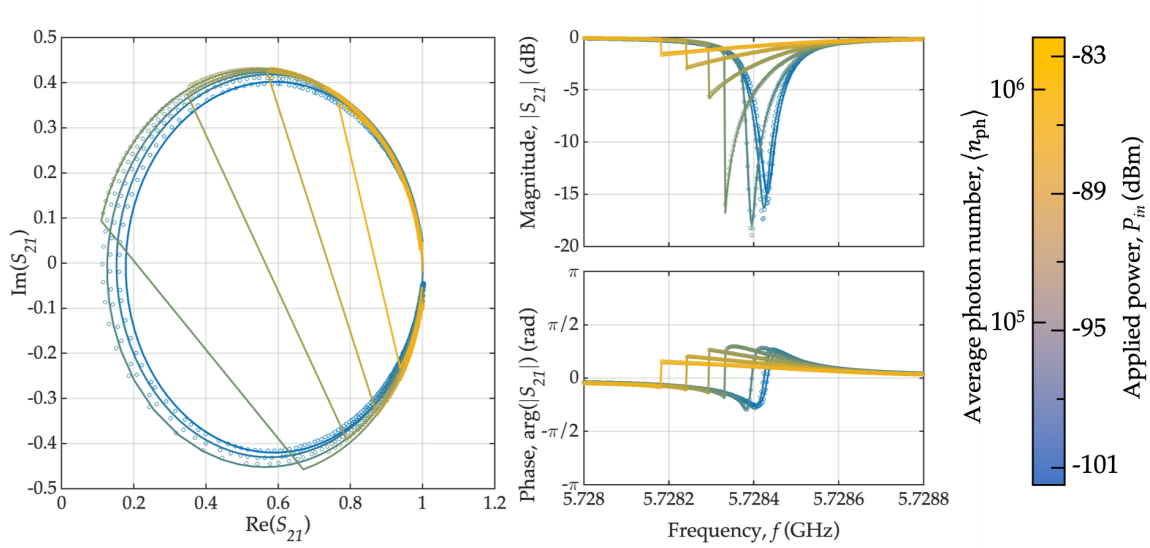


Figure 6.2 | Resonator fitting functions result. Measurements and fitting results obtained using (6.8) to address for the self-Kerr nonlinearity at different powers. The device is dominated by TLS losses, which explain the increase of the diameter (hence the Q_i) of the circle in the complex plane with increasing power. The power scale on the right represents the estimated power reaching the coupling feedline.

systematically overestimating the internal quality factor, which is an unwanted feature of the ϕ RM, and ω_d the drive frequency.

The hanged resonators were measured using a Vector Network Analyzer (ZNA series, Rohde & Schwarz) at the base temperature of the BlueFors system dilution fridge (further information on the system and the setup can be found in Appendix B.2). The resonator power P_{in} was varied to characterize the resonator's quality factor at a wide range of average photon number $\langle n_{\text{ph}} \rangle$.

The internal quality factors of 105 resonators were estimated and are reported in Figure 6.3, at both $\langle n_{\text{ph}} \rangle \approx 1$ (circular datapoints) and $\langle n_{\text{ph}} \rangle \approx 1'000$ (triangular datapoints) photons numbers. The resonators were fabricated on eight different films of the same thickness of 15 nm. Each film kinetic inductance was controlled by properly adjusting the N_2 flow in the chamber, as explained in Section 2.1. On each film, seven resonators with inductor width of 500 nm (filled datapoints) and seven with inductor width of 250 nm (white datapoints) were patterned and hanged each to one of two different 50Ω transmission line.

For single-photon regime excitation, we see no clear trend of the internal quality factor with increasing kinetic inductance until the very last dataset, where we see a decrease of quality factor by an order of magnitude. Despite the internal quality factor of 500 nm wide inductor, the resonator was estimated correctly for the highest L_k film, the 250 nm wide resonators exhibited no resonances, suggesting

suppression of superconductivity. For the resonators made by films in the range 30–100 pH/ \square , potential Q_i – L_k trend is less dominant than the natural variability of quality factors due to fabrication reproducibility. The internal quality factor estimated from the critically-coupled devices exceeds 10^5 for all the 500 nm wide resonators, while ranging between 6×10^4 and 10^5 for the 250 nm wide resonators. However, for the film with kinetic inductance increases of 170 pH/ \square , this is no longer the case, as the Q_i drops to 2×10^4 for 500 nm wide resonators.

These results hint to the fact that two regimes are possible: for lower- L_k films, the resonators loss mechanism is dominated by TLS losses, and that for higher- L_k , intrinsic loss mechanisms related to film composition plays a more relevant role. This leads to an optimum operating point, where both mechanisms contribute equally to the loss mechanisms, so to maximize both internal quality factor and kinetic inductance.

6.1.1 SELF-KERR NONLINEARITY

In [Figure 6.2](#) the scattering parameter evolution is reported for a sample NbN resonator with increasing power (*i.e.* photon number), equivalent to a resonator photon number $\langle n_{\text{ph}} \rangle$ ranging from roughly ten thousand to almost one million. As power increases, the resonator starts to show Duffing-like nonlinear behavior, typical of high- L_k materials. This nonlinear effect is called self-Kerr nonlinearity. Self-Kerr derives from the nonlinear behavior of the kinetic inductance of a superconductor with respect to the current flowing through it. In fact, Ginzburg–Landau theory predicts a current dependence of the kinetic inductance described by [\[29, 144\]](#)

$$L_k(I) = L_{k,0} \left[1 + \left(\frac{I}{I_*} \right)^2 \right], \quad (6.3)$$

where $L_{k,0}$ is the zero bias current kinetic inductance of the superconducting film and I_* is a parameter proportional to the critical depairing current I_{dep} . This nonlinear term of the inductance is called self-Kerr due to its resemblance to the quadratic electro-optic effect, or optical Kerr.

For a quantum harmonic oscillator system with self-Kerr nonlinear effect, the classical harmonic Hamiltonian is modified to the nonlinear Kerr Hamiltonian:

$$H = \hbar\omega_r a^\dagger a + \hbar \frac{K}{2} a^\dagger a^\dagger a a, \quad (6.4)$$

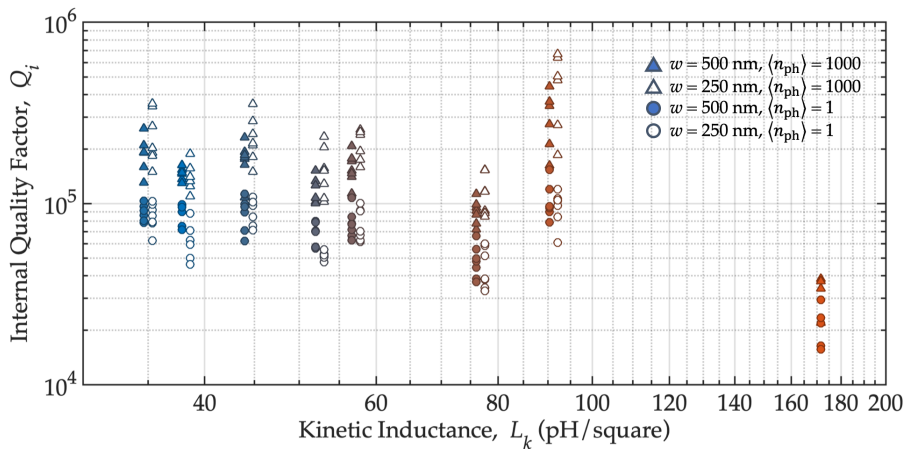


Figure 6.3 | Quality factor dependence on kinetic inductance of high- L_k hanged resonators. All the 105 tested hanged resonators quality factors are reported in figure. The internal quality factor Q_i was estimated according for both signal-photon $\langle n_{ph} \rangle \approx 1$ (circular datapoints) and multi-photon $\langle n_{ph} \rangle \gg 1$ (triangular datapoints) regimes. Filled datapoint refer to 500 nm wide inductors of the resonators, while white datapoints refer to 250 nm inductors. We shifted the white datapoints from the filled datapoints of an arbitrary amount to simplify visualization of the data. Datapoints color represent the N_2 concentration in the film, being blue the lowest concentration and red the highest.

where K is the nonlinearity term. Using input-output theory, and following the same formalism of [145, 146], multiplying both terms for their complex conjugates, (6.4) leads to

$$\begin{aligned} \frac{\kappa}{(\kappa + \gamma)^2} |\alpha_{in}| = & \left(\left(\frac{\omega_p - \tilde{\omega}_o}{\kappa + \gamma} \right)^2 + \frac{1}{4} \right) |\alpha|^2 - \frac{2(\omega_p - \tilde{\omega}_o K)}{(\kappa + \gamma)^2} |\alpha|^4 + \\ & + \left(\frac{K}{\kappa + \gamma} \right)^2 |\alpha|^6. \end{aligned} \quad (6.5)$$

By mathematical simplification and after defining the reduced terms

$$\delta \equiv \frac{\omega_p - \tilde{\omega}_o}{\kappa + \gamma}, \quad \tilde{\alpha}_{in} \equiv \frac{\sqrt{\kappa} \alpha_{in}}{\kappa + \gamma}, \quad \xi \equiv \frac{|\tilde{\alpha}_{in}|^2 K}{\kappa + \gamma}, \quad n \equiv \frac{|\alpha|^2}{|\tilde{\alpha}_{in}|^2}, \quad (6.6)$$

we can now obtain a much more compact version of (6.5) as

$$\frac{1}{2} = \left(\delta^2 + \frac{1}{4} \right) n - 2\delta\xi n^2 + \xi^2 n^3, \quad (6.7)$$

where the adimensional number of photons in the resonator n is function of reduced detuning δ and reduced pumping strength ξ . Being (6.7) cubic in n , we get three solutions, generally one real and two complex conjugated.

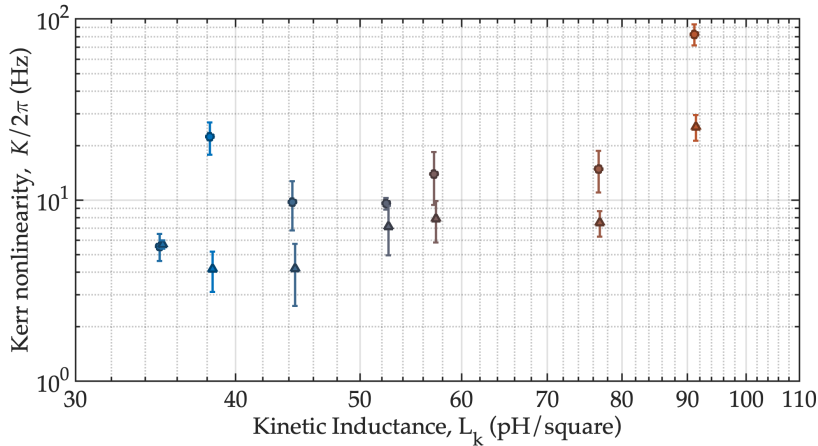


Figure 6.4 | Kerr nonlinearity factor dependence on kinetic inductance of high- L_k hanged resonators. The results reported are the ones of the almost-critically coupled hanged resonators. The self-Kerr values K was estimated according to (6.9). The overall trend seems to follow quite well the approximated formula (6.13). Datapoints color represent the N_2 concentration in the film, being blue the lowest concentration and red the highest.

These equations, together with the scattering parameter for nonlinear hanged resonators, that also comes from input-output theory and is

$$S_{21} = 1 - \frac{\kappa}{\kappa + \gamma} \frac{e^{i\phi}}{\cos \phi} \frac{1}{1 + 2i(\delta - \xi n)}, \quad (6.8)$$

provide a full set of equations that can be fitted to the experimental data to estimate the self-Kerr nonlinear term K . In fact, once the fitting parameter ξ and n are estimated, it is possible to compute K as

$$K = \xi \frac{(\kappa + \gamma)}{|\tilde{\alpha}_{in}|^2}, \quad (6.9)$$

where the average photon number $|\tilde{\alpha}_{in}|^2$ in the resonator in the linear limit is estimated according to [139]

$$|\tilde{\alpha}_{in}|^2 = \frac{\kappa}{(\kappa + \gamma)^2} \frac{P_{in}}{\hbar \omega_r}. \quad (6.10)$$

As shown in Figure 6.4, there is a clear dependence of the Kerr nonlinearity factor with respect to the kinetic inductance. Using the relation of nonlinear kinetic inductance change with bias current reported in [J13] we get:

$$L_k = L_{k,o} (1 - (j_{bias}/j_{crit})^{n_{fr}})^{-1/n_{fr}} \approx L_{k,o} \left(1 + \frac{1}{n_{fr}} \left(\frac{j_{bias}}{j_{crit}} \right)^{n_{fr}} \right), \quad (6.11)$$

which, together with the expression of K from [146], in the limit for small $j_{\text{bias}}/j_{\text{crit}}$, leads to the approximated form

$$K \propto \Delta L \omega_r^2 = \frac{L_{k,0} \omega_r^2}{n_{\text{fr}}} \left(\frac{j_{\text{bias}}}{j_{\text{crit}}} \right)^{n_{\text{fr}}}, \quad (6.12)$$

where $L_{k,0}$ is the zero bias current kinetic inductance of the superconducting film, n_{fr} is the temperature dependent exponential of the fast relaxation limit function defined in [120], which for $T \leq 0.1 T_C$ is 2.21, j_{bias} is the bias current density, and j_{crit} is the depairing critical current density, which is inversely proportional to width w and thickness t of the resonator body. This finally leads to

$$K \propto L_{k,0} \omega_r^2 (w t)^{-2.21}. \quad (6.13)$$

This result suggest that self-Kerr nonlinearity may be directly proportional to the kinetic inductance of the film, quadratically linked to the resonant frequency of the resonator, and inversely dependent on resonator width and thickness, all in accordance with our results in [Figure 6.4](#).

6.1.2 TLS LOSSES AND AGING

In order to understand what is the main loss mechanism of the resonators, the two-level system loss contribution was estimated following the equation in [30]

$$\frac{1}{Q_i} = \delta_0 + F\delta_{\text{TLS}}^0 \frac{\tanh(\hbar\omega_r/2k_B T)}{(1 + \langle n_{\text{ph}} \rangle / n_c)^\beta} \quad (6.14)$$

where δ_0 is the next dominant loss rate of the resonator, F is the filling factor defined as the ratio between the electric field threading the TLS and the total electric field, n_c is the TLS critical number, i.e. number of photons equivalent to the saturation field of the TLS, and $F\delta_{\text{TLS}}^0$ is the TLS loss tangent.

In [Figure 6.5](#) we report the fitted curves, according to (6.14), for six different film compositions, with dataset acquired immediately after the fabrication (in blue) and after 9 months (in red). The devices were stored in a N_2 controlled atmosphere between the measurements. As we can notice from the results, while the quality factor of lower- L_k devices seems slightly higher or average, it appears that films with larger concentration of N_2 are less sensitive to aging, as the quality factor curves remained almost identical despite the 9 months in the cabinet.

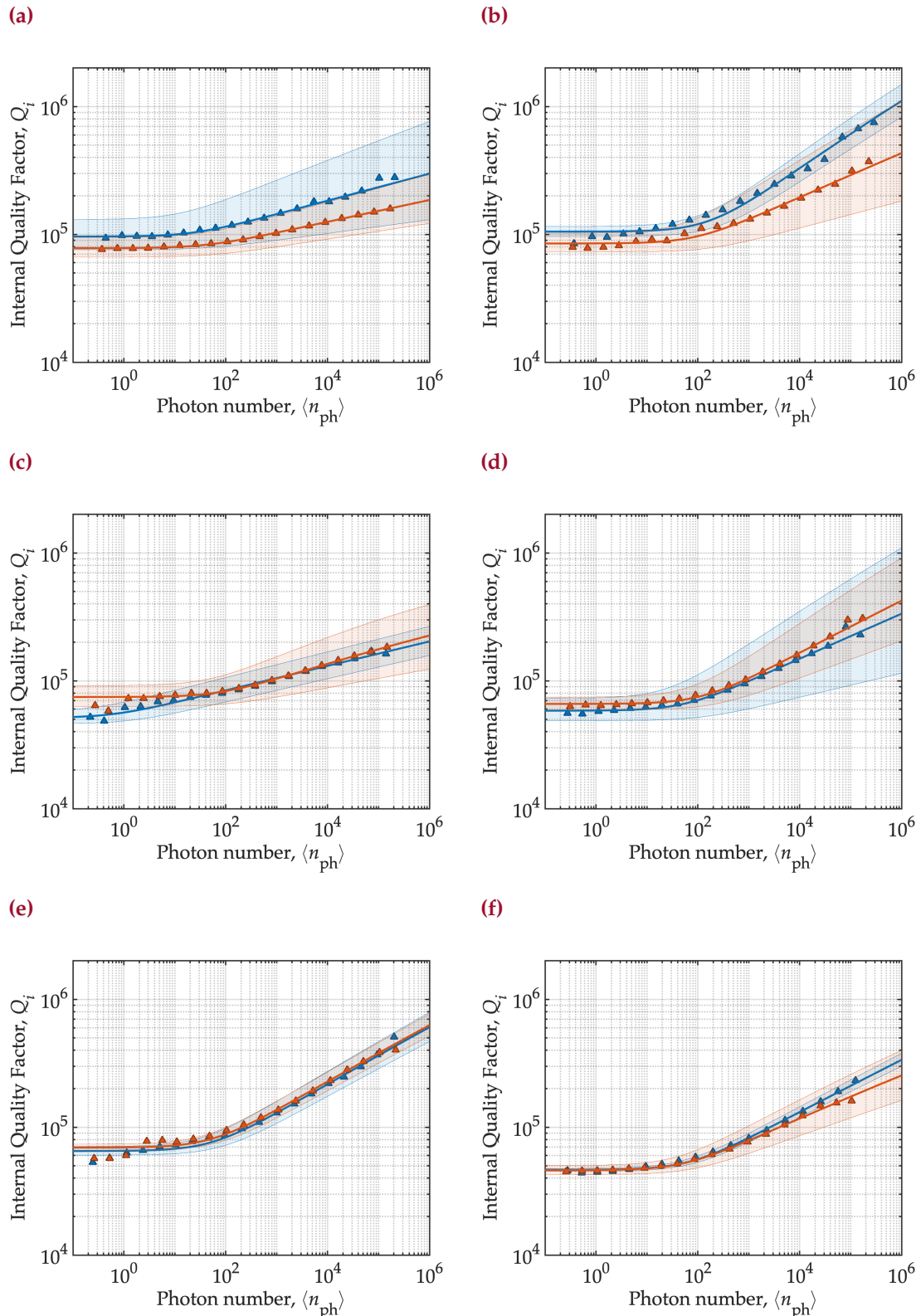


Figure 6.5 | TLS and aging analysis of high- L_k hanged resonators. From left to right, from top to bottom: quality factor estimated for almost critically-coupled hanged resonators as a function of power, for increasing film disorder. In blue, the values and fitting function of TLS (see (6.14)) of the devices measured right after fabrication (less than two weeks from deposition). In red, the values and fitting function of TLS of the devices measured nine months after fabrication. The shaded areas represent the 95% confidence interval of the fitting functions.

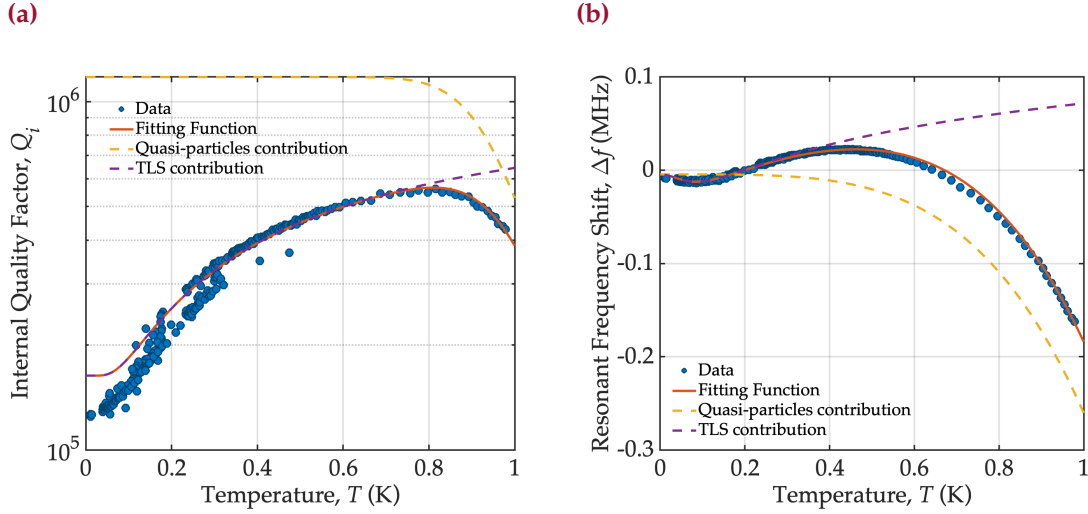


Figure 6.6 | Temperature dependence of internal quality factor. The resonators were characterized at different temperatures to analyze temperature behavior in terms of TLS and quasi-particles contributions (see (6.15)). As expected, at low temperature the TLS losses dominate the internal quality factor, which starts increasing for relatively low temperatures. However, at roughly 10% of T_C , the quasi-particles losses take over as main losses mechanism and cause a drop of quality factor. This behavior is confirmed by the resonant frequency shift Δf analysis (performed following (6.16)).

Finally, to further show the dominance of TLS, we investigated the resonator's quality factor evolution at different operating temperatures. The cryostat was very slowly warmed up from a base temperature of 15 mK to a temperature of almost 1 K, and the resonator's spectrum was acquired while the temperature monitored. The quality factor and resonant frequency behaviors obtained are reported in Figure 6.6.

Following the same approach reported in [147, 148], the quality factor change with respect to temperature was modeled as sum of the two contributions of TLS and quasi-particles. In (6.14) the TLS effect has been already studied, but in that case for a $\langle n_{\text{ph}} \rangle$ perspective; adding the quasi-particles contribution, the equation for internal quality factor Q_i becomes:

$$\frac{1}{Q_i} = \delta_0 + F\delta_{\text{TLS}}^0 \frac{\tanh(\hbar\omega_0/2k_B T)}{(1 + \langle n_{\text{ph}} \rangle / n_c)^\beta} + \frac{\alpha}{\pi} \sqrt{\frac{2\Delta}{hf_r}} \frac{n_{\text{qp}}(T)}{n_s(0)\Delta} \quad (6.15)$$

where α is the ratio between kinetic and total inductance, which we assumed to be 1, $n_{\text{qp}}(T) = n_s(0)\sqrt{2\pi k_B T \Delta} e^{-\Delta/k_B T}$ is the temperature dependent population of quasi-particles [149], and $n_s(0)$ is the zero energy density of states. For the frequency shift of the resonators, we have that [148]:

$$\frac{\Delta f}{f_r} = \frac{F\delta_{\text{TLS}}^0}{\pi} \left(\text{Re} \left\{ \Psi \left(\frac{1}{2} + \frac{hf_r}{2i\pi k_B T} \right) \right\} - \ln \frac{hf_r}{2\pi k_B T} \right) - \alpha \frac{\Delta L_k}{L_k} \quad (6.16)$$

where Ψ is the digamma function [147] and $\frac{\Delta L_k}{L_k}$ is the kinetic inductance change. Since $L_k(T) = \mu_0 \lambda_L^2(T)(l/wd)$, and $\lambda_L(T)$ is the temperature dependent London penetration depth. It follows that, as for $T \leq 0.4 T_C$, the London penetration depth change $\lambda_L(T)/\lambda_L(0) - 1$ is proportional to $(T/T_C)^2$ [150], leading to

$$\frac{\Delta L_k}{L_k} = \left(\frac{k_B T}{\Delta} \right)^4 \quad (6.17)$$

As reported in [Figure 6.6](#), we see that at increasing temperature the internal quality factor begins to raise thanks to the saturation of TLS fluctuators, but then starts dropping due to the losses caused by quasi-particles population. Due to the large T_C of the film characterized ($T_C = 7.5$ K) this effect becomes dominant only reached 700 mK, *i.e.* at roughly 10% of T_C . Same effect is reported also for the resonator frequency shift, where below 400 mK the shift is caused solely by TLS fluctuators, while at larger temperatures quasi-particles shift dominate.

6.2 IMPEDANCE MATCHING TAPER

Developing large impedance structures however leads to matching issues. In fact, as the cryogenic feedlines of cryostats are usually 50Ω coaxial cables, matching them to $k\Omega$ impedance structures may only lead to reflections and signal loss. To overcome this impedance matching issue, it is possible to design an impedance matching tapered transmission line.

The impedance matching taper has been developed following the approach previously described in [37, 49, J14]. By controlling the impedance of the transmission line at a large number of sections, it is possible to design a transformer to minimize reflections from classical readout impedance, *e.g.* 50Ω impedance, to a large impedance device, whether it be for ultra-strong coupling regimes in qubits, or for SNSPDs readouts applications.

The reflections in a nonuniform, lossless transmission lines are governed by the nonlinear differential equation [151]

$$\frac{d\varrho}{dx} - 2j\beta\varrho + \frac{1}{2}(1 - \varrho^2)\frac{d(\ln Z_o)}{dx} = 0, \quad (6.18)$$

where $Z_o = \sqrt{Z/Y}$ (which simplifies to $\sqrt{L/C}$ in the lossless limit) is the characteristic impedance of the line, function of its position x , $\beta = \sqrt{ZY}$ (which simplifies to $\omega\sqrt{LC}$ in the lossless limit) is propagation constant, ϱ is the reflection coefficient,

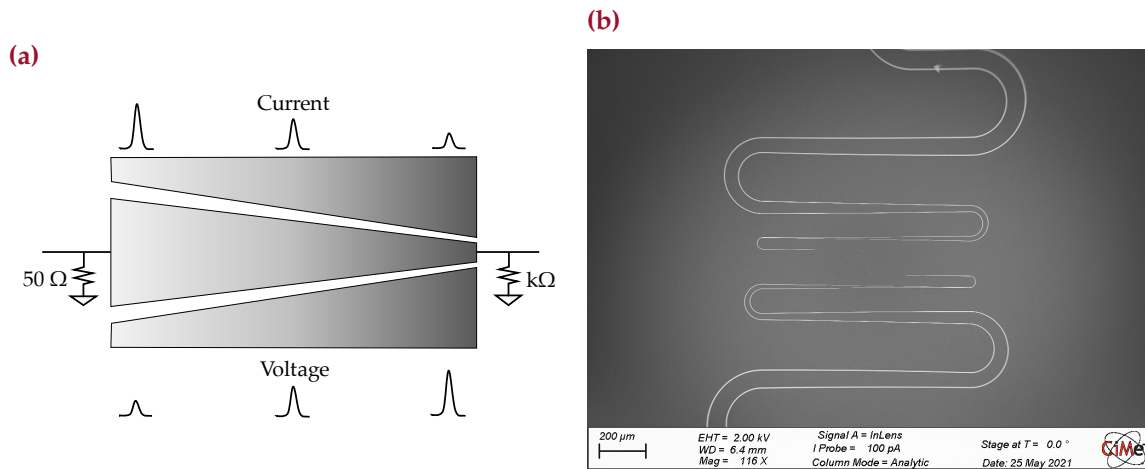


Figure 6.7 | Impedance matching taper. Schematics of the taper distributed transformer function (a). Scanning electron micrograph of a impedance matching taper (b).

$Z = R + j\omega L$ is the series impedance per unit length, $Y = G + j\omega C$ is the shunt admittance per unit length of the transmission line, and in the lossless limit $R = G = 0$.

It has been mathematically proven by Klopfenstein and Collin in the late '50s [151, 152] that a tapered design of a transmission line can lead to minimum reflections, behaving as a distributed transformer. Indeed, under the assumption that $\varrho^2 \ll 1$, the taper impedance profile $Z_o(x)$ described by the equation

$$\ln Z_o = \frac{1}{2} \ln (Z_1 Z_2) + \frac{\varrho_o}{\cosh(A)} \left[A^2 \phi(2x/l, A) + U(x - l/2) + U(x + l/2) \right] \quad (6.19)$$

is a solution of the (6.18), where $\varrho_o = \frac{1}{2} \ln (Z_2/Z_1)$ is the modified reflection coefficient [151] induced by the impedance change if there was no taper, Z_1 is the lower-impedance section, Z_2 is the higher-impedance section, $U(z)$ is the step function which is zero for $z < 0$ and 1 for $z \geq 0$, A is defined from $\cosh(A) = \varrho_o/\varrho_{\max}$, where ϱ_{\max} is the maximum acceptable reflection coefficient set by design, and ϕ defined as:

$$\phi(z, A) = -\phi(-z, A) = \int_0^z \frac{I_1(A\sqrt{1-y^2})}{A\sqrt{1-y^2}} dy, \quad (6.20)$$

with $I_1(z)$ the first kind of modified Bessel function of the first order.

From this model, it is possible to design impedance matching taper where the degrees of freedom are set by bandwidth frequency f_{bw} , which is related to the taper electrical length $l_e = l/v_{ph}$ by the formula $l_e = Ac/2\pi f_{bw}$, where l is the

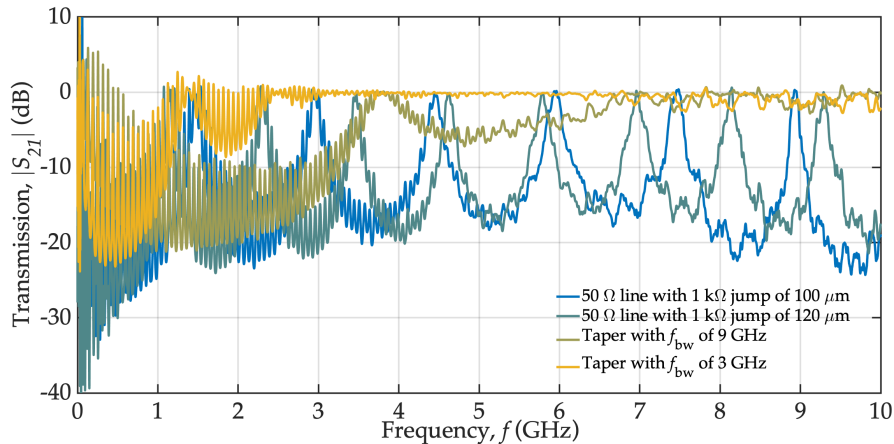


Figure 6.8 | Impedance matching tapers transmission spectra. The S_{21} scattering parameter of the fabricated devices were measured by means of a VNA after proper through-calibration. While the so-called jump lines show periodic resonant peaks of perfect transmission, at the harmonics frequencies of the $1\text{ k}\Omega$ section natural resonant frequency, alternated with lossy transmission as low as -20 dB (in agreement with the static reflection coefficient, *i.e.* $\varrho = (Z_h - Z_l)/(Z_h + Z_l) = 0.9 = -10\text{ dB}$ in voltage, which in power is -20 dB). The tapers instead present a much smoother transmission at frequencies above the cutoff frequency f_{bw} , resulting in almost-perfect transmission of 0 dB .

physical length of the taper, v_{ph} is the phase velocity, c is the speed of light in vacuum, ϱ_{max} the maximum reflection coefficient, and Z_1 and Z_2 the input and output impedance.

The advantage of using high- L_k materials is that, thanks to their very low phase velocity v_{ph} , usually in the 1% range of c , it is possible to shorten dramatically the physical length of the transmission line. For instance, a 1 GHz bandwidth taper with Z_1 of $50\text{ }\Omega$ and Z_2 of $150\text{ }\Omega$ (without L_k contribution it is very hard to reach impedances larger than $200\text{ }\Omega$ in superconductors with coplanar waveguides), and ϱ_{max} of 0.01 has an electrical length l_e of 223.61 mm , for an Al taper the total physical length would be 88.0 mm , for an NbN taper it would reduce to 32.7 mm , and for grAl would be 24.2 mm . This effect is enhanced further when increasing the value of Z_2 .

To characterize the devices, we fabricated on a NbN chip a $50\text{ }\Omega$ calibration lines, two stepwise transmission lines going from $50\text{ }\Omega$ launchers to $1\text{ k}\Omega$, with high impedance section lengths of $100\text{ }\mu\text{m}$ and $120\text{ }\mu\text{m}$, and two double tapers with Z_2 of $1\text{ k}\Omega$ and Z_1 of $50\text{ }\Omega$ and nominal bandwidth frequencies f_{bw} of 3 GHz and 9 GHz , where the transmission line goes from Z_1 to Z_2 and back to Z_1 .

The transmission spectra of the four tested devices, calibrated with respect to the $50\text{ }\Omega$ feedline, are reported in Figure 6.8. The peaks of the stepwise transmission lines are due to the resonant frequency of the $1\text{ k}\Omega$ section, which resonates because of impedance mismatch at the edges. While it is not perfectly clear the origin of

the transmission fluctuations between 0 and 3 GHz, the tapers show almost zero attenuation above their respective design cutoff frequencies.

6.3 MICROWAVE FILTERING USING PERIODIC STRUCTURES

Another potential application of high- L_k compact resonators is the capability of building structures which, for a normal superconductor, would be largely impractical to fabricate. Microwave signal filtering, in particular for quantum computing applications, *e.g.* to reduce the relaxation rate due to Purcell decay (see [Subsection 7.2.1](#) for more), is one example of application where high- L_k superconductors would lead to much more compact chips. The results presented in this Section are part of the work reported in [J5].

As described by [47, 48], it is possible to fabricate microwave photonic-crystals by exploiting the impedance mismatch reflections at the boundaries of the resonators. In order to build such structures, called stepped impedance microwave filter, the device is designed as an array of $\lambda/4$ resonators of impedance Z_1 and Z_2 , to exploit the same constructive and destructive interference we see in more classical examples such as the distributed Bragg reflectors in optics. The spectral bandwidth of the bandgap of a stepped impedance filter is proportional to the ratio Z_2/Z_1 , while its bandgap rejection is dependent on both Z_2/Z_1 and the number of pairs (sections) which compose the structure.

In previous works, aluminum stepped impedance microwave filters have been demonstrated as filtering system for a qubit, but as the device was fabricated in aluminum, it lead to very large structures, which could not be fully integrated on chip and had to be connected via wirebonding on a separate chip [47]. As the freedom of choice of impedance is limited for normal superconductors to Z_{vac} , to enhance the spectral width of the bandgap it is necessary to produce very bulky low-impedance $\lambda/4$ sections and in a large number.

Following the same approach described by Sigillito *et al.* [48], a simple transfer matrix model based on the ABCD matrix approach was built to roughly estimate the coupling quality factor κ of the filters as function of both impedance of choice and number of pairs. Following the same principle of the Fabry-Pérot filters, the presence of a $\lambda/2$ resonator in the middle of the photonic crystal structure causes constructive interference to enhance transmission at the spectral center of the bandgap, leading to a very sharp (for large number of pairs) band-pass filter.

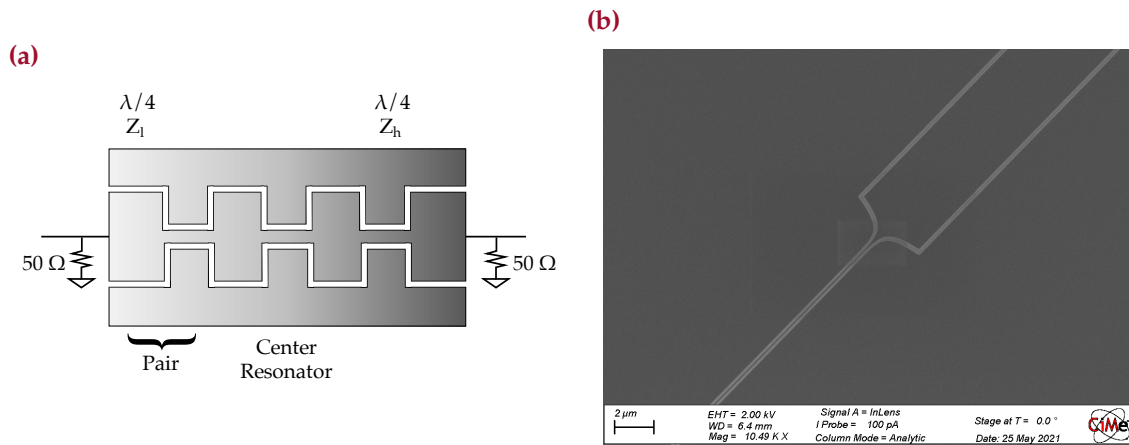


Figure 6.9 | Stepped impedance microwave filter. Simple schematics of the filter (a). Scanning electron micrograph (SEM) of an impedance microwave filter step between low and high impedance sections (b).

However, coupling κ much lower than the internal quality factor γ would only lead to undercoupling and potential overall loss of transmission.

We fabricated devices with smaller number of pairs and large coupling rate to allow better transmission of the in-resonance frequencies, and with large number of pairs to reduce coupling and to show sharper peaks (reported in Figure 6.10). In each device, two sections impedance Z_l and Z_h are designed as coplanar waveguides. In CPW design, controlling transmission line width and gap gives the designer significant control over the impedance. Despite that, it has been shown [140] that resonating CPWs with gap smaller than $3 \mu\text{m}$ lead to large TLS losses. On the other hand, to increase compactness, hence having a slow enough phase velocity $v_{\text{ph}} = 1/\sqrt{L_0 C_0}$, it would be ideal to minimize the gap as to maximize the capacitance per unit length. Because of that, we fixed the gap to $3 \mu\text{m}$ and controlled the impedance with nanowires width.

For very largely coupled devices (*i.e.* $\kappa > \gamma$, number of pairs of 2 and 3 in figure), the effect of edge reflection between the first pair and the 50Ω feedline became more and more dominant, flattening the peak at the center of the bandgap. If properly engineered, this effect may lead to production of flat, wide pass-band filters. This effect is reduced when a taper is placed to impedance match the first pair, as shown from the devices with 3 bilayers Bragg filter and taper. On the other hand, not coupled enough devices (*i.e.* $\kappa < \gamma$, 6 pairs in figure) the peak does not reach 0 dB transmission, hence suggesting undercoupled device with a very sharp central peak.

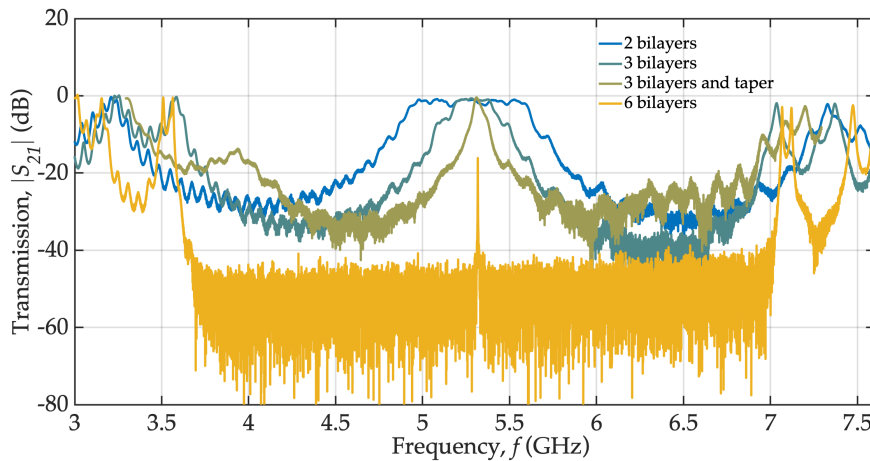


Figure 6.10 | Measured filters transmission spectra for different number of pairs. Comparison of fabricated filters with impedance Z_l of $450\ \Omega$ and Z_h of $900\ \Omega$ with 2 pairs on each side of the central $\lambda/2$ resonator, 3 pairs, and 6 pairs. The 3 pairs design has been fabricated also with an impedance matching taper to avoid the extra standing waves and to maintain a sharp peak at resonance.

Another property of high- L_k superconductors is that kinetic inductance can be tuned by means of dc biasing current, as demonstrated in previous works [29, 153, J13], which opens new potential applications for galvanically connected devices. A schematic of the experimental setup is reported in Figure B.4. By flowing dc current through the device, indeed, it is possible to increase the kinetic inductance of the resonators, which in turn causes the resonant frequency of the resonating parts to shift towards lower frequency.

While driving current through a stepped impedance filter, we generate different response from different sections. As discussed before, the gap distance of the CPW was fixed, leading to larger widths for the lower impedance lines, *i.e.* $w_l > w_h$. When applying a dc biasing current through the device, the high impedance section will experience a larger kinetic inductance enhancement, due to the critical current ratio $I_{bias}/(j_{crit}\ t\ w_h) > I_{bias}/(j_{crit}\ t\ w_l)$. This unbalance between the resonant frequency of high-impedance and low-impedance sections causes the coupling κ to be reduced as it can be shown from simple ABCD matrix approach simulations.

Generally speaking, the larger is the depairing current fraction $I_{bias}/(j_{crit}\ t\ w_h)$ of the central resonator, the larger will be the range of tunability of the stepped impedance filter resonator peak. The tunability limit is eventually reached when I_{bias} reaches the device switching current I_{sw} .

Tuned spectra and quality factor analysis for different biasing conditions are shown in Figure 6.11. The devices are designed as 6 pairs of $\lambda/4$ resonators on each side of the $\lambda/2$ resonator, having impedance Z_l of $450\ \Omega$ (Figure 6.11(a)–(b)) or $300\ \Omega$ (Figure 6.11(c)–(d)) and Z_h of $900\ \Omega$. The central $\lambda/2$ resonator was placed

at a frequency of around 5.3 GHz at zero bias, reaching maximum tunability of about 200 MHz at a switching current of 64 μ A, equivalent to a kinetic inductance increase of roughly 10%.

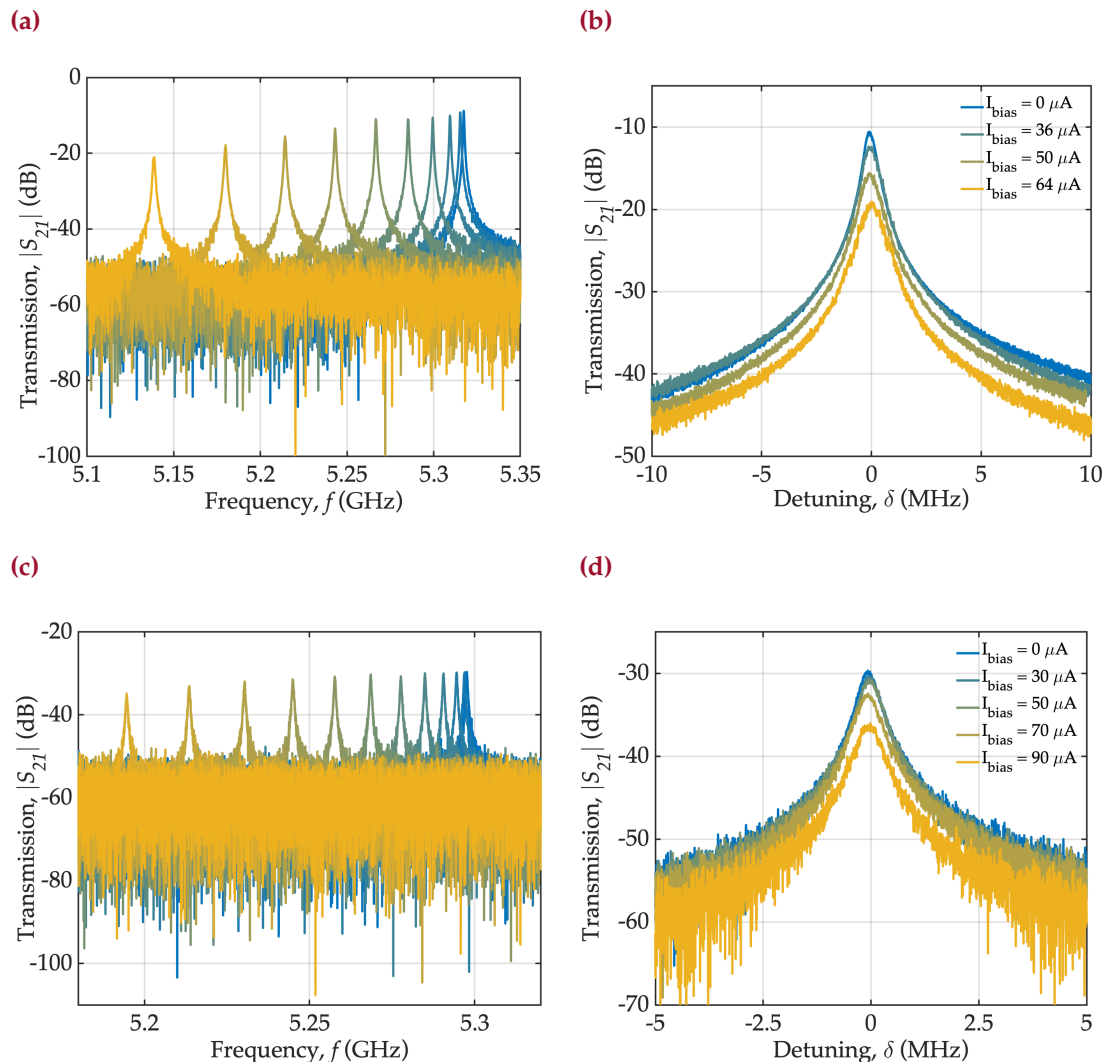


Figure 6.11 | Measured filters transmission spectra at different biasing conditions. Two devices of different designs, with 6-pairs each around the $\lambda/2$ resonator and impedance pairs $Z_1 - Z_h$ of 450–900 Ω (a)–(b) and 300–900 Ω (c)–(d). The spectra tunability (a)–(c) of the two devices, which exceeds 180 MHz for the low mismatch and just above 100 MHz for the high mismatch devices. The analysis of the quality factors of the two devices at different biasing conditions (b)–(d). While increasing current, the coupling rate κ decreases and the loss rate γ increases, making the devices less and less coupled, reducing peak transmission.

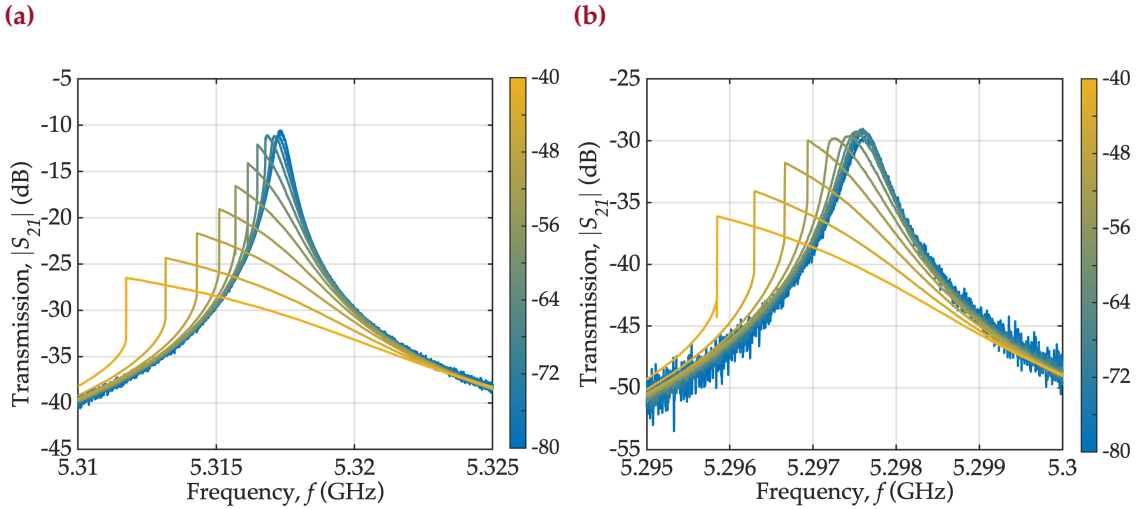


Figure 6.12 | Measured filters transmission spectra at different biasing conditions. Representative figure showing the self-Kerr nonlinearity effect also for these sharp filters. As expected, at the same excitation power the device closer to critical coupling (*i.e.* $\kappa \rightarrow \gamma$, (a)) has a larger number of photons hence shows a more pronounced Kerr inflection than the less coupled device (b).

The transmission was calibrated with $50\ \Omega$ through lines to estimate the resonator baseline, and both losses and coupling were estimated by means of the equation

$$S_{21} = \frac{2\sqrt{\kappa_1\kappa_2}}{\kappa_1 + \kappa_2 + \gamma + 2i(\omega - \omega_r)} = \frac{\kappa}{\kappa + \gamma/2 + i(\omega - \omega_r)}. \quad (6.21)$$

Being the device undercoupled, the sharp peaks never reach 0 dB. We estimated an internal quality factor $Q_i = \omega_r/\gamma$ of 10^4 for both the tested devices, and a coupling quality factor $Q_c = \omega_r/\kappa$ of $7 \cdot 10^4$ (for the device in Figure 6.11(a)) and $6 \cdot 10^5$ (for the device in Figure 6.11(b)). As the device with larger impedance mismatch (300 – $900\ \Omega$) is less coupled, the maximum transmission is lower, as the loss rate is much larger than the coupling rate.

At dc biasing conditions, we noticed that the resonators frequency mismatch caused a drop in external coupling κ , and concurrently, γ is reduced due to quasiparticle population.

While power-scanning the devices, as shown in Figure 6.12, we notice self-Kerr effects. While the estimation of the self-Kerr K is beyond the scope of this work, it is interesting to see that nonlinearity is still relatively dominant for such large nanowire structures. This effect is currently under study as it may lead to potential four-wave parametric amplification regimes [144].

6.4 DISCUSSION

High-kinetic inductance resonant structures presented in this chapter show compact and low-loss devices, which are interesting for large scale integration of superconducting circuits. The compactness in itself is a very valuable tool that can be used to fabricate many-resonators devices for applications such as analog quantum simulations. We presented NbN resonators with internal quality factors in excess of 10^5 at single-photon regime, low nonlinearity in the range of 10 Hz and strong robustness to aging. In terms of applications, impedance matching taper have already shown their utility for SNSPDs [37, J14] and for compact microwave analog circuits [49], but have not yet been employed to readout losslessly high impedance harmonic systems designed to study strong- or ultrastrong- coupling regimes of superconducting qubits. Finally, high-rejection and sharp microwave filters as the one presented can be used as compact on-chip filters to reduce Purcell decay of superconducting qubits, and adding the tunability feature may play a very interesting role in addressing frequency multiplexed qubits. This may potentially lead to a new device, such as a Purcell switch.

CHAPTER

7

Computers are better than we are at arithmetic, not because computers are so good at it, but because we are so bad at it.

— Isaac Asimov, 1988

PLANAR TRANSMON QUBIT

In this chapter we discuss the fabrication and testing of a transmon qubit. In order to couple high-kinetic technology developed in the previous chapters in the quantum computing field, we would like to develop a standard qubit to use as a reference. What is presented in this chapter was the fruit of a collaboration with Prof. Pasquale Scarlino (from the HQC lab in EPFL) and Dr. Marco Scigliuzzo (from the LPQM lab in EPFL, previously in Chalmers University).

Superconducting qubits were first successfully fabricated and tested in 1999 by Nakamura *et al.* [12] and have been widely explored and improved ever since. The first superconducting qubit in a cQED architecture [50] was designed as two parallel Josephson junction connected to an island and coupled to a readout resonator. The presence of a Cooper pair in the island would generate a frequency shift which could be read out from the resonator. This device was called the Cooper pair box (CPB). While the CPB had very large anharmonicity $\alpha = \omega_{12} - \omega_{01}$, *i.e.* the energy difference between the first state transition (ground state to first excited state, with energy $\hbar\omega_{01}$) and the second order transition (with energy $\hbar\omega_{12}$), which made it close to an ideal two-level system, it was extremely sensitive to charge noise, which strongly limited its coherence time [12, 154].

Briefly after the Cooper pair box, a new approach was proposed by the group in Yale lead by Prof. Robert Schoelkopf [155, 156] to solve the issue of the charge noise, shunting the Josephson junctions by means of a large capacitance. The presence of this large capacitance makes the qubit energy levels almost insensitive to charge noise, at the price of a reduction of qubit anharmonicity, which then pushes it away

from an ideal two-level system approximation. It can be shown that the transmon regime satisfies the condition $E_C \ll E_J$, where

$$E_C = \frac{e^2}{2C_q}, \quad E_J = \left(\frac{\Phi_0}{2\pi}\right)^2 \frac{1}{L_J} \quad (7.1)$$

with C_q the total capacitance of the qubit, L_J the Josephson inductance of the junction, and $\Phi_0 = h/2e$ the magnetic flux quantum.

It is also possible to shunt the qubit capacitance with two Josephson junctions, *i.e.* a SQUID producing as a result a frequency tunable qubit. The tunability comes from the fact that the Josephson inductance $L_J = \Phi_0/2\pi I_C$ can be increased by controlling the critical current of the junction by means of an external magnetic field, which causes a phase shift in the SQUID loop. This effect can be written as

$$L(\phi) = \frac{\Phi_0}{2\pi I_C \cos \phi} = \frac{L_J}{\cos \phi} \quad (7.2)$$

where $\phi = 2\pi\Phi_{\text{ext}}/\Phi_0$ is the Josephson phase induced by the external magnetic flux Φ_{ext} .

7.1 DESIGN AND FABRICATION

The devices were designed by taking as inspiration those of the Martinis group at UCSB [157, 158]. Transmon qubit dynamics follow the Jaynes-Cumming Hamiltonian description [159], which can be written as

$$H_{\text{JC}}/\hbar = \omega_r a^\dagger a + \frac{1}{2} \omega_q \sigma_z + g(a^\dagger \sigma^- + \sigma^+ a) \quad (7.3)$$

which, in dispersive regime, *i.e.* when $|\omega_r - \omega_q| \gg g$, reduces to the following dispersion Hamiltonian:

$$H_{\text{disp}}/\hbar = (\omega_r + \chi \sigma_z) a^\dagger a + \frac{1}{2} \left(\omega_q + \frac{g^2}{\Delta} \right) \sigma_z \quad (7.4)$$

where χ is defined as dispersive χ -shift

$$\chi = \frac{\omega_r^{|e\rangle} - \omega_r^{|g\rangle}}{2} = \frac{g^2}{\Delta} \frac{\alpha}{\Delta + \alpha} \quad (7.5)$$

and represents half the readout resonator frequency shift when the qubit is in excited state $\omega_r^{|e\rangle}$ or ground state $\omega_r^{|g\rangle}$, with $\alpha = -E_C/\hbar$ the nonlinearity of the qubit.

While the detuning between qubit and resonator can be controlled by changing the frequency of the qubit by means of the flux line, the coupling rate g is fixed by design. In general, the coupling rate between harmonic systems is defined as

$$g = \frac{1}{2} \frac{C_g}{\sqrt{C_r C_q}} \sqrt{\omega_r \omega_q} = \frac{1}{2} C_g \omega_r \omega_q \sqrt{Z_r Z_q}, \quad (7.6)$$

which differs from the coupling between a harmonic system and a waveguide is expressed by (6.1).

As discussed previously, the capacitance of a transmon has to fall in the 50–100 fF range: less capacitance would break the assumption $E_J \gg E_C$ for the transmon regime, and a larger capacitance would reduce even further the qubit anharmonicity. The resonant frequency of the qubit is set by the inductance of the Josephson junction.

The resonators were designed with python code and simulated with a 2D model of a FEM solver (Sonnet Inc.) to have a resonant frequency $\omega_r/2\pi$ of 6 GHz. The qubit capacitance C_q was estimated to be 90 fF with use of electromagnetic static simulator (COMSOL Multiphysics), associated to a nonlinearity $\alpha/2\pi$ of 215 MHz. The Josephson juctions were designed using the useful approximation

$$R = \frac{\pi \Delta}{2 I_C} = \frac{\pi^2 \Delta}{\Phi_0} L_J, \quad (7.7)$$

where R is the room temperature resistance of the junction for a relatively thick (30–40 nm) Al electrode thickness. From the energy levels of the qubit, we know that

$$\hbar \omega_{qe} \approx \sqrt{8 E_C E_J - E_C}, \quad (7.8)$$

so as we want to design a qubit with frequency at zero external flux Φ_{ext} of 4.5 GHz, from (7.1) we estimate that we need a Josephson inductance L_J of 12.6 nH, which corresponds to a room temperature junction resistance of 10.5 kΩ. The couplings κ_r between the feedline and the readout resonator and g between the resonator and the qubit were simulated with Sonnet and estimated to be $2\pi \times 1$ MHz and $2\pi \times 80$ MHz, respectively. The value of g is chosen in such a way that the qubit can be operated in the dispersive regime, and the value of κ_r has to be chosen not too small, as the readout time is inversely proportional to it, and not too large, as for

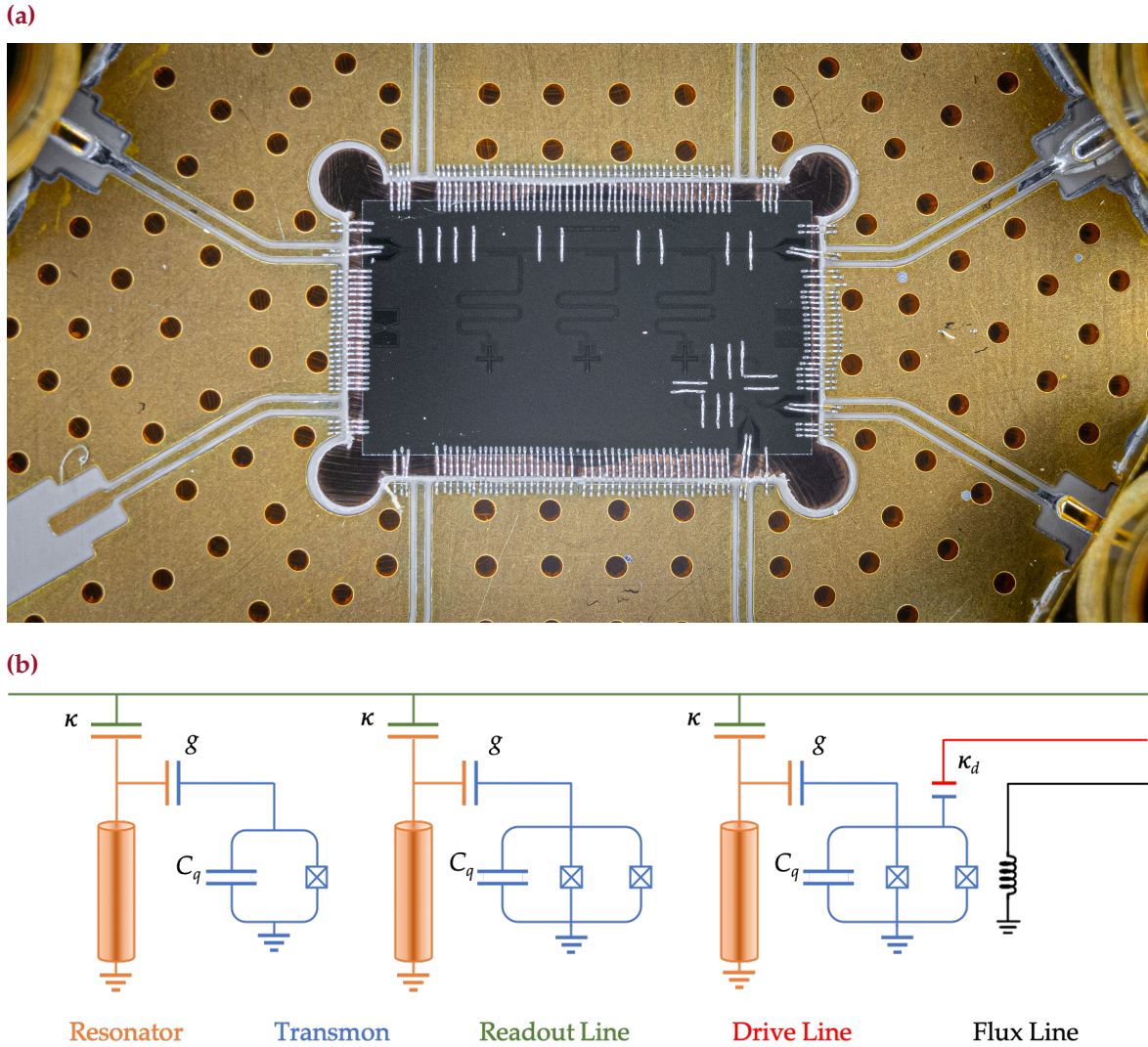


Figure 7.1 | Qubits Chip. Micrograph of a ready-to-be-tested chip glued and wirebonded to the PCB. The chip schematics is presented below it, consisting of three qubits having slightly different design conditions.

good readout fidelity it is required that the χ -shift need to be at least comparable to κ_r . It can be demonstrated that the optimal value for κ_r is exactly χ [159], as having $\kappa_r > \chi$ would lead to loss of SNR, while $\kappa_r < \chi$ would reduce the readout fidelity for fast gating. It is also worth noting that for too large κ_r the qubit may lose the information in the feedline through Purcell decay [160, 161]. Purcell decay, which is defined as

$$\gamma^{\text{Purcell}} = \left(\frac{g}{\Delta} \right)^2 \kappa_r, \quad (7.9)$$

sets an upper limit to the maximum relaxation time of the qubit. In our case, for a detuning Δ of 1.5 GHz, we estimate an upper limit T_1^{Purcell} of 56 μ s.

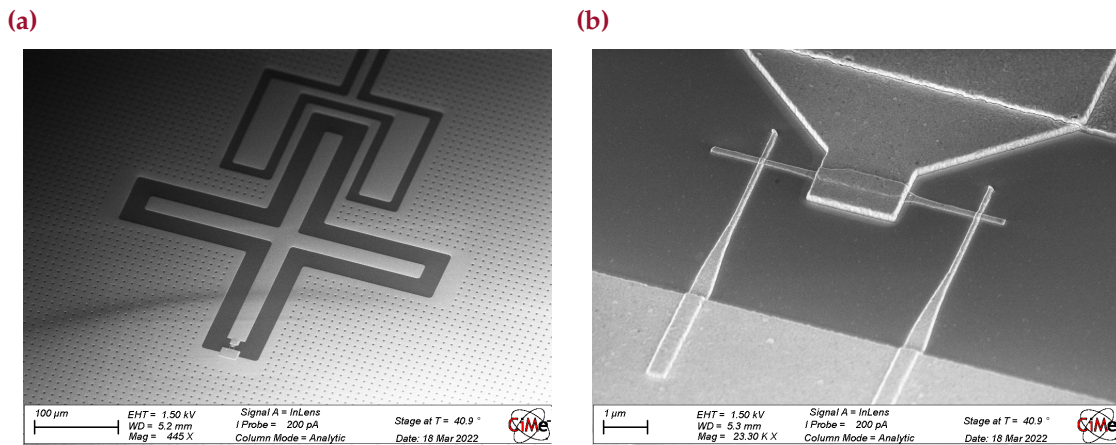


Figure 7.2 | Transmon Qubit. Scanning electron micrograph of the fabricated planar transmon. The superconducting qubit was fabricated in aluminum on an intrinsic silicon wafer. The Josephson junctions were fabricated via Manhattan technique and later patched to the main body of the qubit. The vertical and lateral dimensions of the qubit is roughly 300 and 300 μm , while the Josephson junctions have a junction area of 160 by 160 nm^2 .

The drive of the qubit was performed through the resonator feedline and then coupled to the qubit through the resonator, which simplifies the design and the requirements in terms of cryogenic cabling, and the flux was tuned via a coil, hence avoiding potential noise coupling from the flux lines to the qubits.

The device was fabricated using the process flow reported in [Appendix A.1.4](#), but without the later implemented airbridges technique. Despite airbridges have good impact on the overall quality of the devices as make the grounding more stable, they can be substituted by less clean bridge-bonds made with standard wirebonders, which is what we used in this case to avoid unwanted slot-modes.

Micrographs of the qubits are reported in [Figure 7.2](#). The Josephson junctions are deposited using the Manhattan technique [162] and then patched to the main Al features after an ion-mill step.

7.2 CHARACTERIZATION

In order to characterize the qubits, we tested them in an LD250 BlueFors system in Prof. Scarlino laboratory, wired with all the necessary electronics and the *know-how* to perform the required characterization measurements.

A schematics of the system is reported in [Figure 7.3](#). The system required the use of a vector signal generator (SG, SGS100 series, Rohde & Schwarz), microwave mixers (MIX), an arbitrary wave generator and a analog-to-digital converter (AWG

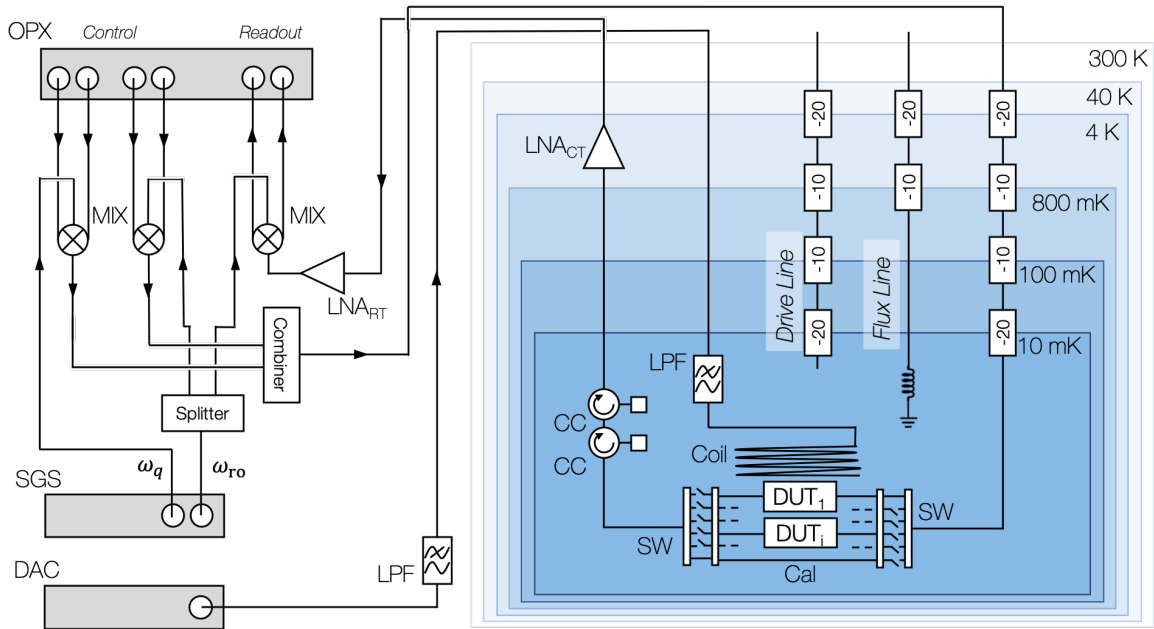


Figure 7.3 | HQC Laboratory Setup. The qubits were tested in the cryogenic system of HQC laboratory (headed by Prof. Scarlino). The devices were tested using an OPX, capable of either send control and readout pulses via an AWG and of reading voltages by means of an integrated ADC. The pulse modulation was performed by means of mixers. A signal generator was used to mix the control pulses with a clean local oscillator at the frequencies of the qubit ω_q and of the readout ω_{ro} . A DAC was used to control the external magnetic field Φ_{ext} .

and ADC, both integrated in the OPX Plus series, Quantum Machines). After preparation of the qubit drive signal by mixing the SG, usually set at a frequency close to ω_q , and the AWG signal, which is set to generate a Gaussian pulse, the convolved pulse is further mixed with the drive pulse at the readout frequency ω_d and sent to the qubit through the resonator feedline. Good readout strategy is to set ω_d between $\omega_r^{|e\rangle}$ and $\omega_r^{|g\rangle}$ [159], so as to be able to read the maximum phase shift of the resonator generated in correspondence of the states $|g\rangle$ and $|e\rangle$ of the qubit. We will refer to this frequency as $\omega_{ro} = (\omega_r^{|g\rangle} + \omega_r^{|e\rangle})/2$.

The signals, properly attenuated at all stages of the cryostat, are sent to the device. After interacting with the readout resonator, the signal is collected from the readout lines for cryogenic and room temperature amplification, and then to a room temperature mixer for demodulation. The demodulated signal is then read out from the analog to digital converter, which senses the status of the qubit by reading the resonance shift of the resonator.

The first thing to do when testing qubits is to adjust the readout parameters to make sure the resonator is properly addressed, and that the photon number in the resonator is not larger than the critical photon number $n_{crit} = \Delta^2/4g^2$ [160, 161]. For this, we run a power scan of the resonator and we check how the position of

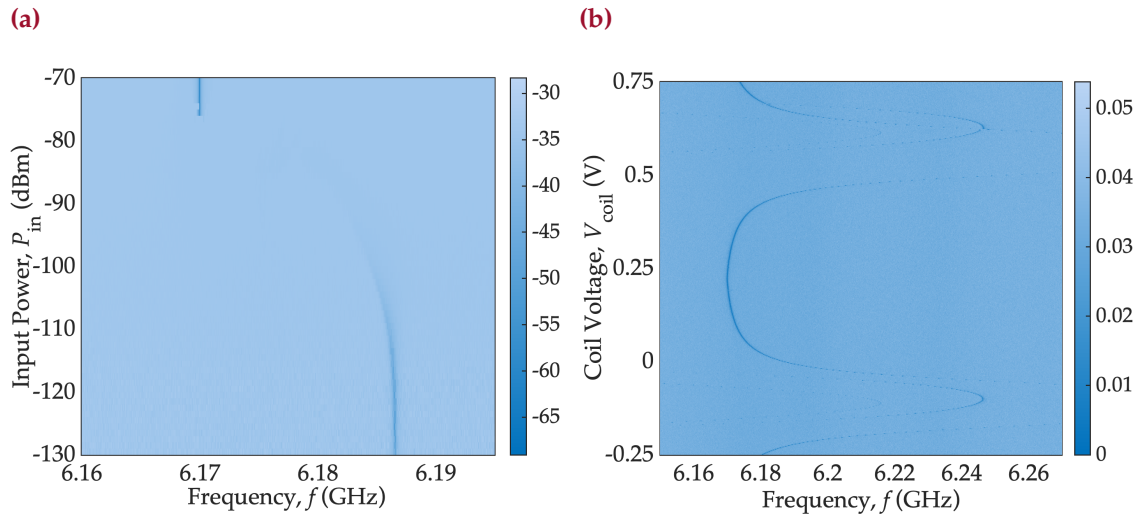


Figure 7.4 | Qubit Punch-out and flux tunability. Readout resonator spectroscopy at different power (punch-out measurement, (a)) and at different external applied magnetic flux Φ_{ext} (tunability measurement, (b)). When the photon number in the resonator reached the critical photon number n_{crit} , the dispersive regime approximation is no more valid, so power sent to the resonator is also sent to the qubit, driving it and causing it to saturate the Josephson junction, exceeding its critical current. By applying magnetic flux into the SQUID, we tune the Josephson inductance of the qubit, hence its resonance frequency ω_q . This causes the resonator to experience a χ -shift dependent on the magnetic flux.

the dip drifts with power (S_{21} , Figure 7.4(a)). At first, increasing the power causes a resonance drift towards the qubit, then photons in the resonator should saturate the qubit, giving a "punch-out" [163]. This is used as preliminary measurement to estimate the drive power that can be sent to the resonator to maximize SNR without disrupting the qubit state, to fast check whether the qubit is alive and if it is parked above or below the resonator frequency.

After the punch-out, we check the external flux tunability of the qubit by recording the spectrum at different flux conditions, *i.e.* at different coil voltage. Due to avoided crossing reasons, when the qubit resonant frequency ω_q comes near the resonator frequency ω_r , the resonator is pushed at higher frequencies. In case where the the qubit zero flux frequency is designed to be larger than the resonator's, *i.e.* if $\omega_q(\Phi_{\text{ext}} = 0) > \omega_r$, there will be an avoided crossing, and the resonator will reappear at lower frequencies (see Figure 7.4(b)).

After these two preliminary measurements are performed, the external flux is maintained constant and two-tone spectroscopy is performed to find in frequency the "position" of the qubit. For two-tone spectroscopy, we send the coupled signal of both the readout frequency ω_{ro} and a drive frequency ω_d , which is the free parameter scanning in frequency. The signal from the output is then demodulated for ω_d and the resonator signal is read out. If ω_d is far from the qubit frequency

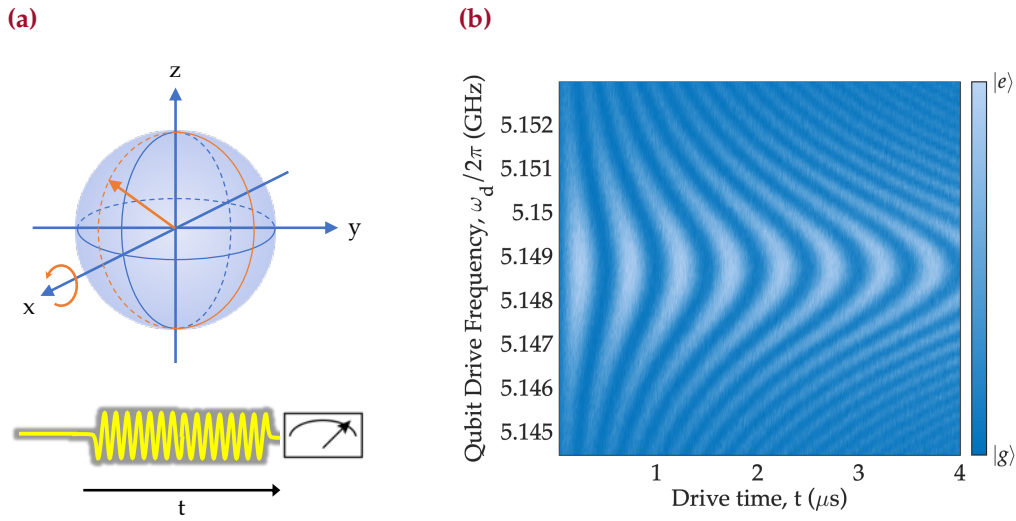


Figure 7.5 | Chevron Pattern. While manipulating the qubit with pulses that are the convolution of the AWG square pulses and the drive frequency ω_d , we perform Rabi oscillations on the qubit, hence we rotate the state of the qubit along the x -axis of the Bloch sphere. The frequency and the magnitude of the oscillations are dependent on the detuning between the qubit frequency and the drive frequency, as detuning of the drive causes also state rotation along the z -axis.

ω_q , the readout will read the resonator as if there was no other signal. When ω_d approaches the qubit frequency, the qubit gets populated: this induces a χ -shift in the resonator frequency, which causes a phase shift in the readout signal.

Following the system study in continuous wave spectroscopy (pulse duration $\tau \gg T_1$), we estimate the frequency of the qubit, and then we can perform a time-resolved measurement. For Rabi oscillations, we send a pulse to the qubit at the drive frequency modulated with a square pulse of varying length. This causes a rotation of the qubit state around the x -axis on the Bloch sphere of different angles in correspondence to different pulse lengths τ . This leads to the characteristic Rabi Chevron pattern, which is presented in Figure 7.5.

From the Chevron pattern, we can very well estimate both the qubit frequency ω_q , and the characteristic time length, dependent on the power applied, of the π -pulse. These two values play a key role to perform the rest of the characterization of the qubits, as we will see in the next sections.

For single qubits, the characterization is mostly performed in estimating relaxation time (T_1), decoherence time (T_2^*), and qubit readout fidelity. Relaxation and decoherence times can be interpreted as noise along the Bloch sphere axes, and have different sources.

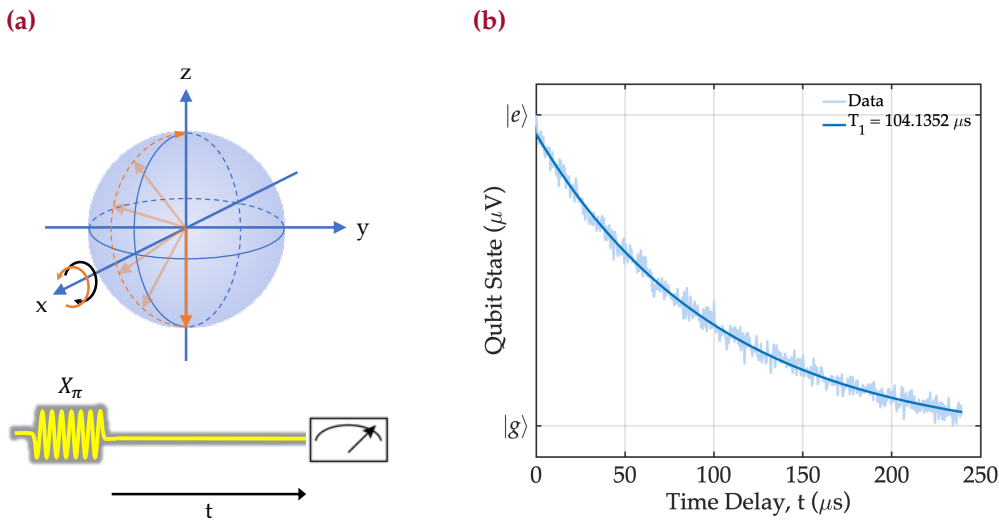


Figure 7.6 | Relaxation Time. The qubit relaxation time is the time required for the qubit to decay from an excited state $|e\rangle$ back to the ground state $|g\rangle$. The readout scheme for such a measurement is $X_\pi - \tau - \text{RO}$, where X_π is a π rotation along the x -axis, τ is the waiting time and RO stands for readout. This causes an exponential decaying function in time, from which we can estimate T_1 (b).

7.2.1 RELAXATION TIME

The first and most critical characteristic time of a qubit is the relaxation time, also called qubit lifetime. Relaxation time is time required for a qubit to relax and release energy from the excited state $|e\rangle$ to the environment, hence it is associated to the noise along the x and y axes of the Bloch sphere [159]. As this process is exponential in time, T_1 is defined as the $1/e$ time of the exponential decay of the qubit excited state population. In accord with [159], we can write the relaxation rate as

$$\Gamma_1 = \frac{1}{T_1} = \Gamma_{1\uparrow} + \Gamma_{1\downarrow} \quad (7.10)$$

where $\Gamma_{1\uparrow}$ is the rate at which the qubit reaches the state $|e\rangle$ from a starting state $|g\rangle$, and $\Gamma_{1\downarrow}$ the opposite. Due to Boltzmann equilibrium statistics we know that the states reach a "detailed balance" relationship where $\Gamma_{1\uparrow} = (-\hbar\omega_q/k_B T)\Gamma_{1\downarrow}$. As the frequency of the qubit is usually in the order of a few GHz and the temperature of the dilution fridges in the range of 20 mK, we can neglect the contribution of $\Gamma_{1\uparrow}$ and safely assume that $\Gamma_1 = \Gamma_{1\downarrow}$.

The source of relaxation is mostly due to TLS fluctuators, microwave radiation, coupling between the qubit and the experimental environment [140]. From the fabrication perspective, this could be the level of cleanliness of the chip, the amount of impurities in the substrate, potential oxides, residual resist on the chip. From the

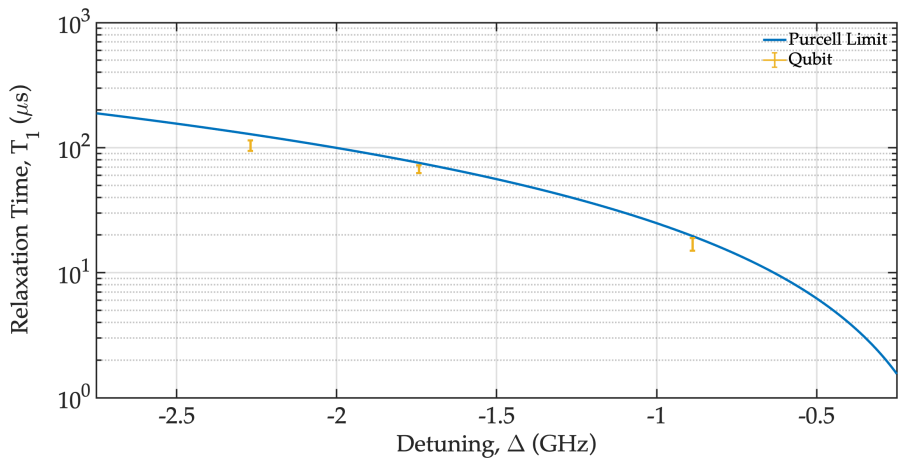


Figure 7.7 | Purcell Relaxation. Due to spontaneous emission from the qubit towards the readout circuitry, the transmon can relax to the ground state due to the so-called Purcell effect. Purcell limited devices show T_1 dependence on the detuning $\Delta = \omega_r - \omega_q$, according to (7.9). The measured qubit shows clear signs of Purcell limited behavior.

setup perspective, relaxation can be caused by off-axis rotation, caused by not clean drive signals, or by electromagnetic couplings to the system.

For the measurement, we first initialize the qubit by waiting a relatively long time of a millisecond. Then, once the qubit is in $|g\rangle$ state, we perform a π -pulse along the x -axis, that we will refer to hereafter as X_π , to bring the qubit in $|e\rangle$ state. After a delay time τ , we will perform readout to address the state of the qubit. By repeating this measurement many times and by scanning the wait time τ , it is possible to recreate this exponential decay. An example of the curve and the fitted T_1 is shown in Figure 7.6.

Our qubit showed a relaxation time T_1 at detuning of 2.2 GHz in excess of 100 μ s, which drops the closer we get to the readout resonator frequency. This hinted for a Purcell limited design, and as shown in Figure 7.6, in fact this was the case.

A solution to Purcell limit is to use a so-called Purcell filter [161], *e.g.* a second resonator in series to the readout resonator, which reduces this decay effect, enhancing the Purcell suppression from Δ^2 to Δ^4 . It can be shown that if a filtering resonator is placed between the readout line and the readout resonator at the same frequency ω_r of the readout resonator, the Purcell decay becomes

$$\gamma_{\text{filter}}^{\text{Purcell}} = \left(\frac{g}{\Delta}\right)^2 \left(\frac{\omega_q}{\omega_r}\right)^2 \left(\frac{\omega_r}{2Q_F\Delta}\right)^2 \kappa_r \quad (7.11)$$

where Q_F is the quality factor of the Purcell filter. This induces an effective coupling κ_{eff} [160]:

$$\kappa_{\text{eff}} = \frac{4Q_F\kappa_r^2}{\omega_r}, \quad (7.12)$$

so by tuning Q_F it is possible to design devices with a good balance between readout time and Purcell limited relaxation time.

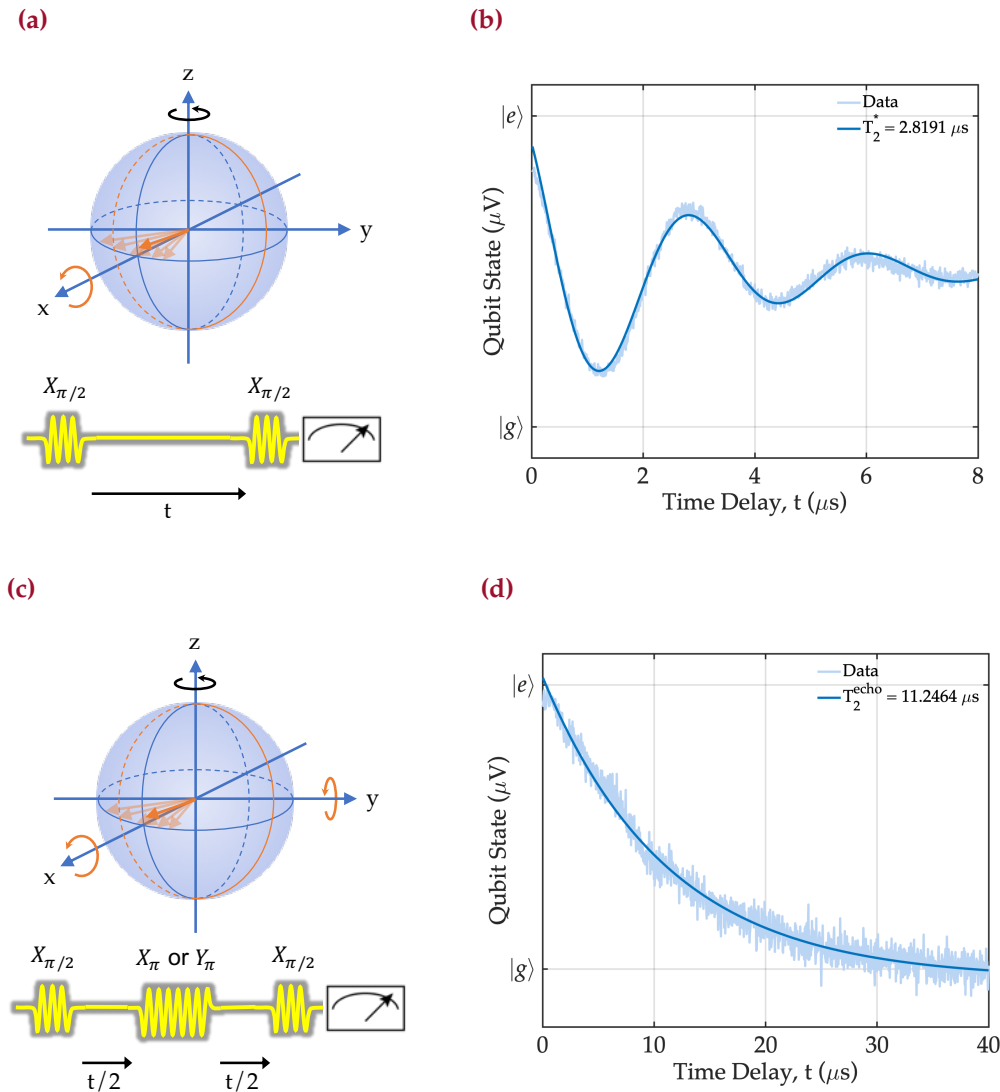


Figure 7.8 | Decoherence Measurements. Decoherence time is defined as time required by a qubit to lose a coherent entangled state. Both relaxation and pure dephasing are involved in the decoherence process. The readout scheme for such a measurement is called Ramsey measurement and is $X_{\pi/2}-\tau-X_{\pi/2}-\text{RO}$, where $X_{\pi/2}$ is a $\pi/2$ rotation along the x -axis, τ is the waiting time and RO stands for readout (a)-(b). Ramsey measurement is extremely sensitive to quasistatic noise. Alternatively, the Hahn echo scheme can be performed to filter out some quasistatic noise. The readout scheme for an echo measurement is $X_{\pi/2}-\tau/2-Y_{\pi}-\tau/2-X_{\pi/2}-\text{RO}$, where Y_{π} is a π rotation along the y -axis (c)-(d).

7.2.2 DECOHERENCE TIME

As the relaxation time is associated to noise along the x and y axes, pure dephasing is associated to noise along the z -axis. Pure dephasing is caused by fluctuations in the qubit frequency ω_q compared to the drive frequency ω_d , which causes a precession of the state vector along the z axis. The pure dephasing is, differently from relaxation, a reversible process, and its rate is defined as Γ_ϕ [159].

The combination of relaxation and dephasing generates decoherence. Decoherence described the loss of coherence of a superposition state, *e.g.* $(1/\sqrt{2})(|g\rangle + |e\rangle)$, and its rate is defined as $\Gamma_2 = 1/T_2 = \Gamma_1/2 + \Gamma_\phi$.

Decoherence is measured in qubits following the Ramsey protocol. After initialization of the system with a safe wait time of the order of $10 T_1$, the qubit state is brought to an entangled state $(1/\sqrt{2})(|g\rangle + |e\rangle)$ with a $X_{\pi/2}$ pulse. The qubit is left free to evolve for a time τ after which a second $X_{\pi/2}$ pulse is performed. For a delay $\tau = 0$, this is equivalent to a X_π pulse, hence we expect the qubit to be in the $|e\rangle$ state. For a finite $\tau < T_1$, we find the so-called Ramsey oscillations, which are damped oscillations with damping rate Γ_2 .

An alternative measurement scheme, called the Hahn "echo" measurement [164], allows us to partially recover the effect of some quasistatic dephasing noise. Differently from the Ramsey protocol, the Hahn echo protocol foresees a Y_π pulse at the middle of the delay time τ : this causes the quasistatic dephasing contributions to partially cancel out, leaving a decay function which is exponential in form.

The reported qubit was measured to have a Ramsey decoherence time T_2^* of $2.8 \mu\text{s}$ and a echo decoherence time T_2^{echo} of $11.2 \mu\text{s}$. Taken together, these results seem to suggest large dephasing noise, as the upper limit of the decoherence time is $2T_1$. In part, operating the qubit far from its sweetspot (*i.e.* at Φ_{ext} far from 0) makes the device extremely susceptible to magnetic noise, which may be causing frequency fluctuations in the qubit and subsequent dephasing. To further improve the decoherence time of the qubit, we need to design the qubit further from the resonator and try and operate it at the sweetspot, to avoid magnetic and $1/f$ noise.

7.2.3 READOUT FIDELITY MEASUREMENTS

The last measurement performed to characterize the system was the estimate of the readout fidelity. The qubit readout fidelity is defined as 1 minus the average error in estimating the state of the qubit after driving it to a known state. Fidelity

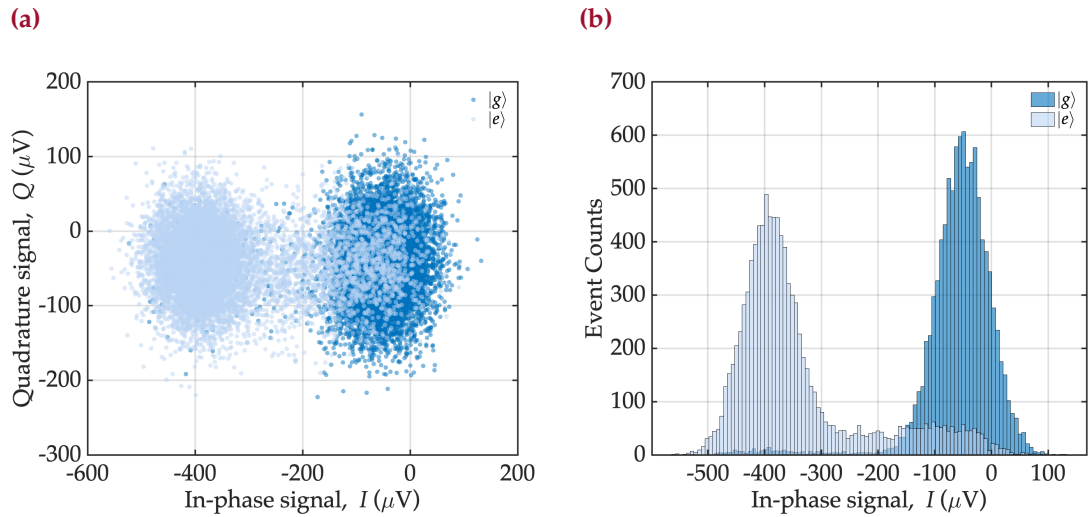


Figure 7.9 | Fidelity measurement. Fidelity was estimated by performing a simple single-qubit gate and correlating the final state with the readout state. In light blue, the measurement after applying an $X_{\pi/2}$ pulse, which would bring the qubit to state $|e\rangle$, in dark blue the non-excited state of the qubit which should be $|g\rangle$. The readout is given by the in-phase signal magnitude (after proper rotation). These value correspond to the fidelity matrix in (7.13)

measurements are strongly dependent on the integration time required to complete the readout protocol, which in this case was 5 μ s.

The measurement consists of an alternation of no pulse and a $\pi/2$ pulse along the x axis to drive the starting state of the qubit from $|g\rangle$ to $|e\rangle$. The measured readout voltages lead to either a readout $|g\rangle$ state or $|e\rangle$ state. The driven states are plotted against the readout states. A threshold voltage to distinguish the states is found that minimizes the overall error, and then the fidelity matrix of states can be built as

$$F = \begin{pmatrix} P(|g\rangle || g\rangle) & P(|g\rangle || e\rangle) \\ P(|e\rangle || g\rangle) & P(|e\rangle || e\rangle) \end{pmatrix} = \begin{pmatrix} 0.961 & 0.112 \\ 0.039 & 0.888 \end{pmatrix} \quad (7.13)$$

The fidelity \mathcal{F} is defined as the trace of the fidelity matrix, hence $\mathcal{F} = 92.49\%$. This is a relatively high value, for a readout frequency of 200 MHz, in particular considering that there is no parametric amplifier in the readout line.

7.3 DISCUSSION

In order to integrate high-kinetic inductance technology within the framework of cQED, it sounded reasonable to start from the conventional approach to get a benchmark of setup and fabrication capabilities making use of a standard aluminum superconducting technology. The qubits performed well, with a best T_1 of roughly

100 μ s and relatively high readout fidelity of 92% for readout time of 5 μ s and for a setup without parametric amplifier. However, dephasing noise currently present the limiting factor for the qubit coherence, as we could only measure a T_2^* of less than 3 μ s. The main reasons for such a low dephasing time seem to be magnetic noise of some kind, also because we are operating the qubit at the shoulder, so any magnetic fluctuation may cause a large frequency shift of ω_q .

To further improve the quality of the qubits, two routes can be followed. First, the fabrication of non-tunable qubits (single Josephson junction) would allow a larger T_2^* as intrinsically less magnetic field noise sensitive. Also, the use of Purcell filters would allow to get large T_1 also at lower detuning, hence reduce magnetic field sensitivity to noise bringing it closer to the sweetspot.

CHAPTER 8

I never think of the future, it comes soon enough.

— Albert Einstein

CONCLUSIONS AND PERSPECTIVES

Superconducting devices exhibit unique properties which make them ideal for a multitude of quantum applications. Among superconductors, high-kinetic inductance material-based devices allow to push even further the limits of the technology, with more compact and higher-impedance devices.

This Thesis presented the potential of high-kinetic inductance superconductors for quantum applications. From the development of the materials required to working sensors and electrical components, dirty superconductors have shown their versatility as platform.

As it happens when working on a full-scale platform, most of the work focused in development and optimization of high-quality devices rather than in their applications. However, there are handful of foreseeable experiments for the near future.

For the Michelangelo process, there are two possible applications once the atomic layer deposition is finalized: the development of a 3D large scale array to be coupled to control electronics, as well as 3D transmon qubit. Exploiting the absence of roughness of the inner walls of the silicon trenches, thin films of superconductors can be used either to connect the top and bottom layer of a Si chip, either to produce in-silicon parallel plate capacitors.

In terms of sensors development, coupling the technology developed in NbN with superconducting TSVs may lead to a scalable multiplexing approach for SNSPDs ready to be coupled with low-power electronics.

Superconducting logic circuit development based on nTrons is the next step in terms of digital electronics based on dirty superconductors. A simple, low power multiplexer operating at 20 mK may impact largely different fields, from sensors

readout schemes to quantum computing applications. On the analog circuit side of the spectrum, high-quality resonating structures in NbN may find their use in quantum computing readout and quantum simulation circuits applications.

Finally, a full-scale qubit based on high-kinetic inductance superconductors may potentially lay bases for a new level of compactness and integration still missing for superconducting qubits.

APPENDIX A

I like the word “nanotechnology”. I like it because the prefix “nano” guarantees it will be fundamental science for decades; the “technology” says it is engineering, something you’re involved in not just because you’re interested in how nature works but because it will produce something that has a broad impact.

— Richard E. Smalley, *Technology Review*, 2001

FABRICATION METHODS

In this chapter are collected all the fabrication processes used during this thesis work, namely for superconducting single-photon detectors, for superconducting microwave and digital circuit components, for the through-silicon vias, and for the transmons. After reporting the process flows, an in-depth outlook of the major technologies used is briefly described.

A.1 PROCESS FLOWS

The process flows were developed in collaboration with the team of the center of Micro- and nanorechnology (CMi) and with the staff of the physics cleanroom at EPFL. While optimized for the facility we had access to, sometimes non-optimal choices are made to properly line-up with the available equipments.

A.1.1 SNSPD PROCESS FLOW

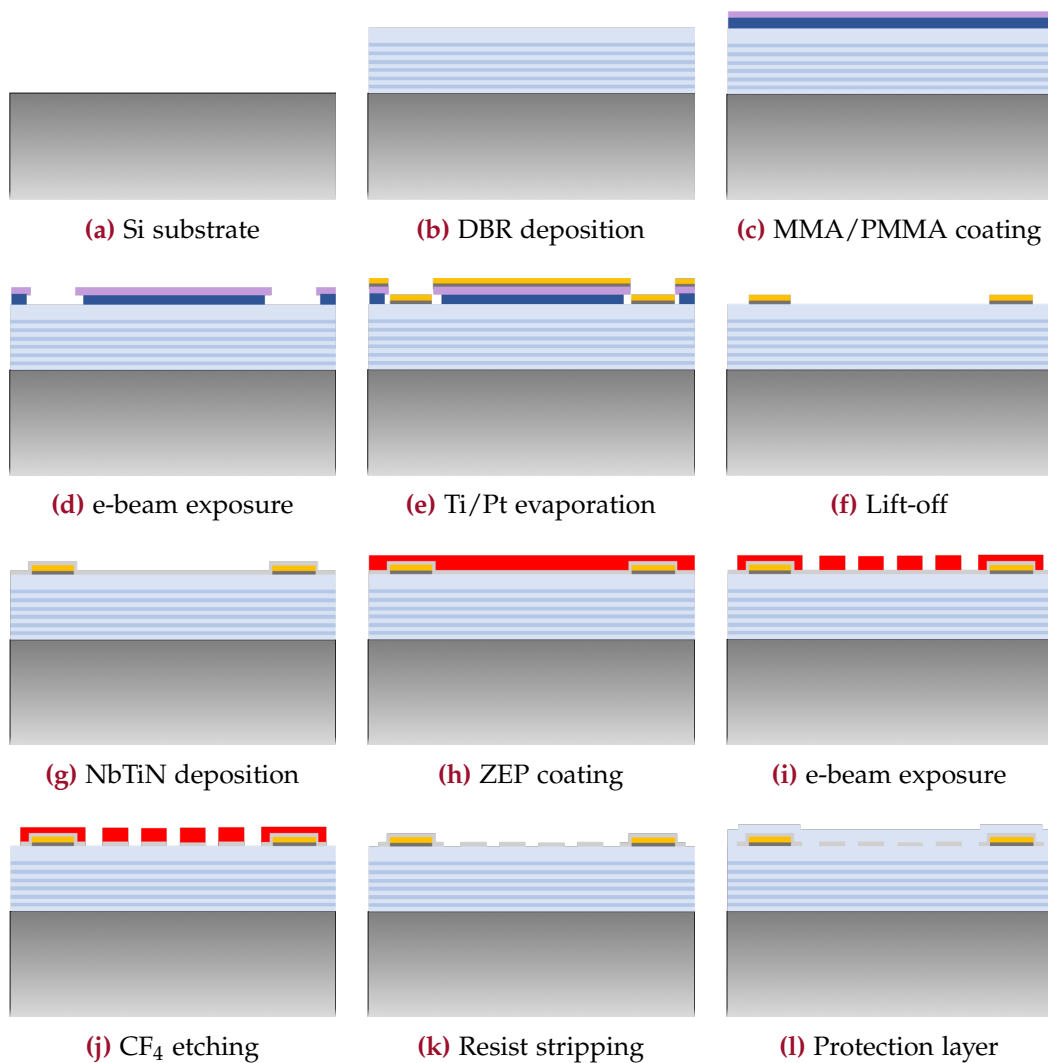


Figure A.1 | Process Flow of SNSPDs. After deposition of a $\lambda/4$ cavity with a Distributed Bragg Reflector (DBR) or with a metallic mirror, follows the evaporation of alignment markers and PADs via lift-off. After cleaning of the substrate, the superconducting material is deposited and patterned via e-beam lithography. Finally, after pattern transfer via plasma etching, the devices are cleaned and covered with a protective layer to avoid ageing.

A.1.2 SUPERCONDUCTING CIRCUITS PROCESS FLOW

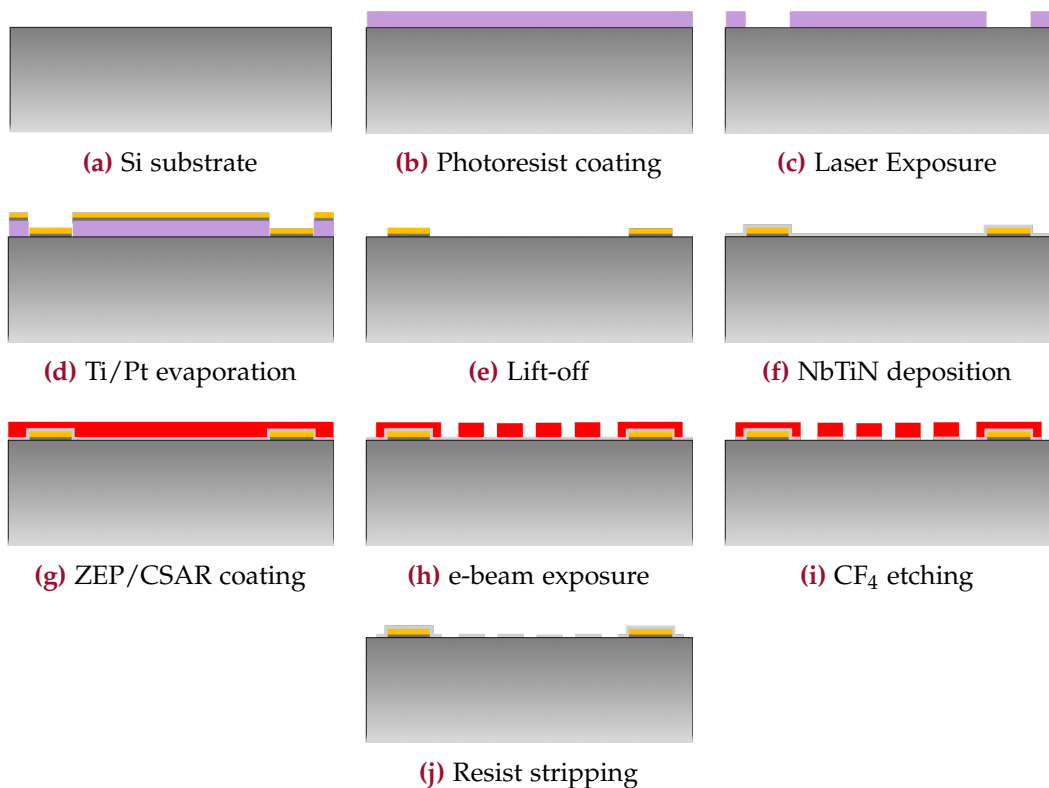


Figure A.2 | Process Flow of Superconducting Circuits. First off, the evaporation of alignment markers and PADs via lift-off and photolithography steps. Then, after cleaning of the substrate, the superconducting material is deposited and patterned via e-beam lithography. Finally, after pattern transfer via plasma etching, the devices are cleaned. No protection layer is deposited as it may influence negatively the internal quality factors of the resonator devices.

A.1.3 THROUGH-SILICON VIAS PROCESS FLOW

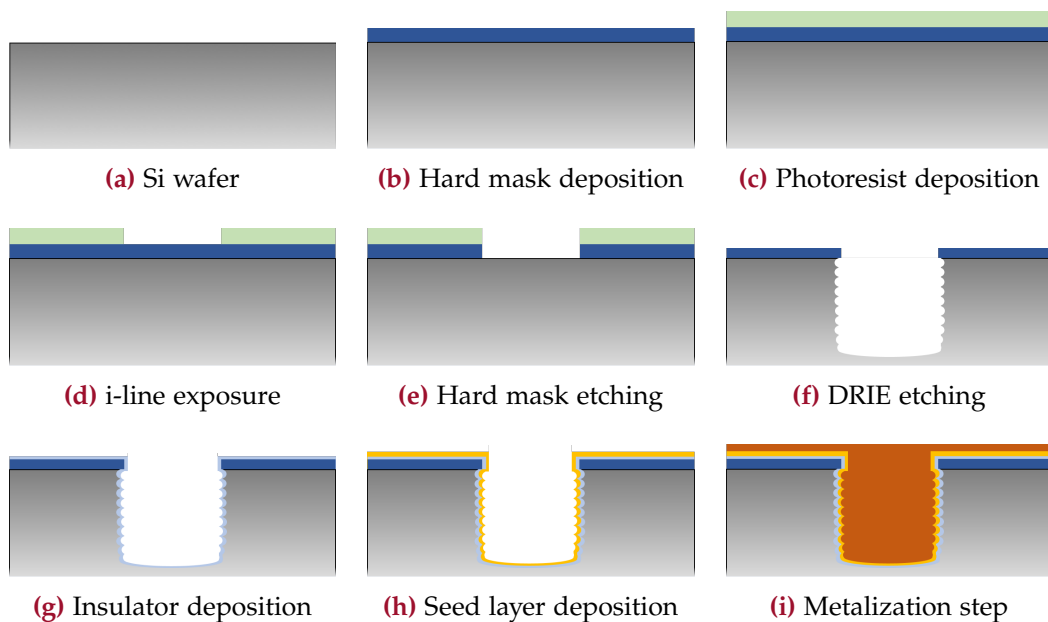


Figure A.3 | Process flow of through-silicon vias. The Silicon wafer is first coated with an hard mask in SiO_2 , which is subsequently patterned and etched. Follows a step of deep reactive ion etching and subsequent insulator deposition via atomic layer deposition. Finally, the metalization step is performed using electroplating after seed layer deposition, usually also achieved by ALD.

A.1.4 TRANSMONS PROCESS FLOW

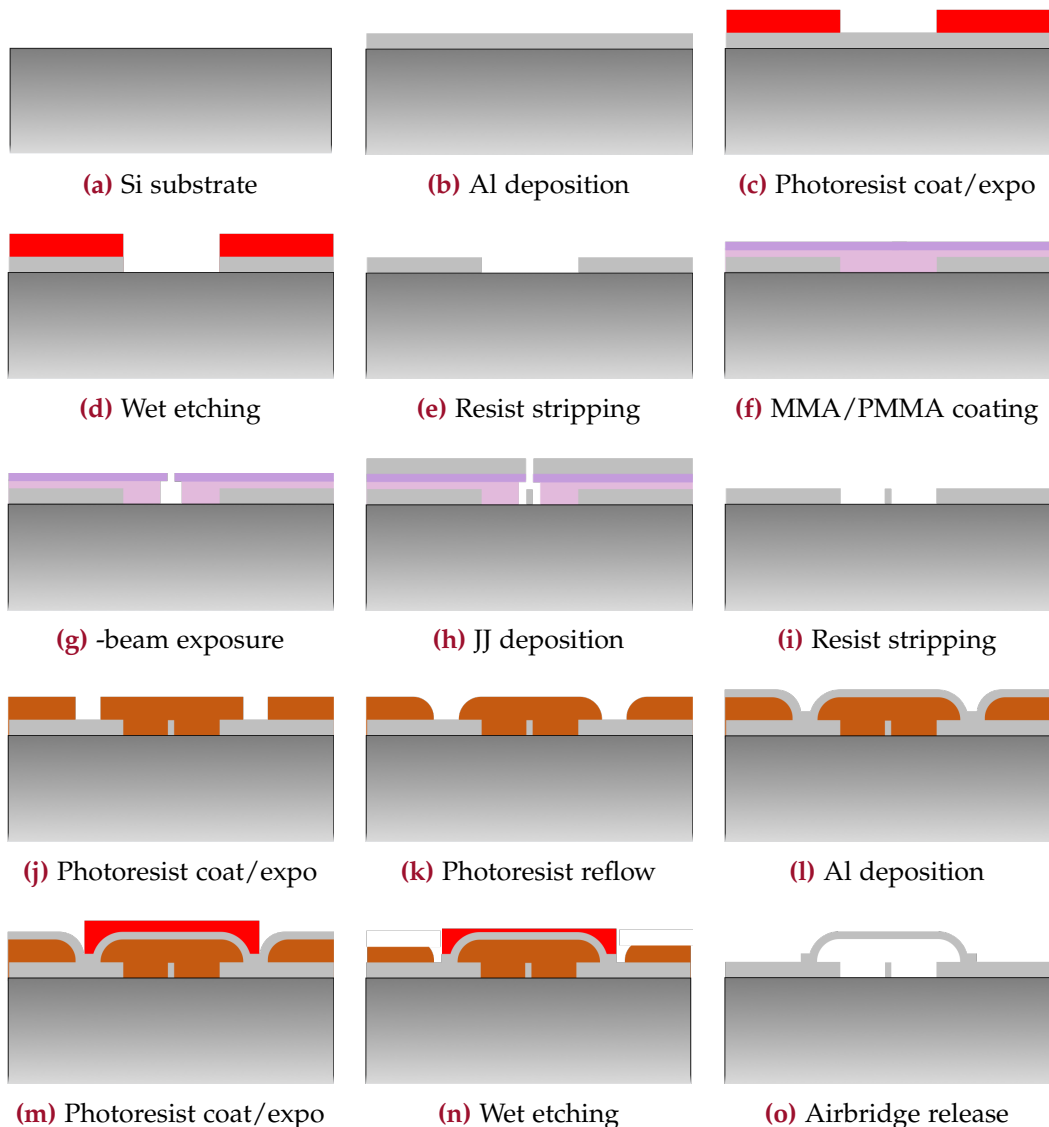


Figure A.4 | Process Flow of Transmons. After deposition of the Al on a clean surface, the ground plane and resonators are patterned via photolithography and etched with a wet etch step. Follows the deposition of the Josephson Junctions via e-beam lithography backed up with evaporation and lift-off steps. Finally, the air bridges are fabricated to ensure good ground stability and dampening of slot modes.

A.2 FABRICATION TECHNIQUES

In the following Section, the main fabrication tools used for this work will be addressed and explained in details. While may result trivial knowledge, the purpose of this Section is to give an overview of the technology and the potential issues behind each process flow.

A.2.1 THIN FILMS DEPOSITION

As shown in [Section A.1](#), all the process flows described in this thesis relies on thin film fabrication methods. Thin films, which generally range from few nanometers to a micron in thickness, can be deposited in different ways. In this thesis, we will focus the attention on two PVD techniques, *i.e.* sputtering and evaporation.

OPTICAL STACK DEPOSITION

The first step of the fabrication process of the SNSPDs ([Subsection A.1.1](#)) is the deposition of the distributed Bragg reflector (DBR), which will be the reflecting component of the vertical optical cavity. The DBR is a periodic structure formed from alternating quarter wavelength stacks of dielectric layers, with alternating refractive index, that can be used to achieve nearly total reflection within a range of frequencies, since each interface between the two materials contributes a Fresnel reflection.

Considering that the range of wavelength we are interested in is the near-ultraviolet (NUV), we chose to use SiO_2 and Ta_2O_5 as materials for the DBR, given the low absorptivity of both materials above 250 nm. The DBR has been deposited using a Kenosistec RF sputtering system.

The DBR layers thicknesses were set to be a quarter wave of the design wavelength, *i.e.* $d_0 = \lambda_0 / 4n(\lambda_0)$. Then, the (n, k) values were provided to a MATLAB code to estimate the reflectivity performance of the mirror which uses classical transfer matrix approach to model the propagation of the wave both in an absorbing medium and at the interface between the two media. The model takes into account both TE and TM polarizations and averages out the two to obtain seemingly-unpolarized reflectivity dependence on the photon angular distribution.

After the fabrication of the DBR, the total reflection was measured using a Varian Cary 500 high performance UV-Vis-NIR spectrophotometer. In [Figure A.5](#)

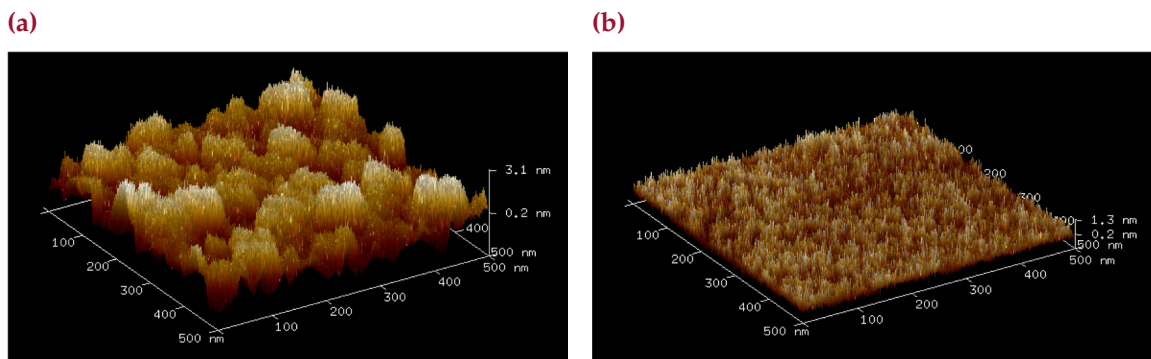


Figure A.5 | Atomic force microscopy scan of the surface roughness of SiO_2 . Fabrication optimization was oriented to minimize surface roughness of the distributed Bragg reflector to increase SNSPDs yield and improve quality factor of the cavity. The roughness of the layer is showed after deposition of 100 nm of material before (a) and after (b) the optimization.

it is possible to see the fabricated DBR. Further information on the reflectivity measurements is reported in [Section 4.1](#). The deviation from the simulated values could be explained in terms of roughness between the layers interface, as well as a non perfectly uniform layer thickness due to fluctuations in growth rate of the material, which could be caused by wear of the sputtering target during the deposition of the DBR. It is worth noting that the fabrication of a 10-bilayer DBR centered at $\lambda_0 = 370$ nm took approximately 16 hours of machine operation time, hence erosion of the target is not to be excluded.

HIGH- L_K SUPERCONDUCTORS DEPOSITION

The high kinetic inductance films were deposited via reactive sputtering or co-sputtering in a Kenosistec RF sputtering system. Detailed characterization of the materials deposited can be found in [Chapter 2](#).

ALUMINUM AND JOSEPHSON JUNCTIONS DEPOSITION

In order to have a controlled oxidation of the barrier layer of Al_2O_3 , Josephson junctions are deposited using a technique called angled evaporation. This technique relies on the use of specific evaporation tools capable of tilting the substrate with respect to the evaporation direction during the process.

EPFL and CMi recently acquired a Plassys angled evaporation system, composed of three chambers: one loadlock, where potential ozone cleanings or ion beam etching process can be run; one evaporation chamber, with base evaporation pressure in the range of 10^{-10} Torr; and one oxidation chamber, where both static or dynamic oxidations can be performed.

The evaporation technique used in this thesis is the Manhattan-style Josephson junction. This technique relies in the partial shading of narrow features when evaporating with a tilt of 45° . By designing openings in a resist of thickness t_r with dimension perpendicular to the evaporation direction narrower than t_r , complete shading is obtained. In a more general sense, it is also possible to design Josephson junctions with three angles evaporation [165], hence skipping the step of patching which usually ensure proper galvanic contact between junctions and qubit/ground.

A.2.2 PATTERNS DESIGN AND LITHOGRAPHY

SNSPDs, nTrons, resonators and qubits were designed by using a custom python code. The python library is based on the gdsCAD¹ package, which allows creating, reading and manipulating GDSII files.

One of the most critical aspects of the superconducting devices fabrication is the quality of the lithography. Given the size of the standard nanowire meanders and the impact that sharp edges have to the switching current [55], the only lithography technique capable of resolution in the order of 5 nm available to us is the electron-beam lithography.

Electron-beam (or more simply e-beam) lithography concept is very similar to the classical lithographic technology: a resist is coated on the chip or wafer and is exposed (by direct writing) by a beam of electrons. The resist is then developed into a chemical mixture which has strong selectivity between the exposed and unexposed areas. Key parameters of the e-beam lithography are electron beam energy and choice of resist. We used a Raith EBPG5000+ e-beam lithography system, which reaches a maximum electron voltage of 100 keV and a maximum writing frequency of 50 MHz.

For what concerns the resists, they have two main parameters: tone and contrast. In a positive tone resist, exposure to electrons means destruction of bonds, which results into absence of resist in the exposed area after resist development, while negative tone means creation of bonds, hence only exposed areas remain after development. The contrast is, instead, related to the resolution of a resist: it is an intrinsic parameter that defines from which dose the reaction starts (D_o) and at which it is completed (D_c); the dose, which for e-beam lithography represents the

¹ <https://pythonhosted.org/gdsCAD/>

amount of charge that needed to clear the exposed area, is commonly expressed in $\mu\text{C}/\text{cm}^2$. The contrast is usually defined as:

$$\gamma = [\log_{10}(D_c/D_o)]^{-1}.$$

The larger the difference between D_c and D_o , the lower is the contrast and then the resolution. In fact, a faster dose curve means steeper developed sidewalls. Low contrast resists are generally used for greyscale patterning.

In the process flows presented in [Section A.1](#), we had to work on two different resists: the bilayer of MMA/PMMA (methyl methacrylate/poly methyl methacrylate) which was used for the fabrication of the PADs, the alignment markers and the Josephson Junctions via lift-off process, and either CSAR or ZEP 502A as high resolution positive resist for the fabrication of the nanowires, as most of the detectors and resonator structures were designed as coplanar waveguides (CPW).

After e-beam lithography optimization, we obtained best results with the bilayer MMA EL9/PMMA 950k A4 for the lift-off process and with the ZEP 502A diluted at 33% for the nanowires. The MMA EL9 was spin-coated at 1500 rpm in order to achieve a thickness of 500 nm, while the PMMA 950k A4 was spin-coated at 4000 rpm for a final thickness of 450 nm. The best design dose for the process was found to be 1600 $\mu\text{C}/\text{cm}^2$. The ZEP 502A was instead diluted at 33% to have a final thickness in the order of 50 nm while spin-coated at 4500 rpm. The design dose for ZEP was strongly design dependent, hence a proximity edge correction (PEC) process was required to obtain optimal results.

HIGH PATTERN-DENSITY OPTIMIZATION

In an e-beam lithography process, electron-scattering induced proximity effects are a well known problem. For this reason, software such as GeniSys BEAMER² have been used to take care of that by adjusting the electron dose according to the pixel surroundings, within a certain, well defined range which is the electron scattering range, which for example for silicon and 100 keV electron beam is in the order of 15 μm . For each pixel, in fact, a different dose is associated depending on the surrounding pattern density, x . This value ranges from 0 in case of a very isolated pattern, to 1 in case of a completely full design, such as at the center of a large PAD,

² <https://pythonhosted.org/gdsCAD/>

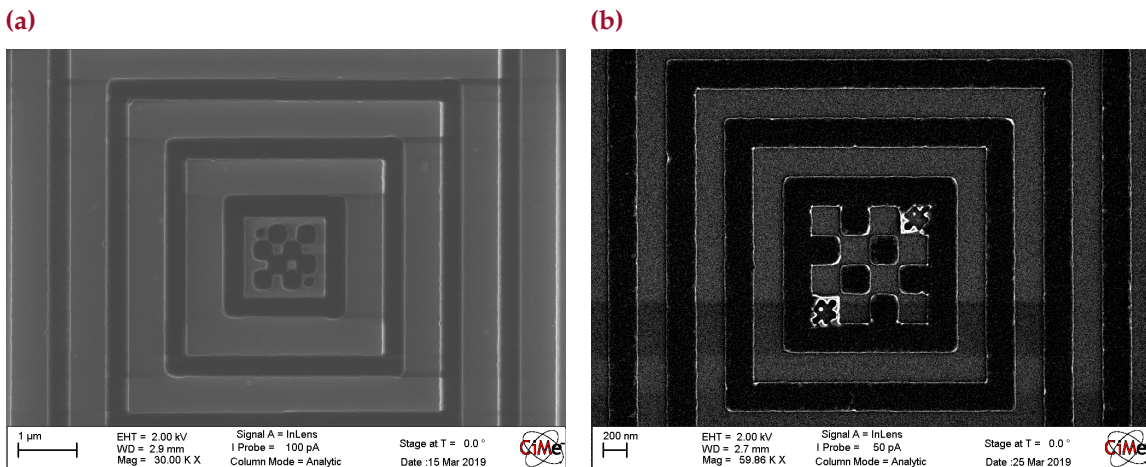


Figure A.6 | Scanning Electron Micrographs of dose test structures on PMMA and ZEP. The high pattern-density dose test were fabricated with both PMMA (a) and with ZEP (b). The PEC lithography parameters for each resist (D_B and η) were obtained from this structures.

for instance. The point spread function PSF of the electron beam, associated to the pattern density x , is:

$$\text{PSF}(x) = \frac{1}{\pi(1+\eta)} \left[\frac{1}{\alpha^2} e^{-\frac{x^2}{\alpha^2}} + \frac{\eta}{\beta^2} e^{-\frac{x^2}{\beta^2}} \right], \quad (\text{A.1})$$

where α is the forward scattering parameter, β is the backscattering parameter, and η is the forward/backscattered energy ratio, and they are determined by the resist and substrate materials.

For simplicity, however, it is possible to approximate the Equation A.1. Given the base dose D_B , which is defined as the dose at 50% pattern density, the forward/backscattered energy ratio η and the pattern density x , it follows that:

$$D(x) = D_B \left(\frac{1+\eta}{1+2\eta x} \right). \quad (\text{A.2})$$

It's easily verified that $D(0.5) = D_B$.

After some optimization with test structure and after testing both PMMA 950k A2 and several diluted versions of ZEP 502A, we obtained that the best results were obtained for the ZEP diluted at 33%. The results are shown in Figure A.6. The difference can be immediately appreciated: the main problem with the PMMA is the resolution of very small features, while its being much cheaper than the ZEP, resulted the perfect resist for larger size features.

A.2.3 LIFT-OFF PROCESS

As we said, after the first lithography follows the lift-off process. The lift-off starts with the deposition of the patterned material, in this case a bilayer of titanium and platinum. The Ti is used to improve the adhesion of Pt on the NbN or NbTiN substrate.

At first, the Ti/Pt bilayer was deposited by means of the Alliace Concept EVA 760 evaporator, which performs very well in terms of film homogeneity and resistivity of the platinum. We deposited 5 nm of Ti and 65 nm of Pt. However, the results were unsuitable for what we required: resist damage appeared on the wafers, causing bad lift-off process. We recognized the case in the high wafer temperature reached during the deposition.

It has to be noted that, since the superconducting ultra-thin film has been already deposited, the temperature of the deposition needs to be controlled and well below 300°C; moreover, melting the resist is a known issue for lift-off process, since damaged resist is much harder to strip off: a whole another reason to keep the temperature as low as possible. For these reasons we moved to the Leybold Optics LAB600H evaporator, which fulfilled all our needs.

We deposited 5 nm of Ti and 65 nm of Pt on the exposed MMA/PMMA or the AZ ECI 3007 on NbN. Then the wafer was immersed in a bath of Shipley Remover 1165 at 65°C for 4 to 6 hours for the lift-off. The results was more than satisfying: we noticed no delamination nor resist damage, all with a good overall pattern resolution.

A.2.4 ETCHING PROCESS

The lithography described in Appendix A.2.2 was used for the patterning of the structures. The pattern is then transferred to the superconductor underneath the resist via physical or chemical etching. In this section, we will focus on the etching processes, which underwent several runs of optimization. Extremely important, as we will see, was the choice of resist for the different etching types.

ION BEAM ETCHING

The physical etching was performed with a Veeco Nexus IBE350 ion beam etcher, which flood exposes the wafer with an argon ion beam. This process was used at the beginning for the NbN and NbTiN pattern transfer. During the NbN etching,

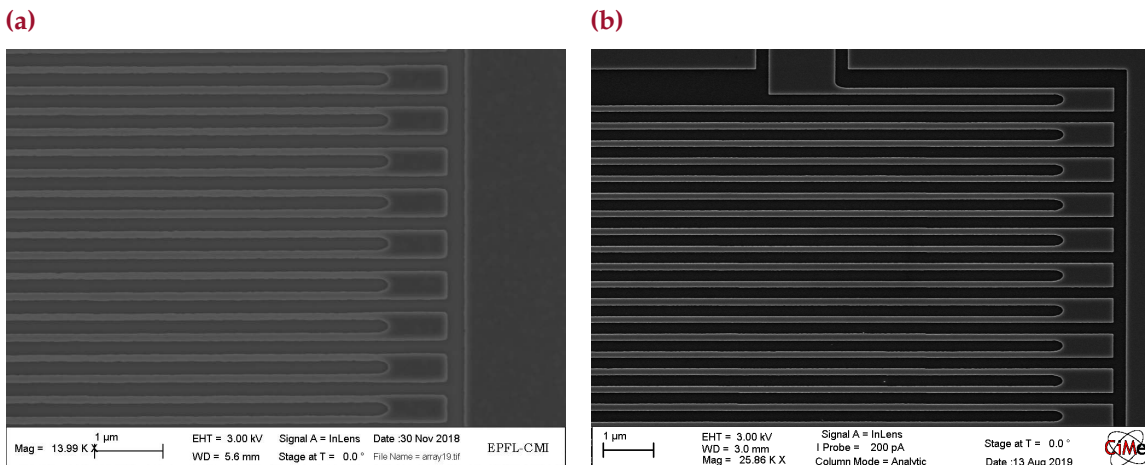


Figure A.7 | Scanning Electron Micrographs of SNSPDs with IBE and RIE. The pixel fabricated with PMMA resist and etched with ion beam etching (a) shows clear residuals of PMMA after the etching due to polarization inversion. On the contrary, by using ZEP etched with CF_4 (b) the quality of the lithography and pattern transfer is much higher.

however, when using either PMMA or ZEP as masking resist, the ion source was heating the resist to the point at which the resist would invert polarity [166]. This is a known effect, documented in the literature for polymethyl methacrylate, and it makes the resist extremely challenging to remove after the etching step. The effect of this unwanted polarity change is illustrated in Figure A.7, where clear resist residuals are fused on top of the nanowire structures.

Another unwanted mechanics was the redeposition of the etched layer on the sidewalls of the resist. This caused, after stripping, "fences"-like structures as high as 40 nm for a 15 nm thick film in the worst case scenario. Overall, Ion beam etching resulted far from optimal for the type of fabrication we needed for the superconducting devices.

REACTIVE ION ETCHING

The chemical etching resulted much more efficient than ion beam etching. Using an Oxford Systems Plasmalab 80, a recipe with low-power reactive ion etching based on CF_4 and Ar mixture chemistry showed very good roughness, slow etch rate which implied good reliability, and good selectivity between either of the e-beam resists and the NbN layer. The silicon was barely affected from the plasma, which is also an important feature when trying to minimize two-level system losses.

However, CF_4 resulted particularly weak in terms of Al etching. For this reason, we tried to develop a recipe using chlorine chemistry based reactive ion etching using a Sentech SI-500 ICP etcher in RIE mode.

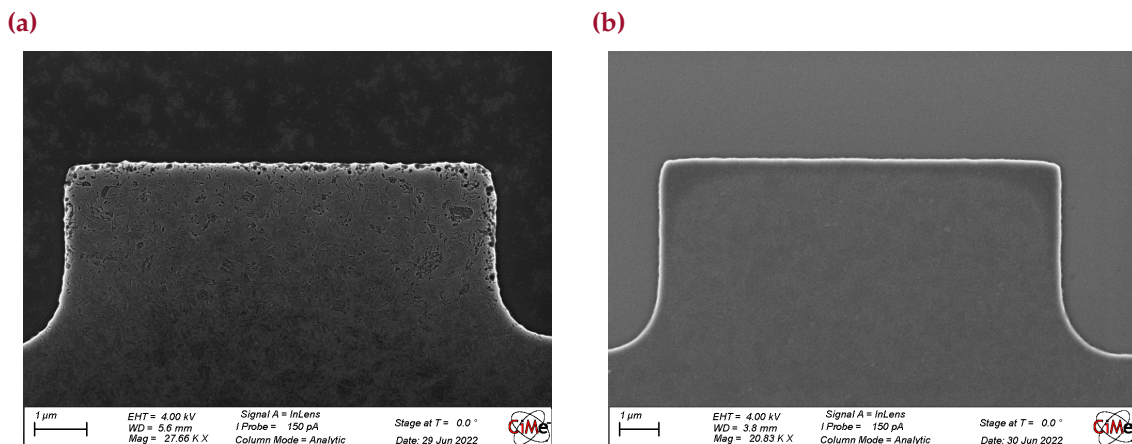


Figure A.8 | Scanning Electron Micrographs of dry and wet etching of Al. The reactive ion etching based on Cl_2/BCl_3 chemistry (*On the left*) creates visible damages both on the Al edges and on the Si substrate. The wet etching with TechniEtch Al80 (*on the right*) on the contrary shows very clean edges and barely affected Si substrate.

While both the etch rate and the roughness were under control at the end of the parameters optimization, the selectivity between Al and Si for the mixture Cl_2/BCl_3 was quite low, resulting in large damage at the substrate level. While for most application the extent of the damage would be negligible, as qubits are extremely sensitive to substrate damage due to TLS losses which may cause loss of the quantum information and cause faster decoherence.

WET ETCHING

The alternative to plasma etch for Al-on-Si etching turned out to be wet etching. Wet etching leads in general to worse process control, as the environment conditions may vary slightly between consecutive etchings, but designing the process with the right amount of margins made it stable enough. We used TechniEtch Al80 from MicroChemicals Inc., a solution of $\text{H}_3\text{PO}_4:\text{HNO}_3:\text{CH}_3\text{COOH}$ in H_2O . The liquid temperature was kept at a controlled value of 30°C , and the wafer was immersed for 3 minutes to etch 150 nm of Al.

The damage on the silicon were completely absent, and while the roughness was limited by both the etching method and the fact that only photolithography resists were usable with this process, it was good enough to etch the main body of the transmon and the readout resonators, which generally had critical dimensions in the order of $10 \mu\text{m}$. A comparison between plasma and wet etching techniques is shown in [Figure A.8](#).

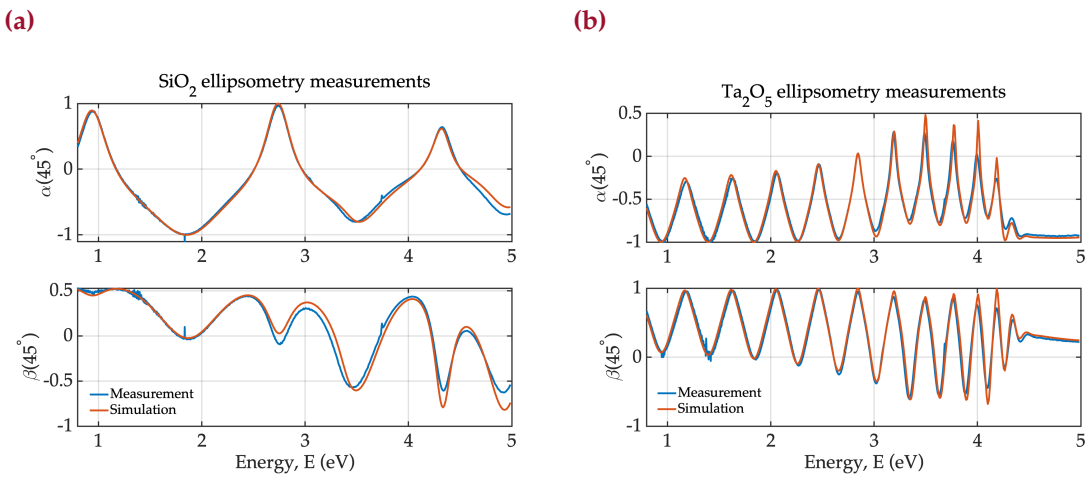


Figure A.9 | Cavity materials ellipsometry results. For transparent films such as the SiO_2 and the Ta_2O_5 used for the optical cavity of the SNSPDs, we used ellipsometry to estimate the (n,k) values. The estimated $n(\lambda)$ and $k(\lambda)$ pairs for each film exhibit a R^2 value of the fitting functions of 99.5% for SiO_2 (a) and 99.8% for Ta_2O_5 (b).

A.3 METROLOGY TECHNIQUES

Several steps of metrology were used throughout the fabrication process to ensure the required quality, and due to the different nature of the several steps, different equipments were used. Scanning Electron Microscopes (SEM), Focused Ion Beam (FIB) systems, Atomic Force Microscopes (AFM), Optical and Mechanical profilometers and reflectometers are type of equipment that can be found in every cleanroom and represent the workhorse of the metrology side of the process flows.

Ellipsometry was a less used technique that we exploited during this thesis work. Thanks to ellipsometry we were able to ensure a stable fabrication process of the thin films used for the DBRs, and both film characterization and simulation were possible.

A.3.1 OPTICAL MATERIALS CHARACTERIZATION

First, thick layers of 500 nm each of SiO_2 and Ta_2O_5 were deposited on a standard silicon wafer. Then the refractive index and the extinction coefficient (n,k) values of the two films as well as the growth rate of the depositions were estimated by means of a Sopra GES 5E spectroscopic ellipsometer. While changing the deposition recipes trying to find the right optical properties, ellipsometry was the sole technique we

used to keep under control roughness, absorption in the NUV, and homogeneity in the films.

APPENDIX B

You cannot spell "cryo" without cry.

— Anonymous

EXPERIMENTAL SETUPS

In this chapter a brief description of the cryogenic systems used is presented. During this work, as reported in the main body of the thesis, we relied mostly on two cryogenic setups: the PhotonSpot and the BlueFors cryostats.

B.1 CRYO-OPTICAL SETUP

The PhotonSpot arrived in AQUA on December 2019 and was installed in January 2020 in EPFL as a temporary solution due to issues in Microcity. After the first COVID-19 pandemic breakout, in June 2020, it was moved in Microcity in Neuchâtel.

The PhotonSpot setup was designed to fill the requirements of the SNSPD, with base temperature just below 1 K, optical access to the fridge both via optical fibres and via free-space access through a window. Below follows the description of the system from the cryogenic, electronics and optics perspective.

B.1.1 ^4He SORPTION CRYOCOOLER

The PhotonSpot system is a customely designed cryogenic system based on a CryoSpot¹ baseline. While the fabrication of the metallic parts was made in Monrovia, California, the design was implemented in collaboration with Dr. Vikas Anant. The system consists of a Cryomech PT415 pulse tube cryocooler to reach liquid helium temperature with a nominal excess cooling power of 1.5 W at 4.2 K (upgraded from the standard PT403 which provides only an excess cooling power

¹<https://www.photonspot.com/cryogenics/cryospot4>



Figure B.1 | PhotonSpot cryostat. The cryogenic systems within the PhotonSpot consist of a pulse tube cryocooler, to bring the system down to 3 K, and a ^4He sorption cryocooler, to cool the cold plate down to 800 mK. The advantages of such a system is the time of cooldown, which is in the order of 2h to reach 3 K and 12h to reach base temperature, and the advantage that being a closed-loop system there is no consumption of cryogens required.

of 0.25 W). A PhotonSpot Freeze4 ^4He sorption cryocooler cools down the cold plate to 850 mK. The whole system is fully closed-cycle, hence there is no consumption of liquid cryogens.

The cryostat consists of three thermalization plates: 40 K stage, 4 K stage and cold plate. Classical cooldown cycle consist of three phases. The first phase is the cooldown of the system to 4 K. The system is pumped into vacuum ($p \leq 5 \times 10^{-3}$ Torr) and the pulse tube is switched on; the two upper stages reach temperatures of around 50 K and 10 K within 3–4 hours. The cold plate however, which is very well thermally insulated by the 4 K stage by design, cools down to 4 K in around 12–16 hours. Usual case is that after 16 hours the two main plates are at nominal temperatures (32 K and 3.1 K) and the cold plate is at 3.1 K.

The second phase consists in condensing the helium into a bath. In order to do so, a pump heater (a charcoal installed inside the sorption unit) is locally warmed up to 40 K to let all the ^4He trapped in it to evaporate and condense elsewhere, *i.e.* in the bath, which is the terminal part of the sorption unit connected to the cold plate. Being the cold plate below 4.2 K (evaporating temperature of ^4He , the bath is generated. This step is called "regeneration".

Once the bath is fully regenerated (takes around 1 hour) the third phase can begin. At this point, the charcoal heater is turned off, and by cooling down it behaves as a pump, condensing the ^4He on its surface: this causes more helium evaporated from the bath to be condensed in the charcoal, causing a drop in pressure which, which in turns cools down the bath. Eventually, equilibrium is achieved when the pump is cooled down below 4.2 K and the bath reaches 800 mK. The weak thermal contact between 4 K stage and cold plate allows the two temperature to stabilize. However, due to structural reasons, some sort of thermal contact between the cold plate and the 4 K stage still exists, hence this heat load, together with other heat sources, *e.g.* radiative heat load, is balanced by evaporation of more ^4He in the bath. The amount of unwanted heat load sets the cold time of the firdge, as the ^4He bath eventually fully evaporates, letting the cold plate warm back up to 3.1 K. This phase is called "evaporation" phase.

Because of the nature of this process, the bath has to be regenerated every once in a while. Thanks also to the extra power at the 4 K plate stage, which allow for a more efficient evaporation phase, the overall cold time before regeneration of the bath was in the order of 36 hours, a very good achievement despite the large cold plate size. This allowed us to schedule via software a "forced" regeneration and evaporation step every early morning, so to have the system operative during the days.

B.1.2 ELECTRONICS

Before going into the details of the equipment used to perform measurements, let us first discuss the wiring of the cryostat. The system has 27 DC lines (custom made post delivery), which were assembled using either phosphor bronze or manganin wiring (WQM or WMW series respectively, LakeShore Inc.) and breakout connections at every stage with three 9-pin micro-D connectors (M83513 series, Amphenol) thermally anchored to ensure signal thermalization. These lines were mostly used to either run powering up of either test CMOS chips operating at the

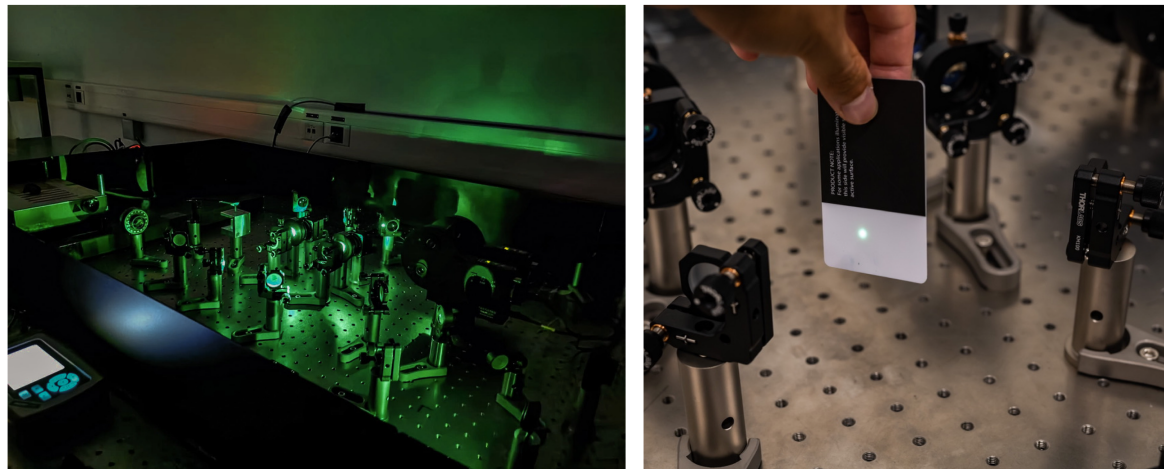


Figure B.2 | PhotonSpot optical table. Classical view of the optical table during measurements.

4 K stage for other projects, HEMT amplifiers (CITLF1 series, Cosmic Microwave Technology Inc.) or thermometers used to estimate locally the temperature of the devices (Cernox series, LakeShore). For high-frequency measurements, the system was equipped with 16 RF lines in CuNi alloy, which is known to be both a good conductor and a good thermally insulative material in the range 40 K–1 K. The lines were not attenuated as SNSPDs require to be biased with DC current, which would cause dissipation at each thermalization stage.

For what concerns the electronics, the system was equipped with a Source and Measurement Unit (B2902A series, Keysight) to perform DC biasing of the devices; an ultrafast oscilloscope (DPS75004SX series, Tektronix) which can be used either as a 2 channels system with 50 GHz bandwidth and 200 GS/s sampling rate, or as a 4 channels system with 33 GHz bandwidth and 100 GS/s sampling rate; several power supplies to power up the amplifiers; a 225 MHz Universal Frequency Counter (53131A series, Hewlett-Packard).

All the equipment were controlled remotely by custom written python codes to run the experiments.

B.1.3 OPTICS

The cryostat was equipped with two possible light paths to bring lasers in the system: either with single-mode optical fibres (SMF-28 series, ThorLabs) which are designed to operate in the telecom wavelength range (1260–1650 nm) or with direct optical access via a 1" window. In order to avoid thermal radiation in the system which would cause the base temperature to rise above 850 mK, we used

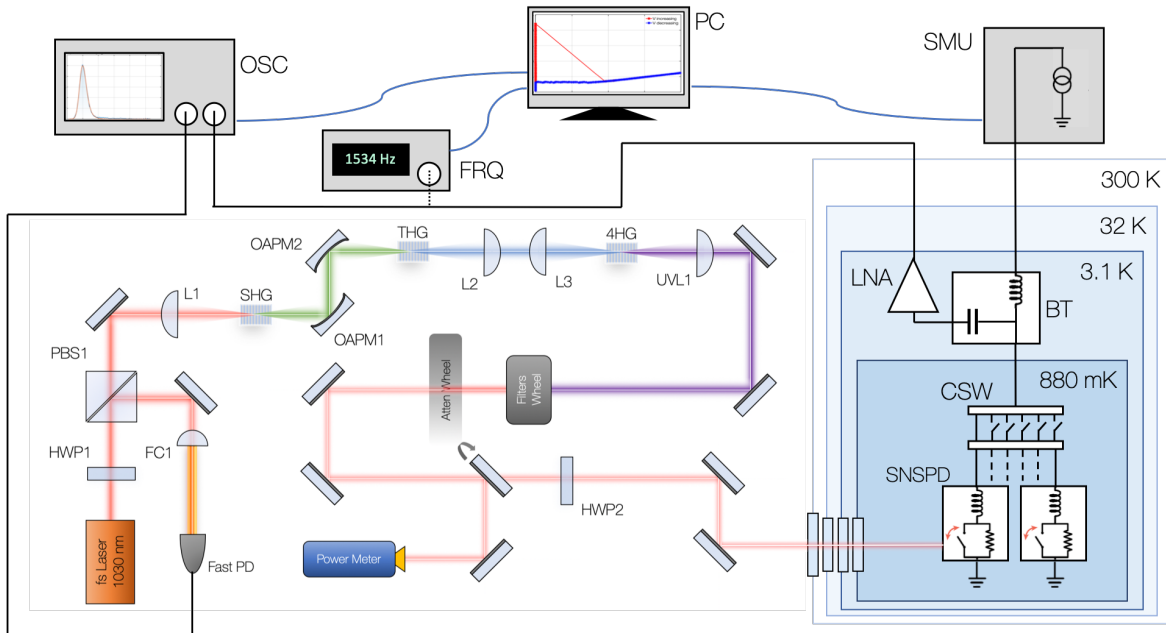


Figure B.3 | PhotonSpot setup. The overall setup consists of three main parts: the cryogenic, the optical, and the electrical. The cryogenics components are included in the cryostat, with the microwave switches, low-noise amplifier and cryogenic bias tee. The optical setup consists of the main laser emitting at 1030 nm wavelength, which is coupled to a second, third and fourth harmonics generation (SHG, THG, 4HG) optics, filters and attenuators to control the power and the transmitted wavelength and a fast photodiode to use as electrical reference pulse. The most used electrical components are the oscilloscope, power supplies, a frequency counter, and a source-measurement unit.

uncoated BK7 windows (WG11010 series, Thorlabs) which have low transmission at MIR wavelenghts and above ($\lambda \geq 10 \mu\text{m}$).

The optical setup was placed nearby the PhotonSpot cryostat on a large optical table and coupled to the system either via fibres or in free-space. A schematic of the system is shown in [Figure B.3](#)

We used a Origami 10-100, free space coupled laser from NKT as our main source of light to test the detectors, as it was a cheap but powerful solution to obtain femtosecond laser pulses with enough power to saturate our detectors. The specs of the laser are presented in [Table B.2](#).

As the main interest of our detectors is quite broadband, from NIR to NUV wavelengths, we built a second, third and fourth harmonic generation setup to shorten the laser wavelength and to get an overall range for NIR at 1030 nm, VIS at 515 nm, and NUV at 343 nm and UV at 257 nm, while keeping the sub-picosecond pulse width resolution.

Second, third and fourth harmonic generation (SHG, THG and 4HG) were obtained by means of nonlinear photonic crystals. In non-linear crystals the light undergoes a resonant effect which ends up into absorption of two photons with a

Table B.1 | Nonlinear Crystals

Harmonics	Manufacturer	Type	Θ	Φ	Thickness
SHG	Oxide Corp.	LBO, type I (ooe)	90°	13.8°	2.8 mm
THG	Oxide Corp.	BBO, type II (oee)	62°	90°	0.8 mm
4HG	Eksma Optics	BBO, type I (ooe)	50°	90°	0.3 mm

Specifications of the nonlinear crystals used for SHG, THG and 4HG.

certain frequency, and emission of a single photon with the sum of the frequencies, hence shortening the wavelength. As it is a strongly nonlinear effect, the larger is the photon density in the crystal, the higher will be the probability and the conversion efficiency of the pumping wavelength into the output wavelength. Good quality lenses are necessary to achieve very high photon concentration by focusing the beam into diffraction limited spot size and generate enough output photons.

For the second harmonic generation, we used lithium triborite (LiB_3O_5 , or LBO) as nonlinear crystal, with $\Theta=90^\circ$, $\Phi=13.8^\circ$, and thickness of 2.8 mm. LBO is a type I (ooe) nonlinear crystal: this means that, in order to satisfy the critical phase-matching, two photons having ordinary polarization with respect to the crystal will combine to form one photon with double the frequency and extraordinary polarization.

For third harmonic generation, we used barium borate (BaB_2O_4 , or β -BBO) type II (oee) crystal, with $\Theta=62.8^\circ$, $\Phi=90^\circ$, and thickness of 0.8 mm: two photons having orthogonal polarizations will combine to form one photon with the sum of the frequencies and ordinary polarization, hence one 1030 nm photon and one 515 nm photon will combine into a 343 nm photon. As the SHG crystal is a type I crystal, the polarization of the 1030 nm and the 515 nm will already be orthogonal, so there is no need for a $\pi/2$ rotation (achievable by means of a half wave plate) to satisfy the critical phase-match condition.

In order to ensure space and time superposition of such short optical pulses, using achromatic lenses would not be enough as they usually introduce a time-walk delay given by the refractive index difference between 1030 nm and 515 nm in the lens medium. For this reason, we used off-axis parabolic mirrors, which despite more challenging to align than normal lenses, are intrinsically achromatic

Table B.2 | Origami 10-100 Specs.

Specification	Value
Central Wavelength	1030 ± 2 nm
Repetition Rate	100 ± 2 MHz
Pulse Duration	≤ 200 fs
Average Power	≥ 200 mW
Beam quality	$M^2 \leq 1.1$
Timing Jitter	≤ 30 fs rms

Specifications of NKT Origami 10-80 laser.

and introduce negligible time delay and cross-polarization due to their external protective coating.

Finally, for the fourth harmonic generation, an optical setup similar to the one of the second harmonics was used. We used again a β -BBO type I (ooe) crystal, with $\Theta=50^\circ$, $\Phi=90^\circ$, and thickness of 0.3 mm. It was necessary to keep in mind that common glass such as BK7 absorbs at 257 nm wavelength, hence UV silica was used. For this reason, UV-transparent lenses and UV-enhanced mirrors were utilized. When using the 4HG wavelength for SNSPDs characterization, the cryostat windows (commonly in BK7) were substituted to UV-silica to ensure good light transmission in the 257 nm range.

After the harmonics generation, the collimated beam crosses path with a filter wheel remotely controlled which had the scope to select the wavelength used for the testing. Finally, another filter wheel with 12 ND filter had the scope to control the light power to ensure single-photon regime for the SNSPD operation. For this, a power meter was placed in line of a remotely controlled flip mirror to close the feedback loop with the attenuators wheel system.

Lastly, an half-wave plate was placed on the beam path in order to control the polarization, if required, manually. A focusing lens was placed before the cryostat to focus the beam on the detectors.

B.2 DEEP CRYOGENIC TEMPERATURE SETUP

The BlueFors LD-250 system was installed in the late spring 2020 in EPFL with the scope to be used as platform for testing quantum computing related chips.

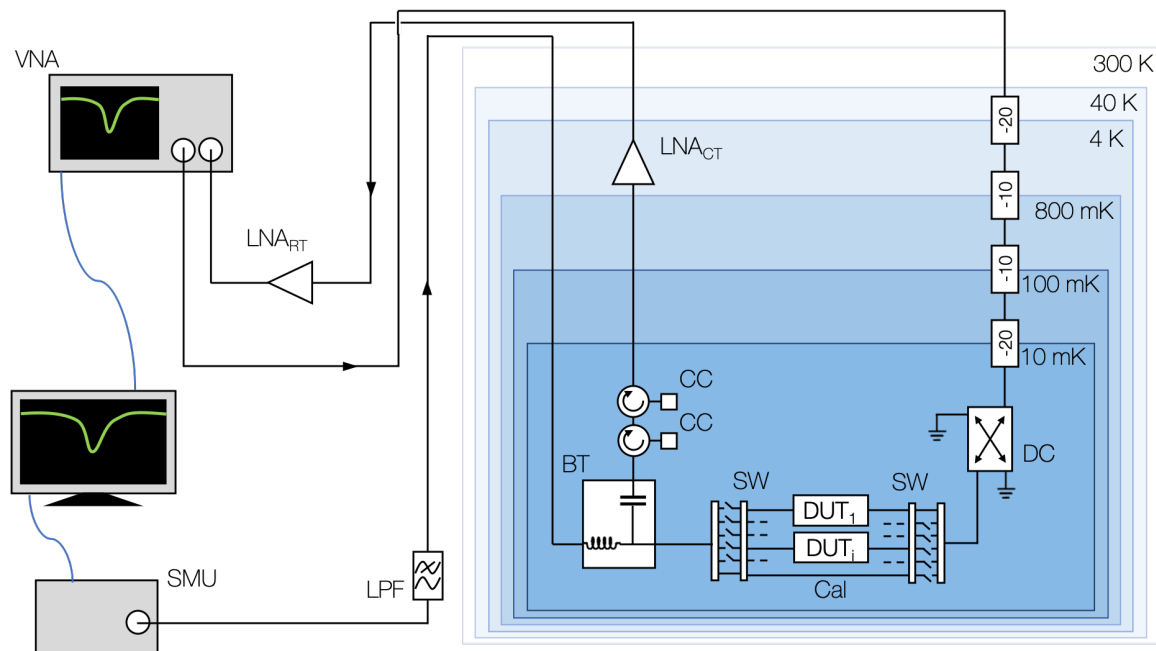


Figure B.4 | BlueFors setup. The cryogenics of the BlueFors system is much more complicated than the one of the PhotonSpot, hence allows to achieve a much lower temperature of 10 mK at base. Due to the type of measurements performed in the system, most of the input lines in the cryostat are attenuated to reduce the number of hot radiation reaching the devices. The system also includes a low-noise amplifier operating at 4 K and circulators to cut-out electrical noise coming from it. Outside the fridge, usual electrical components are the source and measurement unit and the vector network analyzer.

The system was shared with Prof. Moll's headed Quantum Materials Laboratory and was installed in one of their lab. Below follows a brief description from the cryogenic and electronic perspective.

B.2.1 ^3He - ^4He DILUTION REFRIGERATOR

Differently from ^4He sorption cryocoolers, dilutions refrigerators exploit thermal cycles of a particular mixture of liquid ^3He and ^4He to achieve extremely low temperature. A well optimized system can reach base temperatures below 10 mK, as in this case.

A dilution fridge consists of five stages: the 40 K and 4 K stages, which are the same of the sorption fridge and which temperatures are set from the pulse tube; the still plate stage, where ^4He condenses and reaches a temperature between 1 K and 800 mK at regime operation; the cold plate stage, where a first mixture of ^3He and ^4He (high in concentration of ^3He) is condensed to a temperature of the order of 100 mK; and finally the mixing chamber stage, where the lowest temperature is achieved, usually in the range of 5–20 mK.

The operation principle of a dilution fridge is much more involved than the one of the sorption fridge, hence we suggest any interested reader to refer to [167] for a more exhausting explanation. After cooling the whole system down with the pulse tube (PT420, Cryomech), which usually takes around 24 hours due to the size of the cryostat, the ^3He and ^4He is let in the dilution unit and begin condensation. While at the beginning only ^4He condenses due to the temperature being above ^3He evaporation temperature, by pumping on the bath with a scroll pump and a turbopump it is possible to reduce the base pressure of the system, causing a drop in temperature of the bath. Due to the physics of ^3He and ^4He mixture which we will not describe here, the mixing chamber reaches base temperature of 10 mK after few hours. At that point, the system is ready to be used without need of regeneration and evaporation steps, as the circulation keeps pumping on the He keeping it cold.

B.2.2 ELECTRONICS

The BlueFors system came with four feed lines connected all the way between MXC and room temperature, and six lines connected only between the 4 K stage and MXC. The first bundle was split in two attenuated lines in CuNi, thought as input lines, and two not-attenuated lines, one fully in CuNi and one in CuNi (between 40 K and 4 K stages) and NbTi (from 4 K and MXC), which were thought as output lines. The second lines bundle was originally thought to be connected to an FPGA to control cryogenic electronics, and all the lines were attenuated and in CuNi. To make the system experiments-compatible, we had to add to the system cryogenic amplifiers, filters, coldfingers and switches.

At the 4K stage, we added two broadband, low-noise cryogenic amplifiers (LNF-LNCo.3-14A, Low Noise Factory), with a nominal bandwidth range at 4 K operating temperature ranging from 300 MHz to 14 GHz and a noise equivalent temperature T_{noise} of 4.2 K. The amplifiers were optionally connected to a bias-tee (ZFBT-4R2G+, Mini-Circuits) at the MXC stage to allow DC biasing of the resonating devices to tune the kinetic inductance (see [Section 6.3](#)).

At the MXC stage, we added a double junction, 40 dB insulation circulators (LNF-ISISC4-12A, Low Noise Factory) to screen the devices from the noise coming from the amplification stages. We decided to add two cryogenic switches (R591723605, Radiall) to increase the number of samples available for testing per cooldown. This

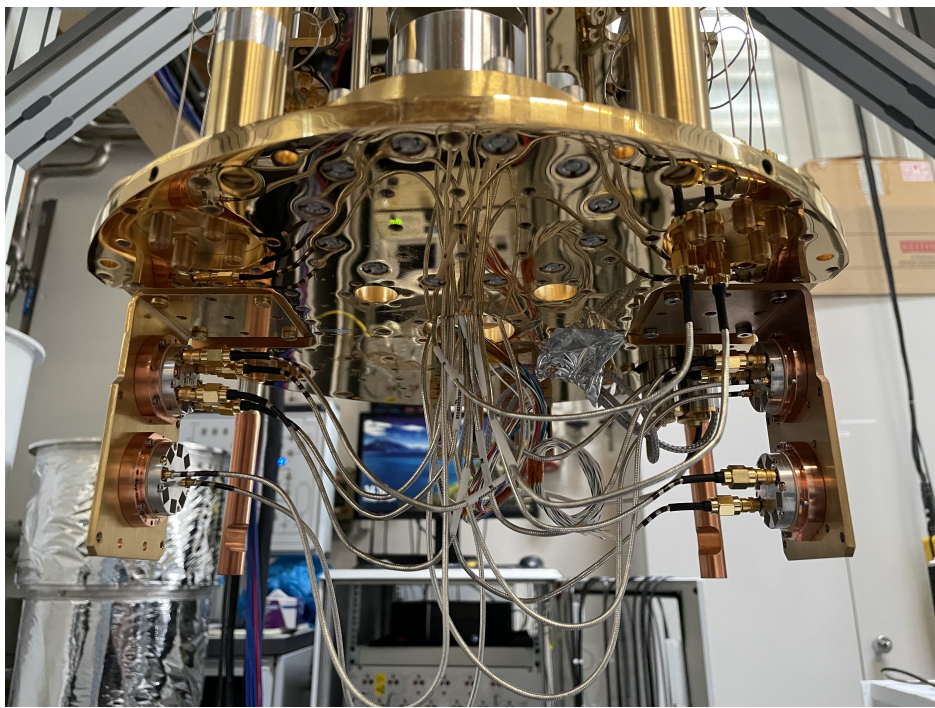


Figure B.5 | BlueFors cryostat. Picture showing the conventional cooldown organization inside the fridge.

way we could test up to six samples in transmission and in reflection by relying only on two cryogenic amplifiers (see [Figure B.4](#)).

For what concerns the electronics required to operate the devices, we used mostly power supplies, a source-measurement unit (SMU, SourceMeter2604B series, Keythley), and a vector network analyzer (VNA, ZNA26 series, Rohde & Schwartz).

For the qubit measurements which are presented in [Chapter 7](#), we used the setup of Prof. Scarlino, head of the Hybrid Quantum Circuits Laboratory (HQC) in EPFL. In order to operate and characterize qubits, it is required to have in the setup a arbitrary waveform generator (AWG) and digitizer (ADC) systems, mixers for up- and down-conversion of the signals and high-frequency sources, which we did not have at the time.

B.3 EXPERIMENTS CONTROL SOFTWARE

All the experiments were performed and controlled via custom python software. A graphic user interface (or GUI) was developed to automate and simplify the experimental experience. The lab computers connected automatically via software to the hardware necessary to perform the experiments, such as power supplies,

voltage sources, voltmeters, oscilloscopes, VNAs and so on. The connection was provided by GPIB (IEEE 488) or LAN connection, and the communication channel was opened by using the pyvisa library for python.

A multitab GUI was designed², allowing the user to choose which experiment to run and, eventually, organize and launch a series of experiments in the automatic mode. The automatic mode allows the user to select how many and which experiments to run, in which order, and with which interval, basically running autonomously overnight if necessary and screening all the devices.

The software interfaces via LAN or GPIB the hardware necessary to perform the experiments, such as source/measurements units (SMUs), power supplies, voltmeters, optical wheels for filtering and attenuating the optical signals on the otpical table, vector network analyzers (VNAs), oscilloscopes.

The cryogenic switches were controlled by means of a python controlled Lin-duino Uno (DC2026, Analog Devices) connected to two analog multiplexers/switches (ADGS1408, Analog Devices) via SPI interface. The switches, working as relays, allowed fast channel switching while ensuring minimum amount of heat generated inside the cryostat thanks to the relatively fast electronic shutters and controlled pulse length.

B.3.1 MEASUREMENT OF T_C

The films thicknesses were obtained by a quick lift-off process followed by Atomic Force Microscopy (AFM). The aim thickness for the test was 15 nm thick films. To measure the critical temperature, the bare films were glued on a copper support with PMMA and wire-bonded to a custom PCB. The PCB line was connected to a 10 k Ω resistor that served as low-noise biasing resistance for the source measurement unit (SMU). The copper support was then mounted on the 3 K stage of the PhotonSpot system (more info on the setup in [Appendix B.1](#)) with very low thermal contact with the 3 K plate. On the support were installed both a heater and a ruthenium oxide resistive temperature device. The mount was slowly heated up to ensure homogeneous thermalization of the entire support, and the resistance of the film was sampled by means of the SMU. The current used to sample the film resistivity was 10 nA, to ensure the condition of being below the critical current density while ensuring enough signal for the SMU to see the superconducting transition. In order to take into account gradients effects, the measurement was performed both

² with the help of Sébastien De Bros, EPFL Master student whose semester project was to integrate existing experiment routines into a single GUI software

warming up and cooling down around the critical temperature, where both the heating and cooling rate were checked by feedback controlling the heater power, to ensure no thermalization bias.

C

APPENDIX

While drawing I discover what I really want to say.

— Dario Fo

CHIP GALLERY

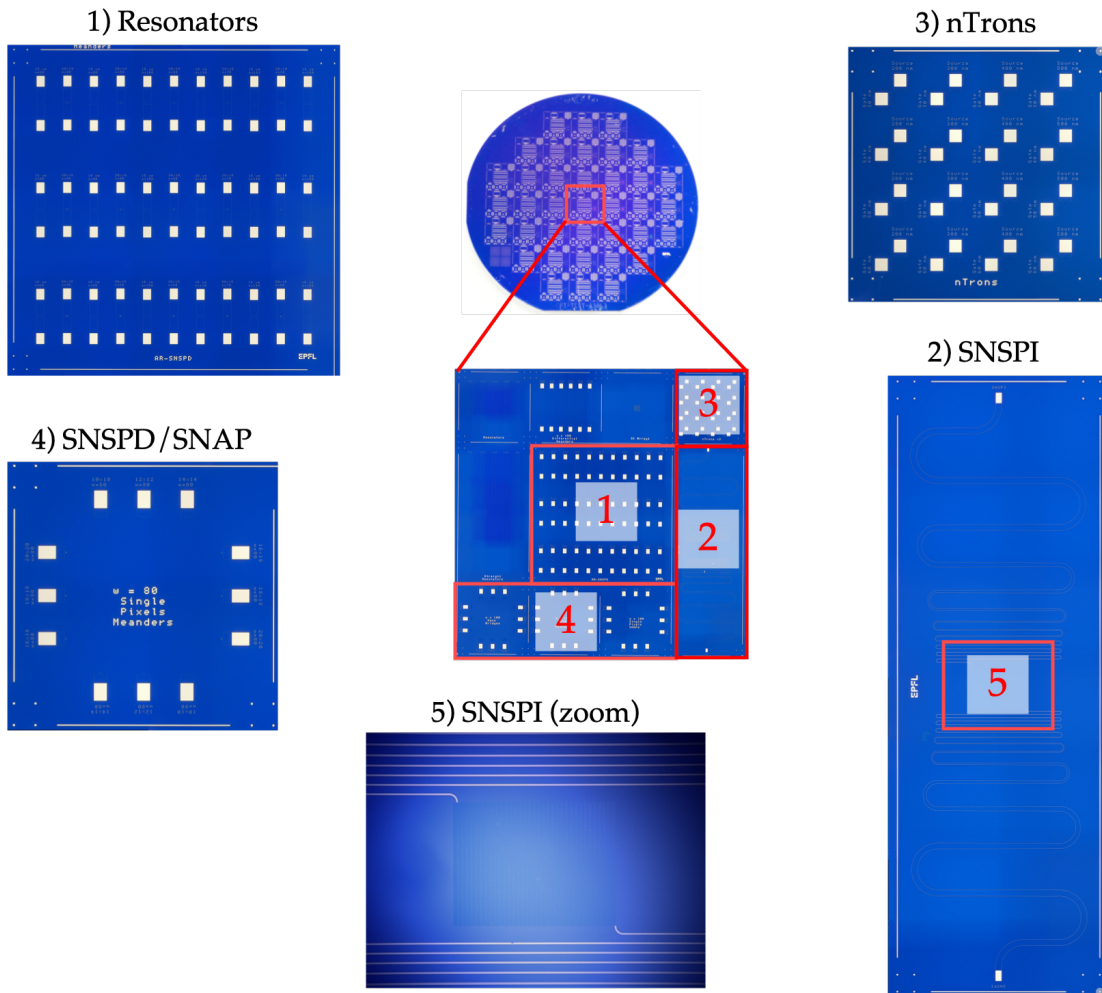


Figure C.1 | Full-scale wafer. Wafer containing multiple devices (SNSPDs, nTrons, SNAPS, SNSPIs, testing resonators). The NbN was deposited on a 100 nm thermal oxide insulating layer on a 100 mm Si wafer, which gives it the characteristic the blue color.

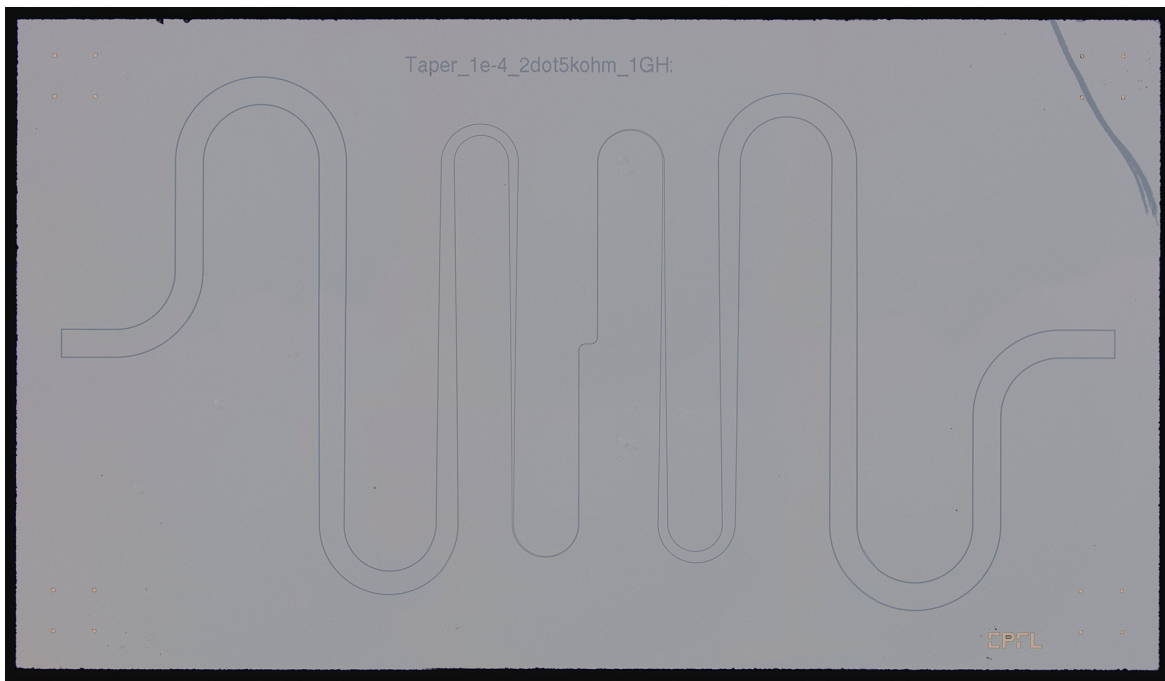


Figure C.2 | Impedance matching taper. $7 \times 4 \text{ mm}^2$ chip with a impedance matching taper. The device was made out of high- L_k NbN with $90 \text{ pH}/\square$ on high-resistivity Si wafer. The taper has a nominal bandwidth frequency of 1 GHz and impedance matching terminations at $Z_1 = 50 \Omega$ and $Z_2 = 2.5 \text{ k}\Omega$.

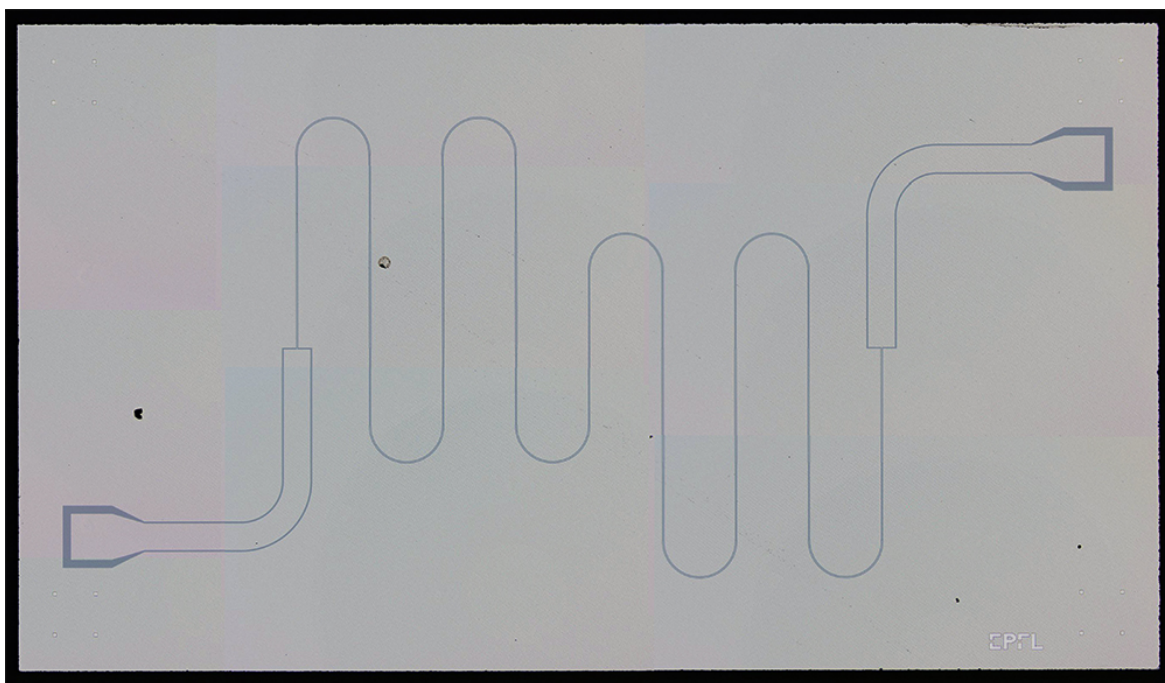


Figure C.3 | Microwave stepped impedance filter. $7 \times 4 \text{ mm}^2$ chip with a microwave stepped impedance filter. The device was made out of high- L_k NbN with $90 \text{ pH}/\square$ on high-resistivity Si wafer. The filter has a nominal bandwidth frequency of 6 GHz, a $\lambda/2$ section at the center of the structure surrounded by seven pairs on each side, and impedances of $Z_1 = 450 \Omega$ and $Z_h = 900 \text{ k}\Omega$.

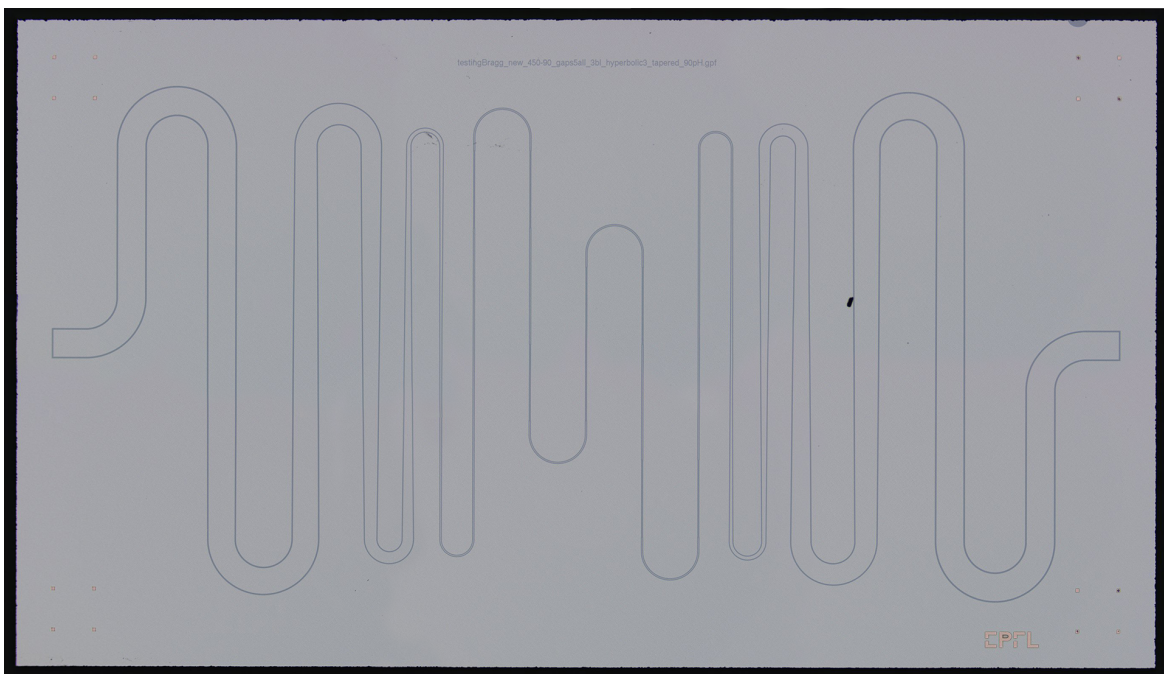


Figure C.4 | Impedance matching taper coupled to a microwave stepped impedance filter. $7 \times 4 \text{ mm}^2$ chip with an impedance matched microwave stepped impedance filter. The device was made out of high- L_k NbN with $90 \text{ pH}/\square$ on high-resistivity Si wafer. The filter has a nominal bandwidth frequency of 6 GHz, a $\lambda/2$ section at the center of the structure surrounded by three pairs on each side, and impedances of $Z_1 = 300 \Omega$ and $Z_h = 900 \text{ k}\Omega$. The taper couples the terminations of $Z_1 = 50 \Omega$ and $Z_2 = 300 \Omega$ with a design bandwidth frequency of 500 MHz.



Figure C.5 | Hanged resonators. $7 \times 4 \text{ mm}^2$ chip with the test structures resonators used for film characterization. The two feedlines are coupled to either seven 500 nm wide resonators or 250 nm wide resonators in hanged configuration. The specific chip was designed to impedance match films with an expected kinetic inductance of 60 pH.

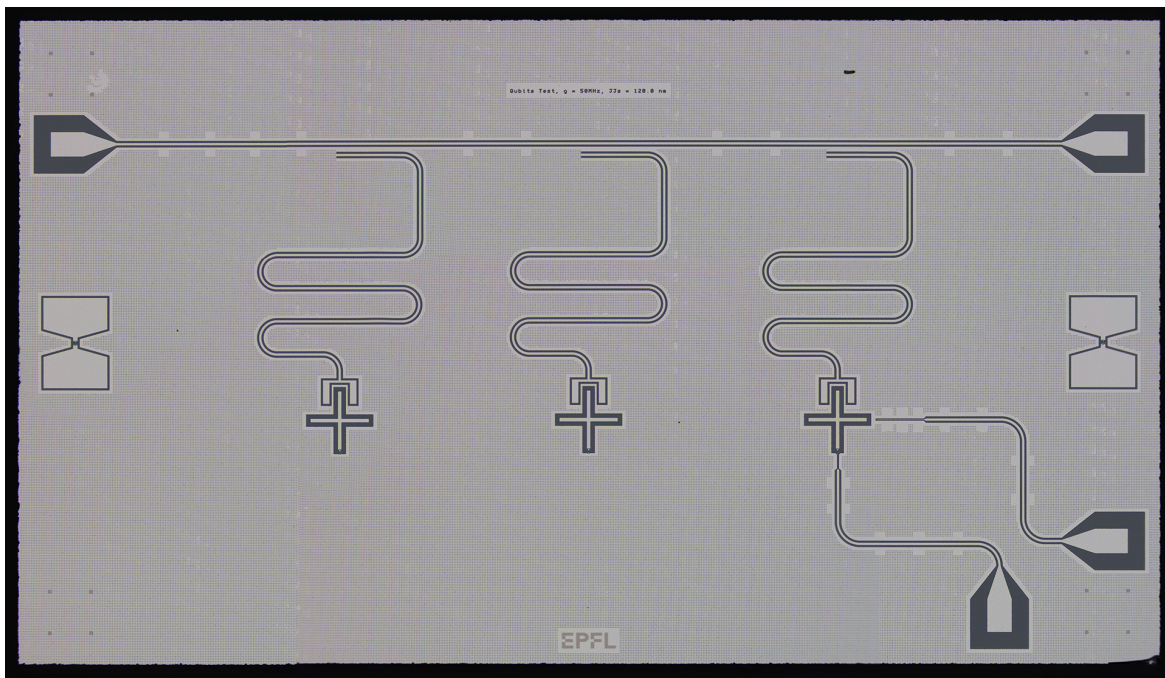


Figure C.6 | Single Qubits. $7 \times 4 \text{ mm}^2$ chip with three variations of a single qubit design. The devices were made out of Al on high-resistivity Si wafer. The first qubit is made out of a single Josephson junction to reduce losses and aim to maximum T_1 , the second is made out of a double junction, and the third is made of two junctions and coupled to both a drive (XY) and flux (Z) lines.

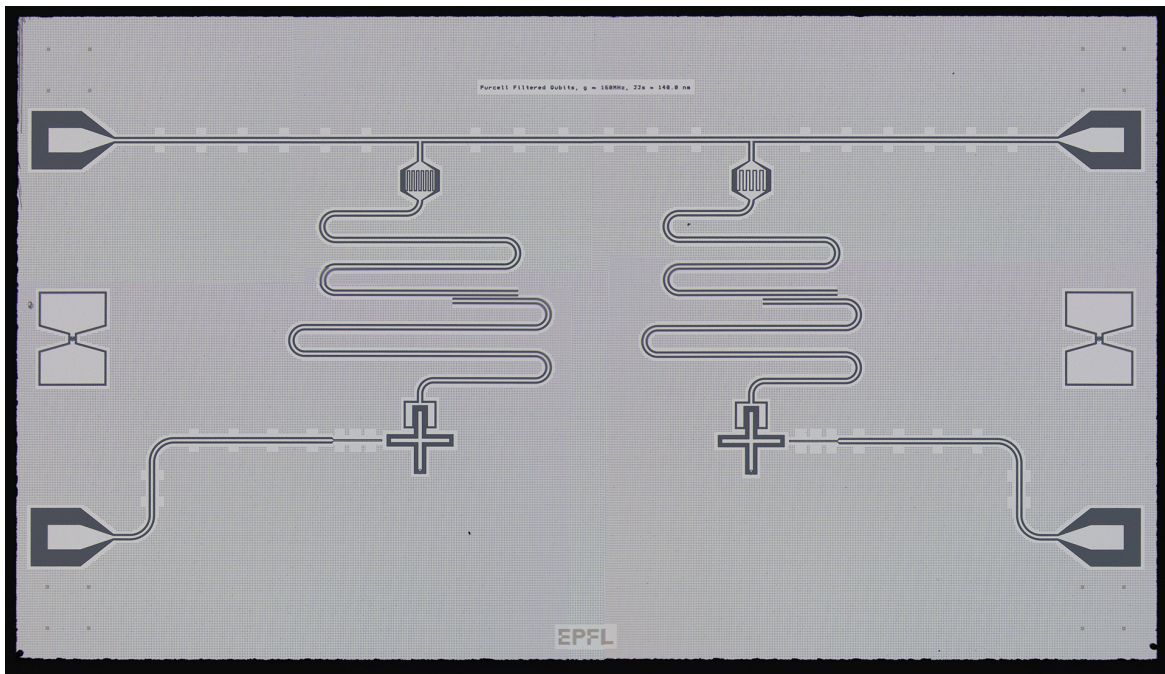


Figure C.7 | Qubits with Purcell filters. $7 \times 4 \text{ mm}^2$ chip with two variations of a single qubit design with Purcell filters. The devices were made out of Al on high-resistivity Si wafer. The qubits are made out of a single Josephson junction to reduce losses and aim to maximum T_1 and coupled to a drive (XY) line. The main differences between the two variants are related to the couplings κ_r and Q_F .

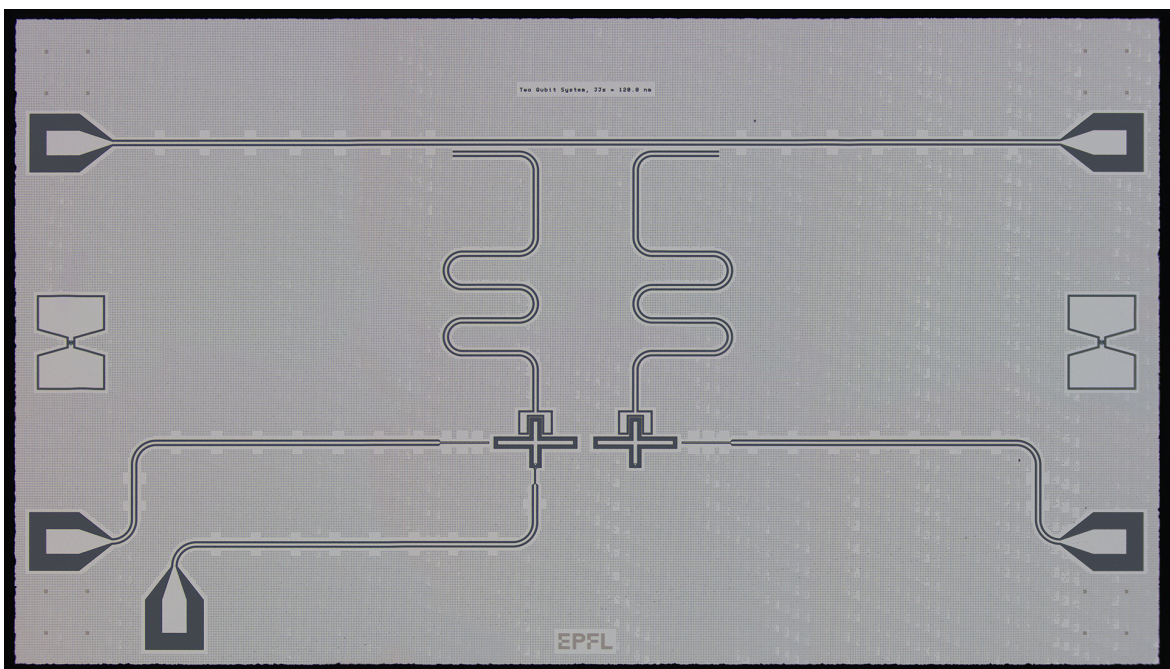


Figure C.8 | Two Qubits processor. 7×4 mm² chip with two coupled qubits. The devices were made out of Al on high-resistivity Si wafer. The goal of this design was to benchmark simple two-qubits gates.

LIST OF FIGURES

Figure 2.1	Disorder analysis of bias–sputtered superconducting thin films in NbN	14
Figure 2.2	Transmission Electron Micrographs (TEMs) of NbN	16
Figure 2.3	Disorder analysis of three plasmas-sputtered superconducting thin films in NbTiN	20
Figure 3.1	Bosch process schematics	24
Figure 3.2	Bosch process	25
Figure 3.3	Sharp process	26
Figure 3.4	DREM process	27
Figure 3.5	Sputtering effect of Cr mask	27
Figure 3.6	Bias Frequency effect on Cr mask.	29
Figure 3.7	Holes depth vs trench depth	30
Figure 3.8	Analysis of the deep reactive ion etching processes	31
Figure 3.9	Michelangelo process	32
Figure 3.10	metallization of the through-silicon vias	33
Figure 3.11	Cu electroplating process.	34
Figure 3.12	Metal infiltration process.	35
Figure 3.13	Metal infiltration TSVs	36
Figure 4.1	Working principle of superconducting nanowire single–photon detectors	40
Figure 4.2	Fabrication of a meandered pixel SNSPD	42
Figure 4.3	Fabrication and optimization of the Bragg reflector	43
Figure 4.4	SNSPDs optical stack simulations	44
Figure 4.5	Thin films estimation of depairing current	46
Figure 4.6	SNSPDs preliminary measurements	47
Figure 4.7	SNSPDs quantum efficiency measurements	49
Figure 4.8	SNSPDs jitter fitting routine	51
Figure 4.9	SNSPDs jitter–efficiency correlation	53
Figure 5.1	nTron operations	56
Figure 5.2	nTron and a_x Tron schematics	58
Figure 5.3	nTrons characterization setup	59
Figure 5.4	nTrons temperature dependence	60

Figure 5.5	Comparison between nTrons and a_x Trons	61
Figure 5.6	nTrons failure causes	62
Figure 6.1	Resonators micrograph and spectrum	66
Figure 6.2	Resonator fitting functions result	68
Figure 6.3	Quality factor dependence on kinetic inductance of high- L_k hanged resonators	70
Figure 6.4	Kerr nonlinearity factor dependence on kinetic inductance of high- L_k hanged resonators	71
Figure 6.5	TLS and aging analysis of high- L_k hanged resonators	73
Figure 6.6	Temperature dependence of internal quality factor	74
Figure 6.7	Impedance matching taper	76
Figure 6.8	Impedance matching tapers transmission spectra	77
Figure 6.9	Stepped impedance microwave filter	79
Figure 6.10	Measured filters transmission spectra for different number of pairs	80
Figure 6.11	Measured filters transmission spectra at different biasing conditions	81
Figure 6.12	Measured filters transmission spectra at different biasing conditions	82
Figure 7.1	Qubits Chip	88
Figure 7.2	Transmon Qubit	89
Figure 7.3	HQC Laboratory Setup	90
Figure 7.4	Qubit Punch-out and flux tunability	91
Figure 7.5	Chevron Pattern	92
Figure 7.6	Relaxation Time	93
Figure 7.7	Purcell Relaxation	94
Figure 7.8	Decoherence Measurements	95
Figure 7.9	Fidelity measurement	97
Figure A.1	Process Flow of SNSPDs	102
Figure A.2	Process Flow of Superconducting Circuits	103
Figure A.3	Process flow of through-silicon vias.	104
Figure A.4	Process Flow of Transmons	105
Figure A.5	Atomic force microscopy scan of the surface roughness of SiO ₂	107
Figure A.6	Scanning Electron Micrographs of dose test structures on PMMA and ZEP	110
Figure A.7	Scanning Electron Micrographs of SNSPDs with IBE and RIE	112
Figure A.8	Scanning Electron Micrographs of dry and wet etching of Al	113

Figure A.9	Cavity materials ellipsometry results	114
Figure B.1	PhotonSpot cryostat	118
Figure B.2	PhotonSpot optical table	120
Figure B.3	PhotonSpot setup	121
Figure B.4	BlueFors setup	124
Figure B.5	BlueFors cryostat	126
Figure C.1	Full-scale wafer	129
Figure C.2	Impedance matching taper	130
Figure C.3	Microwave stepped impedance filter	130
Figure C.4	Impedance matching taper coupled to a microwave stepped impedance filter	131
Figure C.5	Hanged resonators	131
Figure C.6	Single Qubits	132
Figure C.7	Qubits with Purcell filters	132
Figure C.8	Two Qubits processor	133

LIST OF TABLES

Table 1.1	Comparison of Single–Photon Detectors.	6
Table 2.1	NbN Sputtering Deposition Parameters.	15
Table 2.2	TiN Atomic Layer Deposition relevant recipes parameters (values for 4000 ALD cycles).	19
Table 2.3	NbTiN Sputtering Deposition Parameters.	21
Table 3.1	DRIE Processes.	28
Table 3.2	Metals considered for the infiltration process.	36
Table B.1	Nonlinear Crystals	122
Table B.2	Origami 10-100 Specs.	123

BIBLIOGRAPHY

- [1] H. K. Onnes, “*research notebooks 56, 57*”, Kamerlingh Onnes Archive, Boerhaave Museum, Leiden, the Netherlands (1911).
- [2] M. Tinkham, *Introduction to Superconductivity*, Dover Books on Physics Series (Dover Publications, 2004).
- [3] W. Meissner and R. Ochsenfeld, “*Ein neuer effekt bei eintritt der supraleitfähigkeit*”, *Naturwissenschaften* **21**, 787 (1933).
- [4] V. L. Ginzburg, L. D. Landau, and V. L. Ginzburg, “*On the theory of superconductivity*”, in *On Superconductivity and Superfluidity: A Scientific Autobiography* (Springer Berlin Heidelberg, Berlin, Heidelberg, 2009) pp. 113–137.
- [5] J. Bardeen, L. N. Cooper, and J. R. Schrieffer, “*Microscopic theory of superconductivity*”, *Phys. Rev.* **106**, 162 (1957).
- [6] J. Bardeen, L. N. Cooper, and J. R. Schrieffer, “*Theory of superconductivity*”, *Phys. Rev.* **108**, 1175 (1957).
- [7] L. N. Cooper, “*Bound electron pairs in a degenerate fermi gas*”, *Phys. Rev.* **104**, 1189 (1956).
- [8] B. T. Matthias, T. H. Geballe, S. Geller, and E. Corenzwit, “*Superconductivity of Nb_3Sn* ”, *Phys. Rev.* **95**, 1435 (1954).
- [9] M. K. Wu *et al.*, “*Superconductivity at 93 K in a new mixed-phase Y-Ba-Cu-O compound system at ambient pressure*”, *Phys. Rev. Lett.* **58**, 908 (1987).
- [10] E. Snider *et al.*, “*Room-temperature superconductivity in a carbonaceous sulfur hydride*”, *Nature* **586**, 373 (2020).
- [11] J. E. Kunzler, E. Buehler, F. S. L. Hsu, and J. H. Wernick, “*Superconductivity in Nb_3Sn at high current density in a magnetic field of 88 kgauss*”, *Phys. Rev. Lett.* **7**, 215 (1961).
- [12] Y. Nakamura, Y. A. Pashkin, and J. S. Tsai, “*Coherent control of macroscopic quantum states in a single-Cooper-pair box*”, *Nature* **398**, 786 (1999).

- [13] J. M. Martinis, S. Nam, J. Aumentado, and C. Urbina, “Rabi oscillations in a large Josephson-junction qubit”, *Phys. Rev. Lett.* **89**, 117901 (2002).
- [14] J. M. Martinis and K. Osborne, “Superconducting qubits and the physics of Josephson junctions”, *arXiv e-prints*, arXiv:0402.415 (2004).
- [15] J. Clarke and F. K. Wilhelm, “Superconducting quantum bits”, *Nature* **453**, 1031 (2008).
- [16] K. Sternickel and A. I. Braginski, “Biomagnetism using SQUIDs: status and perspectives”, *Superconductor Science and Technology* **19**, S160 (2006).
- [17] G. N. Gol’tsman *et al.*, “Picosecond superconducting single-photon optical detector”, *Appl. Phys. Lett.* **79**, 705 (2001).
- [18] P. Day, H. Leduc, B. A Mazin, A. Vayonakis, and J. Zmuidzinas, “A broadband superconducting detector suitable for use in large arrays”, *Nature* **425**, 817 (2003).
- [19] B. Korzh *et al.*, “Provably secure and practical quantum key distribution over 307 km of optical fibre”, *Nature Photonics* **9**, 163 (2015).
- [20] A. Boaron *et al.*, “Secure quantum key distribution over 421 km of optical fiber”, *Phys. Rev. Lett.* **121**, 190502 (2018).
- [21] A. N. McCaughan, *Superconducting thin film nanoelectronics*, Ph.D. thesis (2015).
- [22] A. N. McCaughan and K. K. Berggren, “A superconducting-nanowire three-terminal electrothermal device”, *Nano Letters* **14**, 5748 (2014).
- [23] B. D. Josephson, “Possible new effects in superconductive tunnelling”, *Physics Letters* **1**, 251 (1962).
- [24] P. W. Anderson, “Theory of dirty superconductors”, *J. Phys. Chem. Solids* **11**, 26 (1959).
- [25] R. Meservy and P. M. Tedrow, “Measurements of the kinetic inductance of superconducting linear structures”, *Journal of Applied Physics* **40**, 2028 (1969).
- [26] W. A. Little, “Decay of persistent currents in small superconductors”, *Phys. Rev.* **156**, 396 (1967).
- [27] F. London and H. London, “The electromagnetic equations of the supraconductor”, *Proc. R. Soc. Lond.* **149**, 71 (1935).

- [28] S. Anlage, H. Snortland, and M. Beasley, “A current controlled variable delay superconducting transmission line”, *IEEE Transactions on Magnetics* **25**, 1388 (1989).
- [29] A. J. Annunziata *et al.*, “Tunable superconducting nanoinductors”, *Nanotechnology* **21**, 445202 (2010).
- [30] D. Niegce, J. Burnett, and J. Bylander, “High kinetic inductance NbN nanowire superinductors”, *Phys. Rev. Applied* **11**, 044014 (2019).
- [31] D. H. Andrews, W. F. Brucksch, W. T. Ziegler, and E. R. Blanchard, “Attenuated superconductors I. for measuring infrared radiation”, *Review of Scientific Instruments* **13**, 281 (1942).
- [32] R. H. Hadfield, “Single-photon detectors for optical quantum information applications”, *Nature Photonics* **3**, 696 EP (2009).
- [33] K. M. Rosfjord *et al.*, “Nanowire single-photon detector with an integrated optical cavity and anti-reflection coating”, *Opt. Express* **14**, 527 (2006).
- [34] H. Takesue *et al.*, “Quantum key distribution over a 40-dB channel loss using superconducting single-photon detectors”, *Nature Photonics* **1**, 343 (2007).
- [35] G. G. Taylor *et al.*, “Photon counting LiDAR at 2.3 μm wavelength with superconducting nanowires”, *Opt. Express* **27**, 38147 (2019).
- [36] M. Ejrnaes *et al.*, “A cascade switching superconducting single photon detector”, *Applied Physics Letters* **91**, 262509 (2007).
- [37] Q.-Y. Zhao *et al.*, “Single-photon imager based on a superconducting nanowire delay line”, *Nat. Photonics* **11**, 247 (2017).
- [38] S. K. Tolpygo *et al.*, “Superconductor electronics fabrication process with MoN_x kinetic inductors and self-shunted josephson junctions”, *IEEE Transactions on Applied Superconductivity* **28**, 1 (2018).
- [39] E. Charbon *et al.*, “Cryo-cmos for quantum computing”, in *2016 IEEE International Electron Devices Meeting (IEDM)* (2016) pp. 13.5.1–13.5.4.
- [40] X. Xue *et al.*, “CMOS-based cryogenic control of silicon quantum circuits”, *Nature* **593**, 205 (2021).

- [41] S. K. Tolpygo *et al.*, “Developments toward a 250-nm, fully planarized fabrication process with ten superconducting layers and self-shunted Josephson junctions”, in *2017 16th International Superconductive Electronics Conference (ISEC)* (2017) pp. 1–3.
- [42] P. A. ’t Hart *et al.*, “Characterization and model validation of mismatch in nanometer CMOS at cryogenic temperatures”, in *2018 48th European Solid-State Device Research Conference (ESSDERC)* (2018) pp. 246–249.
- [43] P. A. ’t Hart, M. Babaie, E. Charbon, A. Vladimirescu, and F. Sebastiano, “Characterization and modeling of mismatch in cryo-CMOS”, *IEEE Journal of the Electron Devices Society* **8**, 263 (2020).
- [44] P. A. ’t Hart *et al.*, “Artificial neural network modelling for cryo-CMOS devices”, in *2021 IEEE 14th Workshop on Low Temperature Electronics (WOLTE)* (2021) pp. 1–4.
- [45] A. N. McCaughan *et al.*, “A superconducting thermal switch with ultrahigh impedance for interfacing superconductors to semiconductors”, *Nature Electronics* **2**, 451 (2019).
- [46] K. Zheng *et al.*, “A superconducting binary encoder with multigate nanowire cryotrons”, *Nano Letters* **20**, 3553 (2020).
- [47] Y. Liu and A. A. Houck, “Quantum electrodynamics near a photonic bandgap”, *Nature Physics* **13**, 48 (2017).
- [48] A. J. Sigillito, A. M. Tyryshkin, T. Schenkel, A. A. Houck, and S. A. Lyon, “All-electric control of donor nuclear spin qubits in silicon”, *Nature Nanotechnology* **12**, 958 (2017).
- [49] M. Colangelo *et al.*, “Compact and tunable forward coupler based on high-impedance superconducting nanowires”, *Phys. Rev. Applied* **15**, 024064 (2021).
- [50] A. Wallraff *et al.*, “Strong coupling of a single photon to a superconducting qubit using circuit quantum electrodynamics”, *Nature* **431**, 162 (2004).
- [51] A. P. M. Place *et al.*, “New material platform for superconducting transmon qubits with coherence times exceeding 0.3 milliseconds”, *Nature Communications* **12**, 1779 (2021).
- [52] L. Grünhaupt *et al.*, “Granular aluminium as a superconducting material for high-impedance quantum circuits”, *Nat. Mater.* **18**, 816 (2019).

- [53] P. Winkel *et al.*, “Implementation of a transmon qubit using superconducting granular aluminum”, *Phys. Rev. X* **10**, 031032 (2020).
- [54] D. Rieger *et al.*, “Gralmonium: Granular aluminum nano-junction fluxonium qubit”, *arXiv e-prints*, arXiv:2202.01776 (2022).
- [55] A. J. Kerman *et al.*, “Constriction-limited detection efficiency of superconducting nanowire single-photon detectors”, *Applied Physics Letters* **90**, 101110 (2007).
- [56] J. Allmaras, A. Kozorezov, B. Korzh, K. Berggren, and M. Shaw, “Intrinsic timing jitter and latency in superconducting nanowire single-photon detectors”, *Phys. Rev. Applied* **11**, 034062 (2019).
- [57] V. B. Verma *et al.*, “Single-photon detection in the mid-infrared up to 10 μm wavelength using tungsten silicide superconducting nanowire detectors”, *APL Photonics* **6**, 056101 (2021).
- [58] A. E. Dane *et al.*, “Bias sputtered NbN and superconducting nanowire devices”, *Applied Physics Letters* **111**, 122601 (2017).
- [59] D. M. Glowacka, D. J. Goldie, S. Withington, H. Muhammad, and G. Yassin, “Development of a NbN deposition process for superconducting quantum sensors”, *arXiv e-prints*, arXiv:1401.2276 (2014).
- [60] D. Depla and R. D. Gryse, “Target poisoning during reactive magnetron sputtering: Part I: the influence of ion implantation”, *Surface and Coatings Technology* **183**, 184 (2004).
- [61] D. Depla and R. D. Gryse, “Target poisoning during reactive magnetron sputtering: Part II: the influence of chemisorption and gettering”, *Surface and Coatings Technology* **183**, 190 (2004).
- [62] D. Depla and R. D. Gryse, “Target poisoning during reactive magnetron sputtering: Part III: the prediction of the critical reactive gas mole fraction”, *Surface and Coatings Technology* **183**, 196 (2004).
- [63] T. Suntola, “Atomic layer epitaxy”, *Thin Solid Films* **216**, 84 (1992).
- [64] L. Hiltunen *et al.*, “Nitrides of titanium, niobium, tantalum and molybdenum grown as thin films by the atomic layer epitaxy method”, *Thin Solid Films* **166**, 149 (1988).
- [65] K.-E. Elers, M. Ritala, M. Leskelä, and E. Rauhala, “NbCl₅ as a precursor in atomic layer epitaxy”, *Applied Surface Science* **82-83**, 468 (1994).

- [66] M. Ritala *et al.*, “Effects of intermediate zinc pulses on properties of TiN and NbN films deposited by atomic layer epitaxy”, *Applied Surface Science* **120**, 199 (1997).
- [67] M. Ziegler *et al.*, “Superconducting niobium nitride thin films deposited by metal organic plasma-enhanced atomic layer deposition”, *Superconductor Science and Technology* **26**, 025008 (2012).
- [68] M. Ukibe and G. Fujii, “Superconducting characteristics of NbN films deposited by atomic layer deposition”, *IEEE Transactions on Applied Superconductivity* **27**, 1 (2017).
- [69] M. J. Sowa *et al.*, “Plasma-enhanced atomic layer deposition of superconducting niobium nitride”, *Journal of Vacuum Science & Technology A* **35**, 01B143 (2017).
- [70] P. Pizzol *et al.*, “Atomic Layer Deposition of Niobium Nitride from Different Precursors”, in *8th International Particle Accelerator Conference (IPAC 2017)* (2017) p. MOPVA100.
- [71] E. Knehr *et al.*, “Nanowire single-photon detectors made of atomic layer-deposited niobium nitride”, *Superconductor Science and Technology* **32**, 125007 (2019).
- [72] G. G. Taylor *et al.*, “Infrared single-photon sensitivity in atomic layer deposited superconducting nanowires”, *Applied Physics Letters* **118**, 191106 (2021).
- [73] C. Sheagren, P. Barry, E. Shirokoff, and Q. Y. Tang, “Atomic layer deposition niobium nitride films for high-Q resonators”, *J. Low Temp. Phys.* **199**, 875 (2020).
- [74] M. Ziegler *et al.*, “Effects of plasma parameter on morphological and electrical properties of superconducting NbN deposited by MO-PEALD”, *IEEE Transactions on Applied Superconductivity* **27**, 1 (2017).
- [75] S. Xie, J. Cai, Q. Wang, L. Wang, and Z. Liu, “Properties and morphology of TiN films deposited by atomic layer deposition”, *Tsinghua Science and Technology* **19**, 144 (2014).
- [76] C. H. Ahn, S. G. Cho, H. J. Lee, K. H. Park, and S. H. Jeong, “Characteristics of TiN thin films grown by ALD using $TiCl_4$ and NH_3 ”, *Metals and Materials International* **7**, 621 (2001).
- [77] H. Machhadani *et al.*, “Improvement of the critical temperature of NbTiN films on III-nitride substrates”, *Superconductor Science and Technology* **32**, 035008 (2019).

- [78] B. Abeles, R. W. Cohen, and W. R. Stowell, “Critical magnetic fields of granular superconductors”, *Phys. Rev. Lett.* **18**, 902 (1967).
- [79] R. W. Cohen and B. Abeles, “Superconductivity in granular aluminum films”, *Phys. Rev.* **168**, 444 (1968).
- [80] L. Grünhaupt *et al.*, “Loss mechanisms and quasiparticle dynamics in superconducting microwave resonators made of thin-film granular aluminum”, *Phys. Rev. Lett.* **121**, 117001 (2018).
- [81] N. Maleeva *et al.*, “Circuit quantum electrodynamics of granular aluminum resonators”, *Nat. Commun.* **9**, 3889 (2018).
- [82] V. B. Verma *et al.*, “A four-pixel single-photon pulse-position array fabricated from WSi superconducting nanowire single-photon detectors”, *Applied Physics Letters* **104**, 051115 (2014).
- [83] M. S. Allman *et al.*, “A near-infrared 64-pixel superconducting nanowire single photon detector array with integrated multiplexed readout”, *Applied Physics Letters* **106**, 192601 (2015).
- [84] E. E. Wollman *et al.*, “Kilopixel array of superconducting nanowire single-photon detectors”, *Opt. Express* **27**, 35279 (2019).
- [85] S. Miki, T. Yamashita, Z. Wang, and H. Terai, “A 64-pixel NbTiN superconducting nanowire single-photon detector array for spatially resolved photon detection”, *Opt. Express* **22**, 7811 (2014).
- [86] D. R. W. Yost *et al.*, “Solid-state qubits integrated with superconducting through-silicon vias”, *npj Quantum Information* **6**, 59 (2020).
- [87] T. Xu, Z. Tao, H. Li, X. Tan, and H. Li, “Effects of deep reactive ion etching parameters on etching rate and surface morphology in extremely deep silicon etch process with high aspect ratio”, *Advances in Mechanical Engineering* **9**, 12 (2017).
- [88] M. Motoyoshi, “Through-silicon via (TSV)”, *Proceedings of the IEEE* **97**, 43 (2009).
- [89] W.-W. Shen and K.-N. Chen, “Three-dimensional integrated circuit (3D IC) key technology: Through-silicon via (TSV)”, *Nanoscale Research Letters* **12**, 56 (2017).

- [90] J. P. Gambino, S. A. Adderly, and J. U. Knickerbocker, “An overview of through-silicon-via technology and manufacturing challenges”, *Microelectronic Engineering* **135**, 73 (2015).
- [91] F. Roozeboom, F. van den Bruele, Y. Creyghton, P. Poodt, and W. M. M. Kessels, “Cyclic etch/passivation-deposition as an all-spatial concept toward high-rate room temperature atomic layer etching”, *ECS Journal of Solid State Science and Technology* **4**, N5067 (2015).
- [92] J. Yeom, Y. Wu, J. C. Selby, and M. A. Shannon, “Maximum achievable aspect ratio in deep reactive ion etching of silicon due to aspect ratio dependent transport and the microloading effect”, *Journal of Vacuum Science & Technology B: Microelectronics and Nanometer Structures Processing, Measurement, and Phenomena* **23**, 2319 (2005).
- [93] B. Chang, P. Leussink, F. Jensen, J. Hübner, and H. Jansen, “DREM: Infinite etch selectivity and optimized scallop size distribution with conventional photoresists in an adapted multiplexed Bosch DRIE process”, *Microelectronic Engineering* **191**, 77 (2018).
- [94] J. Parasuraman *et al.*, “Deep reactive ion etching of sub-micrometer trenches with ultra high aspect ratio”, *Microelectronic Engineering* **113**, 35 (2014).
- [95] H. Jansen, M. de Boer, J. Burger, R. Legtenberg, and M. Elwenspoek, “The black silicon method II: The effect of mask material and loading on the reactive ion etching of deep silicon trenches”, *Microelectronic Engineering* **27**, 475 (1995).
- [96] F. Marty *et al.*, “Advanced etching of silicon based on deep reactive ion etching for silicon high aspect ratio microstructures and three-dimensional micro- and nanostructures”, *Microelectronics Journal* **36**, 673 (2005).
- [97] M. D. Henry, S. Walavalkar, A. Homyk, and A. Scherer, “Alumina etch masks for fabrication of high-aspect-ratio silicon micropillars and nanopillars”, *Nanotechnology* **20**, 255305 (2009).
- [98] M. Shearn, X. Sun, M. D. Henry, A. Yariv, and A. Scherer, “Advanced plasma processing: Etching, deposition, and wafer bonding techniques for semiconductor applications”, in *Semiconductor Technologies*, edited by J. Grym (IntechOpen, Rijeka, 2010) Chap. 5.
- [99] A. Bagolini, P. Scauso, S. Sanguinetti, and P. Bellutti, “Silicon deep reactive ion etching with aluminum hard mask”, *Materials Research Express* **6**, 085913 (2019).

- [100] K. J. Owen, B. VanDerElzen, R. L. Peterson, and K. Najafi, "High aspect ratio deep silicon etching", in *2012 IEEE 25th International Conference on Micro Electro Mechanical Systems (MEMS)* (2012) pp. 251–254.
- [101] S. Killge, V. Neumann, and J. W. Bartha, "Copper-based TSV: Interposer", in *3D Stacked Chips: From Emerging Processes to Heterogeneous Systems*, edited by I. A. M. Elfadel and G. Fettweis (Springer International Publishing, Cham, 2016) pp. 9–28.
- [102] T. Wei *et al.*, "Optimization and evaluation of sputtering barrier/seed layer in through silicon via for 3-D integration", *Tsinghua Science and Technology* **19**, 150 (2014).
- [103] P. Lin *et al.*, "Effects of silicon via profile on passivation and metallization in TSV interposers for 2.5D integration", *Microelectronic Engineering* **134**, 22 (2015).
- [104] N. Ranganathan *et al.*, "Influence of bosch etch process on electrical isolation of TSV structures", *IEEE Transactions on Components, Packaging and Manufacturing Technology* **1**, 1497 (2011).
- [105] S.-S. Yun, S.-K. You, and J.-H. Lee, "Fabrication of vertical optical plane using DRIE and KOH crystalline etching of (110) silicon wafer", *Sensors and Actuators A: Physical* **128**, 387 (2006).
- [106] A. Brucolieri *et al.*, "Potassium hydroxide polishing of nanoscale deep reactive-ion etched ultrahigh aspect ratio gratings", *Journal of Vacuum Science & Technology B* **31**, o6FF02 (2013).
- [107] F. Wang, Z. Zhao, N. Nie, F. Wang, and W. Zhu, "Dynamic through-silicon-via filling process using copper electrochemical deposition at different current densities", *Scientific Reports* **7**, 46639 (2017).
- [108] F. Marsili *et al.*, "Detecting single infrared photons with 93% system efficiency", *Nature Photonics* **7**, 210 EP (2013).
- [109] D. V. Reddy *et al.*, "Exceeding 95% system efficiency within the telecom C-band in superconducting nanowire single photon detectors", in *Conference on Lasers and Electro-Optics* (2019) p. FF1A.3.
- [110] X. Zhang, Q. Wang, and A. Schilling, "Superconducting single X-ray photon detector based on $W_{0.8}Si_{0.2}$ ", *AIP Advances* **6**, 115104 (2016).

- [111] A. Korneev, Y. Korneeva, I. Florya, B. Voronov, and G. Gol'tsman, "NbN nanowire superconducting single-photon detector for mid-infrared", *Physics Procedia* **36**, 72 (2012).
- [112] E. E. Wollman *et al.*, "UV superconducting nanowire single-photon detectors with high efficiency, low noise, and 4 K operating temperature", *Opt. Express* **25**, 26792 (2017).
- [113] A. Engel *et al.*, "Temperature-dependence of detection efficiency in NbN and TaN SNSPD", *IEEE Trans. Appl. Supercond.* **23**, 2300505 (2013).
- [114] J. J. Renema *et al.*, "Experimental test of theories of the detection mechanism in a nanowire superconducting single photon detector", *Phys. Rev. Lett.* **112**, 117604 (2014).
- [115] R. Lusche *et al.*, "Effect of the wire width on the intrinsic detection efficiency of superconducting-nanowire single-photon detectors", *J. Appl. Phys.* **116**, 043906 (2014).
- [116] J. J. Renema *et al.*, "The effect of magnetic field on the intrinsic detection efficiency of superconducting single-photon detectors", *Appl. Phys. Lett.* **106**, 092602 (2015).
- [117] F. Marsili *et al.*, "Hotspot relaxation dynamics in a current-carrying superconductor", *Phys. Rev. B* **93**, 094518 (2016).
- [118] R. Gaudio *et al.*, "Experimental investigation of the detection mechanism in WSi nanowire superconducting single photon detectors", *Appl. Phys. Lett.* **109**, 031101 (2016).
- [119] M. Caloz *et al.*, "Optically probing the detection mechanism in a molybdenum silicide superconducting nanowire single-photon detector", *Appl. Phys. Lett.* **110**, 083106 (2017).
- [120] J. R. Clem and V. G. Kogan, "Kinetic impedance and depairing in thin and narrow superconducting films", *Phys. Rev. B* **86**, 174521 (2012).
- [121] L. N. Bulaevskii, M. J. Graf, and V. G. Kogan, "Vortex-assisted photon counts and their magnetic field dependence in single-photon superconducting detectors", *Phys. Rev. B* **85**, 014505 (2012).
- [122] D. Y. Vodolazov, Y. P. Korneeva, A. V. Semenov, A. A. Korneev, and G. N. Gol'tsman, "Vortex-assisted mechanism of photon counting in a superconducting

- nanowire single-photon detector revealed by external magnetic field”, Phys. Rev. B **92**, 104503 (2015).*
- [123] A. G. Kozorezov *et al.*, “*Quasiparticle recombination in hotspots in superconducting current-carrying nanowires*”, Phys. Rev. B **92**, 064504 (2015).
- [124] A. Engel, J. Lonsky, X. Zhang, and A. Schilling, “*Detection mechanism in SNSPD: Numerical results of a conceptually simple, yet powerful detection model*”, IEEE Trans. Appl. Supercond. **25**, 1 (2015).
- [125] D. Y. Vodolazov, “*Single-photon detection by a dirty current-carrying superconducting strip based on the kinetic-equation approach*”, Phys. Rev. Applied **7**, 034014 (2017).
- [126] A. G. Kozorezov *et al.*, “*Fano fluctuations in superconducting-nanowire single-photon detectors*”, Phys. Rev. B **96**, 054507 (2017).
- [127] S. Jahani *et al.*, “*Probabilistic vortex crossing criterion for superconducting nanowire single-photon detectors*”, arXiv e-prints , arXiv:1901.09291 (2019).
- [128] A. J. Annunziata *et al.*, “*Reset dynamics and latching in niobium superconducting nanowire single-photon detectors*”, Journal of Applied Physics **108**, 084507 (2010).
- [129] T. Gerrits *et al.*, “*Calibration of free-space and fiber-coupled single-photon detectors*”, Metrologia **57**, 015002 (2019).
- [130] R. Baghdadi *et al.*, “*Enhancing the performance of superconducting nanowire-based detectors with high-filling factor by using variable thickness*”, Superconductor Science and Technology **34**, 035010 (2021).
- [131] O. Quaranta *et al.*, “*Superconductive three-terminal amplifier/discriminator*”, IEEE Transactions on Applied Superconductivity **19**, 367 (2009).
- [132] S. Pagano *et al.*, “*Nano-strip three-terminal superconducting device for cryogenic detector readout*”, IEEE Transactions on Applied Superconductivity **21**, 717 (2011).
- [133] K. Zheng *et al.*, “*Characterize the switching performance of a superconducting nanowire cryotron for reading superconducting nanowire single photon detectors*”, Scientific Reports **9**, 16345 (2019).
- [134] A. N. McCaughan, N. S. Abebe, Q.-Y. Zhao, and K. K. Berggren, “*Using geometry to sense current*”, Nano Letters **16**, 7626 (2016).

- [135] Q.-Y. Zhao, A. N. McCaughan, A. E. Dane, K. K. Berggren, and T. Ortlepp, "A nanocryotron comparator can connect single-flux-quantum circuits to conventional electronics", *Superconductor Science and Technology* **30**, 044002 (2017).
- [136] Q.-Y. Zhao *et al.*, "A compact superconducting nanowire memory element operated by nanowire cryotrons", *Superconductor Science and Technology* **31**, 035009 (2018).
- [137] V. E. Manucharyan, J. Koch, L. I. Glazman, and M. H. Devoret, "Fluxonium: Single Cooper-pair circuit free of charge offsets", *Science* **326**, 113 (2009).
- [138] N. A. Masluk, I. M. Pop, A. Kamal, Z. K. Minev, and M. H. Devoret, "Microwave characterization of Josephson junction arrays: Implementing a low loss superinductance", *Phys. Rev. Lett.* **109**, 137002 (2012).
- [139] J. Gao, *The Physics of Superconducting Microwave Resonators*, Ph.D. thesis (2008).
- [140] C. R. H. McRae *et al.*, "Materials loss measurements using superconducting microwave resonators", *Rev. Sci. Instrum.* **91**, 091101 (2020).
- [141] J. Gao *et al.*, "A semiempirical model for two-level system noise in superconducting microresonators", *Applied Physics Letters* **92**, 212504 (2008).
- [142] M. S. Khalil, M. J. A. Stoutimore, F. C. Wellstood, and K. D. Osborn, "An analysis method for asymmetric resonator transmission applied to superconducting devices", *Journal of Applied Physics* **111**, 054510 (2012).
- [143] L. J. Swenson *et al.*, "Operation of a titanium nitride superconducting microresonator detector in the nonlinear regime", *Journal of Applied Physics* **113**, 104501 (2013).
- [144] D. J. Parker *et al.*, "Degenerate parametric amplification via three-wave mixing using kinetic inductance", *Phys. Rev. Applied* **17**, 034064 (2022).
- [145] C. Eichler and A. Wallraff, "Controlling the dynamic range of a josephson parametric amplifier", *EPJ Quantum Technology* **1**, 2 (2014).
- [146] A. Anferov, A. Suleymanzade, A. Oriani, J. Simon, and D. I. Schuster, "Millimeter-wave four-wave mixing via kinetic inductance for quantum devices", *Phys. Rev. Applied* **13**, 024056 (2020).
- [147] D. P. Pappas, M. R. Vissers, D. S. Wisbey, J. S. Kline, and J. Gao, "Two level system loss in superconducting microwave resonators", *IEEE Transactions on Applied Superconductivity* **21**, 871 (2011).

- [148] M. Scigliuzzo *et al.*, “*Phononic loss in superconducting resonators on piezoelectric substrates*”, *New Journal of Physics* **22**, 053027 (2020).
- [149] R. Barends *et al.*, “*Minimizing quasiparticle generation from stray infrared light in superconducting quantum circuits*”, *Applied Physics Letters* **99**, 113507 (2011).
- [150] J. Lee and T. R. Lemberger, “*Penetration depth $\lambda(T)$ of $YBa_2Cu_3O_{7-\delta}$ films determined from the kinetic inductance*”, *Applied Physics Letters* **62**, 2419 (1993).
- [151] R. W. Klopfenstein, “*A transmission line taper of improved design*”, *Proceedings of the IRE* **44**, 31 (1956).
- [152] R. E. Collin, “*The optimum tapered transmission line matching section*”, *Proceedings of the IRE* **44**, 539 (1956).
- [153] D. F. Santavicca, J. K. Adams, L. E. Grant, A. N. McCaughan, and K. K. Berggren, “*Microwave dynamics of high aspect ratio superconducting nanowires studied using self-resonance*”, *Journal of Applied Physics* **119**, 234302 (2016).
- [154] K. Bladh, T. Duty, D. Gunnarsson, and P. Delsing, “*The single Cooper-pair box as a charge qubit*”, *New Journal of Physics* **7**, 180 (2005).
- [155] J. Koch *et al.*, “*Charge-insensitive qubit design derived from the Cooper pair box*”, *Phys. Rev. A* **76**, 042319 (2007).
- [156] J. A. Schreier *et al.*, “*Suppressing charge noise decoherence in superconducting charge qubits*”, *Phys. Rev. B* **77**, 180502 (2008).
- [157] R. Barends *et al.*, “*Superconducting quantum circuits at the surface code threshold for fault tolerance*”, *Nature* **508**, 500 (2014).
- [158] F. Arute *et al.*, “*Quantum supremacy using a programmable superconducting processor*”, *Nature* **574**, 505 (2019).
- [159] P. Krantz *et al.*, “*A quantum engineer’s guide to superconducting qubits*”, *Appl. Phys. Rev.* **6**, 021318 (2019).
- [160] E. A. Sete, J. M. Martinis, and A. N. Korotkov, “*Quantum theory of a bandpass Purcell filter for qubit readout*”, *Phys. Rev. A* **92**, 012325 (2015).
- [161] T. Walter *et al.*, “*Rapid high-fidelity single-shot dispersive readout of superconducting qubits*”, *Phys. Rev. Applied* **7**, 054020 (2017).

- [162] A. Potts, “CMOS compatible fabrication methods for submicron Josephson junction qubits”, *IEE Proceedings - Science, Measurement and Technology* **148**, 225 (2001).
- [163] A. Blais, A. L. Grimsmo, S. M. Girvin, and A. Wallraff, “Circuit quantum electrodynamics”, *Rev. Mod. Phys.* **93**, 025005 (2021).
- [164] E. L. Hahn, “Spin echoes”, *Phys. Rev.* **80**, 580 (1950).
- [165] A. Osman *et al.*, “Simplified Josephson-junction fabrication process for reproducibly high-performance superconducting qubits”, *Applied Physics Letters* **118**, 064002 (2021).
- [166] D. J. Carbaugh, S. Kaya, and F. Rahman, “Lithographic tone reversal in optical exposure of polymethyl methacrylate (PMMA) resist”, *Materials Research Express* **6**, 045308 (2019).
- [167] F. Pobell, *Matter and Methods at Low Temperatures* (Springer Berlin Heidelberg, 2007).

Simone Frasca

Curriculum Vitae

Avenue du Mont-d'Or 40
Lausanne 1007, Switzerland
☎ No: +41 78 722 09 43
✉ simone.frasca@epfl.ch
🌐 people.epfl.ch/simone.frasca
🎓 Simone Frasca
linkedin Simone Frasca
✉ simofras712

Personal information

Gender Male
Place of Birth Naples, Italy
Date of Birth December 7th, 1992
Nationality Italian

Work Experience

- September 2018 – **Doctoral Assistant, EPFL at Microcity, Neuchâtel, Switzerland.**
January 2023 **Project Title:** MEMS based Gamma Ray Detectors for Time-of-Flight Positron Emission Tomography, SNF Sinergia
Project Description: Aim of the project is to develop ultrafast sensors working in the NUV-visible spectrum, to allow an increase of resolution of the PET systems.
Mentor: Prof. Edoardo Charbon
- June 2017 – **Research Affiliate, NASA's Jet Propulsion Laboratory, Pasadena, CA, USA.**
August 2018 **Project Title:** Fundamental Limits of Photon Detection (DETECT), DARPA/DSO
Project Description: Try to establish the first-principles limits of photon detector performance.
Mentor: Dr. Matt Shaw; **Co-Mentors:** Dr. Boris Korzh, Dr. Emma Wollman
- August 2016 – **Research for Master's Thesis, JVRSP Program, NASA's Jet Propulsion Laboratory, Pasadena, CA, USA.**
March 2017 **Project Title:** High-T_C superconducting devices based on MgB₂
Project Description: Characterization of devices based on single pixel MgB₂ superconducting nanowires: single pixel superconducting nanowire single photon detectors (SNSPDs).
Mentor: Dr. Francesco Marsili; **Co-Mentors:** Dr. Matt Shaw, Dr. Angel E. Velasco

Education

- 2018 – 2023 **Ph.D. Candidate in Microsystems and Microelectronics.**
École Polytechnique Fédérale de Lausanne (EPFL), Lausanne, Switzerland.
Laboratory: Advanced Quantum Architecture Laboratory (AQUA)
Thesis: *High-Kinetic Inductance Superconducting Technology for Quantum Applications*
Tutor: Prof. Edoardo Charbon
- 2014 – 2017 **Master of Science in Space Engineering, 110/110 cum laude.**
University of Pisa, Pisa, Italy.
Thesis: *Superconducting Nanowire Single Photon Detectors based on Magnesium Diboride.*
Tutor: Prof. Alessandro A. Quarta; **Co-Tutors:** Dr. Francesco Marsili, Dr. Matt Shaw
- 2011 – 2014 **Bachelor of Science in Aerospace Engineering, 104/110.**
University of Naples "Federico II", Naples, Italy.
Thesis: *Sensibility to Model Parameters of the ICP Algorithm for Autonomous Relative Pose Tracking.*
Tutor: Prof. Giancarlo Rufino; **Co-Tutor:** Dr. Roberto Opronolla

Skills

Computer Languages and Softwares

Programming	MATLAB, Python, C/C++, Arduino, LabVIEW, Simulink
FEM Analysis	Nastran/Patran, ANSYS Workbench, Comsol
CAD Design	Catia V5 – Mechanical Design, SolidWorks, Autodesk's Inventor Professional, EAGLE, ExpressPCB
General Utilities	MS Office, L ^A T _E X, OriginLab, Adobe's Photoshop, Affinity Photo
Operative Systems	Windows, MacOS X, Linux (Ubuntu, RedHat)

Laboratory

Optics	Ultrafast Nonlinear Optics
Cryogenics	Cryogenic System Design and Assembly
Electronics	Ultralow-Noise, High-Speed, RF Electronics, Superconductivity

Fabrication

Deposition	RF Sputtering, Atomic Layer Deposition, Evaporation
Lithography	e-beam Lithography, Photolithography
Etching	Plasma Etching, Deep Reactive Ion Etching, Wet Etching
Metrology	Scanning Electron Microscopy, Focused Ion Beam, Atomic Force Microscopy, Ellipsometry

Languages

Italian	Native speaker	
English	Fluent	TOEFL iBT Score: 96 (December 2017)
French	Intermediate	
Spanish	Intermediate	

Prizes and Awards

2020	EPFL Special Prize for Outstanding Performance , Lausanne, Switzerland. <i>Price awarded for research merit</i>
2020	EPFL PhD Retreat , Les Diablerets, Switzerland. <i>Best Poster Award</i>
2018	683.WE-Heraeus-Seminar on Physics and Applications of Superconducting Nanowire Single Photon Detectors , Bad Honnef, Germany. <i>Best Poster Award</i>
2016	UniPi "Thesis Abroad" Scholarship , University of Pisa, Pisa, Italy. <i>Scholarship awarded for academic merit</i>
2012, 2014	A.Di.S.U. Scholarship , University of Naples "Federico II", Naples, Italy. <i>Scholarship awarded for academic merit</i>
2011	Certamen Nazionale di Matematica "Renato Caccioppoli" , Naples, Italy. <i>First Place Nation-wise</i>
2009 – 2011	Olimpiadi della Matematica , Naples, Italy. <i>Classified to Final Phase</i>
2005	Campionati Italiani dei Giochi Matematici , Bocconi University, Milan, Italy. <i>Classified to Final Phase</i>

Conferences and Workshops

- August 30 – **NCCR SPIN Annual Meeting.**
September 1, 2021 Convention Center, Pontresina, CH
- June 2–4, 2021 **International Workshop on Cryogenic Electronics for Quantum Systems.**
Online
- October 31 – **2020 IEEE Nuclear Science Symposium and Medical Imaging Conference.**
November 7, 2020 Online
- July 22–26, 2019 **18th International Workshop on Low Temperature Detectors.**
Auditorium G. Testori, Milano, ITA
- June 17–20, 2019 **International Workshop on Cryogenic Electronics for Quantum Systems.**
Wilson Hall, Fermi National Accelerator Laboratory, Batavia, IL, USA
- June 6–7, 2019 **Swiss Nano Convention 2019.**
SwissTech Convention Center, Lausanne, CH
- November 12–16, 2018 **683.WE-Heraeus-Seminar on Physics and Applications of Superconducting Nanowire Single Photon Detectors.**
Physickzentrum, Bad Honnef, GER
- December 7–8, 2017 **DARPA/DSO Detect Theory and Technical Exchange Meeting.**
National Institute of Standards and Technology (NIST), Boulder, CO, USA
Team composition: JPL, MIT, NIST and University of Lancaster

Academic Activities

Master Thesis Supervisor

- July 2021 – **Periodic structure filters for optics and superconducting microwave applications.**
Student: Bros de Puechredon, Sébastien (MSc student in Microengineering, EPFL)
- February 2021 – **Fabrication and characterization of nano-cryotrons based on NbN and NbTiN material systems.**
July 2021 Student: Arabadzhiev, Ivo Nikolaev (MSc student in Microengineering, EPFL)

Internship Supervisor

- June 2022 – **Design, fabrication and characterization of Purcell filters in superconducting transmon qubits.**
Student: Musio, Roberto (MSc student in Micro- and nanotechnologies for integrated systems, PoliTo/INPG/EPFL)
- February 2022 – **Fabrication of 3D Superconducting Resonators.**
May 2022 Student: Milward, Philippine (MSc student in Microengineering, EPFL)
- TiN film Atomic Layer Deposition, patterning and characterization for test resonators and 3D capacitors.**
Student: Parma, Giuliano (MSc student in Microengineering, EPFL)
- July 2021 – **Optimization of process parameters for Atomic Layer Deposition of Titanium Nitride.**
September 2021 Student: Dhaliwal, Jashandeep (MSc student in Micro- and nanotechnologies for integrated systems, PoliTo/INPG/EPFL)
- September 2020 – **Superconducting and Optical Characterization of NbTiN Ultrathin Films made by Co-Sputtering.**
March 2021 Student: Arabadzhiev, Ivo Nikolaev (MSc student in Microengineering, EPFL)

Investigation of superconducting nanowire performance of different thin films via superconducting nanowire resonators.

Student: Bros de Puechredon, Sébastien (MSc student in Microengineering, EPFL)

Characterization of Scintillating Crystals with Different Coating Techniques.

Student: Di Stadio, David (MSc student in Microengineering, EPFL)

Fabrication of 2.5D Microstructures Using Single-Shot DRIE and Metal Infiltration.

Student: Nicolet-dit-Félix, Kléber (MSc student in Microengineering, EPFL)

Development of Atomic Layer Deposition of Superconducting Niobium Nitride and Titanium Nitride.

Student: Suter, Louis (MSc student in Microengineering, EPFL)

February 2020 – **Development of Graphic User Interface for Unified Mesurement Setup for SNSPDs.**

Student: Bros de Puechredon, Sébastien (MSc student in Microengineering, EPFL)

Optical simulations of SNSPD stack for multispectral absorption using COMSOL.

Student: Suter, Louis (MSc student in Microengineering, EPFL)

September 2019 – **Fabrication of Amorphous-Silicon Microchannel Plates.**

March 2020 Student: Pasquier, Benoît (MSc student in Microengineering, EPFL)

Fabrication of superconducting high aspect ratio Though-Silicon Vias.

Student: Tomassi, Gregoire (MSc student in Microengineering, EPFL)

February 2019 – **Investigation of NbTiN ultrathin films variations on different substrates.**

July 2019 Student: Arabadzhiev, Ivo Nikolaev (MSc student in Microengineering, EPFL)

Fabrication of high aspect ratio Though-Silicon Vias.

Student: Leghziel, Rebecca Camilla (MSc student in Microengineering, EPFL)

Teaching Assistant

A.Y. 2022–2023 **MICRO-435 – Quanntum and Nanocomputing.**

Lecturers: E. Charbon, M. Graziano

Main Tasks: Presented one class on Superconducting Qubits.

A.Y. 2021–2022 **MICRO-428 – Metrology.**

Lecturers: E. Charbon, C. Bruschini, G. Fantner

Main Tasks: Presented one class on Quantum Metrology.

A.Y. 2018–2019, **MICRO-428 – Metrology.**

2019–2020, Lecturers: E. Charbon, C. Bruschini, G. Fantner, I. Vardi

2020–2021 Main Tasks: Exercise sessions. Main focus on Statistics, Optical and Quantum Metrology sections. Presented one class on Quantum Metrology.

MICRO-406 – Products design and system engineering.

Lecturers: Y. Bellouard and E. Charbon

Main Tasks: Supervision of the project groups.

References

Edoardo Charbon.

Chair at VLSI, École Polytechnique Fédérale de Lausanne

Head of AQUA Laboratory, École Polytechnique Fédérale de Lausanne

edoardo.charbon@epfl.ch

Pasquale Scarlino.

Tenure Track Assistant Professor, École Polytechnique Fédérale de Lausanne
Head of HQC Laboratory, École Polytechnique Fédérale de Lausanne
pasquale.scarlino@epfl.ch

Matt D. Shaw.

Superconducting Materials and Devices Section, Jet Propulsion Laboratory
mattshaw@jpl.nasa.gov

Boris A. Korzh.

Superconducting Materials and Devices Section, Jet Propulsion Laboratory
Boris.A.Korzh@jpl.nasa.gov

Alessandro A. Quarta.

Professor at University of Pisa, Department of Civil and Industrial Engineering
a.quarta@ing.unipi.it